CHEMICAL REVIEWS

pubs.acs.org/CR

Review

Noble-Metal Based Random Alloy and Intermetallic Nanocrystals: Syntheses and Applications

Ming Zhou, Can Li, and Jiye Fang*

Cite This: *Chem. Rev.* 2021, 121, 736−795

Read Online

ACCESS | Metrics & More | Article Recommendations

ABSTRACT: Precise control over the size, shape, composition, structure, and crystal phase of random alloy and intermetallic nanocrystals has been intensively explored in technologically important applications in recent years. Different from the monometallic nanocrystals and other types of structural nanocrystals such as core−shell and heterostructured nanocrystals, well-defined multimetallic random alloy and intermetallic nanocrystals exhibit unique and intriguing physicochemical properties, serving as ideal models for benefiting the structure-to-property studies. As such, random alloy and intermetallic nanocrystals have attracted extensive attention and interest in scientific research and shown huge potential in various fields. In this review, we focus specifically on summarizing the synthetic principles and strategies developed to form random alloy and intermetallic nanocrystals with enhanced performance. Some representative examples are purposely selected for emphasizing basic concepts and mechanistic understanding. We then highlight the fascinating properties and widespread applications of random alloy and intermetallic nanocrystals in electrocatalysis, heterogeneous catalysis, optical and photocatalysis, as well as magnetism and conclude the review by addressing the prospects and current challenges for the controlled synthesis of random alloy and intermetallic nanocrystals.

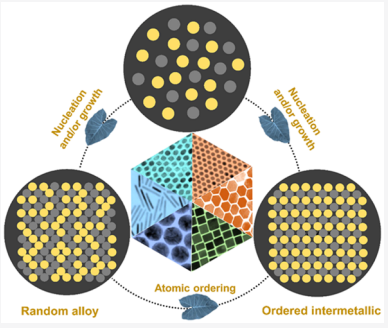

CONTENTS

Special Issue: Advanced Materials and Methods for Catalysis and Electrocatalysis by Transition Metals

Received: May 11, 2020
Published: September 9, 2020

https://dx.doi.org/10.1021/acs.chemrev.0c00436
Chem. Rev. 2021, 121, 736−795

1. INTRODUCTION

Metals, covering more than 75% of the elements in the periodic table, have received wide recognition due to their extensive applications in photonics, catalysis, energy storage and conversion, electronics, and medicine.[1−17] Especially, the metals in a finely divided state known as nanocrystals generally exhibit fascinating properties that are radically different from the bulk materials. It has been widely demonstrated that the intriguing properties of metal nanocrystals mainly stem from the surface effect and quantum size effect that can be manipulated in terms of size, shape, composition, structure, and crystal phase.[18−32] A notable example can be found in Au, where Au nanocrystals showed remarkable catalytic activity for low-temperature carbon monoxide (CO) oxidation even though bulk Au is inactive for this reaction.[33,34] Inspired by this incredible discovery, tremendous efforts have been devoted to developing a wide variety of synthetic approaches to controllably synthesize metal nanocrystals for greatly enhancing their performance over the past two decades.[35−49]

Despite the great success, it is well-documented that monometallic nanocrystals generally cannot meet all the requirements in practical applications, where metal nanocrystals are anticipated to simultaneously possess high activity, high chemical and structural stability, high selectivity, and low cost. To potentially meet all of these requirements, in recent years it has drawn increasing attention in the development of well-defined multimetallic nanocrystals with fascinating performance. Multimetallic nanocrystals composed of distinct metal elements exhibit unique physicochemical properties that are superior to monometallic nanocrystals for a given application due to synergetic effects associated with different metals.[50−59] Typically, the incorporation of a second metal for the formation of bimetallic nanocrystals can dramatically alter their electronic structures and spatial arrangement modes, further benefiting the unprecedented improvement in performance.[60−66] For example, the electrochemical activity toward oxygen reduction reaction (ORR) can be markedly intensified with the incorporation of a 3d transition metal M (M = Ni, Co, Fe, or Cu, etc.) into Pt nanocrystals for the formation of Pt−M bimetallic nanocrystals.[67−76] By incorporating heterometals together, the Pt−M bimetallic nanocrystals could be used not only to endow a bifunctionality but also to greatly reduce the overall cost by decreasing the use of Pt. Additional example further showed that the localized surface plasmon resonance (LSPR) properties of Au nanocrystals can be further improved through alloying with Ag.[23] This strategy has been easily expanded to syntheses of other multimetallic nanocrystals with desirable properties: for example, the synthesis of hexoctahedral $Au_{89}Pd_{11}$ nanocrystals with enhanced electrocatalytic performance toward formic acid oxidation reaction (FAOR), the preparation of pentacle $Au_{86}Cu_{14}$ nanocrystals with enhanced LSPR property and catalytic activity toward the reduction of p-nitrophenol, and the fabrication of rhombic dodecahedral $Ir_{38}Ni_{28}Cu_{34}$ nanoframes (NFs) with enhanced electrocatalytic activity toward oxygen evolution reaction (OER).[21,53,77−91] Aiming at further optimization of their properties, it is of critical importance to rationally manipulate the experimental parameters to synthesize the multimetallic nanocrystals with well-defined size, shape, composition, structure and crystal phase, as their expressed properties strongly depend on these structural parameters.[18,92−104]

The physical structures of multimetallic nanocrystals are known to be multitudinous and complicated.[105−107] In some cases, these multimetallic nanocrystals might present entirely different properties, even though they have the same composition and stoichiometry.[105,108−110] It has been proven that these performance differences can be ascribed to the variation in atomic-scale features (e.g., atomic ordering, spatial element distribution, and surface structure). For example, Cui and co-workers recently demonstrated that ordered intermetallic Pd_3Mn nanocrystals exhibit superior electrocatalytic activity toward ORR as compared with their counterparts in a disordered phase.[111] Sun and co-workers also confirmed that the chemical stability and electrocatalytic activity of FePt nanocrystals toward ORR and hydrogen evolution reaction (HER) could be greatly improved by changing their crystal phase from the atomically disordered phase to the ordered phase.[112] Therefore, it is inappropriate to simply use "composition" to define multimetallic nanocrystals, and thus increasingly attention have been turned to the development of new synthetic protocols to purposefully modulate the atomic-scale features of multimetallic nanocrystals.[113−119]

An alloy generally refers to a single-phase solid solution consisting of mixed metallic components, while part of which could also be a nonmetallic element(s) (e.g., steel). When the atoms of alloy constituents are randomly distributed across the lattice, it can be designed as a random alloy. When the atoms of the components form a structurally ordered solid-state alloy and occupy the lattice with a specific atom stoichiometry, it is conventionally called an intermetallic compound. The ordered atomic arrangements in an intermetallic structure could be isotropic or in a specific crystallographic direction, depending on the stoichiometry and the formation conditions,[10,12,105] but intermetallics always have a long-range atomic ordering. As such, these features endow the intermetallic compounds with unique properties and applications, which is considerably different from other structured nanocrystals such as core−shell and heterostructured nanocrystals.[120−126] It has been well-established that the interconversion between random alloy and intermetallic nanocrystals can be readily achieved when the specific condition (e.g., temperature, stoichiometry, and atom binding environment) is met, significantly facilitating structure-to-property studies.[31,112,127−132] Among them, noble-metal based multimetallic nanocrystals have received comprehensive concern by the many researchers around the world, due to their excellent activities and stabilities. In recent years, it has become a field of active research related to the synthesis of random alloy and intermetallic nanocrystals by rationally manipulating the atomic ordering, due to their remarkable properties toward a broad range of applications.[30,133−143] A large number of such studies have not only deepened our understanding of their fascinating nanoscale properties but also showed the great potential of these noble−metal-based multimetallic nanocrystals in various fields.[92,141,144−148]

https://dx.doi.org/10.1021/acs.chemrev.0c00436
Chem. Rev. 2021, 121, 736−795

Table 1. Some Typical Noble Metal-Based Intermetallic Nanocrystals Reported Previously[a]

intermetallic formula	crystal structure	preparation conditions	ICDD PDF card	literature
Pt_3Ti	Cu_3Au, $Pm\bar{3}m$	Pt_3Ti random alloy annealed at 600 °C, 12 h	03-065-3259	ref 165
Pt_3V	Cu_3Au, $Pm\bar{3}m$	Pt_3V random alloy annealed at 650−700 °C, 24 h	01-072-3016	ref 166
Pt_3Cr	Cu_3Au, $Pm\bar{3}m$	Pt_3Cr random alloy annealed at 700 °C, 24 h	01-071-7609	ref 135
Pt_3Mn	Cu_3Au, $Pm\bar{3}m$	$Pt(acac)_2$ + $Mn(acac)_2$ OAm/OA at 200 °C, 0.5 h	01-071-9674	ref 167
Pt_3Co	Cu_3Au, $Pm\bar{3}m$	Pt_3Co random alloy annealed at 700 °C, 2 h	01-071-7410	ref 168
Pt_3Fe	Cu_3Au, $Pm\bar{3}m$	Pt_3Fe random alloy annealed at 600 °C, 12 h	JCPDS: 29-0716	ref 169
PtFe	AuCu, *P4/mmm*	Pt−Fe random alloy annealed at 700 °C	JCPDS: 65-1051	refs 128, 157, and 161
PtNi	AuCu, *P4/mmm*	$Pt(acac)_2$ + $Ni(acac)_2$ $KBH(Et)_3$ in THF, RT	01-072-2524	ref 170
$PtFe_3$	Cu_3Au, $Pm\bar{3}m$	$PtFe_3$ random alloy annealed at 600 °C, 12 h	01-071-8365	ref 136
$PtCu_3$	Cu_3Au, $Pm\bar{3}m$	$PtCu_3$ random alloy annealed at 1000 °C, 10 h	03-065-3247	ref 171
Pt_3Zn	Cu_3Au, $Pm\bar{3}m$	$Pt(acac)_2$ + $Zn(acac)_2$ PVP in DMF at 180 °C, 9 h	01-072-3028	ref 172
Pt_3Zn	Cu_3Au, $Pm\bar{3}m$	$Pt(acac)_2$ + $Zn(acac)_2$ OAm/OA at 350 °C, 1 h	01-072-3028	ref 173
PtZn	AuCu, *P4/mmm*	Pt/C + Zn chips, heated at 500 °C, 8 h	01-072-3027	ref 174
Pt_3Sn	Cu_3Au, $Pm\bar{3}m$	H_2PtCl_6 + $SnCl_2$, DDA + HDD, at 300 °C, 0.5 h	01-072-2977	ref 175
PdFe	AuCu, *P4/mmm*	PdFe random alloy annealed at 500 °C, 2 h	01-089-2051	ref 176
$Au_{10}Pd_{40}Co_{50}$	AuCu, *P4/mmm*	$Au_{10}Pd_{40}Co_{50}$ random alloy annealed at 800 °C, 0.5 h	01-071-7394 (for PdCo)	ref 177
PdCu	CsCl, $Pm\bar{3}m$	PdCu random alloy annealed at 400 °C	01-080-4575	ref 138
PdCu	CsCl, $Pm\bar{3}m$	PdCu random alloy annealed at 375 °C, 1h	01-080-4575	ref 129
PdZn	AuCu, *P4/mmm*	$Pd_2(dba)_3$ + Et_2Zn OAm at 250 °C, 1 h	01-072-2936	ref 178
Pd_3Pb	Cu_3Au, $Pm\bar{3}m$	Pd/C + $Pb(Ac)_2$, EG, microwave 300W, 0.1 h	01-089-2062	ref 179
Pd_3Fe	Cu_3Au, $Pm\bar{3}m$	Pd_3Fe random alloy annealed at 600 °C, 24 h	JCPDS: 65-7280	ref 110
Cu_3Au	Cu_3Au, $Pm\bar{3}m$	$Cu(Ac)_2$ + Au nanoparticles OAm/OA at 300 °C	01-088-1731	ref 180
AuCu	AuCu, *P4/mmm*	$HAuCl_4$ + $CuCl_2$, glycerol at 300 °C, 5 h	01-089-2037	ref 181
AuCu	AuCu, *P4/mmm*	AuCu random alloy annealed at 500 °C, 12 h	01-089-2037	ref 182
RhBi	NiAs, $P6_3/mmc$	$Bi(Ac)_3$ + $Rh_2(Ac)_4$, EG, microwave 1.6 kW, 240 °C, 1 h		ref 183
Au_3Fe	Cu_3Au, $Pm\bar{3}m$	$HAuCl_4$ + $Fe(acac)_3$, reduced by *n*-butyllithium in OAm and octyl ether at 250 °C		ref 184
Au_3Co	Cu_3Au, $Pm\bar{3}m$	$HAuCl_4$ + $Co(acac)_2$, reduced by *n*-butyllithium in OAm and octyl ether at 250 °C		ref 184
Au_3Ni	Cu_3Au, $Pm\bar{3}m$	$HAuCl_4$ + $Ni(acac)_2$, reduced by *n*-butyllithium in OAm and octyl ether at 250 °C		ref 184
PtBi/Pt	NiAs, $P6_3/mmc$ (PtBi core)	$Pt(acac)_2$ + $Bi(Ac)_3$ in NH_4Br/OAm/1-octadecene,160 °C, 5 h		ref 122

[a]Adapted with permission from ref 130, and modified. Copyright 2019 National Academy of Sciences, USA. Note: the related abbreviations: $Bi(Ac)_3$: bismuth(III) acetate; DDA: dodecylamine; DMF: N,N-dimethylformamide; EG: ethylene glycol; Et_2Zn: diethylzinc; HDD: 1,2-hexadecandiol; $Co(acac)_2$: cobalt(II) acetylacetonate; $Fe(acac)_3$: iron(III) acetylacetonate; $Mn(acac)_2$: manganese(II) acetylacetonate; $Ni(acac)_2$: nickel(II) acetylacetonate; OA: oleic acid; OAm: oleylamine; $Pb(Ac)_2$: lead(II) acetate; $Pd_2(dba)_3$: tris(dibenzylideneacetone)dipalladium(0); PVP: poly(vinylpyrrolidone); $Pt(acac)_2$: platinum(II) acetylacetonate; $Rh_2(Ac)_4$: rhodium acetate dimer; THF: tetrahydrofuran; $Zn(acac)_2$: zinc(II) acetylacetonate.

Although there have been several review articles focusing on random alloy nanocrystals or ordered intermetallic nanocrystals of some specific metals in recent years,[1,5,32,92,93,99,123] a comprehensive outline on noble−metal-based random alloy and intermetallic nanocrystals simultaneously covering their synthetic approaches and applications is still intriguing. It should be worth noting that some of the representative articles are carefully selected to highlight the latest advances as much as possible. The goal of this review is to summarize recent advances related to the syntheses and applications of noble-metal based random alloy and intermetallic nanocrystals. In particular, we highlight the formation mechanisms and the most commonly practiced approaches for syntheses capable of preparing random alloy and intermetallic nanocrystals with tunable and well-controlled properties. After that, we further place a special emphasis on their fascinating properties and widespread applications, including electrocatalysis, heterogeneous catalysis, photocatalysis, as well as optics and magnetism. Finally, we address some of the current challenges and developing trends associated with the controllable synthesis of random alloy and intermetallic nanocrystals based on the previous summary.

2. GENERAL PRINCIPLES FOR THE FORMATION OF RANDOM ALLOY AND INTERMETALLIC NANOCRYSTALS

2.1. Atomic Ordering

As mentioned above, the nanocrystals can be broadly classified into random alloys and atomic-ordered intermetallic compounds.[1,10,12] An intermetallic compound is reserved for alloys that have strict stoichiometry, atomically ordered arrangement, and a well-defined atom binding environment. It should be pointed out that the atomic-scale features including spatial arrangement, atomic ordering, and faceting are critically important parameters to determine their expressed physicochemical properties. Especially, random alloys and intermetallic compounds typically exhibit markedly different properties even if they possess the same atomic ratio and elemental

https://dx.doi.org/10.1021/acs.chemrev.0c00436
Chem. Rev. 2021, 121, 736−795

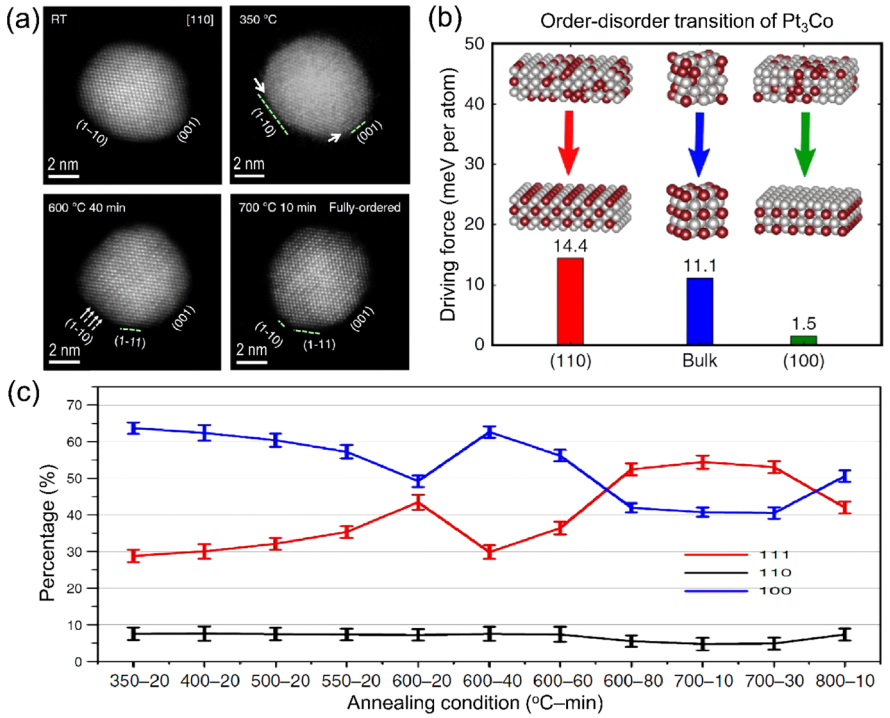

Figure 1. (a) Atomic-resolution HAADF-STEM images of a single Pt_3Co nanoparticle obtained at different temperatures and annealing times. (b) A comparison of the driving force for forming ordered structures at different crystallographic facets and in the bulk derived from DFT calculations. (c) Changes in the percentages of the surface facets, for example, {111}, {110}, and {100}, as a function of annealing condition. Adapted with permission from ref 131 and modified. Copyright 2015 Nature Publishing Group under [Creative Commons Attribution 4.0 International License] [http://creativecommons.org/licenses/by/4.0/].

composition. Thermodynamically, the favorable positions for atoms in the lattice are largely associated with atomic radii, atomic interactions, and lattice parameters.[12] Note that the formation of thermodynamically stable alloys will be favorable during the synthesis when both metallic compositions meet the Hume–Rothery rules: (i) an atomic radii discrepancy of less than 15%; (ii) the similar crystal lattices and electronegativities; (iii) the same valence state.[149] In some cases, the assistance of extra heating is also required to facilitate the interdiffusion of atoms and to avail of an alloy formation, especially for the systems with relatively low reaction temperature that cannot effectively ensure the atoms to reach their favorable positions via a diffusion process.[150,151]

In theory, the generation of ordered intermetallic compounds is energetically more favorable than disordered alloys at low temperatures due to the low entropy associated with the ordered arrangement of atoms and the negative value of the change in enthalpy derived from the higher bonding energy in intermetallics.[152] Some typical noble metal-based intermetallic nanocrystals with information such as crystal structure and preparation conditions that were reported previously are given in Table 1. However, the formation of alloys with disordered atomic arrangements seems to be prevalent instead of ordered intermetallic compounds in most of the practical syntheses, since their synthetic temperatures that are usually below the critical phase-transition temperature can not greatly facilitate the interdiffusion with the high-activation-energy barrier and equilibration. In recent years, ordered intermetallic compounds have gained increasing interest due to their remarkable performance and highly controllable compositions and surface structures.[66,129,153−164] Consequently, an in-depth understanding of the effects governed by the thermodynamic and kinetic parameters and the achievement in the synthesis of high-quality ordered intermetallic nanocrystals are essential.

2.2. Thermodynamic and Kinetic Perspective on Random Alloy and Intermetallic Nanocrystals

2.2.1. Thermodynamic Analysis. For simplicity, here we mainly focus on the ideal bimetallic system. In a bulk system, the excess Gibbs free energy upon mixing can be defined by the changes in enthalpy (ΔH_{mix}) and entropy (ΔS_{mix}) during the formation of a random alloy or intermetallic compound:[1,12,185−187]

$$\Delta G_{mix} = \Delta H_{mix} - T\Delta S_{mix} \quad (1)$$

where T is the absolute temperature. Typically, when ΔG_{mix} is negative, a random alloy or intermetallic compound should form spontaneously under a given set of experimental conditions, resulting in dramatically lowering the overall free energy. It should be mentioned that the change in entropy is generally believed to be always positive upon mixing different metals, and thus the generation of a random alloy or intermetallic compound is entropically favorable. According to eq 1, it is not difficult to find that ΔH_{mix} value played a major role in facilitating the formation of a random alloy or intermetallic compound because $T\Delta S_{mix}$ is constantly positive. If the bond formation between different atoms is exothermic, ΔH_{mix} should be negative. As a result, ΔG_{mix} will be negative under these conditions, thereby benefiting the spontaneous formation of a random alloy or intermetallic compound.

If the mixing between different atoms is endothermic ($\Delta H_{mix} > 0$), the formation of the resultant product should be temperature-dependent. At relatively high temperatures, the contribution from entropy normally becomes much larger than that from enthalpy, the formation of a random alloy or

https://dx.doi.org/10.1021/acs.chemrev.0c00436
Chem. Rev. 2021, 121, 736−795

intermetallic compound will be favorably derived from a negative ΔG_{mix}. In contrast, ΔG_{mix} should be positive at relatively low temperatures, resulting in the segregation between different components.

In addition, eq 1 can also be applied to interpret the transition process from random alloy to ordered intermetallic. In this case, the change in entropy is usually negative due to the disorder-to-order transition, and the change in enthalpy is also negative derived from the higher bonding energy in intermetallics. As a result, low temperatures will be beneficial to the disorder-to-order transition while high temperatures will lead to a favorable transition to the disordered phase. It should be also emphasized that the critical phase-transition temperature is defined by the temperature, at which the changes in total Gibbs free energy are equal to zero.

However, the surface free energies in real systems might lead to completely different scenarios as compared to those cases predicted by the simplified and idealized model. For nanocrystals, the surface free energy has a major influence on the total free energy of the system.[8,101,185] As a result, the surface free energy should also be involved to precisely predict the changes in Gibbs free energy,[185] as given by

$$\Delta G_{mix} = \Delta H_{mix} - T\Delta S_{mix} + \Delta\gamma A \quad (2)$$

where $\Delta\gamma$ is the changes in specific surface free energy and A is the surface area of the nanocrystal. During the disorder-to-order transition, A remains constant by assuming that no shape change is observed. Note that $\Delta\gamma$ is generally positive because the ordered surface has much higher bond energy than a disordered one. To further explain the shifting of disorder-to-order phase transition temperature in nanocrystals as compared with that of the bulk, eq 3 can be established based on eq 2, where T_{nano} and T_{bulk} are the critical phase transition temperatures in nanocrystals and the bulk, respectively.[12]

$$T_{nano}/T_{bulk} = 1 + (A/V)\Delta\gamma/\Delta H_V \quad (3)$$

As is known to all, the change in volume-specific bulk enthalpy (ΔH_V) is negative and the specific surface area (A/V) is inversely proportional to the nanocrystal size.[8,15,39,188−190] Hence, according to eq 3, it suggests that smaller nanocrystals should possess lower disorder-to-order phase transition temperatures. A typical example was demonstrated by Alloyeau and co-workers,[153] who found that PtCo nanocrystals with an average size of 2.4−3 nm had phase-transition temperatures between 175−325 °C. It was well documented that these phase-transition temperatures were significantly lower than that of the bulk PtCo. In addition to the size effect, the shape of a nanocrystal could also dramatically affect the changes in Gibbs free energy,[131] since the facets exposed on a nanocrystal have a strong correlation with the shape and different facets generally possess diverse specific surface free energies. As such, it is concluded that the nanocrystal shape has a non-negligible impact on the disorder-to-order transition temperature associated with the total change in Gibbs' free energy. Obvious changes to the ratio of {100} facets during the *in situ* heating of an individual Pt_3Co nanocrystal together with the formation of the ordered intermetallic phase were observed, and the {111} facets became dominant (Figure 1). Moreover, surface segregation is often observed during the disorder-to-order transition, when the stoichiometric composition of a given nanocrystal deviates slightly from the favored ratio.[181,191−195] Overall, the size, shape, and composition of nanocrystals all have a major influence on their surface free energies and thus the disorder-to-order transition.

2.2.2. Kinetic Analysis. In contrast to thermodynamics, kinetics is affected by a variety of dynamic factors during the formation of a random alloy or intermetallic compound, where the nucleation, growth, and diffusion processes are typically involved. It is important to note that these processes are largely related to bond breaking and formation, as well as atom diffusion. Here, we mainly focus on the key factors to affect the kinetics of the disorder-to-order transition at a given temperature. According to the Johnson-Mehl-Avram-Kolmogorov (JMAK) theory,[196−198] the kinetics of transformation during the disorder-to-order transition are given by

$$f = 1 - \exp(-\pi/3Nv^3t^n) \quad (4)$$

where f is fraction transformed, N is the rate of nucleation, v is the growth rate, t is reaction time, and n is held to have an integer value between 1 and 4. Note that the transformations follow a characteristic s-shaped profile, where the transformation rates are slow at the beginning and the end of the transformation but fast in between. Specifically, many nuclei of the ordered phase form at a slow rate during the initial period, as the formation of the ordered phase is generally required to overcome the larger kinetic energy barriers to reach the thermodynamic minimum. Subsequently, the nuclei grow into nanocrystals at a fast rate and consume the disordered phase while nuclei continue to form in the remaining parent phase. The reaction rate begins to slow when the transformation approaches completion. It should be noted that many significant assumptions and simplifications are made in this equation. First, the nuclei are believed to be distributed randomly in space. Second, the growth rate is independent of the extent of transformation and also keeps at the same rate in all directions. These assumptions do not affect the qualitative trends during the kinetic analyses, so the general conclusions remain valid.

During the disorder-to-order transition, atom diffusion is found to be a kinetically controlled process that involves the motion of atoms through a jumping or hopping mechanism, facilitating atom arrangement. It should be pointed out that jumping or hopping is conceptually the most basic mechanism for adatoms diffusion, and in this model, motion occurs through successive jumps to adjacent sites, the number of which depends on the nature of the surface lattice. The rate of atom migration within a lattice (D) can be defined by considering random atomic jumping:[199,200]

$$D = D_0 \exp(-E_{diff}/RT) \quad (5)$$

where D_0 is the diffusion pre-exponential factor, E_{diff} is the energy barrier for an atom to jump from one site to another, T is the absolute temperature, and R is the ideal gas constant. It should be emphasized that D_0 is largely associated with the bonding strength and the type and effective mass of the atom.[199] In principle, weakly bonded atoms typically possess a lower defect formation energy and jumping barrier in the atom diffusion process. For example, the disorder-to-order transition in the Au−Cu system is much easier as compared to those in Pt-based systems that have relatively stronger bonding atoms.[150,180,201−204] Note that the atom diffusion process is mainly dominated by vacancy diffusion with a much lower energy barrier as compared to the atom-exchange for metals. To greatly accelerate the atom diffusion process during the disorder-to-order transition, a viable mean is to raise the

https://dx.doi.org/10.1021/acs.chemrev.0c00436
Chem. Rev. 2021, 121, 736−795

reaction temperature to facilitate the generation of vacancies or defects and atom migration in the crystal lattice. In addition to thermal activation, another effective strategy is to artificially introduce the vacancies or defects into the parent phase to speed up the diffusion process. For example, introducing Au atoms to the Pt−Fe system is employed to generate vacancies and thus achieve the phase transition.[205] This is most likely because Au atoms with low surface energy are immiscible to FePt and tend to segregate onto the FePt nanocrystal surface at 600 °C, resulting in a formation of vacancies within the nanocrystal. Furthermore, it has been well demonstrated that the size, shape, and composition of nanocrystals have a major impact on the transition kinetics due to their distinctive surface and/or interface free energies and atom diffusion rates.[154,164,177,206−216]

3. SYNTHETIC APPROACHES TO RANDOM ALLOY NANOCRYSTALS

Many efforts have been devoted to the synthesis of a rich variety of random alloy nanocrystals with well-defined size, shape, composition, and structure in the past decades.[50,54,104,120,167,217−231] Typically, the random alloy nanocrystals exhibit unique physicochemical properties, which are superior to nanocrystals consisting of individual metals. Aiming at acquiring the desired random alloy nanocrystals, it is very essential to master over the synthetic approaches. In this chapter, we mainly focus on the common approaches for the synthesis of random alloy nanocrystals and highlight their recent progress. Table 2 summarizes some representative examples related to the synthesis of random alloy nanocrystals using different approaches.

Table 2. Summary of Some Representative Random Alloy Nanocrystals with Corresponding Synthetic Approaches

synthetic approach	metal composition	morphology	reference
co-reduction	PdPt	nanosphere	refs 232 and 233
	Ag@AgAu	core−frame nanocube	ref 234
	Pt_3Ni	nanocube, nano-octahedron	ref 76
	PtCu	nanorod	ref 231
seed-mediated synthesis	AuAg, AuSn, AuPt	nanosphere	ref 235
	AuPd, AuPt, AuCu	nanowire	ref 236
	Pd@PdCu	nanocube	ref 237
	AgPt-tipped Au	nanorod	ref 238
thermal decomposition	PtFe	nanosphere, nanocube, nanowire	refs 239 and 240
galvanic replacement	AuAg	nanocage	refs 241 and 242
	PdPt	hollow nanocube	ref 243
	PdAg	triangular nanoframe	ref 244
Kirkendall effect	PtFe	hollow nanosphere	ref 103
	AuAg, AuPdAg, PdAg	double-walled nanobox	ref 245
oxidative etching	PtNi	nano-octahedron	ref 246
	Pt_3Ni	rhombic dodecahedral and tetrahexahedral nanoframe	refs 68 and 220

3.1. Co-Reduction

Co-reduction is a straightforward and versatile approach for the facile synthesis of random alloy nanocrystals, where rational choice of reducing agent, capping agent, coordination ligand, and reaction temperature all have big effects on the size, shape, composition, and structure of the final product. This approach typically involves the simultaneous reduction of two or more metal-containing precursors to charge neutral atoms, which then undergoes the nucleation and growth.[232,247−251] According to the classic nucleation theory, as proposed by LaMer and co-workers,[252] it is of critical importance to effectively separate the nucleation and growth into two distinct processes to enable tuning the size and dispersity of the resultant alloy nanocrystals in a synthetic system. It should be pointed out that the nucleation and growth processes of nanocrystals are largely related to the reduction rate of the metal precursors in solution. Therefore, the key to the successful synthesis of well-defined random alloy nanocrystals in the co-reduction process is capable of rationally modulating the reduction rate of the metal precursors.

Normally, metal ions possess intrinsic differences in reduction potential. The metal ions with higher reduction potentials are quickly reduced as compared to those with low reduction potentials under the same conditions. To enable forming alloyed nanocrystals via co-reduction, a viable means is to strategically select the metal combinations with pertinent redox potentials and possible alloy phase to ensure their matched reduction rates and the stable product. For example, Pd−Pt random alloy nanocrystals can be readily synthesized through co-reduction, due to their minor differences in reduction potentials (+0.9 V for Pd^{2+}/Pd, +1.18 V for Pt^{2+}/Pt).[232,253−257] Specifically, Sun and co-workers reported their synthesis of Pd−Pt random alloy nanocrystals by simultaneously reducing $Pd(acac)_2$ and $Pt(acac)_2$ with morpholine borane as a reducing agent in the presence of OAm as both the solvent and stabilizer (Figure 2).[232] It was revealed that the use of morpholine borane with strong reducing power and the appropriate temperature were the keys to the success of the synthesis. By simply manipulating the feeding ratio of the two precursors and reaction temperature, the composition and size of the resultant nanocrystals could be precisely controlled. They found that the atomic ratio between Pd and Pt in the final product was nearly proportional to the feeding ratio between $Pd(acac)_2$ and $Pt(acac)_2$. Subsequent studies have also demonstrated this notion.[27,257,258] Therefore, controlling the feeding ratio of precursors has become a simple and viable route to manipulate the composition of the final product. However, the small difference in reduction potentials of the precursors involved is not always essential since it might also enable the opportunity to generate core−shell nanocrystals via a one-pot approach. Skrabalak and co-workers reported that Pd−Pt core−shell nanodendrites could be formed in the presence of $Pd(acac)_2$ and $Pt(acac)_2$ (as the precursors) and OAm (as both reducing agent and solvent) at 160 °C.[233] In comparison with the work reported by Sun and co-workers,[232] it is not difficult to conclude that structures of the final product could be determined by the reducing agents (OAm vs morpholine borane/OAm) and probably the reaction temperatures (160 °C vs 60/90/180 °C) in each case, even though $Pd(acac)_2$ and $Pt(acac)_2$ that have similar reduction potentials were used as the precursors in both reports. Explicitly, to achieve a co-reduction, one needs to comprehensively design various synthetic conditions and reaction parameters such as

https://dx.doi.org/10.1021/acs.chemrev.0c00436
Chem. Rev. 2021, 121, 736−795

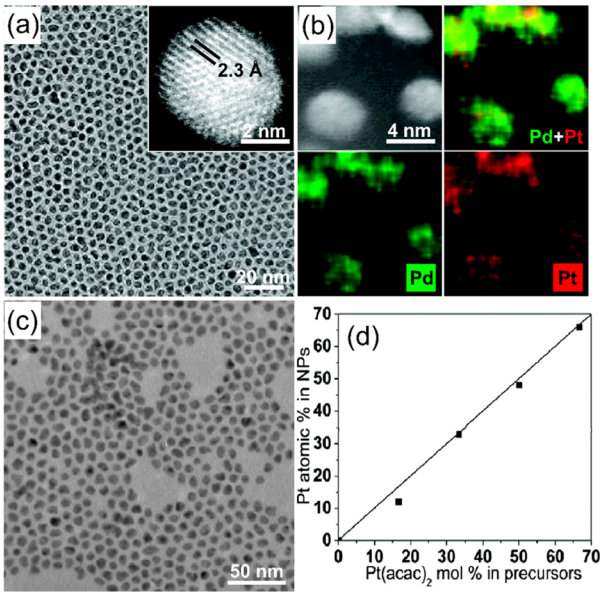

Figure 2. (a) TEM image of the 5 nm $Pd_{67}Pt_{33}$ random alloy nanocrystals via one-pot synthesis. The inset is the HRTEM image of a typical 5 nm $Pd_{67}Pt_{33}$ random alloy nanocrystals. (b) HAADF-STEM image and the corresponding EDX elemental mapping of Pd (green) and Pt (red) for several typical $Pd_{67}Pt_{33}$ random alloy nanocrystals. (c) TEM image of 6.5 nm $Pd_{67}Pt_{31}$ random alloy nanocrystals synthesized by injecting morpholine borane at 40 °C. (d) Correlation between the adding amount of $Pt(acac)_2$ and the amount of Pt in the final product. Adapted from ref 232 and modified. Copyright 2011 American Chemical Society.

the solvent, reducing agent(s), capping agent(s), and reducing temperature, including the comparable precursors but not just a consideration on the closeness of their reduction potentials.

When the two metal precursors have relatively large differences in reduction potential, the core−shell nanocrystals might be favorably generated with great probability due to the sequential reduction in solution. To synchronize the reduction rate of the two precursors to generate random alloy nanocrystals rather than core−shell nanocrystals, a viable route is to tune the molar ratio of the two precursors because the reduction potential of metal ions depends strongly on the concentration of ions. For example, Sun and co-workers demonstrated the one-pot synthesis of uniform Au_xAg_{100-x} random alloy nanocrystals by coreducing $HAuCl_4$ and $AgNO_3$ with OAm as the reducing agent and surfactant in the presence of octadecene (ODE) at 120 °C.[259] It was observed that when the feeding amount of Ag precursor is relatively higher than that of the Au precursor in the reaction stock solution, the difference of the reduction rates between both precursors can be significantly reduced, thus promoting their co-reduction. Specifically, $Au_{60}Ag_{40}$ random alloy nanocrystals could be easily obtained when the molar feeding ratio for $AgNO_3$ and $HAuCl_4$ attained 10. Using a series of characterization methods, such as high-resolution transmission electron microscopy (HRTEM), energy-dispersive spectroscopy (EDS), and UV−Vis spectra, they further confirmed the formation of random alloy nanocrystals. Furthermore, they concluded that the reaction temperature played an important role in the formation of random alloy nanocrystals, while a low temperature (65 °C) or high temperature (180 °C) would promote phase segregation. It was uncovered that the phase segregation mainly resulted from a large gap of the reduction rates between the Au and Ag precursors under similar conditions. For instance, the Au precursor can be generally reduced at 65 °C, whereas the reduction of the Ag precursor occurs at a temperature as high as 180 °C. Meanwhile, the chloride ions from the Au precursor could also alter the relative reduction rates, likely due to the significant difference in reduction potential between $AuCl_4^-$ and Au^{3+}. In addition to the above-mentioned route, it is also viable to alter the relative concentrations of metal precursors by adding the solutions dropwise with the assistance of a syringe pump. A typical example was demonstrated by Qin and co-workers,[234] who synthesized Ag−(Ag−Au) core−frame nanocubes (NCbs) by adding $AgNO_3$ and $HAuCl_4$ dropwise into a solution containing Ag seeds, ascorbic acid (AA), and PVP. It was also demonstrated that this approach could precisely control the relative amounts of Ag and Au atoms in solution. Altogether, altering the relative concentrations of metal precursors is an effective approach for generating the random alloy nanocrystals with precise control over the composition.

It is not always possible to well match the reduction rates by varying the relative concentrations of metal precursors. To solve this problem, it might be often required to introduce appropriate reducing agents, solvents, coordination ligands, capping agents, surfactants, or foreign ions and tune other synthetic parameters to achieve the co-reduction of different metal precursors in the solution system. It should be pointed out that the coordination ligands could strongly coordinate with the metal ions (reactants), profoundly improve their stability, reduction potential, and reduction kinetics, whereas the capping agents could selectively bind to a specific class of facets on the nanocrystals (products), effectively alter the surface energy and anisotropy as well as subsequent adsorption behavior. For example, Wang and co-workers demonstrated the synthesis of Pt_3Sn random alloy nanocrystals by coreducing $PtCl_4$ and $SnCl_2$ in a mixed solution of OAm and OA, with the use of borane tertbutylamine as a reducing agent.[260] Because Pt and Sn precursors have a larger difference in reduction rate, the addition of borane tertbutylamine with strong reducing power was confirmed to be more advantageous for simultaneous reduction of the Pt and Sn precursors to prepare alloyed nanocrystals. This co-reduction approach, with an appropriate selection of the reducing agent and precursors, could also be adopted for preparing random alloy nanocrystals in other metal systems. Previously, Fang and co-workers developed a new strategy for the synthesis of Pt_3Ni octahedra and NCbs (Figure 3) by simultaneously reducing $Pt(acac)_2$ and $Ni(acac)_2$ in the presence of $W(CO)_6$.[76] For the synthesis of Pt_3Ni nano-octahedra, $W(CO)_6$ was added into a mixed solution containing $Pt(acac)_2$, $Ni(acac)_2$, OAm, and oleic acid (OA) under Ar atmosphere at 130 °C and then the reaction temperature was increased to 230 °C under vigorous agitation. It was revealed that the introduction of $W(CO)_6$ was the key to facilitating the formation of random alloy nanocrystals, since the low reduction potential of W decomposed from $W(CO)_6$ could dramatically facilitate the reduction of $Pt(acac)_2$ in the early stage, leading to a fast Pt nucleation, whereas the generated W cations would decelerate the subsequent nanocrystal growth (to match the reduction of Ni). Furthermore, they believed that the use of OAm could stabilize {111} facets of Pt_3Ni nanocrystals via selective adsorption and thus lower the surface free energy on Pt_3Ni {111} facets. More importantly, it was revealed that the introduction of $W(CO)_6$ was the key to controlling the shape

https://dx.doi.org/10.1021/acs.chemrev.0c00436
Chem. Rev. 2021, 121, 736−795

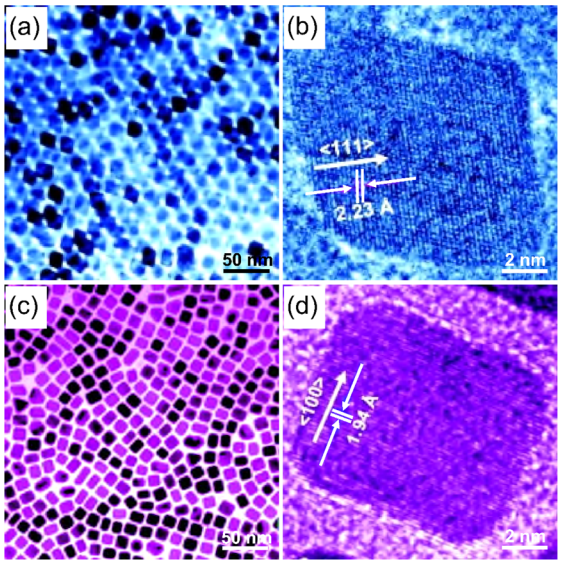

Figure 3. TEM images of (a) Pt_3Ni octahedra and (c) nanocubes synthesized via co-reduction. HRTEM images of (b) a typical Pt_3Ni octahedron and (d) nanocube. Reproduced from ref 262. Copyright 2010 American Chemical Society.

of Pt_3Ni nanocrystals. For the synthesis of Pt_3Ni NCbs, $Pt(acac)_2$, OAm, and OA were first mixed under the Ar atmosphere and then heated to 130 °C, followed by adding $W(CO)_6$ into the reaction solution. After that, a solution containing $NiCl_2{\cdot}6H_2O$, OAm, and OA was added dropwise while the reaction temperature was raised to 200 °C. They ultimately concluded that the formation of {100} facets was due to slowly injecting the $NiCl_2$ solution. In both cases, as discussed above, a slower rate of injecting the Ni precursor favored the formation of Pt_3Ni{100}-bounded NCbs, whereas a faster rate of injecting the Ni precursor resulted in a formation of Pt_3Ni{111}-terminated octahedral nanocrystals. As such, it was demonstrated that the injecting rate of the Ni precursor in the early stage played an important role in adjusting the CO adsorption energy on different facets. Shortly, Yang and co-workers reported the synthesis of truncated octahedral Pt_3Ni nanocrystals by coreducing $Pt(acac)_2$ and $Ni(acac)_2$ with tert-butylamine-borane (TBAB) and hexadecanediol as the reducing agents in the presence of diphenyl ether, long-alkane-chain amines, and adamantanecarboxylic acid.[261] They demonstrated that the simultaneous use of TBAB and hexadecanediol with strong reducing powers was very necessary to precisely synchronize the reduction rates of both precursors and thus to facilitate the formation of Pt_3Ni random alloy nanocrystals while preserving good dispersion and well-defined shape. In another example demonstrated by Schaak and co-workers, PtCu nanorods could be formed by coreducing $Pt(acac)_2$ and $Cu(acac)_2$ in a solution containing OA, OAm, ODE and hexadecanediol.[231] On the basis of UV−visible spectroscopic measurement, it was determined that the initial formation of a Cu−Pt complex through coordination in a mixed solvent and the sequential decomposition of this complex led to the formation of CuPt random alloy nanorods. The length of the nanorods could be precisely controlled by altering the concentrations and types of solvents. Importantly, they demonstrated that OAm could selectively absorb on the {100} facets of the PtCu nanorods, resulting in the preferential growth along the [111] direction. In short, some highly complex interactions could generate in the presence of appropriate reducing agents, solvents, coordination ligands, capping agents, surfactants, or foreign ions, and these interactions can potentially be utilized to precisely control the reduction rates of different precursors during a synthesis.

The use of chemical additives (e.g., reducing agents, solvents, coordination ligands, capping agents, surfactants, and foreign ions) in the reaction system generally can markedly alter the reduction potential and stability of metal ions through coordination and thus their reaction kinetics.[56,60,83,263−274] One successful example was demonstrated by Xia and co-workers. They discovered that the introduction of 63 mM KBr in EG solution consisting of Na_2PdCl_4 and K_2PtCl_4 could immediately cause the ligand exchange between chloride and bromide ions, resulting in a significant decrease of the difference in reduction rate between the Pd and Pt precursors and thus facilitating the formation of random alloy nanocubes.[254] The addition of KBr not only promotes the formation of $PdBr_4^{2-}$ and $PtBr_4^{2-}$ via coordination but also selectively catches and stabilizes the {100} facets. They further observed a core−shell structure on Pd−Pt octahedral nanocrystals in the absence of KBr, due to the significant difference between the initial reduction rates of $PdCl_4^{2-}$ and $PtCl_4^{2-}$. Similarly, the addition of halide ions (e.g., Cl^-, Br^-, and I^-) into a precursor solution containing Au^{3+} and Pd^{2+} can also quickly form the Au−halide and Pd−halide complexes.[275] They identified monodisperse Au−Pd random alloy and core−shell icosahedral nanocrystals by simply tuning the concentration ratio between Br^- and Cl^-. Specifically, the reduction potential and reduction rate decreased in the order of $[AuCl_4]^-$ > $[AuBr_4]^-$ > $[AuI_4]^-$ and $[PdCl_4]^-$ > $[PdBr_4]^-$ > $[PdI_4]^-$. As a result of their dual functions, it can be concluded that the use of some chemical additives in a reaction solution played an critical role in forming random alloy structure and regulating the morphology of the as-obtained nanocrystals. In another report, Fang and co-workers demonstrated the one-pot synthesis of PtCu random alloy NCbs by coreducing $Pt(acac)_2$ and $Cu(acac)_2$ in the presence of 1,2-tetradecanediol, ODE, OAm, tetraoctylammonium bromide, and 1-dodecanethiol (DDT).[276] Importantly, DDT was found to enable promoting the co-reduction of Pt^{2+} and Cu^{2+} ions via coordination. Specifically, the composition of the final product could be readily tuned by varying the amount of DDT. It is worth noting that these chemical additives can also absorb preferentially to specific facets on the nanocrystal and thus affect the subsequent growth process. Yan and co-workers reported the synthesis of sub-10 nm Pd−Pt nanotetrahedra and NCbs by simultaneously reducing K_2PtCl_4 and Na_2PdCl_4 (Figure 4).[277] When HCHO served as the reducing agent in the presence of sodium oxalate ($Na_2C_2O_4$), the tetrahedral nanocrystals enclosed by {111} facets were obtained. They found that the addition of $C_2O_4^{2-}$ could stabilize the {111} facets. Furthermore, by replacing the $Na_2C_2O_4$ with high concentrations of Br^- and low concentrations of I^-, the final product would become NCbs enclosed by {100} facets, due to the selective absorption of the halides on the {100} facets. In summary, the presence of chemical additives in a reaction solution can dramatically affect the reduction rate by complex interactions, and these interactions should be further explored to controllably tune the size, shape, and composition of resultant nanocrystals.

Besides, sonication-assisted reduction, microwave-assisted reduction, or photoassisted reduction can be adopted to

https://dx.doi.org/10.1021/acs.chemrev.0c00436
Chem. Rev. 2021, 121, 736−795

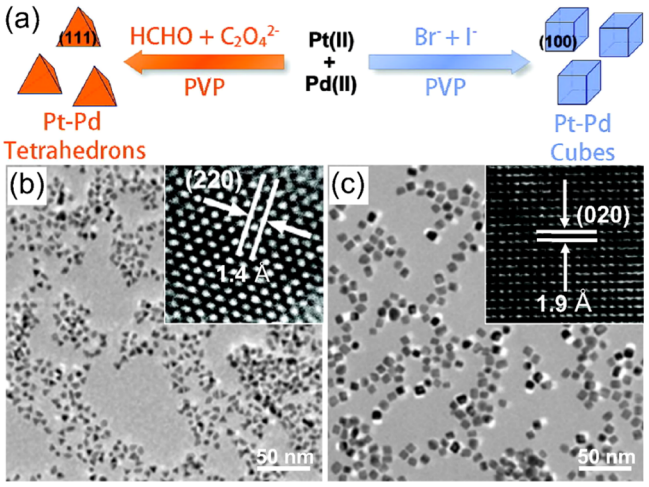

Figure 4. (a) Schematic illustration showing the shape-controlled synthesis of Pt−Pd tetrahedra and nanocubes synthesized via co-reduction. TEM images of (b) Pt−Pd tetrahedra and (c) nanocubes. The insets in panels (b) and (c) are HRTEM images of a single Pt−Pd tetrahedron and nanocube, respectively. Adapted from ref 277 and modified. Copyright 2011 American Chemical Society.

prepare a variety of alloy nanocrystals in the absence of chemical reducing agents.[44,278−286] These approaches can be performed at a relatively low reaction temperature or even room temperature. For example, Grieser and co-workers reported on the synthesis of Pt−Ru random alloy nanocrystals by sonication-assisted co-reduction of K_2PtCl_4 and $RuCl_3$.[283] El-Shall and co-workers utilized a microwave-assisted co-reduction approach to synthesize various random alloy nanocrystals (e.g., CuPd, CuRh, AuPd, AuRh, PtRh, PdRh, and AuPt) in well-controlled size and shape.[284] It should be pointed out that these approaches can also be applied to the preparation of some special random alloy nanocrystals that cannot be obtained by using the chemical reducing agent in the co-reduction synthesis. A typical example was demonstrated by Nenoff and co-workers, who synthesized the stable Ag−Ni random alloy nanocrystals by simultaneously reducing the Ag and Ni precursors via γ-irradiation.[285] Note that the Ag−Ni random alloy nanocrystals are generally believed to be thermodynamically unstable due to low immiscibility and large lattice mismatch between Ag and Ni. In this case, the introduction of γ-irradiation can quickly reduce Ag and Ni ions to atoms and then quench them in the lattice, facilitating the formation of a stable Ag−Ni random alloy.

3.2. Seed-Mediated Synthesis

A well-known, seed-mediated growth approach offers a very effective synthetic route for preparing well-controlled bimetallic nanocrystals, especially for the synthesis of core−shell and heterostructured bimetallic nanocrystals.[1,7,199,287−294] It is worth mentioning that generally the key synthetic challenge for making core−shell nanocrystals is to keep the precursor concentration of the second shell metal always below the critical value on the LaMer plot to prevent homogeneous nucleation. However, it is not very common to adopt the seed-mediated growth approach to synthesize alloy nanocrystals because it can effectively separate the reduction of different precursors as compared to the co-reduction approach. In some cases, by elaborately designing the reaction system, alloyed nanocrystals can also be obtained.[295−303] A common strategy is to utilize a seed-based diffusion route in the synthesis of random alloy nanocrystals. Very recently, Murray and co-workers used this approach to generate a series of Au−L (L = Ag, Pt, Hg, Sn, and Cd) random alloy nanocrystals with tunable compositions at relatively high temperatures (Figure 5).[235] In a typical synthesis of Au−Ag random alloy nanocrystals, a solution containing 5.5 nm Au seeds, $AgBF_4$

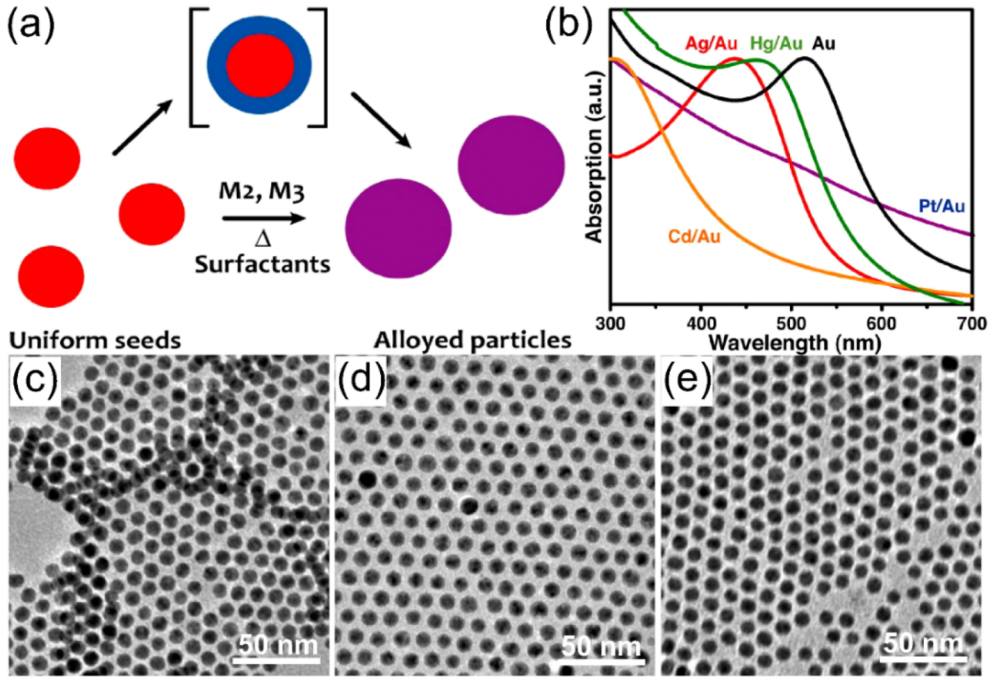

Figure 5. (a) Schematically illustrating the proposed formation mechanism for generating uniform alloyed bimetallic nanocrystals through a possible core−shell structure during a seed-mediated synthesis. TEM images of (c) Au nanocrystal seeds, (d) Au−Ag random alloy nanocrystals, and (e) Au−Sn random alloy nanocrystals. Adapted from ref 235 and modified. Copyright 2015 American Chemical Society.

https://dx.doi.org/10.1021/acs.chemrev.0c00436
Chem. Rev. 2021, 121, 736−795

as a precursor, 1,2-hexadecanediol, and oleyl alcohol as reducing agents, OA, OAm, and ODE as the solvent and stabilizer was heated to 150−180 °C in a flask under N_2 atmosphere. By simply manipulating the amount of Ag precursor added, the final metal ratio in Au−Ag random alloy nanocrystals could be tunable. They found that the choice of reaction temperature was predominantly dictated by the nature of the doping metal. For the easily reducible metals, such as Ag and Hg, completion of the reaction requires temperatures as low as 150 or 180 °C, whereas for metals like Pt, Sn, Cd, relatively higher temperatures up to 200, 210, and 300 °C, respectively, were necessary. It is worth mentioning that the condition of the high reaction temperature is of critical importance to promote the reduction and subsequent alloying. High temperatures can also effectively remove the defects determined in the as-synthesized Au nanocrystals. Furthermore, this approach has also been successfully applied to the synthesis of other bimetallic and trimetallic nanoalloys. Ravishankar and co-workers demonstrated this approach in 2018.[236] They synthesized a series of uniform and monodispersed Au-based random alloy (AuPd, AuPt, and AuCu) nanowires with a controllable composition by employing ultrathin Au nanowires as the seeds in the presence of the second metal precursor and EG. Similarly, the composition of the resultant random alloy nanowires also depended strongly on the second metal precursor concentration.

Another viable strategy for the synthesis of random alloy nanocrystals through a seed-mediated route is to directly convert a core−shell structure to an alloy by controlling the heating process in solution or gas-phase. This approach typically involves an interdiffusion and mixing between two metallic components through a thermal activation process commonly referred to as alloying. Especially, this process became favorable when both metallic compositions meet the Hume−Rothery rules,[149] as discussed in section 2.1. A typical example was demonstrated by Tracy and co-workers, who utilized 8 nm Au as the seeds to successfully synthesize Au−Ag core−shell nanocrystals, followed by dispersing them in OAm and subsequent heating to 250 °C for 2 h.[304] They realized that the heating process could facilitate the interdiffusion of Au and Ag, resulting in a production of Au−Ag random alloy nanocrystals. The key to the successful conversion from a core−shell structure to an alloy is mainly due to satisfying the Hume−Rothery rules for Au and Ag. To further facilitate the interdiffusion process for the formation of atomically homogeneous alloys, a higher reaction temperature is often required. However, because of the limitation of solvent boiling point, it is impossible to complete the reaction in solution at an extremely high temperature. This obstacle can be overcome by carrying out the reaction via annealing in a gas atmosphere. In a recent report, Yin and co-workers synthesized fully alloyed Au−Ag nanospheres by annealing the Au−Ag core−shell nanospheres at elevated temperatures in a nitrogen atmosphere (Figure 6).[305] To avoid the aggregation of nanocrystals during the annealing process, a layer of silica with a thickness of ∼15 nm was required to be uniformly coated on the Au−Ag core−shell nanospheres before the annealing. It was believed that the use of such an elevated temperature could dramatically increase the mobility of the metal atoms, favoring homogeneous distribution for both Ag and Au elements and removing crystallographic defects in the nanosphere. This approach has also been extended to other systems, such as Pt−Ru and Pt−Cu random alloy nanocrystals.[306−308]

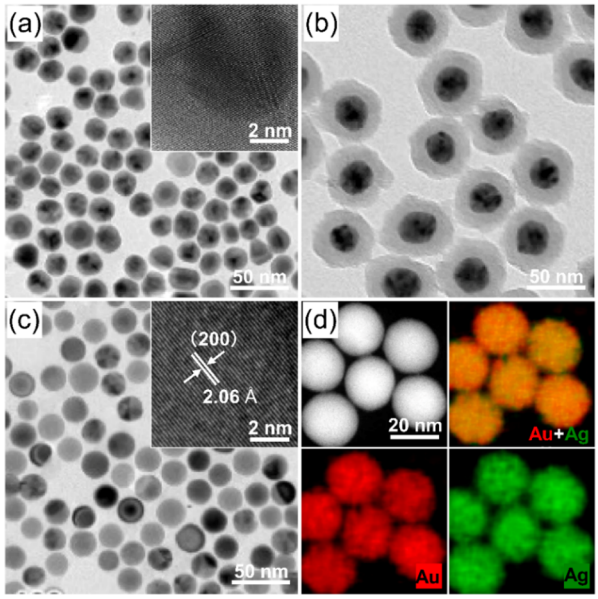

Figure 6. TEM images of (a) Au−Ag core−shell nanocrystals, (b) Au−Ag−SiO_2 onion nanocrystals, and (c) Ag−Au random alloy nanospheres synthesized through a seed-mediated route. (d) HAADF-STEM image of several representative Ag−Au random alloy nanospheres and the corresponding EDX elemental mapping of Au (red) and Ag (green). The insets in panels (a) and (c) are HRTEM images of a single Au−Ag core−shell nanocrystal and Ag−Au random alloy nanosphere, respectively. Adapted from ref 305 and modified. Copyright 2014 American Chemical Society.

In addition to the aforementioned approach, the seed-mediated co-reduction (SMCR) method is also powerful in the synthesis of nanocrystals with alloyed shells with well-defined shapes and compositions.[309] This approach involves a simultaneous reduction of two metal precursors to deposit bimetallic nanocrystals onto well-controlled seeds. Note that the shape of the seeds can be well transferred to the alloyed shells. This method was initially developed by Skrabalak and co-workers to prepare octahedral nanocrystals with alloyed Au−Pd shells.[296] In a typical synthesis, AA as a reducing agent was added into a solution containing Au seeds, H_2PdCl_4, $HAuCl_4$, and cetyltrimethylammonium bromide (CTAB), followed by keeping the system undisturbed at 25 °C for 0.5 h. In this specific case, it seems that the small lattice mismatch between Au and Pd (∼4%), the high stability of Au seeds to prevent galvanic replacement, and easy co-reduction of Au and Pd precursors are the key parameters of SMCR. Importantly, they found that the size and shape of the final products could be well-controlled by tuning the size and shape of the seeds, the pH of the solution, and the metal precursor ratios. However, for those compositions with a larger lattice mismatch, it is still a great challenge to yield alloyed nanostructures in SMCR as generally the large lattice mismatch could result in a phase-separation and island growth rather than conformal deposition during a seed-mediated synthesis. A recent study conducted by the same group demonstrated that random alloy formation and conformal overgrowth are possible in such a system with high lattice mismatch.[237] Specifically, the codeposition of Pd and Cu elements (7% mismatch for Pd−Cu) onto Pd NCbs was achieved in SMCR, where H_2PdCl_4 and $CuCl_2$ were coreduced by AA in a solution containing Pd seeds and CTAB. Similarly, the morphology and element distribution of the resultant

https://dx.doi.org/10.1021/acs.chemrev.0c00436
Chem. Rev. 2021, 121, 736−795

nanocrystals can be readily tuned by adjusting the reaction kinetics of two metal precursors. This study further deepens our understanding of SMCR as a general strategy to synthesize multicomponent nanocrystals with structurally defined nanocrystals.

One more impressive development in seed-mediated synthesis is the construction of heteronanostructured nanocrystals via a site-selective codeposition of binary or ternary metallic random alloy onto the well-defined seeds. In this approach, it is of critical importance to purposely select the growth or control growth rates on different facets of metal seeds, depicted previously.[238,310−313] Chen and co-workers have demonstrated this site-selective seeded growth approach in two steps:[310] (1) synthesizing the well-defined Cu seeds; (2) site-selectively depositing PdCu or PtCu random alloy onto the Cu seeds, yielding bimetallic heterodimer nanocrystals. The key to the successful synthesis mainly relies on judiciously adjusting the reduction kinetics of Cu. More importantly, this approach can also be applied to other systems that utilize CdS nanorods as the seeds for selectively depositing PtNi or PtCo random alloy onto the tips of nanorods.[311] However, it is not always effective to achieve site-selective growth by merely tuning the reduction rate of different precursors. It is often necessary to precoat a protecting shell on specific crystal facets to suppress subsequent deposition on these facets, thereby significantly benefiting an anisotropic growth. A typical example was demonstrated by Wang and co-workers,[238] who preferentially coated a silver layer on the side surface of Au nanobipyramids, followed by codepositing Ag and Pd at their tips. Interestingly, Au nanorods can also be used as the seeds for overgrowth of AgPd or AgPt random alloy at their tips, further demonstrating the generality of this approach.[238]

3.3. Thermal Decomposition

The thermal decomposition of organometallic compounds is a powerful and versatile approach to prepare a variety of highly monodisperse random alloy nanocrystals.[57,314−325] It has been proven that this approach is especially suitable for metal precursors that are difficult to be reduced through a wet-chemical reduction approach with relatively low reduction potentials (e.g., Ni-, Fe-, and Co-precursors). Generally, this approach combines reduction and decomposition processes and chooses some common organometallic compounds, such as including carbonyls, acetylacetonates, and cupferronates, as the precursors that can readily decompose under heating. Similar to the co-reduction approach, all the synthetic factors including solvent, capping agents, surfactants, the molar ratio of the metal precursors, as well as reaction time and temperature, play a critical role in tuning the size, shape, and composition of the resultant random alloy nanocrystals. One successful example was demonstrated by Sun and co-workers, where PtFe random alloy nanocrystals with tunable composition were synthesized by simultaneous reduction of $Pt(acac)_2$ and thermal decomposition of $Fe(CO)_5$ with a long-chain 1,2-hexadecanediol as a reducing agent in the presence of OA and OAm as both the solvent and stabilizer.[323] In this case, $Pt(acac)_2$ is reduced to zerovalent Pt atoms while $Fe(CO)_5$ is synergetically decomposed to zerovalent Fe atoms at an appropriately high temperature. It was observed that the composition of the as-prepared random alloy nanocrystals could be readily controlled by manipulating the molar ratio between $Fe(CO)_5$ and $Pt(acac)_2$. It was reported that the feeding ratio between $Fe(CO)_5$ and $Pt(acac)_2$ was not the same as the Fe/Pt composition ratio in the resultant PtFe random alloy nanocrystals as $Fe(CO)_5$ was hard to completely decompose due to its low decomposition rate. For a given composition in an alloy product, an appropriate tuning of the input precursor ratio is necessary. Later, the same group further optimized this approach to achieve the synthesis of size-, shape-, and composition-controlled PtFe nanocrystals (Figure 7).[239] They found that the overall size of resultant

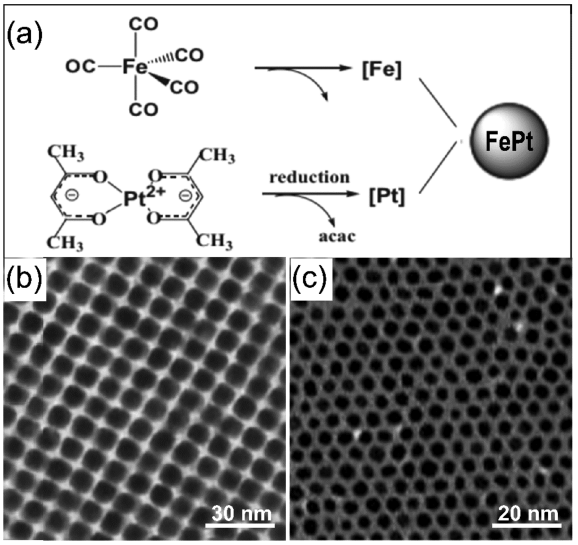

Figure 7. (a) Schematically illustrating the formation of FePt random alloy nanocrystals via thermal decomposition. TEM images of (b) typical 6 nm $Fe_{50}Pt_{50}$ random alloy nanocubes and (c) FePt spherical nanocrystals. (a,b) Adapted with permission from ref 239 and modified. Copyright 2006 WILEY-VCH. (c) Adapted from ref 324 and modified. Copyright 2004 American Chemical Society.

nanocrystals could be greatly affected by the nucleation rate. A faster nucleation rate generates nanocrystals in smaller sizes, whereas a slower nucleation rate yields larger nanocrystals. As a result, the synthesis without the use of an additional reducing agent led to the formation of larger PtFe nanocrystals. Furthermore, they demonstrated that the morphology of resultant nanocrystals could be tuned by adjusting the synthetic parameters, including the feeding molar ratio of stabilizer to the precursor, addition sequence of the precursors and stabilizers, heating temperature, and heating ramp rate.[240] In this synthesis, PtFe NCbs could be synthesized by altering the addition sequence of OA and OAm and the molar ratio of $Fe(CO)_5$ to $Pt(acac)_2$. Once the OA was first introduced into the reaction solution, the cubic Pt-rich nuclei were quickly formed derived from the strong tendency of OA to bind to Fe. Subsequently, preferentially depositing the Fe-rich species on the {100} planes led to the formation of cubic PtFe nanocrystals. In comparison, the PtFe nanowires in an average length of >200 nm could be prepared when only OAm was introduced, since OAm could form an elongated reverse-micelle to limit the radial growth under the synthetic conditions. By further replacing the OAm with a mixed solvent containing of OAm and ODE, the shorter PtFe nanowires could be produced. In short, a great deal of similar thermal decomposition approaches have been widely used for the controlled synthesis of well-defined random alloy nanocrystals.

https://dx.doi.org/10.1021/acs.chemrev.0c00436
Chem. Rev. 2021, 121, 736−795

In some cases, when the reduction rates or thermal decomposition rate of the two metal precursors involved in one reaction system could not be well matched, it is possible to form separate monometallic phases instead of the random alloy phase. However, these problems can be easily overcome by using single-source molecular precursors containing two kinds of metals that possess stable metal−metal bonds within the precursor molecules. The composition of the final product is largely associated with the composition of the bimetallic precursors. For example, as demonstrated by Lukehart and co-workers, FePt random alloy nanocrystals in size of 5.8 nm were synthesized by thermally decomposing presynthesized $Pt_3Fe_3(CO)_{15}$ in toluene as the solvent in the presence of OAm and OA as the surfactants.[326] Specifically, $Pt_3Fe_3(CO)_{15}$ as a bimetallic precursor could be easily prepared by reacting $Fe(CO)_5$ with tris(norbornylene)-platinum(0). In another report, Thanh and co-workers synthesized a series of random alloy nanocrystals through the thermal decomposition of different types of molecular bimetallic carbonyl clusters anions, such as $[Fe_3Pt_3(CO)_{15}]^{1-}$, $[Fe_4Pt(CO)_{16}]^{2-}$, $[FeCo_3(CO)_{12}]^{1-}$, and $[FeNi_5(CO)_{13}]^{2-}$, instead of neutral bimetallic carbonyl clusters (Figure 8).[327] They ultimately concluded that the composition of the resultant random alloy nanocrystals (e.g., FePt, Fe_4Pt, $FeCo_3$, and $FeNi_5$) mainly depended on a metal fraction in the precursor. It is worth noting that, as precursors, molecular bimetallic carbonyl clusters are much easier to decompose as compared with molecular bimetallic carbonyl clusters anions in the context of the practical synthesis, due to the absence of extra ligands in the former. As a result, the size of the resultant random alloy nanocrystals is generally much smaller when the former is used in the synthesis. In brief, the thermal decomposition approach provides a simple but effective route for generating random alloy nanocrystals with precise control over the composition.

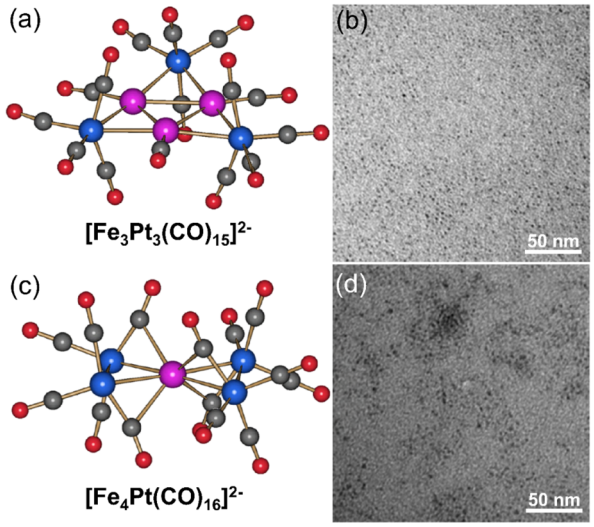

Figure 8. Atomic models of bimetallic carbonyl complexes, for example, (a) $[Fe_3Pt_3(CO)_{15}]^{2-}$ and (c) $[Fe_4Pt(CO)_{16}]^{2-}$, that have been used as precursors for preparing bimetallic nanocrystals (red = O, gray = C, blue = Fe, and purple = Pt). TEM images of the corresponding (b) bimetallic FePt nanocrystals and (d) Fe_4Pt nanocrystals derived from the above-mentioned precursors. Adapted from ref 327 and modified. Copyright 2009 American Chemical Society.

3.4. Galvanic Replacement

Galvanic replacement provides a particularly facile and versatile approach to prepare a wide variety of hollow random alloy nanocrystals with precisely controlled sizes, shapes, and elemental compositions. Galvanic replacement reaction is an electrochemical process that typically involves the oxidation of one metal (often referred to as a sacrificial template) by the ions of another metal with a more positive reduction potential.[51,230,243,328−344] In this process, the metal ions will be rapidly reduced by capturing the electrons from the template and then deposited onto the exterior of the template, while the pristine template will be oxidized to metal ions from special sites and dissolved into the solution due to the favorable difference in the reduction potentials of the two metals. As a result, the final product typically inherits the shape of the original template, except for a slight increment in dimensions. It should be emphasized that the addition of the secondary metal ion and subsequent galvanic replacement process must be carefully manipulated to ensure that the developed shape of the preprepared metal template will not be destroyed.

As mentioned above, the driving force for galvanic replacement reaction originates from the difference in the reduction potentials from both metals involved. The potential difference (ΔE) can be derived using the Nernst equation:

$$\Delta E = \Delta E^0 + (RT/nF)\ln Q \quad (6)$$

where ΔE^0 is the difference of standard potentials between both metals involved at 25 °C, R is the ideal gas constant, T is the Kelvin temperature, n is the molar number of electrons transferred in the redox reaction, F is Faraday's constant, and Q is the reaction quotient based on the concentrations of the reactants and products at a given time. According to equation 6, the actual potential difference of the reduction potentials (ΔE) is strongly determined by the concentrations of relevant ions and temperature, as well as the involvement of other nonstandard conditions. Additionally, ΔE can also be evaluated by the associated change in Gibbs free energy (ΔG):

$$\Delta G = -nF\Delta E \quad (7)$$

A spontaneous galvanic replacement reaction will easily occur once a system has a positive ΔE, leading to a negative ΔG. A notable example is the galvanic replacement reaction between Ag NCbs and $HAuCl_4$ as reported in previous work.[241] Note that Ag has a relatively low reduction potential as compared with Au^{3+}, Pd^{2+}, and Pt^{2+}. The Au^{3+}-involved overall reaction in this process can be summarized as follows:

$$3Ag + AuCl_4^- \rightarrow 3Ag^+ + Au + 4Cl^-$$

Typically, the galvanic replacement will immediately occur once an aqueous $HAuCl_4$ solution is introduced to a suspension of Ag NCbs. It was observed that the reaction generally initiated at those sites of the Ag NCbs with defects, stacking faults, or steps that possess the highest surface energy. In this galvanic replacement reaction, Ag atoms are gradually oxidized to Ag^+ ions and dissolved into solution, while the generated electrons are quickly captured by Au^{3+} ions to produce Au atoms through a reduction process. The newly yielded Au atoms tend to deposit epitaxially on the surface of the Ag template while the lattice mismatch between Ag and Au is small (4.086 vs 4.078 Å for Ag and Au, respectively). It is believed that the formation of a thin and incomplete layer of

https://dx.doi.org/10.1021/acs.chemrev.0c00436
Chem. Rev. 2021, 121, 736−795

Au on the Ag template in the early stages can effectively prevent the underneath Ag from being oxidized. Meanwhile, some formed pits on the surface, accompanying the successive Au deposition, can serve as the reaction channel for the continuous dissolution of Ag, resulting in the formation of a hollow structure. As a result, the formation of the Au−Ag random alloy as the final product is theoretically possible because Ag and Au have similar lattice parameters and the resultant random alloy structure should be more thermodynamically stable as compared with the phase-segregated structure. Inspired by this work, a large variety of shapes (e.g., spheres, rods, and wires) and other templates (e.g., Co, Ni, and Cu) have also been involved in the syntheses of random alloy nanocrystals using this galvanic replacement approach.

Recently, Huang and co-workers reported a one-pot synthesis of rhombic dodecahedral PtCu random alloy NFs with an average size of 17 nm by reducing a mixture of $Pt(acac)_2$ and $CuCl_2$ with glucose as the reducing agent in the presence of OAm and OA as both the solvent and stabilizer.[345] They carried out a systematic study by screening the appropriate precursors, reducing agents, and optimizing the volume ratio between OAm and OA under the same conditions. They found that the generation of rhombic dodecahedral PtCu random alloy NFs was mainly attributed to the initial formation of Cu nanocrystals and subsequent galvanic replacement between Cu nanocrystals and $Pt(acac)_2$ at elevated temperatures. To better control the degree of galvanic replacement, moreover, a relatively low concentration of metal precursors is generally required to be added to partially react with the templates, triggering the selective deposition on the surface of the templates, thereby generating nanocrystals with different structures. This strategy was demonstrated by Xue and co-workers, who prepared triangular PdAg random alloy NFs by utilizing Ag nanoprisms as the templates.[244] By altering the adding amount of the H_2PdCl_4 solution, the ridge thickness of the resultant PdAg random alloy NFs could be readily tuned from 4.0 to 9.2 nm, due to the preferential deposition on the prism edges with high-energy {100} facets. It is noteworthy that introducing a template-selective etchant is also necessary for this approach to completely remove the template and promote the formation of alloy.

Another effective route for facilitating a galvanic replacement reaction is to introduce coordination ligands into a reaction system to accelerate the reaction kinetics, since the use of coordination ligands can dramatically alter the reduction potentials of the metal ions and thus move the equilibrium toward the direction of galvanic replacement. It is believed that the driving force in the galvanic replacement reaction is the potential difference between metal ions and the template. Due to the strong coordination effect, the metal ions will quickly transform into more stable species once the coordination ligands are added. Therefore, the potential difference between the as-formed species and the template will be enhanced, thereby promoting an occurrence of the galvanic replacement at a faster rate. A successful example was demonstrated by Zheng and co-workers who synthesized hollow PdPt random alloy NCbs using iodide ions in a one-step one-pot synthesis to achieve the temporal separation of template formation and galvanic replacement reaction (Figure 9a,b).[243] In a typical synthesis, a mixture of $Pd(acac)_2$, $Pt(acac)_2$, NaI, PVP, and DMF was transferred to a Teflon-lined stainless-steel

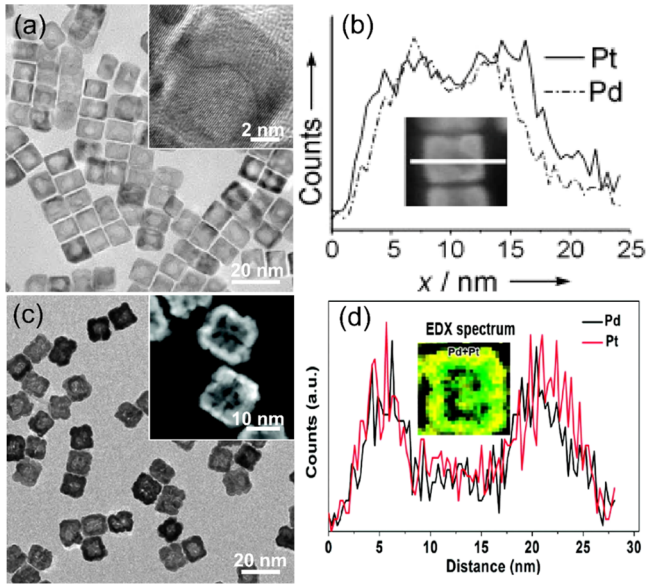

Figure 9. TEM image of (a) Pd−Pt hollow nanocubes and (b) the corresponding line-scanning profile across a hollow Pd−Pt nanocube. The insets in panels (a) and (b) are HRTEM and HAADF-STEM images of a single hollow Pd−Pt nanocube, respectively. TEM image of (c) the Pd−Pt random alloy nanocages prepared via galvanic replacement and (d) the corresponding line-scanning profile across a Pd−Pt random alloy nanocage. The insets in panels (c) and (d) are HAADF-STEM image and the EDX elemental mapping of a single Pd−Pt random alloy nanocage, respectively. (a,b) Adapted with permission from ref 243 and modified. Copyright 2009 WILEY-VCH. (c,d) Adapted from ref 330 and modified. Copyright 2011 American Chemical Society.

autoclave. The system was then heated to 150 °C and maintained for 8 h. Importantly, the addition of iodide ions to the reaction solution led to a generation of $[PdI_4]^{2-}$ as the dominating precursor that could be easily reduced in DMF as compared to $Pt(acac)_2$. Combined with transmission electron microscopy (TEM), energy-dispersive X-ray spectroscopy (EDX), and inductively coupled plasma (ICP) analyses, they identified that Pd NCbs formed first, followed by a galvanic replacement reaction with $Pt(acac)_2$ to generate 12.5 nm hollow PdPt random alloy NCbs during the synthesis. Furthermore, they demonstrated the types of precursors and the reducing agent, and reaction temperature could significantly affect the reduction process of the Pd and Pt precursors, effectively preventing their co-reduction from occurring. Therefore, they believed that the simultaneous use of iodide ions and acetylacetonate precursors played an essential role in effectively separating the formation of the template and subsequent galvanic replacement reaction, resulting in the successful synthesis of hollow random alloy nanocrystals. Most recently, Xia and co-workers further demonstrated that instead of iodide ions, bromide ions could also be used to play the same role.[331,334] It was found that the bromide ions could be strongly complexed with Pt^{2+} ions and markedly facilitate the galvanic replacement while at the same time preserving the shape of the template through selective adsorption.

Besides, the random alloy nanocrystals can also be synthesized by combining the galvanic replacement with co-reduction. This approach involves simply introducing a reducing agent into a reaction solution. Aiming at preparing alloy nanocrystals with desired nanostructures, it is of critical

https://dx.doi.org/10.1021/acs.chemrev.0c00436
Chem. Rev. 2021, 121, 736−795

importance to rationally manipulate both the rates of co-reduction and galvanic replacement reactions. Xia and co-workers established an approach to synthesize the hollow Pd–Pt random alloy nanocages by introducing citric acid (CA) as the reducing agent into a mixture containing Pd NCbs, K_2PtCl_4, KBr, and PVP (Figure 9c,d).[330] Because of the selective adsorption of bromide ions on the {100} facets of the Pd NCbs, the galvanic replacement reaction was initiated at the side faces of the Pd NCbs, promoting the generation of Pd concave nanocubes (CNCs) in the early stage. After this step, both the Pt^{2+} and the generating Pd^{2+} ions were reduced to atoms by CA and the newly formed Pt and Pd atoms were then codeposited on the CNC as a Pd–Pt random alloy shell. With the reaction proceeded, the interior of Pd CNCs was gradually dissolved through the galvanic replacement reaction, eventually yielding hollow Pd–Pt random alloy nanocages. Meanwhile, if CA was replaced by AA that has a stronger reducing power during the synthesis, the morphology of the final product would switch from nanocages to nanodendrites as the reduction of Pt precursor was accelerated and the reaction rate of galvanic replacement was thus decreased. As such, the morphology of the resultant nanocrystals was confirmed to be sensitive to both the rates of co-reduction and galvanic replacement reactions. This general approach has also been extended to the Au–Ag and Pt–Ag systems.[339,346−348] In a recent report, Qin and co-workers reported their synthesis of Au–Ag random alloy nanocages with Ag-enriched walls by utilizing AA as a reducing agent in the presence of NaOH.[242] Note that the reducing power of AA could be observably increased with the pH of a solution. As a result, the released Ag^+ ions, that were formed through the galvanic replacement reaction between Ag NCbs and $HAuCl_4$, were immediately reduced to Ag atoms and redeposited onto the surface of the Ag NCbs, resulting in a formation of hollow Au–Ag random alloy nanostructures with >80% of Ag in the original template being preserved in the walls.

3.5. Kirkendall Effect

It has garnered increasing attention that hollow random alloy nanocrystals with tunable structures and compositions can now be prepared uniquely using a nanoscale Kirkendall effect. The nanoscale Kirkendall effect is a common phenomenon involving an unequal mutual diffusion rate at the interface of coupled materials.[349−354] Usually, when the inward diffusion rate of metal is significantly lower than the outward diffusion rate of another metal, the lattice vacancies would be continuously generated at the boundaries, resulting in a hollow structure. The synthesis of hollow random alloy nanocrystals via Kirkendall effect is a two-step process: (i) synthesizing the well-defined solid metal nanocrystals and (ii) adding second metal-containing precursors into the solution to trigger the reaction with the presynthesized nanocrystals. It should be noted that, since these two metals have relatively large differences in diffusion rate, the unequal atom flow could lead to the continuous generation of vacancies at the interface between these two metals and subsequent condensation of excess vacancies to form void or gap. For example, Wei and co-workers reported their synthesis of hollow PtFe random alloy nanocrystals with a Pt-skin surface via space-confined pyrolysis and the nanoscale Kirkendall effect. They found that, in the presence of the Fe precursor, the solid Pt nanocrystals, covering by a polydopamine layer onto the surface, could be completely transformed into hollow PtFe random alloy nanocrystals with a nitrogen-doped carbon-shell upon heating. It was identified that the formation of hollow alloy nanocrystals was mainly due to the faster outward diffusion rate of Pt as compared with the inward diffusion rate of Fe during the H_2-assisted high-temperature annealing. It is worth noting that the presence of the polydopamine layer could strongly adsorb the Fe ions via chelating effect and be employed to create a confined space for alleviating nanocrystal sintering.[103]

The nanoscale Kirkendall effect can also be applied to precise control of the random alloy nanocrystals in their morphology and composition. Puntes and co-workers developed a synthetic approach to prepare polymetallic hollow nanocrystals with various morphologies and compositions by the simultaneous or sequential action of galvanic replacement with the Kirkendall effect at room temperature (Figure 10).[245]

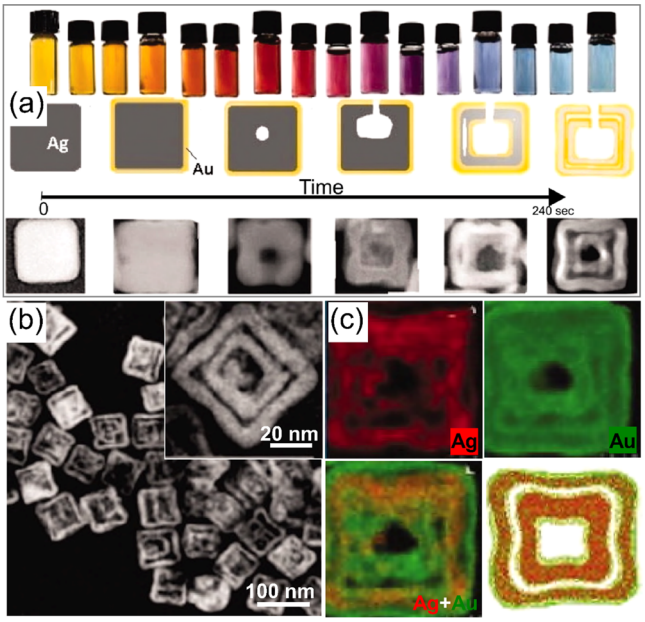

Figure 10. (a) Optical and morphological changes and the corresponding HAADF-STEM images of AuAg double-walled nanoboxes. (b) HAADF-STEM image of AuAg double-walled nanoboxes. The inset in panel (b) is HAADF-STEM image of a single AuAg double-walled nanobox. (c) EDX elemental mapping of Ag (red) and Au (green) for bimetallic AuAg nanoboxes. Reproduced with permission from ref 245. Copyright 2011 AAAS.

In this case, Ag nanocrystals were used as templates in the presence of CTAB as the surfactant and complexing agent and AA as the reducing agent. A series of nanocrystals with different levels of the hierarchical structure was readily formed at room temperature when Au, Pd, or Pt as the oxidizing agents were introduced into the reaction solution. They concluded that the use of CTAB could significantly decrease the reducing ability of AA and drive the Kirkendall effect to take place. Specifically, it was demonstrated that the formation of the cavity via galvanic replacement and subsequent Au deposition on the surface would benefit the generation of a unique nanostructure composed of a thin film of silver between two layers of gold as a diffusion intermetallic couple. This unique nanostructure could result in void formation beneath the surface since the diffusion rate of Ag in Au is faster than that of Au in Ag. Subsequently, the coalescence of excess voids promoted the formation of a continuous cavity parallel to the surface of the template, allowing the inner wall to be coated

https://dx.doi.org/10.1021/acs.chemrev.0c00436
Chem. Rev. 2021, 121, 736−795

with gold. This method can be further extended to a preparation of trimetallic structures of the Pd−Au−Ag double-walled nano box with an Ag core, coated with a PdAu random alloy layer. Despite the success of the hollow interior formation via the nanoscale Kirkendall effect in these syntheses, it might still require more evidence to strongly support this hypothesis. To this end, Mirsaidov and co-workers later experimentally verified the mechanism of the Kirkendall effect by using a liquid cell TEM to directly observe the structural transformation of Ag NCbs in the presence of Au ions.[355] They uncovered the structural evolution from Ag NCbs to hollow structure mainly stemming from the nucleation and growth of voids at the interface between Ag and Au via the coupled action of galvanic replacement and the Kirkendall effect. They further manifested that the Au ion concentration, the oxidation state of Au, and the reaction temperature played an essential role in controllably achieving the structural transition. In summary, approaches based on the nanoscale Kirkendall effect show many advantages in the preparation of hollow nanocrystals with well-defined size and shape as compared to other methods.

3.6. Oxidative Etching

Oxidative etching approach provides access to a large number of random alloy nanocrystals that are unattainable through simple co-reduction, seed-mediated growth, thermal decomposition, or galvanic replacement. This approach typically involves oxidation of zerovalent species, such as atoms, clusters, and seeds, to ionic forms by oxidative etchant (e.g., O_2, CO, H_2O_2, Fe(III) species), together with corrosive species and/or coordination ligands for the metal ions.[71,246,356−362] As a result, the oxidative etching approach is essential to achieve the precise control over the nucleation and growth of nanocrystals based on the synergetic effect of oxidation and reduction reactions involved. For instance, Li and co-workers synthesized concave Pt−Ni random alloy nanocrystals using dimethylglyoxime as a selective coordination ligand for Ni in solution (Figure 11a,b).[246] In this work, the as-synthesized PtNi octahedra nanocrystals were completely converted to concave Pt−Ni random alloy nanocrystals by selective coordination of dimethylglyoxime to Ni and subsequent chemical etching using dilute acetic acid. The chemical etching time plays a crucial role in controlling the concavity degree of the resultant random alloy nanocrystals precisely. Similarly, Yang and co-workers prepared hollow Pt_3Ni rhombic dodecahedra NFs by employing oxidative etching with the assistance of OAm as the coordination ligand in an organic solution containing hexane and chloroform (Figure 11c,d).[220] They first synthesized $PtNi_3$ rhombic dodecahedra nanocrystals in size of 20 nm using an OAm-mediated approach and then stored them in hexane and chloroform for 2 weeks in ambient conditions. The presence of dissolved O_2 could promote the oxidation of Ni surface, yielding soluble metal complexes through the coordination of OAm. Using a series of characterization techniques, including HRTEM, EDX, and X-ray photoelectron spectroscopy (XPS), they demonstrated that the as-obtained $PtNi_3$ rhombic dodecahedra nanocrystals underwent both structural and compositional transformation into hollow Pt_3Ni NFs with the same shape, revealing that the dissolution of Ni initially proceeded in the interior of the polyhedra, rather than on the edges, due to an inhomogeneous elemental distribution in the parent structure.

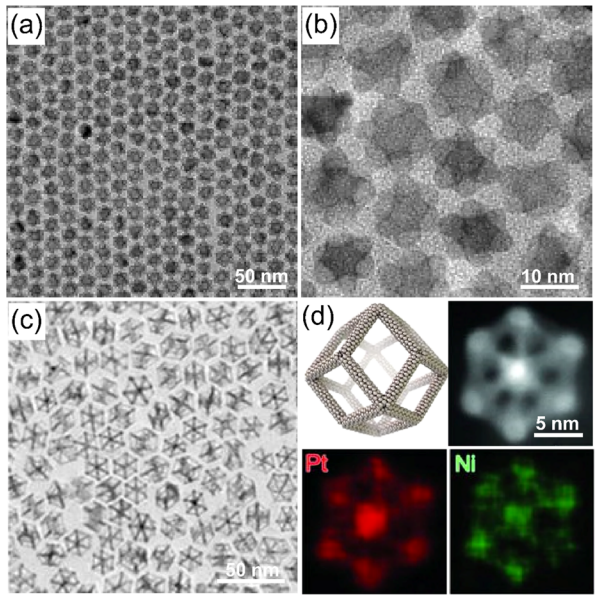

Figure 11. (a) TEM and (b) magnified TEM images of the $PtNi_2$ random alloy nanocrystals synthesized via oxidative etching. (c) TEM image of hollow Pt_3Ni nanoframes. (d) Structural model, HAADF-STEM image, and the corresponding EDX elemental mapping of Pt (red) and Ni (green) for a single hollow Pt_3Ni nanoframe. (a,b) Reproduced with permission from ref 246. Copyright 2012 WILEY-VCH. (c,d) Adapted with permission from ref 220 and modified. Copyright 2014 AAAS.

Except for the solution phase, the oxidative etching approach could also be carried out via annealing in the gas atmosphere. Fang and co-workers demonstrated that Pt_3Ni tetrahexahedral nanoframes (THH NFs) in the average size of ∼22 nm could be harvested by annealing the as-prepared carbon-supported $PtNi_4$ THH nanocrystals in the presence of CO as a gaseous etchant.[68] They reported that the selective removal of Ni from the $PtNi_4$ THH precursors was mainly attributed to the formation of the volatile $Ni(CO)_4$ complexes under CO atmosphere at elevated temperatures. By carrying out a series of control experiments with different annealing times, they concluded that the surface Ni atoms were preferentially etched along the ⟨100⟩ direction, driving the continuous segregation of Ni on the outermost layer, thereby forming the stable hollow THH NFs with a distribution of Pt component at specific positions.

4. SYNTHETIC APPROACHES TO INTERMETALLIC NANOCRYSTALS

Benefiting from the great efforts by many research groups, we extensively searched literature that describes synthetic protocols of intermetallic nanocrystal preparation with well-tunable properties. As discussed in section section 2.1, noble metal-based random alloy nanocrystals, such as Pt−M′ (M′ = Fe, Co, Ni, Mn, etc.), are usually yielded at a synthesis temperature, whereas their ordered intermetallic counterparts are normally generated through relatively high-temperature annealing, despite some exceptions such as the Pt_3Sn system (*vide infra*). In terms of the phase of the converted nanocrystals, as shown in Table 1, Pt_3M' intermetallics typically possess a cubic structure (Cu_3Au-type, $Pm\bar{3}m$) but PtM′ intermetallics generally have a tetragonal structure (AuCu-type, *P*4/*mmm*). In this chapter, we mainly focus on

https://dx.doi.org/10.1021/acs.chemrev.0c00436
Chem. Rev. 2021, 121, 736−795

the most commonly practiced synthetic approaches and discuss the recent progress of these intermetallic conversion strategies. It should be worth noting that parts of these methods would generate analogous products derived from homophyly reaction routes or basic mechanisms. It is also very common to synthesize nanocrystals with complex structures by a combination of two or more different synthetic strategies. Table 3 summarizes some representative examples concerning the synthesis of intermetallic nanocrystals using various approaches.

Table 3. Summary of Some Representative Intermetallic Nanocrystals Obtained from Various Synthetic Approaches

synthetic approach	metal composition	morphology	reference
thermal annealing	Pt_3Co, Pt_3Ti	nanosphere	refs 131 and 165
	PtFe loaded on carbon	nanosphere	ref 363
	Pt_5Ce	nanosphere	ref 364
	PtFe, PtSn, PtZn	nanosphere	refs 365−367
liquid-phase-based method	PtPb@Pt	nanoplate	ref 120
	PtPb	nanorod	ref 368
	PdCu	nanocube	ref 369
	AuPtFe, AuCu	nanosphere	refs 98 and 370
	PdSn, PtSn, AuSn	hollow nanosphere and nanorod	refs 371 and 372
	$PtCu_3$	nanocage	ref 373
	Pt_3Sn	nanocube, concave nanocube	ref 374
	PtNi	excavated nanomultipod	ref 375
other synthetic methods	PtFe, PtPb, PtGa	nanosphere	refs 213, 376, and 377

4.1. Thermal Annealing

In the overview of thermodynamic and kinetic analyses, a random alloyed structure is more prevalent than the intermetallic variants when a synthesis is maintained below the disorder-to-order transition temperature. At elevated temperature, thermal annealing for a sufficient period is arguably the most straightforward and powerful strategy for generating the intermetallic nanocrystals by facilitating the arrangement of metal atoms and d-d orbital interactions. This method has proven effective for the formation of a variety of both bi- or trimetallic intermetallic nanocrystals, as well as intermetallic semiconductor and superconducting nanocrystals.[128,165,378−384] Overall, thermal annealing can lead to a large number of ordered intermetallic nanocrystals, where the atom ordering degree can be easily tailored by varying experimental parameters such as the annealing temperature, annealing time, and the nature of support and protecting template.

4.1.1. Direct Annealing. Direct annealing is the most widely adopted protocol by far to the generation of ordered intermetallic nanocrystals.[385−399] In this process, as-prepared nanocrystals with random characteristics serve as primary intermediates for the conversion into intermetallic nanocrystals with ordered atomic arrangement via thermal treatment in an atmosphere or vacuum. It is often required to have annealing at high temperatures and/or long times due to the relatively high kinetic barriers involved in the atomic ordering. Such a process may cause a nanocrystal aggregation and/or sintering through Oswald ripening, leading to physical structure changes and thus impacting the critical disorder-to-order transition temperature. For example, Abruña, DiSalvo, and co-workers demonstrated that the as-synthesized atomically disordered Pt_3Ti nanocrystals were converted into atomically ordered Pt_3Ti nanocrystals via thermal treatment in vacuum at temperature starting at 500 °C (Figure 12).[165] Note that when the annealing temperature exceeds 550 °C, additional peaks assigned to the 100, 110, 210, 211, 300, and 310 ordering reflections of Pt_3Ti begin to be visible in the X-ray diffraction (XRD) pattern. Further increase of the annealing temperature to 600 °C could increase the intensity of the above-mentioned superlattice peaks compared with the fundamental peaks, demonstrating that the annealing temperature is an important parameter to tune the ordering degree of the as-obtained nanocrystals. Therefore, to completely convert Pt_3Ti nanocrystals from a disordered phase to the ordered structure with a $Pm\bar{3}m$ space group, referred to as Cu_3Au-type structure, an annealing temperature between 550 and 600 °C is required to promote both Pt and Ti atoms interdiffusion. However, the annealing process at or above the disorder-to-order transition temperature inevitably leads to a dramatic increase of particle size, as well as a formation of a thermodynamically stable polyhedral shape to minimize the total surface energy. As evidenced by TEM analysis, the as-synthesized Pt_3Ti nanocrystals in the disordered phase are in the average size of 3 nm, whereas the nanocrystals could grow to 37 nm after annealing at 600 °C with an ordered intermetallic crystal phase. It is hard to control the nanocrystal size in this approach. Particularly, the polydispersity of Pt_3Ti nanocrystals with an atomically ordered structure would make it difficult to extract structure−function relationships for the practical electrocatalytic application. Therefore, it is critical to achieving the disorder-to-order transition, while maintaining the size and shape of the as-developed intermetallic nanocrystals simultaneously.

By regulating *in situ* annealing conditions in a scanning transmission electron microscope (Figure 1), Chi and co-workers synthesized and directly revealed a series of Pt_3Co structures with different atom arrangements during thermal annealing, including face-centered cubic (*fcc*) and disordered Pt-rich shell on the randomly alloyed core, nucleation of structurally ordered domains, fully ordered $L1_2$ phase, and initiation of amorphization phase.[131] They found that structurally ordered domains of Pt_3Co nanocrystals enclosed by predominant {100} facets could be formed by annealing at 600 °C for 20 min. By simply prolonging the annealing time at the same temperature, the formation of a fully ordered phase with a similar morphology became favorable. Furthermore, it was determined that an annealing temperature at as high as 800 °C was critically important in facilitating the formation of the amorphous phase with a rounded shape. It was also observed that the annealing environment in different gases could further tune the surface reshaping and atom diffusion of the Pt−Co nanocrystals. These results suggest that the evolution of surface area on each type of nanocrystal facets, such as {100}, {111}, and {110}, and diffusion behaviors are strongly correlated with the annealing conditions. In all, a broad range of similar approaches has been employed for the synthesis of ordered intermetallic nanocrystals, where a careful selection of annealing temperature, annealing time, and annealing atmosphere plays a crucial role in facilitating the degree of the ordering, size, and shape of the final product.

https://dx.doi.org/10.1021/acs.chemrev.0c00436
Chem. Rev. 2021, 121, 736−795

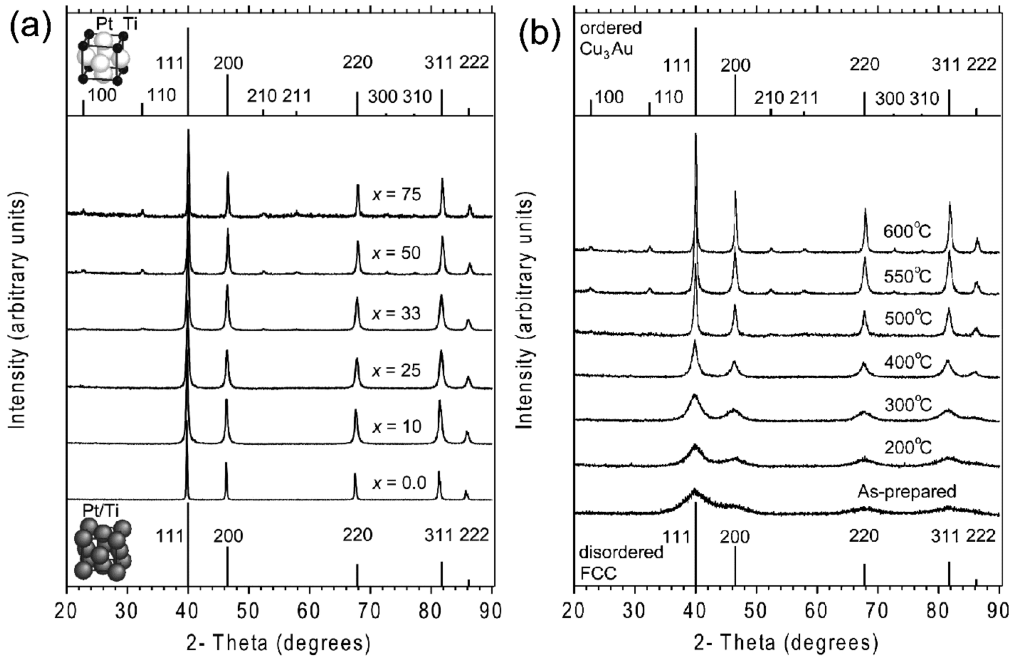

Figure 12. (a) XRD patterns of the Pt−Ti nanocrystals with different compositions that are annealed at 600 °C. Simulated XRD peaks for the disordered *fcc*-type and the ordered Cu_3Au-type structures are indicated by solid markers at the bottom and the top of the figure, respectively, together with the corresponding structural models. (b) XRD patterns of the Pt−Ti nanocrystals annealed in vacuum at different temperatures. Simulated XRD peaks for the disordered *fcc*-type and the ordered Cu_3Au-type structures are indicated by solid markers at the bottom and the top of the figure, respectively. Reproduced from ref 165. Copyright 2008 American Chemical Society.

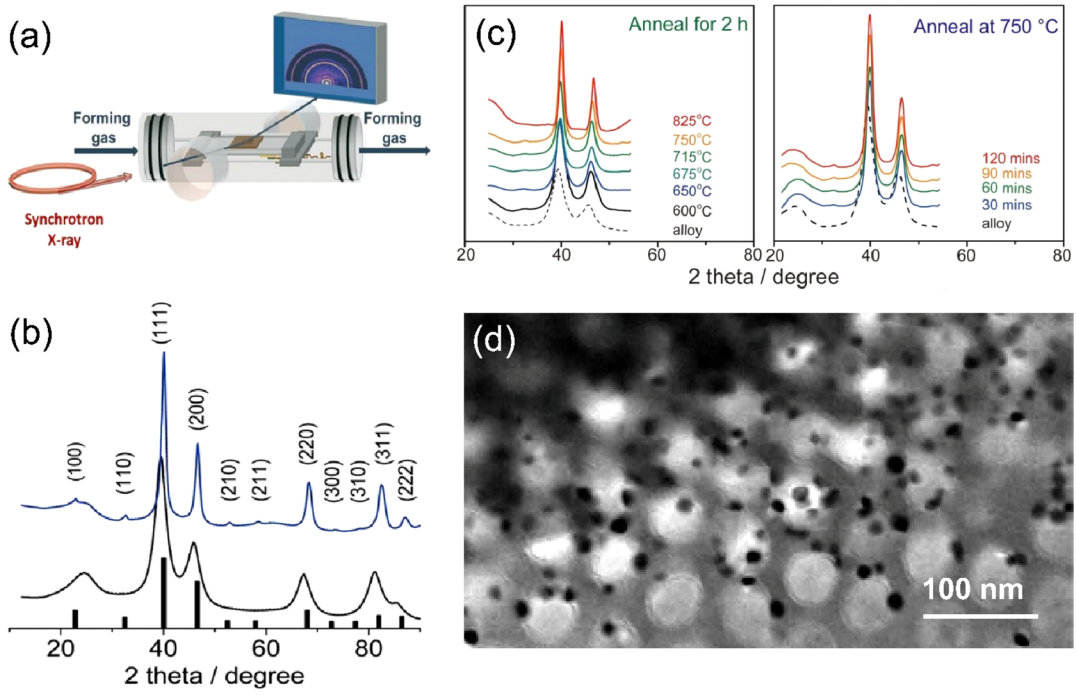

Figure 13. (a) Schematic illustration of the homemade device for the *in situ* annealing and synchrotron-based XRD characterization. (b) XRD patterns of the annealed Pt_3Co/C (700 °C in a conventional tube furnace, the top) and the as-synthesized Pt_3Co/C (the middle) recorded using the homemade device. The lines on the bottom show standard XRD pattern of intermetallic Pt_3Co (ICDD PDF card 01-071-7410). (c) In situ XRD patterns of Pt_3Co/C heated in the homemade device under forming gas as a function of the temperatures (left panel) and annealing time-dependent *in situ* XRD patterns heated at 750 °C in the homemade device under forming gas (right panel). Both dashed lines represent the as-synthesized Pt_3Co/C random alloy. (d) TEM image of ordered intermetallic FePt nanocrystals encapsulated in ordered mesopores. (a−c) Adapted with permission from ref 130 and modified. Copyright 2019 National Academy of Sciences, USA. (d) Adapted from ref 363 and modified. Copyright 2011 American Chemical Society.

4.1.2. Support-Assisted Annealing. Unlike direct annealing, in the support-assisted annealing approach, one is generally required to deposit the nanocrystals on more stable supports with larger surface areas (e.g., porous carbon, porous

https://dx.doi.org/10.1021/acs.chemrev.0c00436
Chem. Rev. 2021, 121, 736−795

oxide/carbon composite, graphene, and carbon nanotubes) before the annealing is carried out to effectively mitigate nanocrystal aggregation/sintering during this thermal process.[138,152,157,159,166,179,363,400−418] It was found that the supports could well immobilize the nanocrystals and prevent them from migration at high temperatures, as their strong anchoring effects could greatly alleviate interparticle diffusion. Meanwhile, the presence of these supports can dramatically improve the electronic density of the nanocrystals and thus accelerate the electrocatalytic process. To avoid uncontrolled nanocrystal aggregation, however, a load of metal on the supports is generally required to be carefully considered before annealing. Carbon black is one of the most common supports extensively used in fuel cells and batteries. Abruña and co-workers demonstrated a successful example in monitoring the conversion of intermetallic phase Pt_3Co loaded on a carbon support and also observed its intermetallic conversion behavior.[130] Cabon-supported Pt_3Co (Pt_3Co/C) random alloy nanocrystals were prepared by a coreducing slurry of H_2PtCl_6 and $CoCl_2$ in the presence of Vulcan XC-72 carbon in a tube furnace at 300 °C under forming gas ($5\%H_2/95\%N_2$) for 2 h. The random alloy Pt_3Co/C was converted to its intermetallic phase through annealing at 700 °C in a conventional tube furnace. Their XRD patterns recorded using a synchrotron source in a homemade device (Figure 13a) are presented in Figure 13b, in which the intermetallic pattern (the top panel of Figure 13b) exhibited multiple superlattice ordering peaks with a distinguished "new peak" (the 110-peak) compared with the random alloy pattern (the middle panel of Figure 13b), and matches the standard XRD card of the ordered Pt_3Co (PDF 01-071-7410, the bottom panel of Figure 13b) perfectly. The authors further heated the random alloy Pt_3Co/C using the homemade device (Figure 13a) under forming gas for 2 h and collected its *in situ* synchrotron XRD patterns as a function of the annealing temperatures (the left panel of Figure 13c), identifying its critical phase-transition temperature (T_c = 750 °C) under this condition. An increase of both fractions of the ordered phase and the average crystal domain sizes with increasing the annealing temperatures between 600 and 750 °C was also observed, which is similar to the behavior of the bulk Cu_3Au and PtCo nanocrystals. At 750 °C (the optimal annealing temperature), heating time-dependent investigation indicated that 2 h was a sufficient time to achieve the conversion equilibrium with an average crystal domain size of 6 nm (the right panel of Figure 13c). Lee and co-workers also reported their synthesis of well-dispersed ordered intermetallic FePt nanocrystals inside ordered mesostructured silica/carbon composites through thermal annealing under mixed Ar/H_2 (5 wt %) (Figure 13d).[363] In the first step, the ordered mesostructured composites were formed via self-assembly of polyisoprene-blockpoly (ethylene oxide) (PI-b-PEO) block copolymers with aluminosilicate sols in the presence of a hydrophobic iron precursor (dimethylaminomethylferrocene) and a hydrophobic platinum precursor [dimethyl (1,5-cyclooctadiene) platinum(II)]. Next, the as-prepared composites were heated at 800 °C for 2 h, generating ordered intermetallic FePt nanocrystals encapsulated in the ordered mesopores. Interestingly, they found that the particle size of the resultant ordered intermetallic FePt nanocrystals could be readily tuned from 2.4 to 10 nm by varying the quantities of the Pt and Fe precursors in the solution. On the other side, one should keep in mind that an extremely high loading of the metals on the support could result in uncontrolled nanocrystal aggregation toward larger nanocrystals eventually.

Nevertheless, support-assisted thermal activation is not always compelling to facilitate the disorder-to-order transition, as it might also create an opportunity to benefit the order-to-disorder conversion during the process. A notable example was recently reported by Tilley and co-workers.[419] They synthesized partially disordered Pt_3Sn NCbs through low-temperature thermal annealing of ordered intermetallic Pt_3Sn NCbs in air. In particular, the size and shape of the Pt_3Sn nanocrystals could be well-preserved after thermal treatment at 200−250 °C. It should be mentioned that these temperatures seem to be around the critical phase-transition temperature of Pt_3Sn nanocrystals. Therefore, they believed that a choice of the right temperature played a critical role in achieving the order-to-disorder transition. Such a phenomenon might also be observed in other bimetallic combinations with the development of synthetic techniques.

In the aforementioned studies, it seems that the simultaneous use of two or more metal precursors (except for the support) in a reaction system is crucial for the preparation of the ordered intermetallic nanocrystals. However, it should be mentioned that, in some cases, strong metal−support interactions can be employed to synthesize ordered intermetallic nanocrystals on the interface between the nanocrystals and support under high-temperature annealing conditions, since some supports such as transition metal oxides, hydroxides, and carbides can act as the precursors of the metals under a reducing atmosphere.[148,162,420−427] This concept was demonstrated by Pérez-Omil and co-workers. They produced ordered intermetallic $CePt_5$ nanocrystals by reducing the Pt/CeO_2 catalyst at elevated temperatures in a reductive H_2 atmosphere (Figure 14).[364] Using the HRTEM technique combined with simulation, they carried out a systematic study and uncovered the structure evolution process

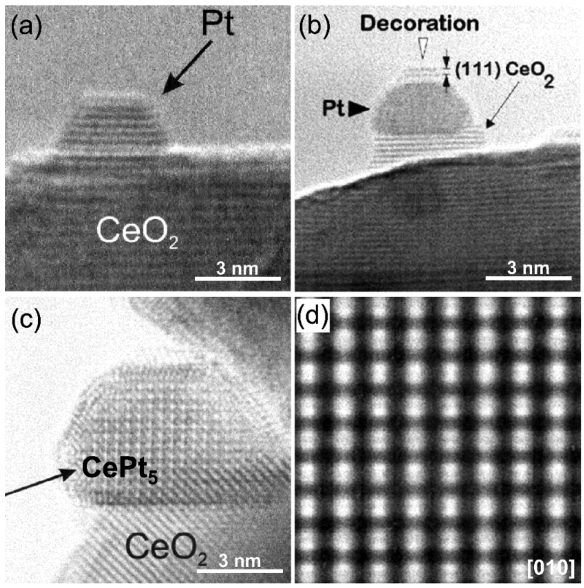

Figure 14. (a,b) HRTEM images recorded on the 4% Pt/CeO_2 nanocrystals annealing at 773 K. (c) HRTEM image recorded on the 4% Pt/CeO_2 nanocrystals annealing at 1173 K. (d) Image simulation of the $CePt_5$ phase along the [010] zone axis. Adapted with permission from ref 364 and modified. Copyright 1997 Academic Press.

https://dx.doi.org/10.1021/acs.chemrev.0c00436
Chem. Rev. 2021, 121, 736−795

of the Pt/CeO_2 catalyst at temperatures ranging from 200 to 950 °C. Particularly, when the Pt/CeO_2 catalyst was annealing at a temperature up to 700 °C, it was observed that a thin, subnanometric ceria decoration layer preferentially orientates with the Pt nanocrystals where they have grown. It was further validated that $CePt_5$ was the only ordered intermetallic phase in the catalyst and the alloying phenomena could only be detected at high reduction temperatures (800−950 °C) that accelerate the interdiffusion of atoms. Recently, Wu and co-workers extended the support-assisted annealing approach to other ordered intermetallic systems, demonstrating that two-dimensional (2D) early transition metal carbides (MXenes), especially Ti_3AlC_2, could serve as supports for the *in situ* formation of Pt_3Ti intermetallic nanocrystals by a thermal reduction under an H_2 atmosphere at 550 °C.[162] Altogether, the support-assisted annealing strategy offers a unique and effective route for the controllable synthesis of ordered intermetallic nanocrystals with uniform dispersity on support.

4.1.3. Protective Shell-Assisted Annealing. The use of oxides (such as MgO, Al_2O_3, and SiO_2) and polymers as protective coating layers is another simple yet versatile approach for preventing the aggregation and regrowth of nanocrystals during the subsequent heat treatment, leading to precise control on the size of the ordered intermetallic nanocrystals as a result of the complete elimination of interparticle diffusion.[366,367,428−439] As compared with the support-assisted annealing approach, this coating confinement method is more efficient in stabilizing the nanocrystals against sintering and in precisely controlling the size of the final products. However, this protective layer must be removable to expose the nanocrystal surface in the post-treatment for further applications. It is worth mentioning that, in most cases, it is difficult to complete the structural transition from the random alloy to the ordered intermetallic phases with the confinement of the coating layer since the coating shell dramatically limits the atomic mobility/diffusion and increases the kinetic energy barrier in the atom ordering process. For the formation of fully ordered intermetallic nanocrystals rather than partially ordered phases, elevated annealing temperatures are required in this approach. As an example, Sun and co-workers successfully demonstrated this approach by employing a thin layer of MgO as the protecting shell to prepare ordered intermetallic PtFe nanocrystals at high annealing temperatures (Figure 15).[365] In a typical synthesis, a mixture of $Pt(acac)_2$, $Fe(CO)_5$, OAm, OA, and octadec-1-ene was heated to 240 °C for 1 h, and then MgO was coated on the as-obtained PtFe nanocrystals with a chemical disorder structure by decomposing a mixture of $Mg(acac)_2$, 1,2-tetradecanediol, OAm, OA, and benzyl ether. By carrying out a thermal treatment under Ar + 5% H_2 at 750 °C for over 6 h and subsequent removal of MgO via acid leaching, the as-prepared PtFe nanocrystals could be converted into ordered intermetallic phase while a good dispersibility was preserved. More importantly, this approach has also been extended to the synthesis of ordered intermetallic nanocrystals with different structures and components, for instance, PtCo, PtSn, and PtZn nanocrystals.[13,105,366,367]

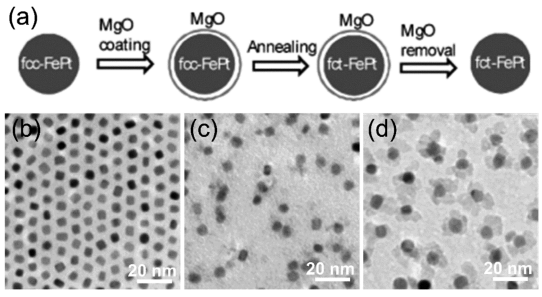

Figure 15. (a) Schematically illustrating the synthesis of *fct* FePt nanocrystals from *fcc* FePt/MgO nanocrystals via a protective shell-assisted annealing approach. TEM images of (b) 7 nm *fcc* FePt nanocrystals, (c) as-synthesized *fcc* FePt/MgO nanocrystals, and (d) *fct* FePt/MgO nanocrystals synthesized via thermal annealing of *fcc* FePt/MgO nanocrystals at 750 °C for 6 h. Adapted with permission from ref 365 and modified. Copyright 2009 Wiley-VCH.

As the second example, Hyeon and co-workers further expanded the protective shell-assisted annealing method to other systems, showing that N-doped carbon with a porous structure could serve as a protective shell for the formation of atomically ordered intermetallic PtFe nanocrystals with an average size of 6.5 nm during the annealing treatment process.[157] In this case, by simply impregnating the as-prepared carbon-supported PtFe nanocrystals in a dopamine hydrochloride aqueous solution followed by polymerization at 700 °C, the polydopamine-coated *fcc* PtFe nanocrystals were readily converted into N-doped carbon-coated PtFe nanocrystals with an ordered phase. It is noteworthy to point out that the *in situ* formed carbon shell plays a significant role in preventing the nanocrystals from the emergence of agglomeration/sintering during the thermal annealing process. Furthermore, they revealed that the thickness of the N-doped carbon shell could be precisely controlled within a range from subnanometer to 3.5 nm by tuning the impregnating time of polydopamine. In summary, from the aforementioned examples, the major advantage of the protective shell-assisted annealing strategy is the ability to effectively stabilize the nanocrystals against sintering and thus potentially improve the dispersion of resultant-ordered intermetallic nanocrystals.

4.1.4. Defects/Vacancies-Assisted Annealing. To achieve the disorder-to-order transition, defects/vacancies are generally introduced to decrease the diffusion barrier and thereby promote the ordering process of metal atoms under high-temperature annealing conditions. Unlike other annealing approaches, this method is mainly used for tuning the composition of nanocrystals by introducing other metals to generate defects/vacancies, significantly benefiting the structure transition upon heating and performance improvement. Taking ordered intermetallic PtFeL′ (L′ = Au, Cu, Ag, Mn, and Sb) nanocrystals as representative examples, it is believed that doping other metals to the disordered PtFe nanocrystals could help facilitate the atomic ordering process, generating the ordered intermetallic PtFe nanocrystals at a relatively lower temperature as compared to the case without doping.[195,207,209,215,394,440] Depending on the alloying power of the L′ atoms with either Pt or Fe atoms, it was determined that the strong interaction between Pt and Fe atoms would squeeze the L′ atoms out to the nanocrystal surface upon high-temperature annealing since the above-mentioned L′ atoms possess weaker interaction with either Pt or Fe atoms. Along with L′ atoms segregating onto the nanocrystal surface, defects would be created within each nanocrystal to promote metal atom diffusion and structural conversion from disorder to order. For example, as demonstrated by Sun and co-workers, monodisperse 4 nm *fcc* FePtAu nanocrystals with tunable compositions were converted to ordered intermetallic FePtAu nanocrystals by annealing at 600 °C, with Au segregating on

https://dx.doi.org/10.1021/acs.chemrev.0c00436
Chem. Rev. 2021, 121, 736−795

the FePt nanocrystal surface derived from the lower intersolubility between Au and PtFe.[205] In this process, the disorder-to-order transition could be strongly affected by the doping content of 20 at % Au, generating optimal atomic ordering in the FePt structure. They ultimately concluded that the doped Au atoms were able to enhance the mobility of the host matrix atoms by creating defects/vacancies, thus promoting the kinetics of the ordering process. Later on, the same group reported that the ordered intermetallic PtFe nanocrystals could also be prepared by annealing dumbbell structured PtFe−Fe_3O_4 nanocrystals or core−shell structured PtFe−Fe_3O_4 nanocrystals in a reducing H_2/Ar gas, where atomic ordering was promoted by creating vacancies upon the Fe_3O_4 reduction to Fe.[112,161] Similarly, this approach was also extended to other ordered intermetallic fabrication, such as PdFe, PdCo, and PtCo.[10,177,394,420]

4.1.5. Other Thermal Annealing Approaches. Apart from the above-mentioned strategies, several other methods have been developed to suppress the sintering/aggregation during the disorder-to-order transition process at elevated temperatures. These approaches involved the usages of a surfactant-free KCl matrix, linker molecules, mixed salt powders, and pulsed-laser annealing.[169,380,441−444] For example, DiSalvo and co-workers reported their synthesis of ordered intermetallic nanocrystals with various components through a surfactant-free KCl matrix method.[169] In this approach, an insoluble KCl byproduct would be formed *in situ* upon the fast reduction of chloride-based precursors in the presence of a strong reducing agent (e.g., KEt_3BH) and served as a protective matrix to stabilize the nanocrystals in a subsequent thermal annealing treatment. By simply tuning the annealing conditions or the content of KCl in the precursors, the size of the resultant products can be readily controlled. Before this work, Liu and co-workers also disseminated that the ordered intermetallic nanocrystals could be prepared by direct high-temperature annealing in the presence of NaCl powders.[443] It is important to note that these inorganic salts used in the nanocrystal sintering may not be very efficient in assisting the phase conversion, as they can only act as a physical barrier rather than a microstructural shell around each nanocrystal. Additionally, Inoue and co-workers released an approach for yielding ordered intermetallic nanocrystals by employing linker molecules to stabilize the nanocrystals as well as to suppress the nanocrystal coalescence upon annealing.[444] Overall, the growing interest in developing new synthesis strategies for the conversion of ordered intermetallic nanocrystals is stimulated by their enhanced properties and promising applications as compared to those from the random alloy nanocrystals.

4.2. Liquid-Phase-Based Synthesis Approaches

Liquid-phase-based synthesis is the foremost and effective approach to generate a variety of ordered intermetallic nanocrystals with well-defined sizes, shapes, compositions, and structures, including bimetallic nanocrystals and multimetallic nanocrystals.[47,120,172,184,369,375,445−456] As compared with the solid-state annealing in the gas atmosphere, the liquid-phase synthesis usually carries out at a relatively low temperature (typically, < 350 °C) mainly due to the limitation of the solvent boiling point, which is lower than the required structure transition temperature. To overcome this obstacle, it is of critical importance to significantly lower the kinetics energy barrier in the disorder-to-order transition by simply adjusting the experimental conditions, including the addition of various reducing agents and/or capping agents in the reaction solution, introduction of a dopant metal, and diffusing of a second metal into the as-synthesized seeds.

4.2.1. One-Pot Synthesis. One-pot synthesis is arguably the most straightforward and powerful approach for synthesizing ordered intermetallic nanocrystals with well-defined size, shape, dispersity, and composition at relatively mild conditions.[374,457−467] This approach involves the simultaneous addition of all reactants, such as precursors, solvents, reducing agents, stabilizers, and capping ligands, in just one reactor, where the reactions can proceed at a given temperature until the reactions reach equilibrium, effectively avoiding a lengthy separation of the intermediates while dramatically increasing the product yield. Traditionally, the simultaneous reduction of different metal-containing precursors with a strong reducing agent, such as AA, TBAB, $NaBH_4$, or n-butyllithium, has turned out to be an effective strategy for generating the ordered intermetallic nanocrystals in one-pot synthesis, especially for metals with a relatively large difference in reduction potential, high binding energy, low electronegativity, or immiscibility in the bulk state.[120,144,184,368,457,468−470] For example, Huang and co-workers adopted this approach to synthesize nanoplates consisting of intermetallic PtPb core and Pt shell of ∼1 nm in thickness by using AA as the reducing agent in the presence of OAm/1-octadecene as mixed solvent (Figure 16a,b).[120] They reported that the use of AA was

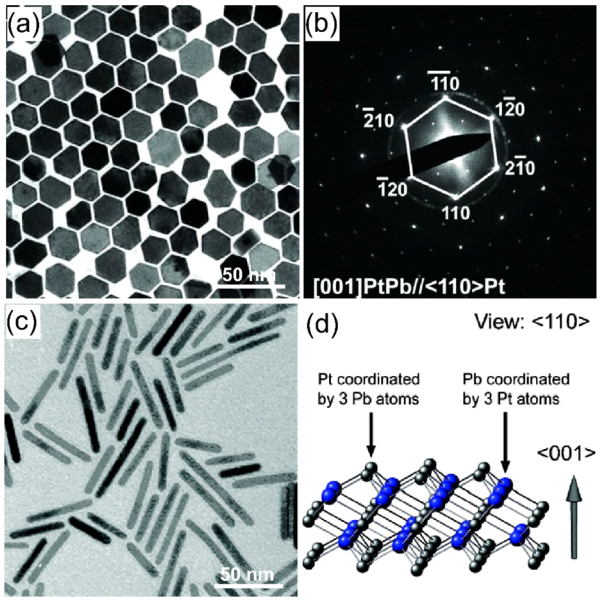

Figure 16. (a) TEM image of core−shell PtPb−Pt nanoplates with *hcp* PtPb cores and Pt shells acquired in a one-pot synthesis and (b) the corresponding SAED pattern of a single hexagonal nanoplate. (c) TEM image of the *hcp* PtPb nanorods acquired in a one-pot synthesis. (d) The growing surfaces of the *hcp* PtPb nanorods viewed along ⟨110⟩ direction. (a,b) Reproduced with permission from ref 120. Copyright 2016 AAAS. (c,d) Adapted from ref 368 and modified. Copyright 2007 American Chemical Society.

critical for the formation of PtPb/Pt nanoplate as AA can act as a weak acid to remove the Pb atoms during the synthetic process, facilitating the Pt atoms to diffuse inward and rearrange. By simply reducing the amount of AA, the formation of ordered intermetallic PtPb phase became favorable. As an additional example, Yang and co-workers demonstrated the

https://dx.doi.org/10.1021/acs.chemrev.0c00436
Chem. Rev. 2021, 121, 736−795

synthesis of ordered intermetallic PtPb nanorods. They used TBAB as the reducing agent to simultaneously reduce Pt and Pb precursors in the presence of diphenyl ether, adamantanecarboxylic acid (ACA), hexadecanethiol (HDT), and hexadecylamine (HDA) at 180 °C under an argon atmosphere (Figure 16c,d).[368] The shape of PtPb products could be precisely controlled by varying the amount of TBAB and HDT, the molar ratio of ACA to HDT, and the reaction time. Interestingly, they claimed that the formation of nanorods could be attributed to the difference in coordination numbers along with low-indexed facets of the PtPb nanocrystals with their hexagonal crystal structure, where adatom preferably incorporates into the top and bottom facets with relatively high-binding numbers, benefiting the growth along the ⟨001⟩ direction. Around the same time, Schaak and Cable reported their synthesis of R−Sn, (R = Ag, Au, Co, Cu, Fe, and Ni) and Pb−R′ (R′ = Bi, Pb, Sn, and Sb) binary intermetallic nanocrystal systems with ordered phases using $NaBH_4$ as a strong reducing agent in polyol systems at relatively low temperatures.[445] To promote the formation of the ordered intermetallic nanocrystals, this work indicates that a strong reducing agent is essential to achieve the co-reduction of different precursors with relatively large differences in reduction potential.

It was found that certain capping agents (e.g., halide ions, organic phosphine, or organic amines) in the reaction solution can selectively bind to specific crystal facets of the nanocrystal through surface chemisorption, effectively redefining the anisotropy in surface free energy and thus driving the disorder-to-order phase transition in the one-pot synthesis.[59,173,452,471,472] To this end, Hou and co-workers synthesized ordered intermetallic PtBi nanoplates using NH_4Br as the capping agent to simultaneously reduce the Pt- and Bi-precursors in the presence of OAm at 200 °C under a nitrogen stream.[452] They further carried out a systematic study and explored the function of other halide ions (e.g., F^-, Cl^-, or I^-) and different types of bromide-containing reagents while other synthetic parameters were kept the same. They concluded that bromide ions played a significant role in the formation of nanoplates with predominant exposed {101} facets via selective absorption. In a later report, the same group demonstrated that the crystal phase of FePt nanocrystals could be tuned to an ordered structure by the addition of different halide ions (e.g., Cl^-, Br^-, or I^-) in the solution containing $Pt(acac)_2$, $Fe(acac)_3$, and OAm at 350 °C under nitrogen.[113] For a synthesis without the addition of halide ions, disordered FePt nanocrystals in the mean size of ∼5 nm were obtained. Another typical example of ordered intermetallic nanocrystal synthesis in cubic shape has been given by Yu and co-workers. They prepared ordered intermetallic PdCu NCbs by simultaneously reducing Pd- and Cu-precursors using trioctylphosphine (TOP) as a capping agent and stabilizer in the presence of OAm as both a solvent and a reducing agent at 250 °C under N_2 atmosphere.[369] The shape of the PdCu nanocrystals could be readily controlled by tuning the amount of TOP, reaction temperature, and the molar ratio of Pd/Cu. Interestingly, they found that the P atom derived from TOP could selectively cap the {100} facets of the PdCu nanocrystals, resulting in a dramatic decrease in total surface energy on the {100} facets and thereby producing PdCu NCbs in the average size of 12 nm. In summary, the presence of desirable capping agents in the reaction solution is of critical importance to simultaneously control the shape and the crystal phase of the resultant products in the one-pot synthesis since the capping agent can decrease the surface energy of specific crystal facets via selective adsorption and thus facilitate the atomic ordering process.

In addition to using the reducing agents and capping agents in the reaction solution, the introduction of a dopant metal in one-pot synthesis has also been demonstrated to be viable for the preparation of ordered intermetallic nanocrystals. This is suggested to be largely associated with defects and lattice strain introduced by the doping atoms, as discussed previously in section 4.1.4 about the annealing approach. In general, doping metals that are immiscible to the parent metals might be squeezed out of the parent metal lattice at a relatively high synthesis temperature, leading to lattice vacancies and inducing the mobility of parent metals to a rearrangement. As demonstrated by Kinge and co-workers, the addition of the Au precursor to a solution containing $Pt(acac)_2$, $Fe(CO)_5$, 1,2-hexadecanediol, octyl ether, HDA, OAm, and OA led to a formation of ordered intermetallic FePtAu nanocrystals in the size of ∼6 nm.[370] The group systematically investigated the effect of the reaction temperature on the crystallographic phase of the as-prepared products, revealing that the onset of reaction temperature for generating the ordered face-centered tetragonal (*fct*, e.g., $L1_0$) phase was as low as 150 °C. Meanwhile, the composition of the ordered intermetallic FePtAu nanocrystals could also be readily tuned by varying the reaction temperature. Furthermore, by prolonging the reaction time to 3 h, the domination of the highly ordered phase in FePtAu nanocrystals could be observed due to the kinetic development. Several years later, Wang and co-workers further studied the FePt system using this approach with other dopants, showing that Ag and Cu could be incorporated into the lattice of FePt nanocrystals in one-pot synthesis, thereby forming ordered intermetallic FePtAg and FePtCu nanocrystals.[195,473] Altogether, introducing a dopant metal in one-pot synthesis provides exquisite control over both the composition and crystal phase of final products via adjusting the synthetic parameters, such as the concentration of doping metal precursor, reaction temperature, and duration of the reaction. More importantly, this concept and strategy could be potentially extendible to other systems.[160,209,215,394]

4.2.2. Seed-Mediated Synthesis. Seed-mediated synthesis is the most viable approach to control the size, shape, and composition of ordered intermetallic nanocrystals by effectively separating the complicated nucleation from the subsequent growth processes.[174,175,178,371,474−480] Typically, this approach involves two steps: (i) synthesizing seeds with well-defined size, shape, composition, and structure and (ii) diffusing a second metal into the as-prepared seeds. This approach was initially adopted in 2007 by Schaak and Cable, who used a series of single-component metal nanocrystals including Pd, Cu, and Au as the seeds for the entire synthesis of ordered intermetallic L″−Zn (L″ = Pd, Cu, and Au) nanocrystals.[178] In the first step, different types of metal-containing precursors dissolved in 1-octylamine were added into a hot solution of HDA, respectively, in which the metal-containing precursors were completely reduced to generate zerovalent metal nanocrystals. A 1-octylamine solution of Et_2Zn was then quickly injected in the system, forming ordered intermetallic Zn-based nanocrystals via seed-mediated diffusion growth at relatively high temperatures. Recently, Zhu and co-workers utilized the seed-mediated diffusion approach to prepare ordered intermetallic AuCu nanocrystals in the average

https://dx.doi.org/10.1021/acs.chemrev.0c00436
Chem. Rev. 2021, 121, 736−795

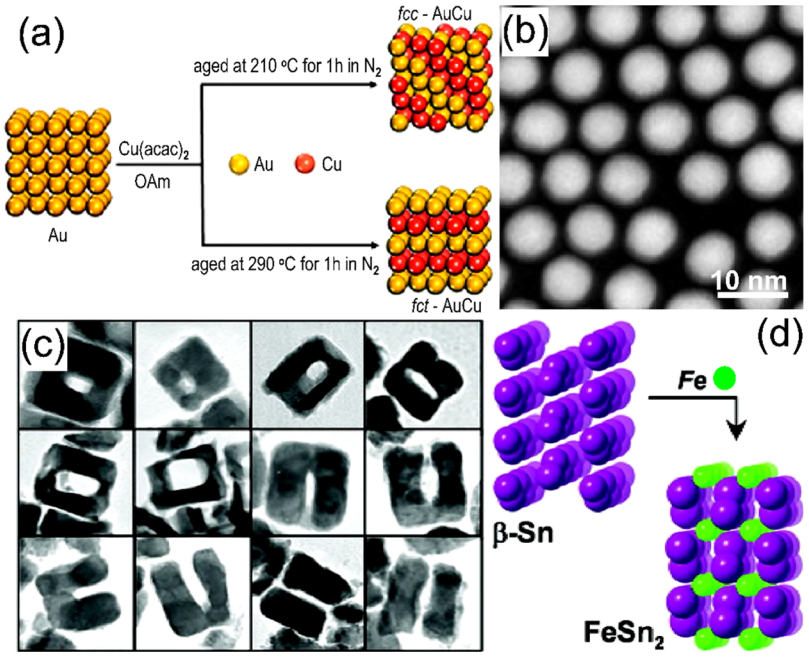

Figure 17. (a) Schematic illustration of the synthesis of *fcc* and *fct* AuCu alloy nanocrystals by utilizing the Au nanocrystals as seeds. (b) HAADF-STEM image of as-synthesized AuCu alloy nanocrystals with the *fct* structure. (c) TEM images of ordered intermetallic $FeSn_2$ nanocrystals with different types of hollow structures (scale on each: ~50 nm). (d) formation scheme of ordered intermetallic $FeSn_2$ nanocrystals via a seed-mediated growth. (a,b) Adapted from ref 98 and modified. Copyright 2017 American Chemical Society. (c,d) Adapted from ref 371 and modified. Copyright 2007 American Chemical Society.

size of 8 nm by employing Au nanocrystals as the seeds in the presence of OAm (Figure 17a,b).[98] In this example, the reduced Cu atoms by OAm could rapidly diffuse into Au seeds, resulting in the formation of ordered intermetallic AuCu nanocrystals at 290 °C and disordered AuCu nanocrystals at 210 °C, while preserving the product in the similar size, shape, and composition. They found that the composition of AuCu nanocrystals could be readily controlled by simply tuning the mass ratio of Au seed and $Cu(acac)_2$. These results indicate that the formation of ordered intermetallic nanocrystals might require high reaction temperatures in the presence of single-component metal nanocrystals as the seeds due to the involvement of the relatively higher diffusion barriers and the longer diffusion distances. Skrabalak and co-workers recently demonstrated a paradigm in achieving core−shell ORR nanocatalysts, containing randomly alloyed PtCu shells and PdCu cores that could be either the atomically random *fcc* phase (A1, $Fm\bar{3}m$) or the intermetallic CsCl-like phase (B2, $Pm\bar{3}m$).[464] Similarly, the authors deposited randomly alloyed Pt−M (M = Ni, Co, Cu, or Fe) shells on intermetallic PdCu B2 cores with a variation of the shell thickness and composition (Pt:M ratios), showing a 230% and 270% ORR activity increment on PtCu- and PtNi-shells, respectively, in comparison with the Pt reference.[481] These studies show that both the surface structure and the core nature could impact the ORR performance in acidic media.

In some cases, the large difference in diffusion rate between different metals enables an opportunity of harvesting ordered intermetallic nanocrystals with hollow structures during the seed-mediated synthesis. This phenomenon is commonly referred to as the nanoscale Kirkendall effect. Typically, when the inward diffusion rate of metal is significantly lower than the outward diffusion rate of another metal, the lattice vacancies would be continuously generated at the boundaries, resulting in the emergence of a hollow structure. One typical example was given by Schaak and co-worker, where a series of ordered intermetallic M*−Sn (M* = Pd, Fe, Co, and Ni) nanocrystals with hollow structures were formed by using shape- and size-controlled Sn nanocrystals as the seeds in the presence of tetraethylene glycol (TTGE) (Figure 17c,d).[371] Taking the synthesis of ordered intermetallic $FeSn_2$ nanocrystals as a demonstration, they found that unequal diffusion rates between the Sn and Fe atoms led to the void formation through the Kirkendall effect, driving the conversion of the cubic Sn nanocrystals into ordered intermetallic $FeSn_2$ nanocrystals with various shapes containing hollow squares, U-shaped structures, and nanorod dimers. The shape variation was attributed to the anisotropic nanostructure of the tetragonal Sn seeds, where the top and bottom faces are possible to be more reactive sites as compared with the four side faces with a higher atomic density of Sn atoms, triggering an anisotropic Kirkendall effect. Importantly, it was further confirmed that the transition from the cubic structure of Sn seeds to ordered intermetallic $FeSn_2$ nanocrystals largely associated with the size and shape of seeds. Shortly, the same group further extended this approach to their synthesis of various ordered intermetallic L‴−Sn (L‴ = Au, Ag, Pt, and Ru) nanorods with hollow structures using Sn nanorods as the seeds.[372]

In addition to the use of single-component metal nanocrystals as seeds for ordered intermetallic nanocrystal preparation, random alloy structure of bimetallic or multimetallic nanocrystals is accessible to convert into the intermetallic structure during the seed-mediated synthesis. For example, Skrabalak and co-workers adopted the seed-mediated co-reduction route and synthesized ordered intermetallic PdCu nanocrystals with a high monodispersity using disordered PdCu nanocrystals as the seeds in a solution

https://dx.doi.org/10.1021/acs.chemrev.0c00436
Chem. Rev. 2021, 121, 736−795

containing $PdBr_2$, $Cu(ac)_2$, OAm, and TOP at 270 °C (Figure 18).[208] The morphology and crystal structure of the ordered

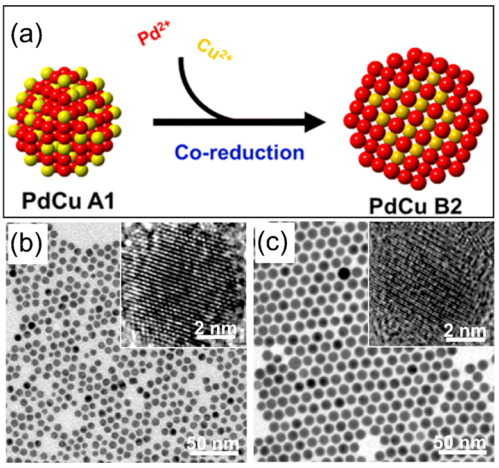

Figure 18. (a) Schematic illustration of the synthesis of ordered intermetallic PdCu alloy nanocrystals by utilizing the disordered PdCu alloy nanocrystals as seeds. (b) TEM images of (b) disordered PdCu nanocrystals and (c) ordered intermetallic PdCu nanocrystals. The insets in panels (b) and (c) are HRTEM images of a typical PdCu nanocrystal with a disordered structure and PdCu nanocrystal with an ordered structure, respectively. Adapted from ref 208 and modified. Copyright 2016 American Chemical Society.

intermetallic PdCu nanocrystals were confirmed by HRTEM and XRD. HRTEM images showed that the nanocrystals were comprised of atomically ordered PdCu cores and segregated thin Pd shells. The team also found that the use of bromide ions could destabilize the interaction between TOP and nanocrystal surfaces during the seed-mediated co-reduction process, which promotes the deposition of the monomers on PdCu seeds via heterogeneous nucleation instead of homogeneous nucleation. Moreover, carrying out a time-evolution study by quenching the reactions at different periods revealed that the atomic ordering process associated with intraparticle diffusion of atoms in the seed-mediated co-reduction synthesis was expected to be size-dependent, most likely due to the activation barrier originating from the size-dependent surface free energetics. In contrast, they proposed that the thermal annealing process was strongly related to interparticle diffusion with relatively longer diffusion length and higher diffusion barrier, resulting in the particles sintering/aggregation after annealing. Subsequent studies by the same group expanded this methodology to simultaneously overgrow Au and Cu atoms on random alloy AuCu nanocrystals for the synthesis of monodisperse ordered intermetallic AuCu nanocrystals in solution.[154] They first prepared random alloy AuCu nanocrystals in size of 6.5 nm by injecting a precursor solution, consisting of $Au(ac)_3$, $Cu(ac)_2$, and OAm, into a preheated solution containing ODE, OA, and 1,2-dodecanediol at 185 °C under Ar. The random alloy AuCu seeds were then added to a solution of $Au(ac)_3$, CuBr, ODE, 1,2-dodecanediol, and OAm at 280 °C, leading to the formation of monodisperse ordered intermetallic AuCu nanocrystals in size of 9.7 nm via a size refocusing mechanism. Using TEM and XRD characterization, they verified the proposed size refocusing mechanism, where smaller nanocrystals with a larger surface-to-volume ratio were constantly dissolved and redeposited onto energetically more stable larger nanocrystals along with the disorder-to-order transformation. Significantly, this concept related to the use of size refocusing to achieve the disorder-to-order conversion is anticipated to be potentially expandable to other systems in the seed-mediated co-reduction synthesis.

4.2.3. Hydrothermal/Solvothermal Approach. Hydrothermal and solvothermal approaches, which are typically carried out at an elevated temperature and pressure in water (hydrothermal) or organic solvent (solvothermal) media in a sealed Teflon-lined stainless-steel autoclave, are considered to be good choices for the scalable production of ordered intermetallic nanocrystals with controlled size and shape.[373−375,482−485] In general, water and nonaqueous media at a reaction temperature beyond their boiling point or high-pressure display an obvious variation in their physicochemical properties, such as viscosity, solubility, and dissociation constant, resulting in a remarkable enhancement in the reactivity of reactants and an input of external energy. As a result, hydrothermal and solvothermal approaches offer a potential platform for achieving the disorder-to-order transformation by overcoming the high energy barriers. However, in the context of practical synthesis, the structural types of the final product are strongly dependent on specific synthetic parameters, including temperature, pressure, metal combination, composition, types of capping agent and reducing agent, and so on. For example, Chen and co-workers utilized the hydrothermal method and prepared ordered intermetallic PtPb nanodendrites with controllable compositions by coreducing the Pt and Pb inorganic precursors in an aqueous solution consisting of formic acid as the reducing agent.[484] It was uncovered that the use of formic acid, specific metal combination and composition, had an important influence on the formation of ordered intermetallic nanocrystals. This strategy can also be expanded to a series of ordered intermetallic Pt−Q (Q = Bi, Au, Pd, and Ru) and PdRu nanodendrite syntheses by simply altering the types of precursors involved. Furthermore, the compositions of these ordered intermetallic nanodendrites could also be tuned by varying the molar ratio of different precursors.[484] Shortly, Peter and co-workers reported that the ordered intermetallic Pd_3Pb nanocrystals in different shapes could be prepared via the hydrothermal method using $NaBH_4$ as the reducing agent in the presence of PVP as the surfactant at 240 °C for 24 h.[483] They identified that the addition of $NaBH_4$ and PVP might be crucial in determining the formation of ordered intermetallic nanocrystals. Importantly, this approach can also be extended for the formation of other Pd and group IV metal-based ordered intermetallic nanocrystals by carefully choosing appropriate precursor salts.[483]

Besides the hydrothermal approach, the solvothermal approach has also been widely adopted for the generation of ordered intermetallic nanocrystals by simply replacing water with organic solvents, such as OAm, TTEG, and DMF. Specifically, the boiling point of these organic solvents decreased in the order of OAm > TTEG > DMF, and their polarity increased in the order of OAm < DMF < TTEG. Realizing that these mentioned solvents can also act as reducing agents during the synthesis and their reducing powers could be increased with the temperature and pH. Therefore, in the context of practical synthesis, it is critically important to correctly choose appropriate solvents based on their respective characteristics. For example, Lou and co-workers employed the solvothermal approach to synthesize the ordered intermetallic $PtCu_3$ nanocages by utilizing OAm as both the reducing agent

https://dx.doi.org/10.1021/acs.chemrev.0c00436
Chem. Rev. 2021, 121, 736−795

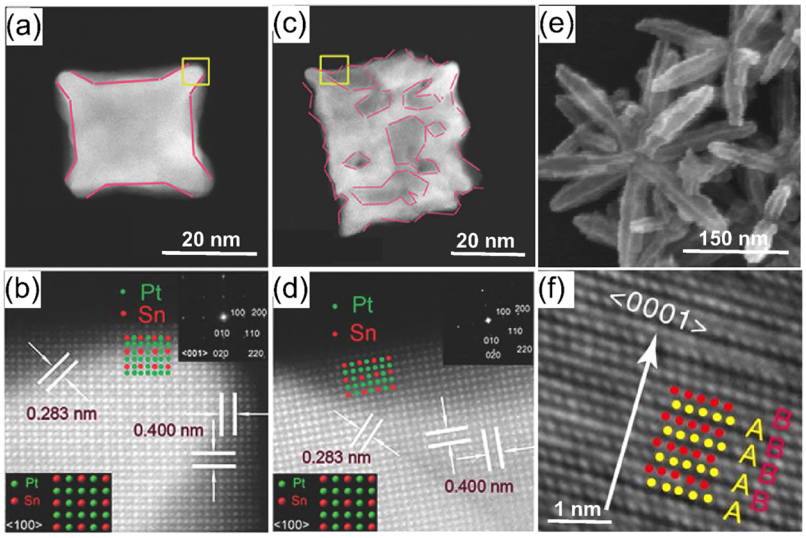

Figure 19. HAADF-STEM images of (a) a single concave cubic and (c) defect-rich cubic intermetallic Pt_3Sn nanocrystal and (b, d) the corresponding atomic-resolution HAADF-STEM images taken from the yellow regions in HAADF-STEM images. (e) SEM image of *hcp* Pt−Ni excavated nanomultipods. (f) HRTEM image taken from a single branch of a representative *hcp* Pt−Ni excavated nanomultipod. (a−d) Adapted with permission from ref 374 and modified. Copyright 2016 Wiley-VCH. (e,f) Adapted with permission from ref 375 and modified. Copyright 2017 Springer Nature.

and solvent in the presence of CTAB as both the capping agent and surfactant.[373] On the basis of a series of control experiments, they ultimately concluded that the formation of intermetallic $PtCu_3$ nanocages was mainly due to the galvanic replacement between preformed Cu nanocrystals and Pt species. In a later report, Li and co-workers successfully synthesized cubic, concave cubic, and defect-rich cubic intermetallic Pt_3Sn nanocrystals by simply tuning the concentrations of the Pt− and Sn−precursors under the solvothermal conditions (Figure 19a−d).[374] In a typical synthesis, a solution of $Pt(acac)_2$, $SnCl_2$, and DMF was added to an autoclave and then the system was heated to 180 °C for 12 h. They believed that the high reaction temperature and high pressure in the solvothermal synthesis process provided extra energy for achieving the atomic ordering and thus generating the ordered intermetallic nanocrystals with surface defects. Specifically, the formation of surface defects was derived from the oxidative etching caused by O_2 and Cl^- from the Sn precursor. Moreover, this approach can also be applied to the synthesis of Pt−Mn nanocrystals with an atomically ordered structure. Later, Xie and co-workers also reported a solvothermal synthesis of hexagonal close-packed Pt−Ni excavated nanomultipods, in which the mean diameter and length of the branches were around 35 and 145 nm (Figure 19e,f).[375] They determined that the use of formaldehyde might be of critical importance for the successful generation of the unique hexagonal closest packed (*hcp*) structure. Meanwhile, it was believed that CO molecules generated by decomposing formaldehyde would induce the diffusion of Pt to the edge of nanomultipods, followed by diffusion of Ni to the edge to form excavated branches.

4.2.4. Electrochemical Approach. The electrochemical approach has been used as an efficient and convenient strategy for the synthesis of ordered intermetallic nanocrystals with controllable compositions and high yields due to its simple setup and facile operation.[171,486−497] Generally, the extra electric current is required to drive the transfer of electrons by supplying the energy to the system and thus stimulate the chemical reactions that do not occur spontaneously. For instance, Hall and co-workers developed the electrochemical deposition approach to synthesize the metastable ordered intermetallic $Pd_{31}Bi_{12}$ nanocrystals in an aqueous electrolyte at room temperature.[498] In this process, a potential of −0.1 V was constantly applied for 1000 s in an aqueous solution containing Na_2PdCl_4, $Bi(C_2H_3O_2)_3$, CH_3COOH, and $C_{10}H_{16}N_2O_8$ (EDTA). Using a series of characterization methods including XRD, HRTEM, XPS, and selected area electron diffraction (SAED), the group demonstrated that the as-synthesized $Pd_{31}Bi_{12}$ nanocrystals in the average diameter of 35 nm possessed an atomically ordered crystal structure. Shortly, they reported an electrochemical dealloying approach to directly convert colloidally synthesized ordered intermetallic $PdBi_2$ nanocrystals to ordered intermetallic Pd_3Bi nanocrystals under ambient conditions (Figure 20).[488] Briefly, the ordered intermetallic $PdBi_2$ nanocrystals were first synthesized via a reduction of $Pd(acac)_2$ and $Bi(C_2H_3O_2)_3$ in OAm at 300 °C, yielding ordered intermetallic $PdBi_2$ nanocrystals. The as-prepared colloidal products were further electrochemically cycling under O_2 at 1600 rpm in 0.1 M KOH repeatedly, generating ordered intermetallic Pd_3Bi nanocrystals. They reported that the facile removal of Bi from $PdBi_2$ by the controlled electrochemical corrosion and subsequent atomic restructuring played an important role in generating the ordered intermetallic Pd_3Bi nanocrystals under the experimental conditions.

4.2.5. Microwave-Assisted Reduction Approach. The microwave-assisted reduction approach is an emerging strategy for the preparation of ordered intermetallic nanocrystals with greater precision as compared with those methods using the conventionally heating process.[499−503] Typically, microwave treatment can rapidly and uniformly heat the reagents including solvents, intermediates, and products, accelerating the fast reduction of metal-containing precursors and favoring instantaneous nucleation in the solution. For example, as demonstrated by Armbrüster and co-workers, Rh−Bi nanoplates with *hcp* structure could be formed by simultaneously

https://dx.doi.org/10.1021/acs.chemrev.0c00436
Chem. Rev. 2021, 121, 736−795

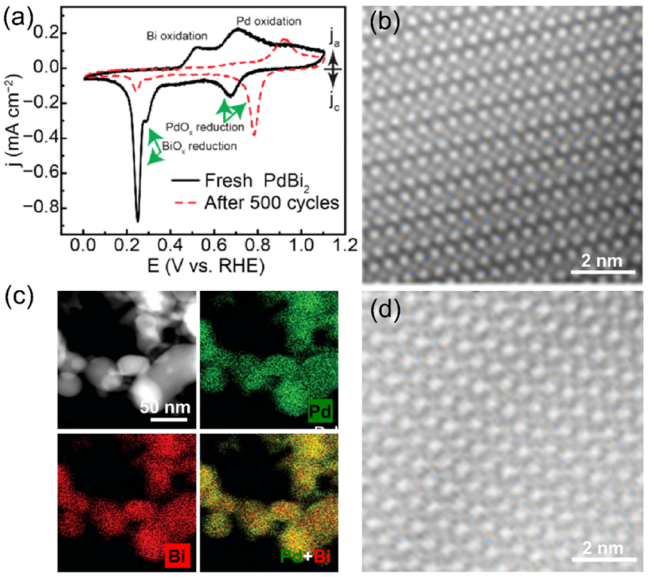

Figure 20. (a) Cyclic voltammograms of the $PdBi_2$ nanocrystals in Ar-saturated 0.1 M KOH before and after the electrochemical dealloying. (b) HAADF-STEM image shows the ordered atomic arrangement of as-prepared $PdBi_2$ nanocrystals. (c) HAADF-STEM image and the corresponding EDX elemental mapping of Pt (green) and Bi (red) for as-prepared $PdBi_2$ nanocrystals. (d) HAADF-STEM image of a typical Pd_3Bi nanocrystal with the ordered atomic arrangement after 10,000 cycles of accelerated durability testing. Adapted from ref 488 and modified. Copyright 2019 American Chemical Society.

reducing $Rh_2(C_2H_3O_2)_4$ and $Bi(C_2H_3O_2)_3$ in EG (as both the reducing agent and solvent) in the absence of surfactants under rapid microwave heating.[183] These as-synthesized nanoplates possessed an average diameter of about 60 nm and thickness of less than 20 nm. According to quantum chemical LMTO-ASA calculations, it was reported that the chemical bonding in RhBi comprised heteropolar covalent Rh−Bi bonding via three-center bonds and homoatomic covalent Rh−Rh bonding, benefiting the electron transfer from bismuth to rhodium. In a recent report, Ruck and co-workers utilized the microwave-assisted reduction route and obtained a series of ordered intermetallic Pd−Bi nanocrystals by simply varying the molar ratio of different precursors, reaction temperature, heating time, solvent, and the addition of auxiliaries like OAm, OA, and KOH at relatively low temperatures in minutes.[504] It was determined that the optimal reaction temperatures and heating times were between 170 and 240 °C and a few minutes up to 1 h, respectively.

4.3. Other Synthetic Approaches

In addition to the aforementioned synthetic approaches, there are also some unique methods used for the preparation of ordered intermetallic nanocrystals, such as biological templates, w/o microemulsion media, and sonication-assisted reduction.[213,376,377] For example, Belcher and co-workers used a biological template to directly synthesize ordered intermetallic FePt nanocrystals with the desired composition under ambient conditions.[376] They realized that a selective addition of specific peptides could promote the formation of FePt nanocrystals and their crystallization with a chemically ordered structure. As an additional example, Magno and co-workers utilized w/o microemulsions as reaction media to prepare PtPb nanocrystals with precise size-control in the range of 3−6 nm.[213] According to the authors, the PtPb product was ordered intermetallic, having the same crystal structure as Pt. By altering the reaction temperature and the microemulsion compositions including the metal-precursors and reducing agent, the size of the droplets could be readily tuned, resulting in a precise size-control in the resultant nanocrystals with ordered structure. Furthermore, Gedanken and co-workers showed that the ordered intermetallic Ga−Pt nanocrystals embedded on graphene could be successfully formed by sonicating an aqueous solution containing H_2PtCl_6 and molten gallium.[377] The aforementioned examples showcase that many alternative pathways are capable of being developed for the fabrication of ordered intermetallic nanocrystals.

5. APPLICATIONS OF RANDOM ALLOY AND INTERMETALLIC NANOCRYSTALS

The noble metal-based nanocrystals have been widely used in various fields, including electrochemical reactions [e.g., ORR, hydrogen oxidation, small carbohydrate molecular oxidation and CO_2 electrochemical reduction reaction (eCO_2RR)[505,506]], other reactions related to photochemical reactions,[507,508] and heterogeneous catalysis in the petroleum industry, as well as magnetism. These applications are strongly dependent on their sizes, shapes, compositions, structures, and crystal phases. In this chapter, we mainly outline the applications of noble-metal-based random alloy and intermetallic nanocrystals in catalytic, optical and photocatalytic, and magnetic aspects, with an extended discussion of property and catalysis on other associated systems such as core−shell structured and surface index-dependent catalysts if necessary.

5.1. Electrochemical Applications

Electrocatalytic reactions generally involve a series of complex pathways, including the adsorption of reactants, the reaction of the adsorbed species, and desorption of reaction products.[509−511] It is intensively demonstrated that the catalytic performance (e.g., activity, selectivity, and durability) of the electrocatalysts is largely associated with their sizes, shapes, compositions, structures, and crystal phases over the past few decades.[267,512,513] Aiming to develop efficient catalysts, these parameters are required to be elaborately controlled during the synthesis. According to the general Sabatier principle raised by Paul Sabatier,[514] the optimal catalytic performance can be readily achieved for a given reaction when the interactions between the catalyst surface and the reactants/intermediates/product are "just right", that is, neither too strong nor too weak. Note that the principle can be described by plotting the reaction rate as a function of the heat of adsorption, and such a plot is generally shown as a volcano plot with a clear trend, where the highest activity corresponds to be the appropriate value of the binding energy.[515] As such, the volcano plot has been extensively applied to the design of advanced catalysts for varieties of chemical reactions.[510,516−518] Later, Nørskov and co-workers further demonstrated that, in fact, the binding energy is strongly correlated to the position of the *d*-band center of a catalyst defined by the surface electronic structure of the transition metal alloys.[519] Variations in the width of the *d*-band could inevitably cause alternations in the position of the *d*-band center, as *d*-filling would not change for any transition metals, and thus keeps the *d*-band at the Fermi level. To compensate for variations in the width of the *d*-band derived from changes in metal coordination number, it is required to accordingly shift the *d*-states up or down, totally

https://dx.doi.org/10.1021/acs.chemrev.0c00436
Chem. Rev. 2021, 121, 736−795

depending on the nature of the change. Normally, the catalyst with a higher *d*-band center can strongly bind to the adsorbed species as compared to that with a lower *d*-band center. By taking advantage of density functional theory (DFT) calculations, the in-depth understanding of molecule interactions on catalyst surfaces paves a way for knowing the effects of different factors and thus facilitates the development of efficient catalysts through less of a trial and error practice.[520−522] Moreover, with the emergence and development of a series of characterization techniques in recent years, more invaluable evidence in enhancing the overall catalytic performance is correlated with atomic-scale features of the catalysts.[523,524]

Relative to monometallic nanocrystals, random alloy and intermetallic bimetallic nanocrystals have served as modeling systems for investigating the ligand (electronic), geometric (surface strain), and ensemble (coordination) effects on the overall electrocatalytic performance.[14,90,525] Ligand effect associates with binding strength of adsorbates by surface electronic structures of nanocrystals with the electron interaction between metals, which is much more obvious when a second or third metal introduced into the nanocrystal. As demonstrated by Strasser and co-workers,[526] these fundamental effects are typically derived from the introduction of a second metal and have also been confirmed to significantly alter the *d*-band center position with regard to the Fermi-level of a bimetallic catalyst, thus enhancing the catalytic performance. Geometric effect, normally caused by a lattice mismatch, twined structure, or structure defectiveness, can also alter the characteristics of nanocrystals when their surface atoms are restructured. The strain due to a lattice mismatch can also be classified as an expansive (tensile) or compressive strain compared with the bulk counterpart materials. Specifically, the compressive strain causes the *d*-band center downward, dramatically leading to a decrease of the bonding strength of the adsorbed species on the catalyst surface. In contrast, the *d*-band center upshifts in the presence of the tensile strain, increasing the bonding strength. Ensemble effect or synergistic effect resulting from more than one reactive site often enhances the catalytic performance including catalytic activity and selectivity. Take the Pd−Ag alloy system as an example, Stevenson and co-workers found that by introducing Pd into a Ag particle surface, the single Pd sites surrounded by Ag are favorable to the steps of oxygen bond breaking and desorption for the ORR due to the ensemble effect.[91] However, it should be emphasized that these effects are difficult to be fully identified and isolated due to the coexistence of geometric and ligand effects, and, in some cases, all three effects.[527−530] These aforementioned effects all have been exploited to develop advanced catalysts with a significantly enhanced electrocatalytic performance for a broad range of catalytic reactions. In this section, we mainly concentrate on electrocatalytic applications of random alloy and intermetallic nanocrystals by exquisitely presenting plenty of representative examples.

5.1.1. Oxygen Reduction Reaction (ORR). Being a cathode half-reaction of fuel cell and metal-air (such as Li−air and Zn-air) batteries, the electrochemical ORR has a high overpotential and is sluggish mainly due to the strong interaction between oxygen-based intermediates generated in the electrochemical reaction and the catalytic surface (i.e., Pt atoms). In acid or alkaline media, ORR occurs mainly through two pathways: the indirect two-electron pathway to generate H_2O_2 (eqs 8 and 9) as an intermediate and the direct four-electron pathway to produce H_2O (eqs 10 and 11).[531,532] For fuel cell performance, normally a four-electron ORR pathway is preferred.

$$O_{2(g)} + 2H^+_{(aq)} + 2e^- = H_2O_{2(aq)} \quad E_0 = +0.680 \text{ V vs RHE}$$

$$H_2O_{2(aq)} + 2H^+_{(aq)} + 2e^- = 2H_2O_{(aq)} \quad E_0 = +1.776 \text{ V vs RHE} \tag{8}$$

$$O_{2(g)} + H_2O_{(aq)} + 2e^- = HO^-_{2(aq)} + OH^-_{(aq)} \quad E_0 = +0.080 \text{ V vs RHE}$$

$$HO^-_{2(aq)} + H_2O_{(aq)} + 2e^- = 3OH^-_{(aq)} \quad E_0 = +0.880 \text{ V vs RHE} \tag{9}$$

$$O_{2(g)} + 4H^+_{(aq)} + 4e^- = 2H_2O_{(aq)} \quad E_0 = +1.230 \text{ V vs RHE} \tag{10}$$

$$O_{2(g)} + 2H_2O_{(aq)} + 4e^- = 4OH^-_{(aq)} \quad E_0 = +0.401 \text{ V vs RHE} \tag{11}$$

This section will outline the strategies of recently designed and developed noble metal (especially Pt- and Pd-based) random alloy and intermetallic nanocatalysts, and will also discuss how to promote their catalytic performance such as activity and durability toward ORR.

5.1.1.1. Pt-Based Random Alloy Catalysts. Pt is the most promising metal as the cathode catalyst in the proton-exchange membrane fuel cell (PEMFC). However, it is a low-abundance element in the Earth's crust and notoriously expensive. To minimize the use of Pt and boost its ORR performance simultaneously, researchers have developed several synthetic approaches to explore the solution. The first strategy is to synthesize core−shell nanocrystals in which Pt[533,534] or Pt-based random alloy[140,535,536] is designed as the shell to maximize the utilization of Pt. Meanwhile, the electronic and structural behaviors of the Pt-based shell can be easily tailored by carefully tuning the shell thickness, core−shell composition, particle size, and shape to improve the ORR activity and durability over state-of-the-art pure Pt nanocatalysts. The tensile or compressive strain effect possibly existing in such a structure could be an additional contribution to the enhancement of the ORR performance. The design, synthesis, and performance of these core−shell ORR catalysts have been extensively outlined in recent years.[533,535,537] It is worth mentioning that shape-controlled cores have also been introduced into this strategy to induce the shell lattice with the preferred facet such as {111} and to enhance the ORR activity. Examples include a Pd nano-octahedral core with an ultrathin Pt−Ni shell,[67] Pd nanoicosahedral core,[538] and nano-octahedral core[42,254] with an ultrathin Pt shell, respectively.

The second strategy is to incorporate the 3d transition metals (Fe, Co, Cu, especially Ni) into Pt lattice with shape and composition control. The use of a 3d transition metal could decrease the fraction of Pt in the cathode catalyst.[19,38,69,104,115,219,227,318,539−545] Most importantly, the randomly alloyed transition metal could adjust the Pt d-band center[546−549] to optimize the ORR activity and selectivity together with the ligand effect, geometric effect, and strain effect. The d-band center theory could be used to explain/predict the ORR reaction behavior via the electronic structure.[550,551] For example, if the Pt d-band center position shifts downward after alloying a 3d transition metal, the catalyst surface would show not only a reduced binding affinity to oxygen and weakened O−O bond breaking but also an enhanced bonding formation between adsorbed reactants. This

https://dx.doi.org/10.1021/acs.chemrev.0c00436
Chem. Rev. 2021, 121, 736−795

would increase the selectivity of H_2O_2. In contrast, if the d-band center position shifts upward, it could lead to stronger binding between oxygen and active sites, facilitating O−O bond breaking and generating H_2O as the final product.[550] Stamenkovic and co-workers uncovered a fundamental relationship in electrocatalytic trends on Pt_3M'* (M'* = Co, Ni, Fe, Ti, V) surface between the surface electronic structure and their ORR catalytic activity, providing a strategy to optimize the composition and crystallographic facets of Pt-based bimetallic random alloy toward ORR.[547,549] They further demonstrated an ORR catalytic activity order of $Pt_3Ni(111) \gg Pt_3Ni(110) > Pt_3Ni(100)$ using extended single-crystal surfaces and showed the surface on $Pt_3Ni(111)$ exhibits an enhanced ORR activity that is 10-fold higher than Pt(111) and 90-fold higher than the current state-of-the-art Pt/C catalysts.[547] This performance enhancement is attributed to the surface-sensitive adsorption of OH_{ad} on $Pt_3Ni(hkl)$ and its inhibiting effect on O_2 adsorption. The $Pt_3Ni(111)$ surface contains an unusual electronic structure (downshift of *d*-band center position) and surface atoms rearrangement in the near-surface region, exhibiting the highest ORR kinetics in comparison with $Pt_3Ni(110)$ and $Pt_3Ni(100)$.

The third strategy is to "transfer" the crystal facet-defined advantages from bulk catalysts and single-crystal surfaces to the nanoscale realm through a particle shape-controlled synthetic approach, which is more practical for the next development of fuel cell nanocatalysts. Since the $Pt_3Ni(111)$ that has its unique position of d-band center and weak interaction between its surface atoms and nonreactive oxygenated species exhibits the highest ORR kinetics in an acidic environment, nanocatalysts containing the exclusive $Pt_3Ni(111)$ facets have drawn growing attention. By sharing the insight of outstanding ORR performance on the $Pt_3Ni(111)$ surface,[547] as the first "nano-transferring" example, Fang and co-workers created a novel synthesis route in which $W(CO)_6$ was used as a special reducing agent and demonstrated their shape-controlled preparation of Pt_3Ni nano-octahedra exclusively terminated by {111} facets,[262] exhibiting much improved ORR activity. Shortly, Xia and co-workers refined this synthesis and modified the post-treatment process, reporting an ORR mass activity of the harvested Pt−Ni nano-octahedra as high as 3.3 A/mg_{Pt}.[73] Yang and co-workers also disseminated their shape-controlled synthesis of {111}-bound Pt_3Ni nano-octahedra[258] and nanoicosahedra,[272] reporting 0.44 A/mg_{Pt} and 0.62 A/mg_{Pt} as their ORR mass activities in 0.1 M $HClO_4$, respectively. After this work, Strasser and co-workers reported their synthesis of octahedral Pt_xNi_{1-x} random alloy nanocrystals with an ORR mass activity of ~1.7 A/mg_{Pt}.[115] Subsequently, Pt_3Ni NFs with a Pt-skin structure evolved from $PtNi_3$ rhombic dodecahedra were reported by Chen and co-workers, exhibiting an enhanced ORR mass activity of 5.7 A/mg_{Pt}.[220] In the next year, Huang and co-workers revealed their synthetic work of Mo-doped Pt_3Ni nano-octahedra, showing ORR mass activity as high as 6.98A/mg_{Pt}.[72] It is believed that element Mo prefers staying at subsurface positions near the particle edges in vacuum and surface vertex/edge sites in oxidizing conditions, enhancing the ORR performance and stability.[104,116] Shortly, this group also synthesized a class of 2D PtPb−Pt core−shell nanoplate catalysts with large biaxial strains that help to optimize the Pt−O bond strength, exhibiting an ORR mass activity of 4.30 A/mg_{Pt}.[120] Recently, Tian and co-workers developed Pt−Ni random alloy nanocages with an ORR mass activity of 3.52 A/mg_{Pt}.[71] Remarkably, the existence of fewer strongly bonded platinum−oxygen (Pt−O) sites in the as-synthesized nanocatalysts induced by the strain and ligand effects was attributed to the high stability with negligible activity decay after 50,000 potential cycles.

Although other shape-controlled Pt-based random alloy nanocatalysts, such as Pt−Cu,[276,552] Pt−Fe,[323,553] and Pt−Co,[76,249,317] have also been well-developed in recent years, an excellent paradigm of the facet-dependent Pt−Ni random alloy nanocatalyst synthesis with precise size- and composition-control demonstrate a novel way in the ORR activity improvement potentially used in PEMFCs. Such progress is outlined in Figure 21a.

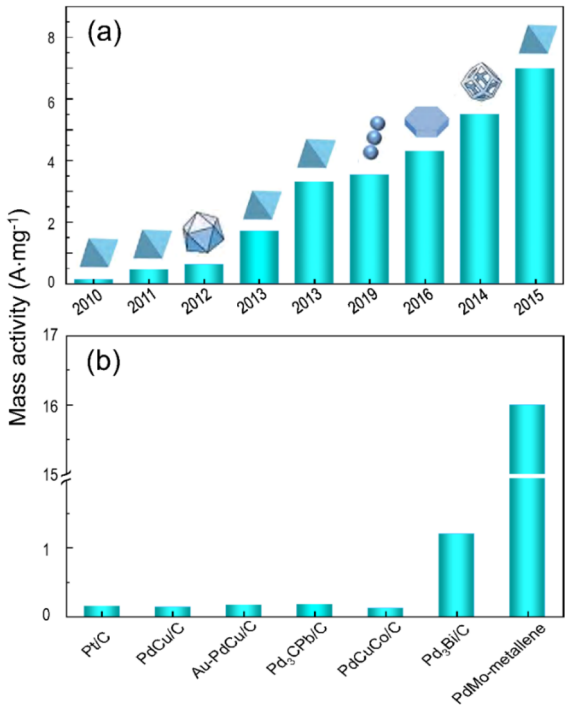

Figure 21. (a) Mass activity comparison of various crystal facet-dependent Pt−Ni nanocatalysts toward ORR in the acidic electrolyte, reported by the following groups: Fang,[262] Yang,[258,272] Strasser,[115] Xia,[73] Huang,[72,120] Tian,[71] and Chen.[220] (b) Mass activity comparison of various types of Pd-based catalysts toward ORR in O_2-saturated 0.1 M KOH solution, reported by the following groups: Myers,[450] Adzic,[177] DiSalvo,[382] Huang,[129] Hall,[488] and Guo.[554] Data are adapted from the mentioned publications.

5.1.1.2. Pt-Based Intermetallic Nanocatalysts. As mentioned above, the (111) facets of Pt_3Ni possess the most active ORR sites in the acidic electrolyte. However, this is limited by possible leaching of the Ni-composition due to the potentially unstable nature of the 3d metals.[10,92] To stabilize the Pt-based nanocatalysts against chemical oxidation and dealloying during the electrochemical process, researchers have dedicated to the fabrication of atomically ordered intermetallic nanocrystals. Compared with the random alloy phase as a counterpart, the atomically ordered structures of Pt-based intermetallics, including Pt−Fe,[112,136,157,161,555] Pt−Ni,[108] Pt−Co,[118,168,385,387,393,396,400,431] Pt−Ga,[377] Pt−Cu,[127,144,171,402,413,486] Pt−Bi,[122,397,457] and Pt−Pb,[120,446] have a strong d-d orbital interaction between Pt and transition metal M″ (M″ = Fe, Co, Ni, Cu, Bi, Pb, etc.) and can be more efficient to stabilize the component M″ from non-noble metal leaching. In other words, the electronic and geometric effects

https://dx.doi.org/10.1021/acs.chemrev.0c00436
Chem. Rev. 2021, 121, 736−795

in Pt−M″ could substantially be strengthened once the random alloys are transformed into intermetallic compounds. For instance, Sun and co-workers compared the ORR performance between 8 nm *fcc*-structured PtFe random alloy nanocrystals and their corresponding $L1_0$ PtFe−Pt core−shell intermetallic nanocatalysts in 0.1 M $HClO_4$ solution,[161] demonstrating that Fe can be stabilized more efficiently than the intermetallic structure with a 5 Å Pt shell. The fully ordered $L1_0$ PtFe nanocatalysts were fabricated by annealing the MgO-coated dumbbell-like Fe_3O_4−FePt nanocrystals under the Ar/H_2 atmosphere. By etching Fe atoms on the surface of $L1_0$ PtFe nanocatalysts followed by a further heat-treatment at 400 °C, a compressive Pt-shell consisting of about 2 atomic layers could be generated, leading to the formation of $L1_0$ PtFe−Pt core−shell nanocatalysts. This core−shell intermetallic structure exhibits superior mass activity (0.7 A/mg_{Pt} at 0.9 V) and excellent durability with no obvious dropping down of the ORR activity after 30,000 potential cycles between 0.6 and 0.95 V in oxygen-saturated 0.1 M $HClO_4$ at 80 °C, meeting the DOE 2020 target (<40% loss in mass activity). In a later report, they further improved the ORR performance by replacing Fe in the $L1_0$ PtFe−Pt ordered intermetallic structure with Co.[114] To effectively stabilize Co in the corrosive fuel cell environment, ordered $L1_0$ PtCo−Pt core−shell nanocatalysts with 2−3 atomic layers of strained Pt shell were synthesized. The Pt layers possess a shorter Pt−Pt distance on the surface of core−shell nanocatalysts, leading to more evident biaxial compressive strains that can further weaken the bonding of oxygen species (such as O_2*) to the Pt surface and thus lower the overpotential kinetically.

The same method of stabilizing the transition metal M″ in the intermetallic Pt−M″ structure by coating a layer of Pt skin or a thin-shell of Pt-based alloy has successfully been applied to other systems, such as Pt-skinned intermetallic $L1_2$ $PtCu_3$ (with an ORR specific activity of 8.4-time higher than that of Pt/C in 0.1 M $HClO_4$).[556] As another example, *fcc* Pt−Cu random alloy as the shells were deposited on PdCu B2 intermetallic seeds in a facet-dependent manner, generating PdCu−PtCu core−shell nanocatalysts with highly strained surfaces. These compressively strained PdCu−PtCu nanocatalysts demonstrated high ORR mass activities (2.55 A/mg_{Pt} at 0.9 V versus RHE) and enhanced durability with no apparent structural changes after 10,000 potential cycles in 0.1 M $HClO_4$. This strategy can also be extended to other metal nanoparticle systems. Huang and co-workers reported their synthesis of intermetallic PtPb−PtNi octahedra as a new class of catalysts.[446] These nano-octahedra with an ordered PtPb core and active Pt−Ni surface showed superior ORR specific (5.16 A/cm^2) and mass activities (5.16 A/mg_{Pt}) in 0.1 M $HClO_4$ solution. They can also endure over 15,000 potential cycles with negligible activity decay. Similarly, Guo and co-workers developed a class of 2D nanoplates comprising an intermetallic *hcp*-PtBi core and ultrathin Pt shell, showing little loss in ORR activity during the accelerated durability test (ADT) in 0.1 M $HClO_4$ solution.[122]

5.1.1.3. Pd-Based Catalysts. As a class of Pt-free catalysts, Pd-based nanocatalysts are efficient toward ORR, not only in acidic solutions[557] but also in alkaline media. In recent years, extensive efforts have been dedicated to the improvement of ORR activities in alkaline media.[177,208,369,415,450,554,558] Unlike acidic solutions, the alkaline media confer many beneficial features to ORR, such as the reduced adsorption energies of anions,[559] the surface-independent outer-sphere electron transfer processes in its initial stage which enables the utilization of a wide range of non-Pt catalysts,[560] less corrosive environment to the catalysts, and more importantly, much faster kinetics.[561] Just like the case in acidic media, alloying a transition metal M″ into Pd will result in electronic structure modifications (e.g., the d-band shift) that will directly affect the catalyst-adsorbate bond strength.[562,563] Reports from previous studies already suggest that many Pd,[564] Pd-based random alloys (such as Pd−Ag,[565] Pd−Ir,[566] and Pd−Cu[567]) and Pd-based intermetallic (such as Pd−Cu,[129,487] Pd−Pb,[59,382,456,568] Pd−Bi,[488] Pd−Fe,[434] Pd−Cu−Co,[129] Pd−Cu−Fe,[569] Au−O−PdZn,[570] and Pd−Cu−Au[194]) nanocatalysts exhibit superior alkaline ORR performance than Pt. Some particular results in this aspect are recounted as follows.

Adzic and co-workers reported their synthesis of Au decorated ordered PdCu nanocatalysts, exhibiting comparable activity to Pt in acid and alkaline media.[177] The superior stability, after 10,000 potential cycles, was also attributed to the ordered structure as well as the protective effect of the Au clusters from the catalyst surface. DiSalvo and co-workers developed a high-performance ordered Pd_3Pb intermetallic catalyst with a significant increase in mass activity in O_2-saturated 0.1 M KOH media.[382] Shortly, intermetallic PdCuCo as a trimetallic ORR nanocatalyst was demonstrated.[129] Under the dual tuning on the composition and intermetallic phase, the ordered catalysts exhibited preponderant activity enhanced stability over those from a disordered PdCuCo counterpart and those of the commercial Pt/C catalysts. This could arise from the ligand effect and the compressive strain effect from the Pd surface due to the smaller atomic size of Cu and Co. Remarkably, Hall and co-workers reported an electrochemical dealloying process to convert the as-synthesized $PdBi_2$ to Pd_3Bi nanocrystals under ambient conditions by removal of the Bi from the surface with simultaneously enabling interdiffusion of the constituent atoms via vacancy diffusion.[488] Both the $PdBi_2$ to Pd_3Bi are ordered intermetallic phases. However, the converted Pd_3Bi exhibited 11-time higher ORR mass activity (1.2 A/mg_{Pd}) than that of Pt/C in 0.1 M KOH. Recently, it was also demonstrated that intermetallic Pd_3Pb nanoflowers show 11.4-fold higher ORR mass activity (1.14 A/mg_{Pd}) than that of commercial Pt/C and high stability toward ORR in 0.1 M KOH solution (23.7% loss vs 35% Pt/C loss in mass activity after 10,000 potential cycles). These features were attributed to the contribution from various ultrathin nanoplates terminated by {200} facets on both the planar surfaces of these Pd_3Pb nanoflowers.[571] Besides, Guo and co-workers demonstrated that the PdMo random alloy in the form of a highly curved and subnanometer-thick metal nanosheet (metallene) is an efficient and stable electrocatalyst toward ORR in alkaline electrolytes.[554] The high atomic utilization, as well as the large electrochemically active surface area, of this thin-sheet-structure results in a mass activity as high as 16.37 A/mg_{Pd}, which is 78-times higher than those of commercial Pt/C and Pd/C catalysts. ORR mass activities of the above-mentioned achievements are illustrated in Figure 21b.

5.1.2. Small Molecule Oxidation (MOR/EOR/FAOR). Since the electrochemical oxidation of small molecules, such as hydrogen oxidation reaction (HOR), FAOR, methanol oxidation reaction (MOR), and ethanol oxidation reaction (EOR), is a class of typical anode reactions in fuel cells, development of highly efficient electrocatalysts for these reactions is the key to achieve high power density fuel cells. Pt-based nanocatalysts are still favorable candidates due to

https://dx.doi.org/10.1021/acs.chemrev.0c00436
Chem. Rev. 2021, 121, 736−795

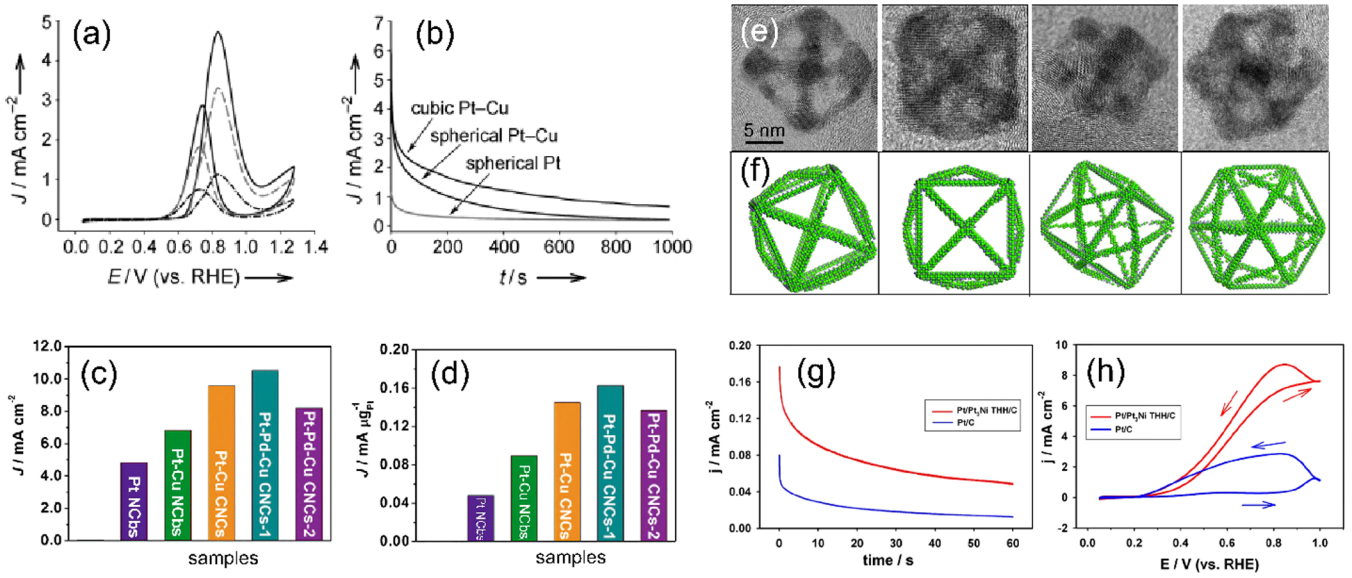

Figure 22. (a) Cyclic voltammograms of MOR on Pt−Cu on Pt−Cu nanocubes (—), Pt−Cu nanospheres (− −), and Pt nanospheres (−·−·) in 0.1 M $HClO_4$/1 M CH_3OH solution (scan rate: 0.02 V s^{-1}). (b) Chronoamperometric results of MOR at 0.8 V on the same samples in the same solution. (c) Specific activity and (d) mass activity for MOR on Pt−Pd−Cu concave nanocubes (CNCs), Pt−Cu CNCs, Pt−Cu nanocubes (NCbs), and Pt NCbs with similar sizes in 0.1 M $HClO_4$/1 M CH_3OH solution. For (d), the current density was normalized in reference to the unit weight of total metal and Pt loaded on the working electrode, respectively. (e) HRTEM images of THH NFs in different zone axes as illustrated in models of (f). For (f), the pewter and green colors represent Pt and Pt_3Ni (not to the atomic ratio), respectively. (g) Current density−time curves of Pt_3Ni THH NFs/C and Pt/C (40 wt % Pt) recorded in (0.1 M $HClO_4$ + 0.5 M HCOOH) solution 0.30 V (vs RHE). (h) Cyclic voltammograms of Pt_3Ni THH NFs/C and Pt/C (40 wt % Pt) in the same solution for (g) at a scan rate of 0.1 V s^{-1}. (a,b) Reproduced with permission from ref 552. Copyright 2009 WILEY-VCH. (c,d) Adapted with permission from ref 572 and modified. Copyright 2012 WILEY-VCH. (e−h) Reproduced from ref 68. Copyright 2017 American Chemical Society.

their superb catalytic nature. As recounted above, Pt is a scarce element. In addition to increasing the surface area-to-volume ratio of Pt nanocrystals by appropriately reducing the particle size, strategies for improving the anode catalytic performance include alloying with other metal(s) and modulating the atom arrangement on the surface (crystal facet) of the random alloy nanocrystals. Fang and co-workers synthesized cubic Pt−Cu random nanoalloys using a co-reduction approach and applied them as MOR catalysts[552] in 2009. These Pt−Cu NCbs demonstrated the highest MOR electrocatalytic activity (Figure 22a) in comparison with their counterparts (spherical Pt−Cu and monometallic Pt nanocrystals in similar sizes) as shown in the cyclic voltammograms (CVs), which was further confirmed by the chronoamperometric measurements performed at 0.8 V (Figure 22b). This superior performance was attributed to both the composition and shape (crystal facet) effects. Yan and co-workers reported their in-depth investigations of both effects on MOR three-years later.[572] They comparatively evaluated the MOR catalytic activities of high-indexed bimetallic Pt−Cu CNCs, high-indexed trimetallic Pt−Pd−Cu CNCs, {100}-terminated bimetallic Pt−Cu NCbs, and {100}-terminated monometallic Pt NCbs in similar sizes. As shown in Figure 22c,d, high-index random alloy samples were identified as the more promising MOR catalysts than both the low-indexed random alloy and monometallic Pt NCbs in terms of both Pt-based mass activity and specific activity toward MOR. Between both high-indexed samples, it seems that the presence of the third element Pd could also alter the activity. This study validates that high-index facets of Pt-based random alloy nanostructures possess a high density of low-coordinated atoms[14] possibly with lattice strain and could serve as promising catalytic promoters for MOR with cleaving C−H and C−O bonds.

The synthesis and application of high-indexed Pt-based nanopolyhedra as advanced electrocatalysts have drawn growing attention in recent years.[192,403,459,540,573−575] Since it has been reported that high-indexed crystal planes of Pt can also effectively promote the activity of FAOR,[576,577] Fang and co-workers developed a series of Pt-based nanocrystals exposed with high-indexed planes using a co-reduction approach in a high-temperature organic solution system, including Pt_3Co CNCs,[40] Pt_3Fe CNCs,[578] $PtNi_4$ THH nanocrystals, and Pt_3Ni THH NFs.[68] The $PtNi_4$ THH nanocrystals prepared via a colloidal method as catalytic precursors are terminated with well-defined (730)-facets and enriched Pt component was segregated on the edges. Mond process was further applied to the THH precursors through thermal annealing in the presence of CO by extracting most of the Ni component, leading to a generation of Pt_3Ni THH NFs that possess a 3D open-structure comprising ridges as thin as a few nanometers (Figure 22e,f). The temperature-controlled post-thermal treatment further promotes an alloying between the segregated Pt and the remaining Ni atoms through surface restructuring, which is different from the traditional vacancy defect-involved and ill-defined acid etching.[220] In comparison with the state-of-the-art Pt/C (40 wt % Pt), the resultant Pt_3Ni THH NFs exhibit high FAOR activity as shown in Figure 22g (e.g., 4 times at 60 s) and low cathodic-to-anodic-scan current ratio as indicated in Figure 22h (1.7 vs 9.1), suggesting that they are much less vulnerable to surface poisoning.

The dealloy process and oxidation behavior of the anode nanocatalysts in fuel cells are much more severe than that of the cathode counterparts. To tackle this problem, intermetallic

https://dx.doi.org/10.1021/acs.chemrev.0c00436
Chem. Rev. 2021, 121, 736−795

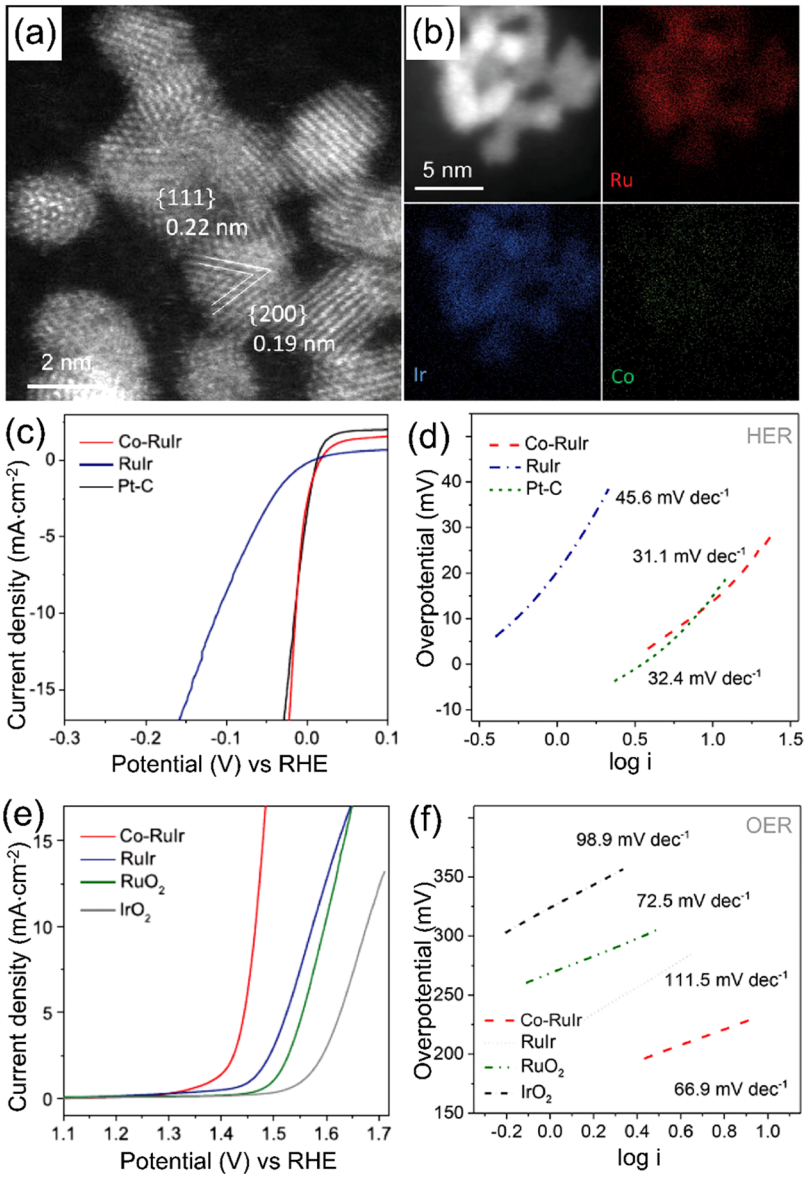

Figure 23. (a) High-resolution HAADF-STEM image of Co-doped (Co−RuIr) nanocrystals. (b) STEM-EDX mappings of Co−RuIr nanocrystals. (c,d) LSV curves and Tafel plots of Co−RuIr, RuIr, and commercial Pt−C electrocatalysts for HER in H_2-saturated $HClO_4$ solution (0.1 M), respectively. (e,f) LSV curves and Tafel plots of Co−RuIr, RuIr, as well as state-of-the-art (commercial) RuO_2 and IrO_2 electrocatalysts for OER in H_2-saturated $HClO_4$ solution (0.1 M), respectively. Adapted with permission from ref 603 and modified. Copyright 2019 Wiley-VCH.

catalysts demonstrated superior activity and durability toward the electrochemical oxidation against the component leaching and chemical oxidation.[107,129,163,166,205,367,373,475,579] For example, Li and co-workers reported that intermetallic Pt_3Ga coupled with an atomic-layer Pt through the engineering of the surface strain and showed apparent high specific activity (7.195 mA/cm^{-2}) and mass activity (1.094 mA/ug_{Pt}) for MOR compared with its unstrained counterpart and commercial Pt/C catalysts. This study implied that the strained Pt_3Ga surface was more energetically favorable for MOR and the stronger binding to OH* on the stretched atomic-layer-Pt-sites enabled an easier removal of CO*.[463] Wang and co-workers also prepared ordered $PtFe_xCu_{1-x}$ ternary intermetallic nanocatalysts,[107] in which facilitates the phase formation from a disordered *fcc* structure to an ordered body-centered tetragonal (*bct*) PtFe phase at the low annealing temperature. These ternary nanocatalysts exhibit significantly enhanced activity and stability due to the ordered intermetallic *bct*-PtFe structure and the relatively inert Cu that partially replaced Fe and mitigated the dissolution, respectively. Most recently, $L1_0$-PtZn intermetallic nanocatalysts were prepared through a Pt^{2+}-exchanged zeolitic imidazolate framework-8 (ZIF-8) NCbs by Kwon et al. The $L1_0$-PtZn intermetallics were embedded in a hollow, N-doped carbon nanocage via one-step calcination and demonstrated an excellent MOR specific activity in 0.1 M $HClO_4$ (3-times higher than that of Pt/C).[580]

In alkaline media, the oxidation reactions such as HOR are sluggish compared with the cases in acidic solutions, requiring new anode catalysts that can further improve the HOR kinetics in alkaline fuel cells.[581] Abruña and co-worker recently developed a series of Rh- and Rh-based random alloy nanocatalysts, including Pt_7Rh_3/C, Ir_9Rh_1/C, Rh_9Ru_1/C, and Rh_9Pd_1/C, that outperformed Ir/C and Pt/C toward HOR in alkaline media.[581] In this work, Ir_9Rh_1/C was identified as the

https://dx.doi.org/10.1021/acs.chemrev.0c00436
Chem. Rev. 2021, 121, 736−795

most effective anode catalyst among all the studied analogs in terms of its specific activity. Zhang and co-workers reported multimetallic core−shell nanoplates using selective element segregation and the etching approach.[582] The obtained PtCuPd−Ru possesses a unique yolk−cage nanostructure, exhibiting superior electrocatalytic activity and stability toward MOR compared with the PtCu nanoplates and commercial Pt/C catalysts. Recently, one-pot synthesis of PdZn nanosheets with an unconventional *fct* structure and thickness of less than 5 nm was also demonstrated.[583] Compared to the Pd counterpart catalysts, the PdZn nanosheets show a much enhanced PdO reduction peak in the 1.0 M NaOH aqueous solution, which indicates large electrochemical surface area of the Pd exposure. Consequently, much improved EOR mass acidity and stability in alkaline media were reported.

5.1.3. Water Electrolysis. The water-splitting as an efficient and environmentally benign process is promising for sustainable hydrogen production.[584] The design of the water electrolysis, first reported in 1789,[585] is related to two half-cell reactions: the HER and OER. Both reactions require efficient electrocatalysts such as platinum-group metals, 3d transition metals, their corresponding metal random alloys, and 3d transition metal-based materials such as carbides,[586,587] nitrides,[588−590] phosphides,[591] sulfides,[592,593] and hydroxides.[594−596] In this section, we focus on the discussion of recent progress in noble-based metal electrocatalysts for HER and OER.

5.1.3.1. Hydrogen Evolution Reaction (HER). Although the conversion of water to hydrogen in both acid and alkaline media has been extensively studied, there are still many challenges in this technique, especially, the sluggish kinetics in alkaline electrolytes.[61,375,597−599] Among various electrocatalysts, platinum group metals (PGMs), especially Pt and Ir, possess superior hydrogen adsorption characteristics and are still promising catalysts for HER.[82,264,600−603] Markovic and co-workers found that Ir and $Pt_{0.1}Ru_{0.9}$ exhibit enhanced activity toward HOR/HER in alkaline solution, and they proposed that the more oxophilic sites on active sites (Ru atoms of Pt−Ru and Ir atoms) promoted the adsorption of OH_{ad} species, which reached an optimal balance between the adsorption/dissociation of H_2 and the adsorption of hydroxyl species (OH_{ad}).[604] On the other hand, coupling PGMs with water-dissociation promoters is commonly used to boost HER activity in alkaline media. For example, Gao and co-workers introduced a sulfite while synthesizing Pt−M‴ (M‴ = Ni, Co, Fe) random alloy nanowires, leading to the formation of M‴−S bonds on the surfaces.[602] Thus, atomic level Pt/M‴-S(OH) interfaces promote hydrogen generation in alkaline media. Similarly, Wang and co-workers developed nitrogen-modified Pt−Ni nanowires to resolve the kinetic issue successfully.[61] The in-depth analysis suggested that the introduced nitrogen could modulate the electron structure around Ni sites, generating empty d_{z^2} orbitals for water adsorption and activation. This strategy could be extended to other bimetallic systems such as Pt−Co, Pt−Ni, and Pt−Cu for boosting the performance toward HER.

Another strategy to boost HER activity of the PGM-based catalysts is the improvement of the intrinsic activity on every single site. One of the examples is to alloy the PGMs with a transition metal, not only reducing the PGM loading but also improving the electrochemical performance on an atomic scale. As a case study, Qiao and co-workers designed and synthesized Co-doped RuIr random alloy (Co−RuIr) nanocrystals as the strengthened electrocatalysts to promote HER using the engineered electronic structure.[603] The high-resolution HAADF-STEM image indicates that the Co dopants do not change the intrinsic lattice distances in the RuIr nanocrystals (Figure 23a), whereas EDX elemental maps (Figure 23b) suggest that Co atoms are distributed randomly at a low concentration. These characterizations conclude that the Co dopant only modified the surfaces of the nanocatalysts, which was validated by its electrochemical performance compared with its counterparts. Figure 23c,d presents linear sweep voltammetry (LSV) curves and Tafel plots as HER performance evaluated in H_2-saturated $HClO_4$ solution (0.1 M), showing that Co−RuIr with an overpotential of 14 mV only (Figure 23c) and low Tafel slope of 31.1 mV dec^{-1} at 10 mA cm^{-2} (Figure 23d) exhibits a significant enhancement compared with the undoped RuIr counterpart (with an overpotential and Tafel slope of as high as 110 mV and 45.6 mV dec^{-1}, respectively) and is comparable with the state-of-the-art Pt/C toward HER.[603]

5.1.3.2. Oxygen Evolution Reaction (OER). As an anode half-cell reaction in both acidic polymer electrolyte water electrolyzers (PEWEs) and alkaline water electrolyzers (AWEs), the OER has been widely studied for decades to improve its kinetics that is hindered by the significant overpotential.[605] The catalysts used for OER are mainly metal oxides with high activity, stability, and electronic conductivity, such as PtO_2, RuO_2, and IrO_2,[606] although nanostructured metal sulfide ($CuCo_2S_4$) was recently reported as well.[607] Despite the limited reports on the metal random alloy nanocatalysts toward OER, the following examples are insightful and prospective.[271,595,596] Lee and co-workers reported a rational synthetic strategy of yielding robust, multimetallic, Ir-based, double-layered NFs.[85] In this work, core−shell alloy nanostructures could be fabricated in a one-plot synthesis by leveraging the different kinetics of dual Ir precursors and transition metal (Ni and Cu) precursors, followed by transforming into a multimetallic IrNiCu dual NFs-NFs rhombic dodecahedral structure via selective etching. Such IrNiCu nanocatalysts provided a high specific surface area and demonstrated excellent activity and durability toward OER in acidic media.

In the above-discussed Co-RuIr system (section 4.1.4),[603] transition metal Co modified the surface characteristic of the RuIr catalysts. To deliver a current density of 10 mA cm^{-2}, as shown in Figure 23e,f, the Co-RuIr required an overpotential and Tafel slope of as low as 235 mV and 66.9 mV dec^{-1} in comparison with 344 mV and 111.5 mV dec^{-1} from the undoped RuIr counterpart, respectively, indicating fast OER kinetics. The improved OER (as well as the discussed HER) performance of Co-RuIr is attributed to a dual effect that modifies the concentration of O-based species and Ru sites valence states.[603] Additional exploration for the dopant elements by Qiao and co-workers suggests that Co outperforms Fe and Ni toward the water-splitting reaction among their studied systems.[603]

5.1.4. CO_2 Reduction Reaction (eCO_2RR). Despite the extensive efforts on exploring sustainable energy resources, today's majority of global energy consumption is still derived from nonsustainable fossil fuels, including petroleum, coal, and natural gas. Plentiful use of these flammable resources is causing the rapid concentration-increase of the emitted carbon dioxide (CO_2) in the atmosphere as well as the subsequent environmental concerns (e.g., greenhouse effects, sea level rise,

https://dx.doi.org/10.1021/acs.chemrev.0c00436
Chem. Rev. 2021, 121, 736−795

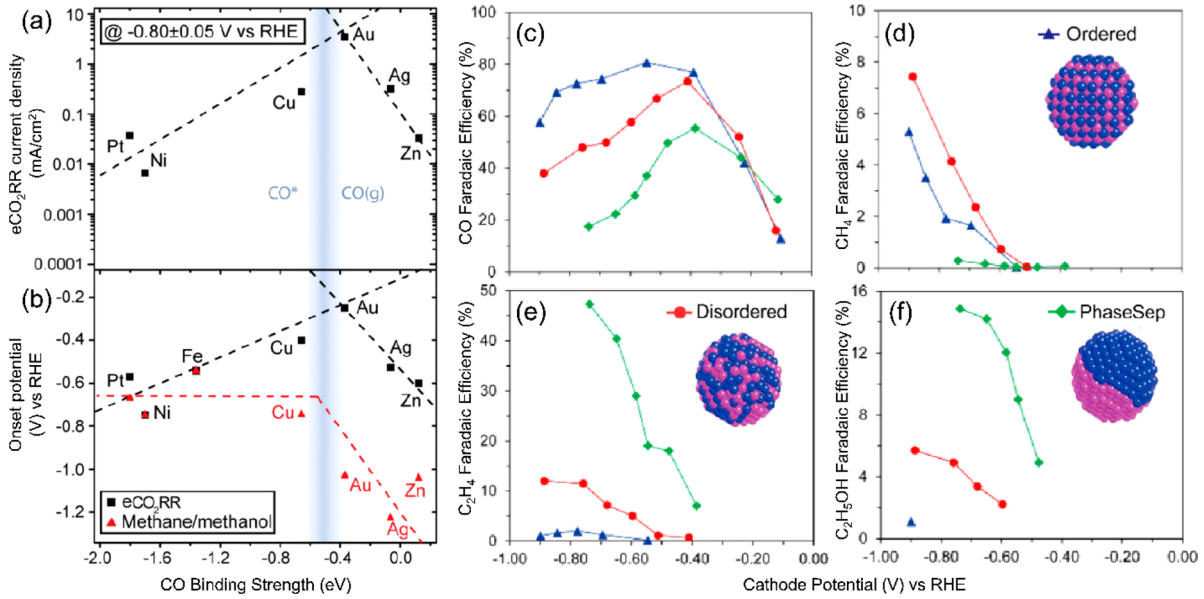

Figure 24. (a, b) Volcano plots: (a) partial current density for eCO_2RR at −0.8 V as a function of CO binding strength; (b) distinct onset potentials as a function of CO binding energy: the overall eCO_2RR, and methane or methanol. (c-f): Faradaic efficiencies of eCO_2RR as a function of cathode potential for each of the major products using three types of different Pd−Cu nanocatalysts (insets in d-f): (c) for product CO; (d) for product CH_4; (e) for product C_2H_4; (f) for product C_2H_5OH. Adapted with permission from ref.s[142,627] and modified. Copyright © 2014, 2017 American Chemical Society.

and ocean acidification). To tackle this problem, CO_2 reduction is one of the most promising pathways to achieve a carbon-neutral chemical synthesis due to its dual potentials in environmental protection and storage of intermittent renewable energy. The CO_2 reduction could be realized through a wide range of possible methodologies, such as the Fischer−Tropsch process,[608,609] photochemical reductions,[508,610,611] hydrogenation,[523,608] and eCO_2RR.[612−615] Among these conversion approaches, eCO_2RR is one of the most attractive and promising routes that have been recognized by far.[505,613,616]

Although some single noble (as well as transition) metals, such as platinum (Pt),[617,618] palladium (Pd),[437,619] gold (Au),[620] copper (Cu),[621−623] cobalt (Co),[624] indium (In),[625] and silver (Ag)-based metals,[626,627] show remarkable performance as superior eCO_2RR catalysts, it has been reported that their random alloys such as indium(In)-based,[628] Pd-based,[64,142,629,630] Ag-based,[91] especially Cu-based[631] (such as bimetallic Cu−Au,[66,109] Cu−Pt,[97] Cu−In,[632,633] and Cu−Pd[142,629,630]) random alloys are also promising eCO_2RR catalysts with a tunable control. In addition to durable stability, catalytic activity, and catalyst selectivity are critical challenges for catalyst development in eCO_2RR. It was reported that some noble/post-transition metals generally exhibit satisfactory catalytic selectivity (for example, Ag and Au for CO and tin (Sn) and lead (Pb) for formic acid) but with relatively high onset overpotentials on their surfaces,[505,626] whereas Cu-based catalysts are the only known metallic electrocatalysts with an appreciable activity to directly produce hydrocarbons,[634−636] such as methane,[635,637] ethylene,[636] and ethanol with acceptable efficiencies,[638] although its selectivity in bulk form still needs to improve.[634,639,640] In a remark, the partial current densities for eCO_2RR and distinct onset potentials (vs CO binding strength) of some metals are presented in Figure 24a,b.

It has been reported that the eCO_2RR performance is greatly dependent on the catalyst particle size, shape, composition, and phase structure. In the case of Cu eCO_2RR, for example, previous investigations indicate that nanometer-sized Cu could enhance the current densities of methanation compared with a high-purity Cu foil.[635] Experimental results also suggest that selectivity is dependent on the adsorption strength of eCO_2RR intermediates on the catalyst surfaces. For instance, the study on single crystal Cu electrodes shows that the formation of ethylene is favored on Cu(100),[641] formation of methane is dominant on Cu(111),[642,643] and formation of a primary alcohol is preferred on Cu(110).[642] Due to various reaction mechanisms, eCO_2RR usually occurs via two pathways. That is, a C_1 pathway yielding methane or methanol and a C_2 pathway leading to ethylene or ethanol. Koper and co-workers reported that for the C_1 pathway the CHO_{ads} is the key intermediate of the C−O bond breaking toward the formation of methane, whereas for the C_2 pathway, a CO dimer is first generated, followed by the formation of a surface-bonded enediol, enediolate, or an oxametallacycel that are in relation to the formation of ethylene.[627] Further study showed that the reduction of ethylene oxide to ethylene is significantly faster on Cu(100) terraces compared with Cu (111) at low overpotentials.[629] Literature further indicates that different shapes of Cu nanocrystals exhibit distinct selectivity of eCO_2RR.[644−647] Coincidently, Cu NCbs with the Cu(100) surface favors the formation of C_2 products, especially ethylene at a low overpotential compared with methane,[648,649] whereas Cu nano-octahedra with exclusive Cu(111) facets facilitate the generation of methane and other C_1 products.[640,642,650] Bimetallic catalysts exhibit phase- and composition-dependent eCO_2RR selectivity as well. For example, bimetallic Cu−Pd nanocatalysts with different elemental arrangements (ordered, disordered, phase-separated) demonstrated diverse selectivities (Figure 24c−f).[142] In particular, the random alloy and ordered intermetallic CuPd nanocatalysts exhibit high selectivity for C_1

https://dx.doi.org/10.1021/acs.chemrev.0c00436
Chem. Rev. 2021, 121, 736−795

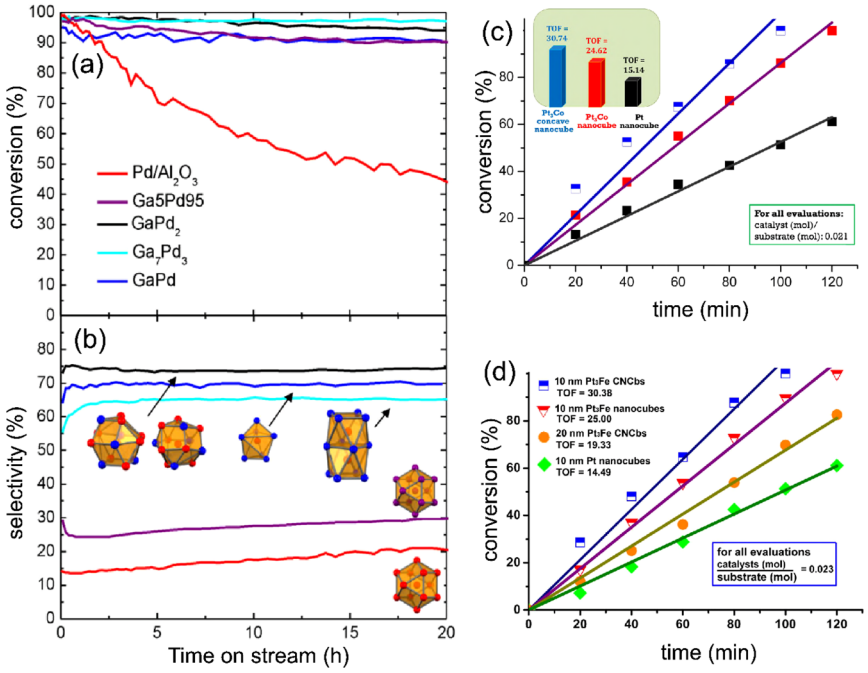

Figure 25. (a,b) Performance of Pd−Ga bimetallic catalysts as well as commercial 5% Pd/Al_2O_3 toward hydrogenation of acetylene: (a) conversion percentage of acetylene and (b) selectivity to ethylene. (c,d) Conversion percentage of styrene hydrogenation as a function of reaction time (TOF unit: [mol converted styrene]/[mol catalyst × h]) on Pt_3Co, Pt_3Fe, and Pt nanocatalysts: (c) Pt_3Co concave nanocubes, Pt_3Co nanocubes, and Pt nanocubes (all sizes are ∼15 nm) and (d) 10 and 20 nm Pt_3Fe concave nanocubes, 10 nm Pt_3Fe nanocubes, and 10 nm Pt nanocubes. (a,b) Adapted with permission from ref 665 and modified. Copyright 2014 IOP Publishing. (c,d) Adapted with permission from refs 40 and 578, and modified. Copyright 2014 and 2015 Wiley-VCH, respectively.

products (CO, CH_4, >80%), whereas the phase-separated CuPd and Cu_3Pd (not shown in Figure 24) avail high selectivity for C_2 chemicals (C_2H_4, C_2H_5OH, >60%).

While electrochemical conversion of CO_2 to multicarbon products has remaining challenges in selectivity, Faradaic efficiency, and overpotential, catalytic transform CO_2 to single-carbon products, especially CO, provides more opportunities for electrochemical CO_2 valorization.[651] Given the above, another strategy to yield CO_2 to C_2 and larger hydrocarbons is to combine the eCO_2RR with the synthesis gas (syngas) conversion process associated with a catalyst modification like controlling Cu enrichment of Au surfaces.[652] As an advantage in this strategy, the mechanism in the generation of CO through eCO_2 RR is clearer than the formation of C_2 species and the rate-limiting step for CO is generally understood to proceed through a *COOH intermediate.[653] Also, syngas made from eCO_2 RR can subsequently be upgraded to high-value chemicals through the Fischer−Tropsch process.[652] Moreover, tailoring the syngas composition with high production rates by designing different electrocatalytic systems makes it particularly attractive and flexible for the downstream process.[651] Since the binding properties of the intermediate from CO_2 to CO are determined by the electronic density of nanocatalysts, Yang and co-workers demonstrated that both the electronic effect and the geometric effect on the surface of Au_xCu_{1-x} nanoalloys dictate the activity toward eCO_2RR and thus enable tuning the binding strength between the catalytic surfaces and the intermediates to an optimal value.[66,652] To this end, several bimetallic alloys such as dendritic Cu−In,[121] Pd−Sn nanocrystals,[381] and Ag−Sn based nanostructures[91] are promising electrocatalysts. Interestingly, the ordered intermetallic AuCu nanocrystals promote the Faradaic efficiency of eCO_2 RR to CO as high as 80%, whereas their disordered counterpart demonstrates a high catalytic activity toward HER.[109]

5.2. Other Associated Applications

In addition to their ubiquitous applications as electrocatalysts, noble-metal-based random alloy and intermetallic nanocrystals have also shown promising potential for applications in heterogeneous catalysis, optics, photocatalysis, and magnetics. In recent years, tremendous efforts have been devoted to optimizing and enhancing their heterogeneous catalytic, optical, photocatalytic, and magnetic properties by precisely engineering their atomic-scale features using a rich variety of synthetic approaches. Here we try to cover these related applications as much as possible in order to comprehensively present the significance of random alloy and intermetallic nanocrystals. In this section, the latest progress in random alloy and intermetallic nanocrystals is specifically addressed by exclusively listing some typical cases associated with these applications.

5.2.1. Heterogeneous Catalytic Applications. Noble-metal-based nanocrystals also exhibit their interesting properties as a class of heterogeneous nanocatalysts, such as hydrogenation, dehydrogenation, and reforming reaction,[6,654] being widely used in petrochemical, pharmaceutical, and fine chemical industries. To yield high-value chemicals with enhanced activity and selectivity in fine chemical engineering, the development of noble metal-based catalysts randomly alloyed with 3d transition metals with a tunable ligand effect, geometric effect, and ensemble effect has attracted increasing interest. For a long time, Pt-based random alloys (Pt−Cu,[655,656] Pt−Fe,[657] Pt−Pd,[257,658] Pt−Co,[40,250,316] Pt−Ni,[246,659] and Pt−Rh[217]), Pd−based random alloys,[248,273,660,661] Au−based random alloys,[662,663] and Ag−

https://dx.doi.org/10.1021/acs.chemrev.0c00436
Chem. Rev. 2021, 121, 736−795

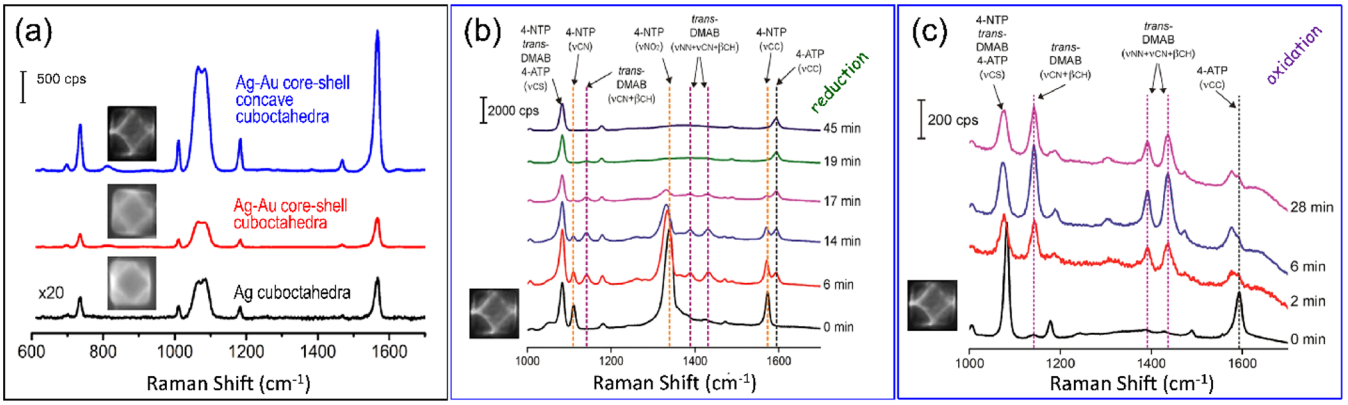

Figure 26. SERS spectra at an excitation wavelength of 785 nm. (a) Spectra were collected from 1,4-BDT adsorbed on substrates of Ag cuboctahedra, Ag−Au core−shell cuboctahedra, and Ag−Au core−shell concave cuboctahedra, respectively. (b) Spectra were recorded during the reaction of 4-nitrothiophenol to 4-aminothiophenol reduced by $NaBH_4$ and catalyzed by Ag−Au core−shell concave cuboctahedra. (c) Spectra were recorded during the oxidation of 4-aminothiophenol oxidized by $NaBH_4$ and catalyzed by Ag−Au core−shell concave cuboctahedra. Adapted from ref 686 and modified. Copyright 2016 American Chemical Society.

based random alloys[79,664] systems have been extensively investigated. Chaudhari and co-workers developed a series of Pt-based nanocatalysts toward oxidation of glucose, glycerol with enhanced catalytic activity and selectivity,[655,657,658] reporting that the PtPd catalysts displayed significantly enhanced activity [turnover frequency (TOF) = 2404 h^{-1}] and improved selectivity of 44% toward glucaric acid from glucose.[625] Their study also indicates an unusual oxidation activity (TOF = 3543h^{-1}) and 46% glucaric acid selectivity on a catalyst of $PtCu_3$ supported on TiO_2.[622]

As discussed previously, the disordered−ordered "phase effect" and particle shape effect of the bimetallic catalysts can also be observed in the heterogeneous reactions. As a model reaction of C_3 polyol conversion from biomass feedstocks, for example, a study on oxidation of glycerol to tartronic acid in the aqueous phase indicated that the ordered intermetallic *fct*-$PtFe_{4.5}$ nanocatalysts displayed an activity as high as ∼3-times that from the disordered *fcc*-$PtFe_{4.5}$ random nanoalloys (TOF in mol mol_{Pt}^{-1} h^{-1}: 26,340 vs 8126) at 70 °C under 1 atm O_2-pressure. It was believed that the surface interfacial strain and appropriate electronic structure modification in the ordered intermetallic *fct*-$PtFe_{4.5}$ were the major driving force of activating the C−H and C−O bonds more efficiently.[657] This "phase effect" from geometric and electronic differences can also be determined from the catalytic performance of Pd−Ga random alloy and intermetallic particles (20−32 μm) toward the gaseous hydrogenation of acetylene.[665] Despite diverse compositions and testing conditions applied, it can be seen that intermetallic Pd−Ga (GaPd, Ga_7Pd_3, and $GaPd_2$) catalysts showed higher selectivity to ethylene than the random alloy Ga_5Pd_{95} counterpart (Figure 25a,b) as well as the commercial 5% Pd/Al_2O_3, although the conversion rates for all the tested bimetallic catalysts are comparable.

The shape effect of bimetallic catalysts on the hydrogenation of olefins has been extensively studied in recent years.[666] Fang and co-workers systematically prepared Pt_3Co and Pt_3Fe nanocatalysts with shape-control and applied them in the hydrogenation of styrene as a model reaction.[40,578] They demonstrated that the TOF of high-indexed Pt_3Co concave NCbs is ∼1.25-fold and ∼2-fold of that of {100}-terminated Pt_3Co and Pt NCbs, respectively, and the turnover rate closely connects to the dissociative adsorption of H_2 and activation of the unsaturated bond in the Pt_3Co evaluation (Figure 25c).[40] They shortly showed that the hydrogenation of styrene can also be promoted by high-indexed Pt_3Fe concave NCbs that possess a superior reactivity of H−H cleavage and C═C bond activation to the {100}-bounded Pt_3Fe NCbs of similar particle size (Figure 25d).[578]

Another case study is about how to efficiently converse syngas or CO_2 to chemical fuels, which was also mentioned in section 5.1.4. Pd-based catalysts are considered as efficient candidates for hydrogenation, especially CO_2 hydrogenation.[421,667−671] Schlögl and co-workers reported that Pd−Ga intermetallic nanocatalysts with different structures and compositions displayed highly selective semihydrogenation catalytic characteristics for acetylene outperforming, and they believed that the electronic modification and isolation of active sites are the origin of the excellent catalytic improvement.[667] Shortly, the intermetallic Pd_2Ga supported on SiO_2 was applied for low-pressure CO_2 hydrogenation to methanol, exhibiting higher activity than that of the conventional $Cu/ZnO/Al_2O_3$ catalysts.[669] Recently, bimetallic Pd−In nanocrystals also showed superior performance for CO_2 hydrogenation reaction.[670] Williams and co-workers identified that the optimized intermetallic PdIn nanocrystals displayed improved methanol selectivity in the temperature range of 190−270 °C, reaching >80% selectivity at 270 °C compared with 45% selectivity from the conventional heterogeneous $Cu/ZnO/Al_2O_3$ catalysts.[670]

5.2.2. Optical and Photocatalytic Applications. Normally, noble metal-based nanocrystals exhibited different colors originating from their strong interactions between the incident light and the confined free electrons of metal nanocrystals under the resonant condition.[672,673] This optical phenomenon is typically known as the LSPR,[674] and the resonance peak position and profile are dependent on the type of metal nanocrystals, with the visible region for Cu, Au, and Ag and the ultraviolet region for Rh, Ru, Pt, and Pd.[1,675] The LSPR peak position and profile could be modulated by forming random alloys, intermetallic compounds, and core−shell structures, such as bimetallic Au−Ag[263,676−681] and Au−Cu[310,678,679,682−684] nanostructures. For example, Chen and co-workers demonstrated that the LSPR peak of the Cu_3Au random alloyed nanorods could be readily tuned over the spectrum from the visible spectrum to near-infrared.[310] Also, it demonstrated that the LSPR behavior could be determined by

https://dx.doi.org/10.1021/acs.chemrev.0c00436
Chem. Rev. 2021, 121, 736−795

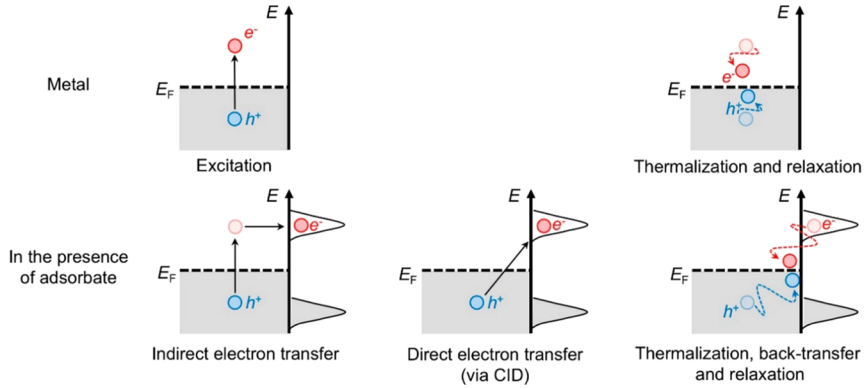

Figure 27. Plasmon-induced hot-carrier generation and hot-electron transfer/back-transfer processes in clean metal and metal/adsorbate. In each case, the left component (relative to energy *y* axis) displays the Fermi level (E_F) of plasmonic metals and the right component (relative to energy *y* axis) illustrates the highest occupied molecular orbitals (HOMOs) and lowest unoccupied molecular orbitals (LUMOs) for adsorbates. The gray parts represent the population of electronic states. CID: chemical interface damping. Adapted from ref 704 and modified. Copyright 2018 American Chemical Society.

the size, shape, composition, structure, and crystal phase of metal nanocrystals.[672,673,685] There are a variety of applications in utilizing the LSRP phenomenon, e.g., the surface-enhanced Raman scattering (SERS), photocatalysis, artificial photosynthesis, solar cell, biomedicine, and sensing. Figure 26a presents the SERS spectra collected from 1,4-benzenedithiol (1,4-BDT) adsorbed on the Ag cuboctahedra, Ag−Au core−shell cuboctahedra, and Ag−Au core−shell concave cuboctahedra, which were prepared through a galvanic replacement reaction in solution.[686] SERS enhancement factor (EF) of the Ag−Au core−shell concave cuboctahedra outperforms both the regular Ag−Au core−shell cuboctahedra and the Ag cuboctahedra as the counterparts, showing SERS signal of as high as a ∼74-fold increment at an excitation wavelength of 785 nm. Besides the structure and shape effect (existing more "hot spots"), in this case, it was reported that the stronger bond between Au-thiolate over that between Ag-thiolate could make an additional contribution to such a SERS signal increase since the composition distribution in the Ag−Au concave cuboctahedra are not homogeneous.[687] By taking advantage of this Ag−Au concave cuboctahedra, the superb SERS performance can be applied to monitor a reaction as an example of the applications using the catalytic feature of their surface Au atoms. Figure 26b,c presents time-dependent SERS spectra during a reduction of 4-nitrothiophenol to 4-aminothiophenol by $NaBH_4$ through a 4,4′-dimercaptoazobenzene (trans-DMAB) intermediate and subsequent oxidation of 4-ATP back to trans-DMAB upon the introduction of H_2O_2, respectively, demonstrating that the Ag−Au core−shell concave cuboctahedra could be a unique SERS probe for monitoring these reactions. These characteristic properties make random alloy and intermetallic nanocrystals promising for applications in SERS, photocatalysis, artificial photosynthesis, plasmon-assisted nanocrystal synthesis, photothermal therapy, biomedicine, sensing, and solar cells.[674,688−697] Similarly, it can also be extended to other photocatalytic systems with tunable size, shape, and composition, such as Pt−Au,[698] Pd−Au,[275,301,699] Cu−Au,[268,310] and Ag−Au.[700]

It has also been observed, by integrating a plasmonic metal (e.g., Cu, Au, or Ag) with a highly catalytic nanocrystal (e.g., Rh, Ru, Pd, or Pt) in a system, the catalytic performance of bimetallic nanocrystals is dramatically improved by coupling with light, and some interesting photochemical transformations become more favorable.[689] In this case, light is absorbed in particularly resonant plasmonic frequencies and then released as the input energy to drive the overall reactions occurring on the surface of bimetallic nanocrystals. Extensive investigations have demonstrated that this concept can be further extended to other polymetallic systems.[309,701,702]

Unlike the phonon-driven chemical reaction triggered by thermal heating of a catalyst, charge-carrier-driven reactions can be activated in a different mechanism, where a stimulus from outside (i.e., light) is provided to excite the hot-carrier.[689] The resonant optical excitation of surface plasmon produces energetic hot-carriers (hot-electron and hot-hole) to allow the photochemical reactions. Figure 27 illustrates the surface-plasmon-driven hot-carrier generation and hot-electron transfer/back-transfer process on a clean metal surface and metal/adsorbates. Although numerous hot electron-driven processes have been reported, few examples that rationalize the hot-holes extracted from metallic nanostructures were released while some interesting work in plasmonic photochemistry demonstrated the use of sacrificial reagents for the hole scavenging reactions.[703−705] For example, Li and co-workers investigated the plasmonic hot-holes on the Au/TiO_2 photocatalyst toward water oxidation.[705] They utilized Kelvin probe force microscopy to image the distribution of holes probed by surface photovoltage and applied photodeposition together with electron microscopic element mapping to position the reaction sites. They reported that most of the plasmonic holes, the active sites, are concentrated near the $Au−TiO_2$ interface. This interfacial effect on the plasmonic water oxidation reaction can be extended to other Au-based photocatalytic systems, such as $Au/SrTiO_3$ and $Au/BaTiO_3$.

In recent years, there have been wide applications associated with the LSPR optical in artificial photocatalysis.[23,24,706,707] For instance, Neretina and co-workers adapted a vapor phase template-assembly technique and synthesized nanoprism-like AuCu structures with a strong LSPR.[684] With an illumination of 10 mW/cm^2 laser light, the AuCu photocatalysts were evaluated using 4-nitrophenol reduction by $NaBH_4$ as a model reaction and showed a 32-fold enhancement in terms of the reaction rate constant. With the incorporation of plasmonic elements like Au, Ag, and Cu with catalytic metals such as Pt, Pd, and Rh, such metal random alloys could exhibit enhanced catalytic activity under light illumination, paving the way for

https://dx.doi.org/10.1021/acs.chemrev.0c00436
Chem. Rev. 2021, 121, 736−795

photocatalysis development as well.[1,700,708,709] For core−shell structures, Huang and co-workers pointed out the LSPR properties of Au−Pd can be maintained by turning the Pd−shell thickness and shape.[699] The LSPR absorption band can be seen when the Pd shell is less than 1 nm for the cubes, cuboctahedra, and truncated octahedra of 35 and 45 nm Au core nanostructures. For smaller Au−Pd core−shell octahedra, the Pd−shell thickness can be extended to 5 nm with an observation of the visible band, while for 74 nm Au−core nanostructure, the LSPR band is more recognizable for all-shaped nanocrystals. The Au−Pd and Au−Pt core−shell systems generally show no plasmon resonance in the visible region if the shell is too thick. It was also demonstrated by Sun and co-workers that the LSPR of $Pd_{20}Ag_{80}$ random nanoalloys almost damped.[551] Besides, Kuo and co-workers demonstrated a one-step synthesis of core−shell nanoicosahedra containing AuPd random alloy cores and ultrathin Pd−shells (<2 nm). The AuPd−Pd core−shell nanostructures displayed LSPR-enhanced conversion of 4-nitrophenol.[275]

While most researchers focused their work on random alloy-based photocatalysis, there are limited reports involving the intermetallics in terms of their optical and photocatalytic applications. Matsumoto and co-workers synthesized PtPb-ordered intermetallic nanocrystals (NiAs-type structure, $P6_3/mmc$) on WO_3 using a photodeposition/polyol method and studied the photocatatlytic decomposition of acetic acid as well as its reaction mechanism on the as-prepared nanocatalysts.[501] In comparison with pure WO_3 and WO_3-supported Pt catalysts, enhanced catalytic activities from the synthesized $PtPb/WO_3$ toward the decomposition of the organic compounds under an oxygen-rich atmosphere and visible light were determined.

Biomedicine and biomedical applications, such as cancer diagnosis and therapy, are additional fields where the optical properties of metal LSRP, including optical sensing and optical imaging, can be used.[16,696,710] For example, Xia and co-workers have extensively manipulated and studied Au-based nanostructures with tunable surface plasmon resonance peak, biocompatible, and a well-established functional surface.[711,712] To sculpture the Au-based nanocages with tunable layer-thickness, they synthesized Ag NCbs first, followed by a galvanic replacement and oxidative etching process.[712] Using a multimodal nonlinear optical microscopic technique,[713] they subsequently found that the Au/Ag nanocages emit a two-photon luminescence (2PL).[712] Although the 2PL process is efficient because of the enhancement of the plasmon resonance, three-photon luminescence (3PL) has more merit for cellular imaging in the aspect of phototoxicity. Figure 28 presents a comparison of 2PL and 3PL imaging of Au/Ag nanocages (49% Ag/51% Au) in KB cells (a carcinoma cell line) and liver tissues. As shown in Figure 28a,b, Au/Ag nanocages in cells could be visualized by both 2PL and 3PL at the same level of intensity. After 90 s scanning using a 760 nm laser, it was determined that a membrane blebbing occurred and the damage was confirmed by ethidium bromide staining, associated with a reduced 2PL intensity from nanocages as shown in Figure 28c. With the same treatment, however, Figure 28d displays a different result in which neither membrane blebbing nor reduced 3PL intensity was observed since no thermal effect was involved in 3PL. By comparing 2PL with 3PL micrographs imaged from the same liver tissue slice (Figure 28e,f), one can discern that fluorescence from the issue can be completely suppressed at 1290 nm excitation and a weak background made it much easier to identify the Au/Ag nanocages, which is another benefit for the imaging with 3PL.

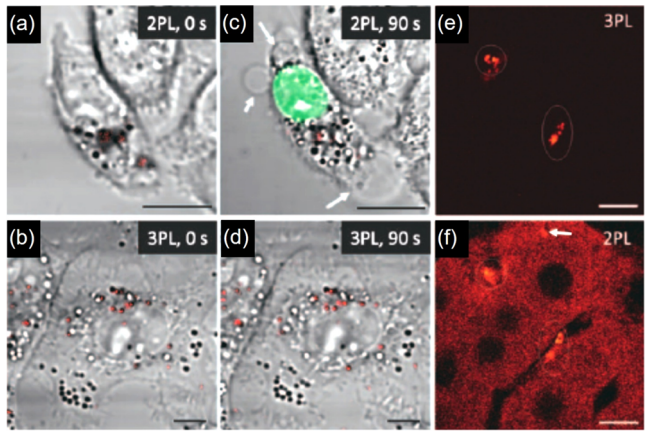

Figure 28. Comparison of 2PL and 3PL imaging of Au/Ag nanocages (51% Au/49% Ag) in KB cells (a−d) and liver tissues (e,f). (a) 2PL image and (b) 3PL image of Au/Ag nanocages (red) in KB cells before laser scanning. (c) Image of the same cell as in (a) after scanning with a 760 nm femtosecond laser for 90 s. Laser power after objective: 1.9 mW. After scanning, membrane blebbing (arrowed) and compromised membrane integrity indicated by ethidium bromide labeling (green) were observed. (d) 3PL image of the same cell as in panel (b) after scanning with a 1290 nm femtosecond laser for 90 s. Laser power after objective: 4.0 mW. No morphological change or plasma membrane damage was observed. (e) 3PL imaging of Au/Ag nanocages (white circles) in liver tissue. (f) 2PL imaging in the same area as in panel (e). White arrow: anomalously strong autofluorescence from the tissue. Laser power after objective: 7.0 mW. Scale bars: 10 mm. Adapted with permission from ref 712 and modified. Copyright 2010 Wiley-VCH.

5.2.3. Magnetic and Magnetism-Featured Applications. Magnetic nanocrystals represent an important class of functional nanomaterials and have attracted increasing interest for their nanoscale magnetism and widespread applications. Over the years, bimetallic magnetic nanocrystals have been widely exploited and applied to a broad range of areas, including biochemistry, medicine, medical therapy, and ultrahigh density information storage et al.[714−720] It has been found that nanocrystals can transform from multidomain to single domain with the apparent increase in coercivity when the size of ferromagnetic nanocrystals reduces down to a critical size.[721−723] As such, tremendous efforts have been devoted to precisely tuning the size of magnetic nanocrystals via different approaches.[724−726] With the blooming development of synthetic approaches, more and more studies seem to turn to magnetic applications related to nanocrystals with well-defined shape, composition, structure, and crystal phase.[727−730] Actually, it has been confirmed that the structural parameters are dependent on their magnetism. More importantly, these investigations deepen our understanding of their magnetic properties and also exhibit the great potential of these nanocrystals in magnetism-related applications.[406,731−733]

Typically, nanomaterials containing Fe-, Co-, Ni-, Cr-, and Mn-based metals, random alloy, oxides may possess ferromagnetic or paramagnetic properties.[395,420,428,447,718,734−736] Since noble-transition-metal-based random alloys and intermetallic compounds for magnetic applications represent a typical topic and have been systematically discussed elsewhere,[13] we focus on the case study of FePt in this section.

https://dx.doi.org/10.1021/acs.chemrev.0c00436
Chem. Rev. 2021, 121, 736−795

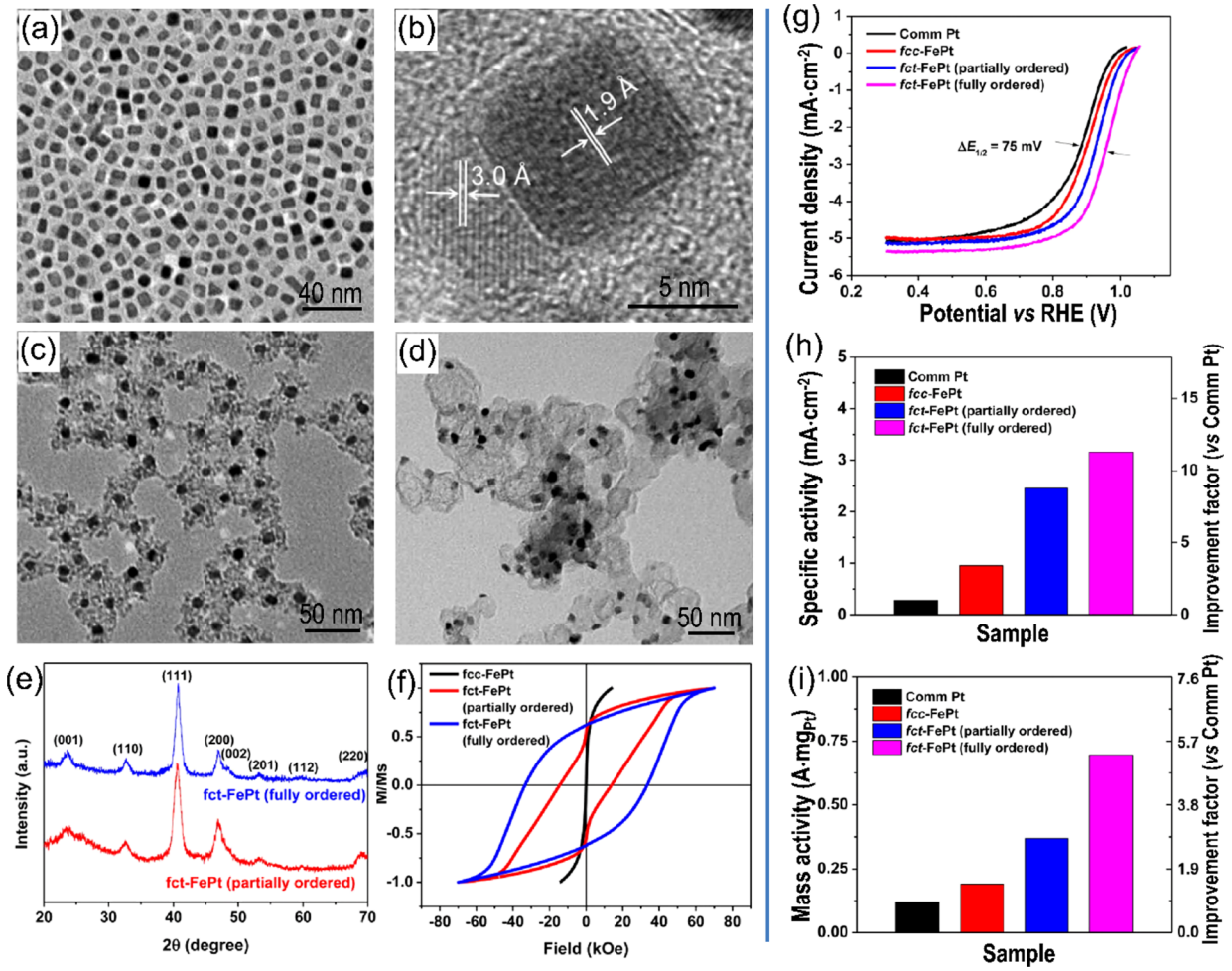

Figure 29. TEM images and magnetic/electrochemical properties of FePt-based nanocrystals. (a) TEM and (b) HRTEM images of dumbbell *fcc* FePt–Fe_3O_4 nanocrystals. (c) TEM image of MgO-supported *fcc* FePt–Fe_3O_4 nanocrystals. (d) TEM image of carbon-supported *fct* FePt nanocatalysts (fully ordered) after thermal annealing at 700 °C under Ar + 5% H_2 for 6 h followed by acid washing. (e) XRD patterns of the fully and partially ordered *fct* FePt nanocatalysts. (f) Hysteresis loops of the *fcc* FePt, the fully and partially ordered *fct* FePt nanocatalysts. (g) ORR polarization curves of comm Pt (commercial catalysts Pt/C, 20 wt % Pt) and carbon-supported *fcc*-FePt, partially and fully ordered *fct*-FePt nanocatalysts in 0.1 M $HClO_4$ (rotating speed: 1600 rpm; scan rate, 10 mV/s). (h) and (i) Specific activities and mass activities of all the catalysts mentioned in panel (g) at 0.9 V. Adapted from ref 112 and modified. Copyright 2015 American Chemical Society.

FePt random alloy and intermetallic nanocrystals could be prepared from a high-temperature organic colloidal system with a postannealing treatment[323] and have been inspired as potential magnetic storage media.[239,737] For a magnetic domain, the energy barrier required to reverse the magnetization, from one to another, generally needs to be >60 times higher than the thermal energy. It was reported that the $L1_0$-FePt nanocrystal was one of the most promising candidates for heat-assisted magnetic recording because of its large K (7×10^6 J m^{-3}), T_c (750 K), and robust stability.[13] Also, the magnetic properties of the FePt nanocrystals are very sensitive to their size, size distribution, composition, and crystal structure. It is therefore essential to control the quality of as-prepared magnetic nanocrystals.[1,13] The mentioned colloidal synthesis approach has demonstrated the possibility of size-, composition-, and particle shape-control.[240] However, a post-treatment of thermal annealing may be necessary to convert the disordered *fcc*-type FePt nanocrystals to ordered $L1_0$-FePt nanocrystals.[738] Sun and co-workers facilitated fully ordered $L1_0$-FePt nanocrystals with strong ferromagnetism using a developed annealing strategy (Figure 15) from MgO-coated dumbbell-like *fcc*-FePt–Fe_3O_4 nanocrystals as the starting point (Figure 29a–c).[112,161,438] The success in the ordered phase conversion is ascribed to the MgO-coated shell and conjugated Fe_3O_4. MgO functions as a tentative particle protection layer, preventing particle aggregation and sintering during the annealing stage, whereas the Fe_3O_4 attached on the FePt nanocrystals helps to create defects upon reduction and such a dumbbell structure facilitates Fe/Pt diffusion to generate fully ordered *fct*-phase (Figure 29d,e). This *fcc*-to-*fct* phase transition was further monitored by the determined hysteresis loops that descript the change of the magnetic moment as a function of the applied magnetic field strength. Different from the superparamagnetic behavior from the *fcc*-FePt nanocrystals at room temperature (the black loop in Figure 29f), the annealed FePt nanocrystals (for 1 and 6 h) showed a two-phase (superparamagnetic and ferromagnetic, the red loop in Figure 29f) and a single-phase (ferromagnetic, the blue loop in Figure 29f) hysteresis characteristics, respectively. The structure-based magnetic behaviors of these FePt nanocrystals coincide with their electrocatalytic performance very well. As shown in Figure 29g–i, the fully ordered,

https://dx.doi.org/10.1021/acs.chemrev.0c00436
Chem. Rev. 2021, 121, 736–795

ferromagnetic *fct*-FePt intermetallic nanocrystals exhibit the much higher ORR activity than the disordered, superparamagnetic *fcc*-FePt random alloy nanocrystals.

The *fcc*-FePt random alloy nanocrystals with a relatively small K_u are regarded as "soft" magnetic materials (small coercivity), while the fully ordered *fct*-FePt intermetallic nanocrystals show a larger K_u and are treated as "hard" (large coercivity) magnetic media.[239] A similar phenomenon was observed when Fe was replaced by Co to achieve fully ordered hard-magnet $L1_0$-CoPt intermetallic nanocrystals.[114,406] It was also found that the $L1_0$-CoPt nanocrystals obtained from 6 h annealing are strongly ferromagnetic, whereas the *fcc* CoPt nanocrystals received directly from the synthesis process without annealing are superparamagnetic.[114] Those magnetic nanocrystals possessing superparamagnetic properties have the potential of being applied to biomedicine study. They could serve as sensitive magnetic probes in magnetic resonance imaging (MRI), efficient separation of biomolecules, and targeted drug delivery.[51,715,718−720] Among these applications, surface-functionalized bimetallic noble metal magnetic nanocrystals, especially Ag-based nanocrystals, are promising for the isolation and detection of bacteria.[714,719] FePt nanocrystals conjugated with Vancomycin (Van) exhibit high sensitivity to bacteria with a terminal peptide of D-Ala-D-Ala on cell walls.[715]

6. CONCLUDING REMARKS

Noble metal-based random alloy and intermetallic nanocrystals pertain to the big family of solid solution structure. They often exhibit different properties and applications from their bulk counterparts. It has been well established that the remarkable properties are closely associated with their size, shape, composition, structure, and crystal phase that can be precisely controlled and optimized. As such, a vast set of noble metal-based random alloy and intermetallic nanocrystals are currently attainably derived from the tremendous efforts from many research groups and then explored to apply in various fields. Despite the significant achievement, there is still much space to be left in terms of attaining robust and reproducible synthetic approaches that can generate well-controlled noble metal-based random alloy and intermetallic nanocrystals, in parallel with deeply understanding the formation mechanisms involved in the syntheses. It should be emphasized that a large number of unsolved issues need to be addressed jointly combined with experiments, theories, and instruments, further driving the transition from empirical syntheses to theoretically supported syntheses.

During the syntheses, the most common issue is to the reproducibility. Considering that the significant deviation in the quality of chemicals involved in different laboratories might impose a great challenge to reproduce some of the syntheses, it seems to be an urgent task to improve the quality of present chemicals at this stage for enabling reproducing these nanocrystals. For example, Mirkin and co-workers discovered that different batches of CTAB from various manufacturers could lead to the final products with diverse morphologies under the same experimental conditions during the synthesis of Au nanocrystals, due to the different contents of iodide ions as an impurity.[739] Moreover, it is possible to draw ambiguous or incorrect conclusions from experimental observations, as some of the syntheses are highly sensitive to a subtle difference in experimental conditions, leading to misunderstanding the key parameters to the syntheses. Typically, qualitative assessments are primarily concluded based on controlled experiments by purposely altering one or two parameters in most of the previous reports related to the synthesis of nanocrystals. It is worth pointing out that, in some cases, it is hard to completely distinguish each parameter effects on the outcome in practical syntheses, ultimately resulting in the speculative conclusions for the formation mechanism. As compared to the qualitative assessment, it seems that increasingly interests begin to focus on the more precise and reliable quantitative evaluation to enable gaining deep insights into the synthesis of the nanocrystals. Once the reaction kinetics are acquired, the protocols for these nanocrystals should be easily reproduced by exquisitely controlling the nucleation and growth processes predictably.

Extensive studies have demonstrated that the size, shape, composition, structure, and crystal phase all play an essential role in the properties of resultant nanocrystals. As a result, it is of critical importance to simultaneously achieve control over these parameters during the syntheses, especially for ordered intermetallic nanocrystals with well-defined size, shape, and composition. High-temperature annealing approach is generally believed to be a commonly used approach for generating ordered intermetallic nanocrystals. While this approach allows for precise control over the composition and atomic ordering, it is still a big challenge to manipulate the size and shape of the nanocrystals, as annealing process at high temperature often destroy the original shape of as-synthesized nanocrystals in most cases and lead to severely nanocrystals aggregation/sintering. To solve this issue, a robust coating layer is required to deposit on the surface of the as-synthesized nanocrystals before annealing. Unfortunately, it is demonstrated that the coating layers will dramatically impede nanoscale mass transport, resulting in forming the partially ordered nanocrystals. In comparison, liquid synthesis approaches exhibit great potential for the formation of well-controlled ordered intermetallic nanocrystals under a relatively mild condition. Due to the lack of enough insights for the fundamental parameters involved in the synthesis, the limited availability of ordered intermetallic nanocrystals with well-controlled size and shape is reported up to now, and thus more new synthetic protocols need to be developed.

To meet the demand from future industrial applications, nanocrystals on the kilogram level are typically required. As such, it is very essential to develop new synthetic approaches for achieving scalable production. In general, most current approaches for the synthesis of nanocrystals involves the reaction with volumes in the range of 1−100 mL and the production on the milligram scale in each batch. It is not realistic to raise the yields by simply increasing the volume of the reaction solution while maintaining the same molar ratio of all reagents. To this end, new effective approaches related to continuous flow and droplet-based reaction systems have recently been developed. These approaches hold the potential for realizing automation, significantly decreasing the overall cost, and achieving precise control over the quality of the product as compared to the conventional batch approaches. Further studies associated with rationally manipulating the experimental parameters are still needed to be completed in scalable production.

Compared with the random alloy nanocrystals, it was furthermore determined that the ordered intermetallic nanocrystals possess predictable electronic and lattice structure with high activity in a given application and high stability in harsh

https://dx.doi.org/10.1021/acs.chemrev.0c00436
Chem. Rev. 2021, 121, 736−795

environments. It seems that migration of more components, high active surface defects, and high-indexed facets to those promising intermetallic nanocrystals could be an effective strategy to further enhance their intrinsic activities and stabilities. For example, Yamaguchi and co-workers demonstrated that the incorporation of Cu into ordered intermetallic PtFe nanocrystals to facilitate a formation of PtFeCu nanocrystals with the same crystal phase could dramatically improve their electrocatalytic stability toward ORR.[378] Meanwhile, it is also expected that the ordered intermetallic nanocrystals could serve as templates for the formation of core−shell nanostructures with well-defined surface structures, which could remarkably reduce the use of noble metals and enhance the catalytic properties. For instance, Skrabalak and co-workers have demonstrated that core−shell nanocrystals with random alloy Pt-M (where M = Ni, Co, Cu, or Fe) shells and ordered intermetallic PdCu core exhibited enhanced activity and durability toward ORR.[481] On the basis of these studies, it can be predicted that there is large room to extensively develop intermetallic improved synthetic strategies to further improve the material performance in various practical applications.

Overall, the development of a synthetic approach for shape-controlled random alloy and ordered intermetallic nanocrystals and the exploration of their pivotal applications create prosperous opportunities yet with new challenges. The critical importance in this blossoming field has been highlighted in some paradigms provided by several research groups. It is foreseeable that these efforts will pay off in a great way, as the best is yet to come.

AUTHOR INFORMATION

Corresponding Author

Jiye Fang − *Department of Chemistry, State University of New York at Binghamton, Binghamton, New York 13902, United States;* orcid.org/0000-0003-3703-3204; Phone: 607 777 3752; Email: jfang@binghamton.edu

Authors

Ming Zhou − *Department of Chemistry, State University of New York at Binghamton, Binghamton, New York 13902, United States*

Can Li − *Department of Chemistry, State University of New York at Binghamton, Binghamton, New York 13902, United States*

Complete contact information is available at: https://pubs.acs.org/10.1021/acs.chemrev.0c00436

Notes

The authors declare no competing financial interest.

Biographies

Ming Zhou received his B.S. and Ph.D. degrees in chemical engineering from Chongqing University in 2011 and 2017, respectively. He worked as a postdoctoral fellow at Nanyang Technological University from 2017−2019 under the supervision of Prof. Hua Zhang. Currently, he is a postdoctoral fellow in Prof. Jiye Fang's group at State University of New York at Binghamton. His research interests include the development of synthetic protocols for controllably synthesizing novel nanocrystals for applications in catalysis and renewable energy.

Can Li received his B.S. degree (2012) and M.S. degree (2015) in Chemical Engineering and Technology from China University of Petroleum (Eastern). He joined Prof. Jiye Fang's group in 2016 and is currently a Ph.D. candidate in the Chemistry Department at State University of New York at Binghamton. His research interests include the shape-controlled synthesis of metal oxide, metal alloys, and intermetallic compounds for catalytic applications, especially PGM-based catalysts used in fuel cells.

Jiye Fang received his Ph.D. degree in Materials Science from National University of Singapore in 1999. He was a Postdoctoral Associate and subsequently Research Specialist from 1999 to 2002 at Advanced Materials Research Institute. He joined the Chemistry Department at University of New Orleans as an Assistant Professor in 2002 and then moved to State University of New York at Binghamton in 2006. He was an NSF CAREER award recipient. He is now the Professor of Chemistry and MSE at Binghamton. His current research interests are the synthesis of shape-controlled nanocrystals, self-assembly and superstructure, pressure-induced phase transition, lattice strain study on noble metal-based nanocrystals, and advanced catalysts for fuel cell applications in acidic and alkaline media.

ACKNOWLEDGMENTS

M.Z. is primarily supported by the Center for Alkaline-Based Energy Solutions, an Energy Frontier Research Center program supported by the U.S. Department of Energy, under Grant DE-SC0019445, and C.L. is primarily supported by National Science Foundation (DMR 1808383). The authors also acknowledge financial support by ACS PRF (58196-ND10) and thank Kevin Fang for his help in editing the manuscript. Work done at Binghamton was supported by General Motors LLC, Custom Electronics Inc. and S3IP at Binghamton University.

ABBREVIATIONS

ΔG	Gibbs free energy
ΔH	enthalpy
ΔS	entropy
2D	two-dimensional
3D	three-dimensional
AA	ascorbic acid
ACA	adamantanecarboxylic acid
acac	acetylacetonate
ADT	accelerated durability test
AWEs	alkaline water electrolyzers
bct	body-centered tetragonal
1,4-BDT	1,4-benzenedithiol
$Bi(Ac)_3$	bismuth(III) acetate
CA	citric acid
CO	carbon monoxide
CO_2	carbon dioxide
$Co(acac)_2$	cobalt(II) acetylacetonate
CNC	concave nanocube
CTAB	cetyltrimethylammonium bromide
CV	cyclic voltammograms
DDA	dodecylamine
DDT	1-dodecanethiol
DFT	density functional theory
trans-DMAB	4,4′-dimercaptoazobenzene
DMF	N,N-dimethylformamide
DOE	department of energy, U.S.
eCO_2RR	CO_2 electrochemical reduction reaction
EDS	energy-dispersive spectroscopy
EDTA	ethylenediaminetetraacetic acid
EDX	energy-dispersive X-ray spectroscopy

https://dx.doi.org/10.1021/acs.chemrev.0c00436
Chem. Rev. 2021, 121, 736−795

EF	enhancement factor
EG	ethylene glycol
EOR	ethanol oxidation reaction
Et_2Zn	diethylzinc
FAOR	formic acid oxidation reaction
fcc	face-centered cubic
fct	face-centered tetragonal
$Fe(acac)_3$	iron(III) acetylacetonate
HAADF	high-angle annular dark-field
HCHO	formaldehyde
hcp	hexagonal closest packed
HDA	hexadecylamine
HDD	1,2-hexadecandiol
HDT	hexadecanethiol
HER	hydrogen evolution reaction
HOR	hydrogen oxidation reaction
HRTEM	high-resolution transmission electron microscopy
ICP	inductively coupled plasma
JMAK	Johnson-Mehl-Avram-Kolmogorov
LMTO-ASA	linear muffin-tin orbitals in the atomic sphere approximation
LSPR	localized surface plasmon resonance
LSV	linear sweep voltammetry
$Mn(acac)_2$	manganese(II) acetylacetonate
MOR	methanol oxidation reaction
MRI	magnetic resonance imaging
MXenes	metal carbides
NCb	nanocube
NFs	nanoframes
$Ni(acac)_2$	nickel(II) acetylacetonate
OA	oleic acid
OAm	oleylamine
ODE	octadecene
OER	oxygen evolution reaction
OMC	ordered mesoporous carbon
ORR	oxygen reduction reaction
$Pb(Ac)_2$	lead(II) acetate
$Pd_2(dba)_3$	tris(dibenzylideneacetone)dipalladium(0)
PEMFC	proton-exchange membrane fuel cell
PEWEs	polymer electrolyte water electrolyzers
PGMs	platinum group metals
PI-b-PEO	polyisoprene-blockpoly (ethylene oxide)
2PL	two-photon luminescence
3PL	three-photon luminescence
PVP	poly(vinyl pyrrolidone)
$Pt(acac)_2$	platinum(II) acetylacetonate
$Rh_2(Ac)_4$	rhodium acetate dimer
SAED	selected area electron diffraction
SEM	scanning electron microscope
SERS	surface-enhanced Raman scattering
SMCR	seed-mediated co-reduction
STEM	scanning transmission electron microscopy
TBAB	tert-butylamine-borane
TEM	transmission electron microscopy
THF	tetrahydrofuran
THH	tetrahexahedral
TOF	turnover frequency
TOP	trioctylphosphine
TTGE	tetraethylene glycol
Van	vancomycin
w/o	water-in-oil
XPS	X-ray photoelectron spectroscopy
XRD	X-ray diffraction
ZIF-8	zeolitic imidazolate framework-8
$Zn(acac)_2$	zinc(II) acetylacetonate

REFERENCES

(1) Gilroy, K. D.; Ruditskiy, A.; Peng, H.-C.; Qin, D.; Xia, Y. Bimetallic Nanocrystals: Syntheses, Properties, and Applications. *Chem. Rev.* **2016**, *116*, 10414−10472.

(2) Grim, J. Q.; Manna, L.; Moreels, I. A Sustainable Future for Photonic Colloidal Nanocrystals. *Chem. Soc. Rev.* **2015**, *44*, 5897−5914.

(3) Escudero-Escribano, M.; Jensen, K. D.; Jensen, A. W. Recent Advances in Bimetallic Electrocatalysts for Oxygen Reduction: Design Principles, Structure-Function Relations and Active Phase Elucidation. *Curr. Opin. Electrochem.* **2018**, *8*, 135−146.

(4) Dong, L.; Liu, Y.; Lu, Y.; Zhang, L.; Man, N.; Cao, L.; Ma, K.; An, D.; Lin, J.; Xu, Y.-J.; Xu, W.-P.; Wu, W.-B.; Yu, S.-H.; Wen, L.-P. Tuning Magnetic Property and Autophagic Response for Self-Assembled Ni−Co Alloy Nanocrystals. *Adv. Funct. Mater.* **2013**, *23*, 5930−5940.

(5) Bing, Y.; Liu, H.; Zhang, L.; Ghosh, D.; Zhang, J. Nanostructured Pt-Alloy Electrocatalysts for PEM Fuel Cell Oxygen Reduction Reaction. *Chem. Soc. Rev.* **2010**, *39*, 2184−2202.

(6) Losch, P.; Huang, W.; Goodman, E. D.; Wrasman, C. J.; Holm, A.; Riscoe, A. R.; Schwalbe, J. A.; Cargnello, M. Colloidal Nanocrystals for Heterogeneous Catalysis. *Nano Today* **2019**, *24*, 15−47.

(7) Wang, D.; Li, Y. Bimetallic Nanocrystals: Liquid-Phase Synthesis and Catalytic Applications. *Adv. Mater.* **2011**, *23*, 1044−1060.

(8) Xia, Y.; Xiong, Y.; Lim, B.; Skrabalak, S. E. Shape-Controlled Synthesis of Metal Nanocrystals: Simple Chemistry Meets Complex Physics? *Angew. Chem., Int. Ed.* **2009**, *48*, 60−103.

(9) Zhu, J.; Hu, L.; Zhao, P.; Lee, L. Y. S.; Wong, K.-Y. Recent Advances in Electrocatalytic Hydrogen Evolution Using Nanoparticles. *Chem. Rev.* **2020**, *120*, 851−918.

(10) Li, J.; Sun, S. Intermetallic Nanoparticles: Synthetic Control and Their Enhanced Electrocatalysis. *Acc. Chem. Res.* **2019**, *52*, 2015−2025.

(11) Li, Q.; Sun, S. Recent Advances in the Organic Solution Phase Synthesis of Metal Nanoparticles and Their Electrocatalysis for Energy Conversion Reactions. *Nano Energy* **2016**, *29*, 178−197.

(12) Yan, Y.; Du, J. S.; Gilroy, K. D.; Yang, D.; Xia, Y.; Zhang, H. Intermetallic Nanocrystals: Syntheses and Catalytic Applications. *Adv. Mater.* **2017**, *29*, 1605997.

(13) Wu, L.; Mendoza-Garcia, A.; Li, Q.; Sun, S. Organic Phase Syntheses of Magnetic Nanoparticles and Their Applications. *Chem. Rev.* **2016**, *116*, 10473−10512.

(14) Quan, Z.; Wang, Y.; Fang, J. High-Index Faceted Noble Metal Nanocrystals. *Acc. Chem. Res.* **2013**, *46*, 191−202.

(15) Wu, J.; Yang, H. Platinum-Based Oxygen Reduction Electrocatalysts. *Acc. Chem. Res.* **2013**, *46*, 1848−1857.

(16) Yang, X.; Yang, M.; Pang, B.; Vara, M.; Xia, Y. Gold Nanomaterials at Work in Biomedicine. *Chem. Rev.* **2015**, *115*, 10410−10488.

(17) Watt, J.; Cheong, S.; Tilley, R. D. How to Control the Shape of Metal Nanostructures in Organic Solution Phase Synthesis for Plasmonics and Catalysis. *Nano Today* **2013**, *8*, 198−215.

(18) Fan, Z.; Zhang, H. Crystal Phase-Controlled Synthesis, Properties and Applications of Noble Metal Nanomaterials. *Chem. Soc. Rev.* **2016**, *45*, 63−82.

(19) Gan, L.; Rudi, S.; Cui, C.; Heggen, M.; Strasser, P. Size-Controlled Synthesis of Sub-10 nm $PtNi_3$ Alloy Nanoparticles and Their Unusual Volcano-Shaped Size Effect on ORR Electrocatalysis. *Small* **2016**, *12*, 3189−3196.

(20) Han, S.; Mullins, C. B. Surface Alloy Composition Controlled O_2 Activation on Pd−Au Bimetallic Model Catalysts. *ACS Catal.* **2018**, *8*, 3641−3649.

https://dx.doi.org/10.1021/acs.chemrev.0c00436
Chem. Rev. 2021, 121, 736−795

(21) Li, X.; Wang, X.; Liu, M.; Liu, H.; Chen, Q.; Yin, Y.; Jin, M. Construction of Pd-M (M = Ni, Ag, Cu) Alloy Surfaces for Catalytic Applications. *Nano Res.* **2018**, *11*, 780−790.
(22) Lim, B.; Yu, T.; Xia, Y. Shaping a Bright Future for Platinum-Based Alloy Electrocatalysts. *Angew. Chem., Int. Ed.* **2010**, *49*, 9819−9820.
(23) Liu, S.; Chen, G.; Prasad, P. N.; Swihart, M. T. Synthesis of Monodisperse Au, Ag, and Au−Ag Alloy Nanoparticles with Tunable Size and Surface Plasmon Resonance Frequency. *Chem. Mater.* **2011**, *23*, 4098−4101.
(24) Luo, M.; Lu, P.; Yao, W.; Huang, C.; Xu, Q.; Wu, Q.; Kuwahara, Y.; Yamashita, H. Shape and Composition Effects on Photocatalytic Hydrogen Production for Pt−Pd Alloy Cocatalysts. *ACS Appl. Mater. Interfaces* **2016**, *8*, 20667−20674.
(25) Nie, Y.; Li, L.; Wei, Z. Recent Advancements in Pt and Pt-free Catalysts for Oxygen Reduction Reaction. *Chem. Soc. Rev.* **2015**, *44*, 2168−2201.
(26) Porter, N. S.; Wu, H.; Quan, Z.; Fang, J. Shape-Control and Electrocatalytic Activity-Enhancement of Pt-Based Bimetallic Nanocrystals. *Acc. Chem. Res.* **2013**, *46*, 1867−1877.
(27) Rong, H.; Cai, S.; Niu, Z.; Li, Y. Composition-Dependent Catalytic Activity of Bimetallic Nanocrystals: AgPd-Catalyzed Hydrodechlorination of 4-Chlorophenol. *ACS Catal.* **2013**, *3*, 1560−1563.
(28) Antolini, E. Alloy vs. Intermetallic Compounds: Effect of the Ordering on the Electrocatalytic Activity for Oxygen Reduction and the Stability of Low Temperature Fuel Cell Catalysts. *Appl. Catal., B* **2017**, *217*, 201−213.
(29) Chung, D. Y.; Yoo, J. M.; Sung, Y.-E. Highly Durable and Active Pt-Based Nanoscale Design for Fuel-Cell Oxygen-Reduction Electrocatalysts. *Adv. Mater.* **2018**, *30*, 1704123.
(30) Gamler, J. T. L.; Ashberry, H. M.; Skrabalak, S. E.; Koczkur, K. M. Random Alloyed versus Intermetallic Nanoparticles: A Comparison of Electrocatalytic Performance. *Adv. Mater.* **2018**, *30*, 1801563.
(31) Howard, L. E. M.; Nguyen, H. L.; Giblin, S. R.; Tanner, B. K.; Terry, I.; Hughes, A. K.; Evans, J. S. O. A Synthetic Route to Size-Controlled *fcc* and *fct* FePt Nanoparticles. *J. Am. Chem. Soc.* **2005**, *127*, 10140−10141.
(32) Luo, M.; Sun, Y.; Wang, L.; Guo, S. Tuning Multimetallic Ordered Intermetallic Nanocrystals for Efficient Energy Electrocatalysis. *Adv. Energy Mater.* **2017**, *7*, 1602073.
(33) Haruta, M.; Yamada, N.; Kobayashi, T.; Iijima, S. Gold Catalysts Prepared by Coprecipitation for Low-Temperature Oxidation of Hydrogen and of Carbon Monoxide. *J. Catal.* **1989**, *115*, 301−309.
(34) Chen, M. S.; Goodman, D. W. The Structure of Catalytically Active Gold on Titania. *Science* **2004**, *306*, 252−255.
(35) Zhang, W.; Yang, J.; Lu, X. Tailoring Galvanic Replacement Reaction for the Preparation of Pt/Ag Bimetallic Hollow Nanostructures with Controlled Number of Voids. *ACS Nano* **2012**, *6*, 7397−7405.
(36) Qiu, X.; Dai, Y.; Zhu, X.; Zhang, H.; Wu, P.; Tang, Y.; Wei, S. Template-Engaged Synthesis of Hollow Porous Platinum−Palladium Alloy Nanospheres for Efficient Methanol Electro-Oxidation. *J. Power Sources* **2016**, *302*, 195−201.
(37) Lim, B.; Wang, J.; Camargo, P. H. C.; Cobley, C. M.; Kim, M. J.; Xia, Y. Twin-Induced Growth of Palladium−Platinum Alloy Nanocrystals. *Angew. Chem., Int. Ed.* **2009**, *48*, 6304−6308.
(38) Li, M.; Zhao, Z.; Cheng, T.; Fortunelli, A.; Chen, C.-Y.; Yu, R.; Zhang, Q.; Gu, L.; Merinov, B. V.; Lin, Z.; Zhu, E.; Yu, T.; Jia, Q.; Guo, J.; Zhang, L.; Goddard, W. A.; Huang, Y.; Duan, X. Ultrafine Jagged Platinum Nanowires Enable Ultrahigh Mass Activity for the Oxygen Reduction Reaction. *Science* **2016**, *354*, 1414−1419.
(39) You, H.; Yang, S.; Ding, B.; Yang, H. Synthesis of Colloidal Metal and Metal Alloy Nanoparticles for Electrochemical Energy Applications. *Chem. Soc. Rev.* **2013**, *42*, 2880−2904.
(40) Wang, C.; Lin, C.; Zhang, L.; Quan, Z.; Sun, K.; Zhao, B.; Wang, F.; Porter, N.; Wang, Y.; Fang, J. Pt_3Co Concave Nanocubes: Synthesis, Formation Understanding, and Enhanced Catalytic Activity toward Hydrogenation of Styrene. *Chem. - Eur. J.* **2014**, *20*, 1753−1759.
(41) Li, K.; Li, X.; Huang, H.; Luo, L.; Li, X.; Yan, X.; Ma, C.; Si, R.; Yang, J.; Zeng, J. One-Nanometer-Thick PtNiRh Trimetallic Nanowires with Enhanced Oxygen Reduction Electrocatalysis in Acid Media: Integrating Multiple Advantages into One Catalyst. *J. Am. Chem. Soc.* **2018**, *140*, 16159−16167.
(42) Zhang, L.; Roling, L. T.; Wang, X.; Vara, M.; Chi, M.; Liu, J.; Choi, S.-I.; Park, J.; Herron, J. A.; Xie, Z.; Mavrikakis, M.; Xia, Y. Platinum-Based Nanocages with Subnanometer-Thick Walls and Well-Defined, Controllable Facets. *Science* **2015**, *349*, 412−416.
(43) Pal, S.; De, G. A New Approach for the Synthesis of Au−Ag Alloy Nanoparticle Incorporated SiO_2 Films. *Chem. Mater.* **2005**, *17*, 6161−6166.
(44) Mathe, N. R.; Scriba, M. R.; Rikhotso, R. S.; Coville, N. J. Microwave-Irradiation Polyol Synthesis of PVP-Protected Pt−Ni Electrocatalysts for Methanol Oxidation Reaction. *Electrocatalysis* **2018**, *9*, 388−399.
(45) Wu, F.; Zhang, D.; Peng, M.; Yu, Z.; Wang, X.; Guo, G.; Sun, Y. Microfluidic Synthesis Enables Dense and Uniform Loading of Surfactant-Free PtSn Nanocrystals on Carbon Supports for Enhanced Ethanol Oxidation. *Angew. Chem., Int. Ed.* **2016**, *55*, 4952−4956.
(46) Zhang, Z.; Blom, D. A.; Gai, Z.; Thompson, J. R.; Shen, J.; Dai, S. High-Yield Solvothermal Formation of Magnetic CoPt Alloy Nanowires. *J. Am. Chem. Soc.* **2003**, *125*, 7528−7529.
(47) Kang, Y.; Qi, L.; Li, M.; Diaz, R. E.; Su, D.; Adzic, R. R.; Stach, E.; Li, J.; Murray, C. B. Highly Active Pt_3Pb and Core−Shell Pt_3Pb−Pt Electrocatalysts for Formic Acid Oxidation. *ACS Nano* **2012**, *6*, 2818−2825.
(48) Zhu, C.; Wen, D.; Oschatz, M.; Holzschuh, M.; Liu, W.; Herrmann, A.-K.; Simon, F.; Kaskel, S.; Eychmüller, A. Kinetically Controlled Synthesis of PdNi Bimetallic Porous Nanostructures with Enhanced Electrocatalytic Activity. *Small* **2015**, *11*, 1430−1434.
(49) Liu, J.; Zheng, Y.; Hong, Z.; Cai, K.; Zhao, F.; Han, H. Microbial Synthesis of Highly Dispersed PdAu Alloy for Enhanced Electrocatalysis. *Sci. Adv.* **2016**, *2*, No. e1600858.
(50) Chen, H.-C.; Chou, S.-W.; Tseng, W.-H.; Chen, I.-W. P.; Liu, C.-C.; Liu, C.; Liu, C.-L.; Chen, C.-h.; Wu, C.-I.; Chou, P.-T. Large AuAg Alloy Nanoparticles Synthesized in Organic Media Using a One-Pot Reaction: Their Applications for High-Performance Bulk Heterojunction Solar Cells. *Adv. Funct. Mater.* **2012**, *22*, 3975−3984.
(51) Lu, Y.; Shi, C.; Hu, M.-J.; Xu, Y.-J.; Yu, L.; Wen, L.-P.; Zhao, Y.; Xu, W.-P.; Yu, S.-H. Magnetic Alloy Nanorings Loaded with Gold Nanoparticles: Synthesis and Applications as Multimodal Imaging Contrast Agents. *Adv. Funct. Mater.* **2010**, *20*, 3701−3706.
(52) Xiao, Q.; Sohn, H.; Chen, Z.; Toso, D.; Mechlenburg, M.; Zhou, Z. H.; Poirier, E.; Dailly, A.; Wang, H.; Wu, Z.; Cai, M.; Lu, Y. Mesoporous Metal and Metal Alloy Particles Synthesized by Aerosol-Assisted Confined Growth of Nanocrystals. *Angew. Chem., Int. Ed.* **2012**, *51*, 10546−10550.
(53) Liu, Y.; Walker, A. R. H. Monodisperse Gold−Copper Bimetallic Nanocubes: Facile One-Step Synthesis with Controllable Size and Composition. *Angew. Chem., Int. Ed.* **2010**, *49*, 6781−6785.
(54) Choi, B.-S.; Lee, Y. W.; Kang, S. W.; Hong, J. W.; Kim, J.; Park, I.; Han, S. W. Multimetallic Alloy Nanotubes with Nanoporous Framework. *ACS Nano* **2012**, *6*, 5659−5667.
(55) Cui, C.; Gan, L.; Li, H.-H.; Yu, S.-H.; Heggen, M.; Strasser, P. Octahedral PtNi Nanoparticle Catalysts: Exceptional Oxygen Reduction Activity by Tuning the Alloy Particle Surface Composition. *Nano Lett.* **2012**, *12*, 5885−5889.
(56) Wang, S.-B.; Zhu, W.; Ke, J.; Lin, M.; Zhang, Y.-W. Pd−Rh Nanocrystals with Tunable Morphologies and Compositions as Efficient Catalysts toward Suzuki Cross-Coupling Reactions. *ACS Catal.* **2014**, *4*, 2298−2306.
(57) Wang, L.; Holewinski, A.; Wang, C. Prospects of Platinum-Based Nanostructures for the Electrocatalytic Reduction of Oxygen. *ACS Catal.* **2018**, *8*, 9388−9398.
(58) Wang, M.; Wang, L.; Li, H.; Du, W.; Khan, M. U.; Zhao, S.; Ma, C.; Li, Z.; Zeng, J. Ratio-Controlled Synthesis of CuNi Octahedra

https://dx.doi.org/10.1021/acs.chemrev.0c00436
Chem. Rev. 2021, 121, 736−795

and Nanocubes with Enhanced Catalytic Activity. *J. Am. Chem. Soc.* **2015**, *137*, 14027−14030.
(59) Bu, L.; Shao, Q.; Pi, Y.; Yao, J.; Luo, M.; Lang, J.; Hwang, S.; Xin, H.; Huang, B.; Guo, J.; Su, D.; Guo, S.; Huang, X. Coupled *s-p-d* Exchange in Facet-Controlled Pd_3Pb Tripods Enhances Oxygen Reduction Catalysis. *Chem.* **2018**, *4*, 359−371.
(60) Peng, Y.; Cui, M.; Zhang, Z.; Shu, S.; Shi, X.; Brosnahan, J. T.; Liu, C.; Zhang, Y.; Godbold, P.; Zhang, X.; Dong, F.; Jiang, G.; Zhang, S. Bimetallic Composition-Promoted Electrocatalytic Hydrodechlorination Reaction on Silver−Palladium Alloy Nanoparticles. *ACS Catal.* **2019**, *9*, 10803−10811.
(61) Xie, Y.; Cai, J.; Wu, Y.; Zang, Y.; Zheng, X.; Ye, J.; Cui, P.; Niu, S.; Liu, Y.; Zhu, J.; Liu, X.; Wang, G.; Qian, Y. Boosting Water Dissociation Kinetics on Pt−Ni Nanowires by N-Induced Orbital Tuning. *Adv. Mater.* **2019**, *31*, 1807780.
(62) Ren, X.; Lv, Q.; Liu, L.; Liu, B.; Wang, Y.; Liu, A.; Wu, G. Current Progress of Pt and Pt-Based Electrocatalysts Used for Fuel Cells. *Sustainable Energy Fuels* **2020**, *4*, 15−30.
(63) Ye, H.; Crooks, R. M. Effect of Elemental Composition of PtPd Bimetallic Nanoparticles Containing an Average of 180 Atoms on the Kinetics of the Electrochemical Oxygen Reduction Reaction. *J. Am. Chem. Soc.* **2007**, *129*, 3627−3633.
(64) Wang, Y.; Cao, L.; Libretto, N. J.; Li, X.; Li, C.; Wan, Y.; He, C.; Lee, J.; Gregg, J.; Zong, H.; Su, D.; Miller, J. T.; Mueller, T.; Wang, C. Ensemble Effect in Bimetallic Electrocatalysts for CO_2 Reduction. *J. Am. Chem. Soc.* **2019**, *141*, 16635−16642.
(65) Goulas, K. A.; Sreekumar, S.; Song, Y.; Kharidehal, P.; Gunbas, G.; Dietrich, P. J.; Johnson, G. R.; Wang, Y. C.; Grippo, A. M.; Grabow, L. C.; Gokhale, A. A.; Toste, F. D. Synergistic Effects in Bimetallic Palladium−Copper Catalysts Improve Selectivity in Oxygenate Coupling Reactions. *J. Am. Chem. Soc.* **2016**, *138*, 6805−6812.
(66) Kim, D.; Resasco, J.; Yu, Y.; Asiri, A. M.; Yang, P. Synergistic Geometric and Electronic Effects for Electrochemical Reduction of Carbon Dioxide Using Gold−Copper Bimetallic Nanoparticles. *Nat. Commun.* **2014**, *5*, 4948.
(67) Zhao, X.; Chen, S.; Fang, Z.; Ding, J.; Sang, W.; Wang, Y.; Zhao, J.; Peng, Z.; Zeng, J. Octahedral $Pd@Pt_{1.8}Ni$ Core−Shell Nanocrystals with Ultrathin PtNi Alloy Shells as Active Catalysts for Oxygen Reduction Reaction. *J. Am. Chem. Soc.* **2015**, *137*, 2804−2807.
(68) Wang, C.; Zhang, L.; Yang, H.; Pan, J.; Liu, J.; Dotse, C.; Luan, Y.; Gao, R.; Lin, C.; Zhang, J.; Kilcrease, J. P.; Wen, X.; Zou, S.; Fang, J. High-Indexed Pt_3Ni Alloy Tetrahexahedral Nanoframes Evolved through Preferential CO Etching. *Nano Lett.* **2017**, *17*, 2204−2210.
(69) Huang, X.; Zhu, E.; Chen, Y.; Li, Y.; Chiu, C.-Y.; Xu, Y.; Lin, Z.; Duan, X.; Huang, Y. A Facile Strategy to Pt_3Ni Nanocrystals with Highly Porous Features as an Enhanced Oxygen Reduction Reaction Catalyst. *Adv. Mater.* **2013**, *25*, 2974−2979.
(70) Zhu, Z.; Zhai, Y.; Dong, S. Facial Synthesis of PtM (M = Fe, Co, Cu, Ni) Bimetallic Alloy Nanosponges and Their Enhanced Catalysis for Oxygen Reduction Reaction. *ACS Appl. Mater. Interfaces* **2014**, *6*, 16721−16726.
(71) Tian, X.; Zhao, X.; Su, Y.-Q.; Wang, L.; Wang, H.; Dang, D.; Chi, B.; Liu, H.; Hensen, E. J. M.; Lou, X. W.; Xia, B. Y. Engineering Bunched Pt-Ni Alloy Nanocages for Efficient Oxygen Reduction in Practical Fuel Cells. *Science* **2019**, *366*, 850−856.
(72) Huang, X.; Zhao, Z.; Cao, L.; Chen, Y.; Zhu, E.; Lin, Z.; Li, M.; Yan, A.; Zettl, A.; Wang, Y. M.; Duan, X.; Mueller, T.; Huang, Y. High-Performance Transition Metal−Doped Pt_3Ni Octahedra for Oxygen Reduction Reaction. *Science* **2015**, *348*, 1230−1234.
(73) Choi, S.-I.; Xie, S.; Shao, M.; Odell, J. H.; Lu, N.; Peng, H.-C.; Protsailo, L.; Guerrero, S.; Park, J.; Xia, X.; Wang, J.; Kim, M. J.; Xia, Y. Synthesis and Characterization of 9 nm Pt−Ni Octahedra with a Record High Activity of 3.3 A/mg_{Pt} for the Oxygen Reduction Reaction. *Nano Lett.* **2013**, *13*, 3420−3425.
(74) Wang, Y.-J.; Zhao, N.; Fang, B.; Li, H.; Bi, X. T.; Wang, H. Carbon-Supported Pt-Based Alloy Electrocatalysts for the Oxygen Reduction Reaction in Polymer Electrolyte Membrane Fuel Cells: Particle Size, Shape, and Composition Manipulation and Their Impact to Activity. *Chem. Rev.* **2015**, *115*, 3433−3467.
(75) Sun, X.; Jiang, K.; Zhang, N.; Guo, S.; Huang, X. Crystalline Control of {111} Bounded Pt_3Cu Nanocrystals: Multiply-Twinned Pt_3Cu Icosahedra with Enhanced Electrocatalytic Properties. *ACS Nano* **2015**, *9*, 7634−7640.
(76) Zhang, J.; Fang, J. A General Strategy for Preparation of Pt 3*d*-Transition Metal (Co, Fe, Ni) Nanocubes. *J. Am. Chem. Soc.* **2009**, *131*, 18543−18547.
(77) Chen, Y.; Yu, Z.; Chen, Z.; Shen, R.; Wang, Y.; Cao, X.; Peng, Q.; Li, Y. Controlled One-Pot Synthesis of RuCu Nanocages and Cu@Ru Nanocrystals for the Regioselective Hydrogenation of Quinoline. *Nano Res.* **2016**, *9*, 2632−2640.
(78) Zhang, L.; Zhang, J.; Kuang, Q.; Xie, S.; Jiang, Z.; Xie, Z.; Zheng, L. Cu^{2+}-Assisted Synthesis of Hexoctahedral Au−Pd Alloy Nanocrystals with High-Index Facets. *J. Am. Chem. Soc.* **2011**, *133*, 17114−17117.
(79) He, W.; Wu, X.; Liu, J.; Hu, X.; Zhang, K.; Hou, S.; Zhou, W.; Xie, S. Design of AgM Bimetallic Alloy Nanostructures (M = Au, Pd, Pt) with Tunable Morphology and Peroxidase-Like Activity. *Chem. Mater.* **2010**, *22*, 2988−2994.
(80) Tao, F. Excavation of Precious-Metal-Based Alloy Nanoparticles for Efficient Catalysis. *Angew. Chem., Int. Ed.* **2016**, *55*, 15212−15214.
(81) He, R.; Wang, Y.-C.; Wang, X.; Wang, Z.; Liu, G.; Zhou, W.; Wen, L.; Li, Q.; Wang, X.; Chen, X.; Zeng, J.; Hou, J. G. Facile Synthesis of Pentacle Gold−Copper Alloy Nanocrystals and Their Plasmonic and Catalytic Properties. *Nat. Commun.* **2014**, *5*, 4327.
(82) Pi, Y.; Shao, Q.; Wang, P.; Guo, J.; Huang, X. General Formation of Monodisperse IrM (M = Ni, Co, Fe) Bimetallic Nanoclusters as Bifunctional Electrocatalysts for Acidic Overall Water Splitting. *Adv. Funct. Mater.* **2017**, *27*, 1700886.
(83) Rai, R. K.; Gupta, K.; Behrens, S.; Li, J.; Xu, Q.; Singh, S. K. Highly Active Bimetallic Nickel−Palladium Alloy Nanoparticle Catalyzed Suzuki−Miyaura Reactions. *ChemCatChem* **2015**, *7*, 1806−1812.
(84) Arandiyan, H.; Wang, Y.; Scott, J.; Mesgari, S.; Dai, H.; Amal, R. In Situ Exsolution of Bimetallic Rh−Ni Nanoalloys: a Highly Efficient Catalyst for CO2Methanation. *ACS Appl. Mater. Interfaces* **2018**, *10*, 16352−16357.
(85) Park, J.; Sa, Y. J.; Baik, H.; Kwon, T.; Joo, S. H.; Lee, K. Iridium-Based Multimetallic Nanoframe@Nanoframe Structure: An Efficient and Robust Electrocatalyst toward Oxygen Evolution Reaction. *ACS Nano* **2017**, *11*, 5500−5509.
(86) Sugano, Y.; Shiraishi, Y.; Tsukamoto, D.; Ichikawa, S.; Tanaka, S.; Hirai, T. Supported Au−Cu Bimetallic Alloy Nanoparticles: An Aerobic Oxidation Catalyst with Regenerable Activity by Visible-Light Irradiation. *Angew. Chem., Int. Ed.* **2013**, *52*, 5295−5299.
(87) Lai, J.; Niu, W.; Luque, R.; Xu, G. Solvothermal Synthesis of Metal Nanocrystals and Their Applications. *Nano Today* **2015**, *10*, 240−267.
(88) Kusada, K.; Kobayashi, H.; Ikeda, R.; Kubota, Y.; Takata, M.; Toh, S.; Yamamoto, T.; Matsumura, S.; Sumi, N.; Sato, K.; Nagaoka, K.; Kitagawa, H. Solid Solution Alloy Nanoparticles of Immiscible Pd and Ru Elements Neighboring on Rh: Changeover of the Thermodynamic Behavior for Hydrogen Storage and Enhanced CO-Oxidizing Ability. *J. Am. Chem. Soc.* **2014**, *136*, 1864−1871.
(89) Long, J.; Liu, H.; Wu, S.; Liao, S.; Li, Y. Selective Oxidation of Saturated Hydrocarbons Using Au−Pd Alloy Nanoparticles Supported on Metal−Organic Frameworks. *ACS Catal.* **2013**, *3*, 647−654.
(90) Slanac, D. A.; Hardin, W. G.; Johnston, K. P.; Stevenson, K. J. Atomic Ensemble and Electronic Effects in Ag-Rich AgPd Nanoalloy Catalysts for Oxygen Reduction in Alkaline Media. *J. Am. Chem. Soc.* **2012**, *134*, 9812−9819.
(91) Luc, W.; Collins, C.; Wang, S.; Xin, H.; He, K.; Kang, Y.; Jiao, F. Ag−Sn Bimetallic Catalyst with a Core−Shell Structure for CO_2 Reduction. *J. Am. Chem. Soc.* **2017**, *139*, 1885−1893.

https://dx.doi.org/10.1021/acs.chemrev.0c00436
Chem. Rev. 2021, 121, 736−795

(92) Xiao, W.; Lei, W.; Gong, M.; Xin, H. L.; Wang, D. Recent Advances of Structurally Ordered Intermetallic Nanoparticles for Electrocatalysis. *ACS Catal.* **2018**, *8*, 3237−3256.
(93) Yu, W.; Porosoff, M. D.; Chen, J. G. Review of Pt-Based Bimetallic Catalysis: From Model Surfaces to Supported Catalysts. *Chem. Rev.* **2012**, *112*, 5780−5817.
(94) Wang, X. X.; Swihart, M. T.; Wu, G. Achievements, Challenges and Perspectives on Cathode Catalysts in Proton Exchange Membrane Fuel Cells for Transportation. *Nat. Catal.* **2019**, *2*, 578−589.
(95) Borbáth, I.; Gubán, D.; Pászti, Z.; Sajó, I. E.; Drotár, E.; de la Fuente, J. L. G.; Herranz, T.; Rojas, S.; Tompos, A. Controlled Synthesis of Pt_3Sn/C Electrocatalysts with Exclusive Sn−Pt Interaction Designed for Use in Direct Methanol Fuel Cells. *Top. Catal.* **2013**, *56*, 1033−1046.
(96) Peng, Z.; You, H.; Yang, H. Composition-Dependent Formation of Platinum Silver Nanowires. *ACS Nano* **2010**, *4*, 1501−1510.
(97) Zhao, X.; Luo, B.; Long, R.; Wang, C.; Xiong, Y. Composition-Dependent Activity of Cu−Pt Alloy Nanocubes for Electrocatalytic CO_2 Reduction. *J. Mater. Chem. A* **2015**, *3*, 4134−4138.
(98) Zhan, W.; Wang, J.; Wang, H.; Zhang, J.; Liu, X.; Zhang, P.; Chi, M.; Guo, Y.; Guo, Y.; Lu, G.; Sun, S.; Dai, S.; Zhu, H. Crystal Structural Effect of AuCu Alloy Nanoparticles on Catalytic CO Oxidation. *J. Am. Chem. Soc.* **2017**, *139*, 8846−8854.
(99) Pan, L.; Ott, S.; Dionigi, F.; Strasser, P. Current Challenges Related to the Deployment of Shape-Controlled Pt Alloy Oxygen Reduction Reaction Nanocatalysts into Low Pt-Loaded Cathode Layers of Proton Exchange Membrane Fuel Cells. *Curr. Opin. Electrochem.* **2019**, *18*, 61−71.
(100) Huang, L.; Zhang, X.; Wang, Q.; Han, Y.; Fang, Y.; Dong, S. Shape-Control of Pt−Ru Nanocrystals: Tuning Surface Structure for Enhanced Electrocatalytic Methanol Oxidation. *J. Am. Chem. Soc.* **2018**, *140*, 1142−1147.
(101) Ruditskiy, A.; Peng, H.-C.; Xia, Y. Shape-Controlled Metal Nanocrystals for Heterogeneous Catalysis. *Annu. Rev. Chem. Biomol. Eng.* **2016**, *7*, 327−348.
(102) Chen, S.; Su, H.; Wang, Y.; Wu, W.; Zeng, J. Size-Controlled Synthesis of Platinum−Copper Hierarchical Trigonal Bipyramid Nanoframes. *Angew. Chem., Int. Ed.* **2015**, *54*, 108−113.
(103) Wang, Q.; Chen, S.; Shi, F.; Chen, K.; Nie, Y.; Wang, Y.; Wu, R.; Li, J.; Zhang, Y.; Ding, W.; Li, Y.; Li, L.; Wei, Z. Structural Evolution of Solid Pt Nanoparticles to a Hollow PtFe Alloy with a Pt-Skin Surface via Space-Confined Pyrolysis and the Nanoscale Kirkendall Effect. *Adv. Mater.* **2016**, *28*, 10673−10678.
(104) Chang, Q.; Xu, Y.; Duan, Z.; Xiao, F.; Fu, F.; Hong, Y.; Kim, J.; Choi, S.-I.; Su, D.; Shao, M. Structural Evolution of Sub-10 nm Octahedral Platinum−Nickel Bimetallic Nanocrystals. *Nano Lett.* **2017**, *17*, 3926−3931.
(105) Liang, J.; Ma, F.; Hwang, S.; Wang, X.; Sokolowski, J.; Li, Q.; Wu, G.; Su, D. Atomic Arrangement Engineering of Metallic Nanocrystals for Energy-Conversion Electrocatalysis. *Joule* **2019**, *3*, 956−991.
(106) Loukrakpam, R.; Shan, S.; Petkov, V.; Yang, L.; Luo, J.; Zhong, C.-J. Atomic Ordering Enhanced Electrocatalytic Activity of Nanoalloys for Oxygen Reduction Reaction. *J. Phys. Chem. C* **2013**, *117*, 20715−20721.
(107) Zhu, J.; Yang, Y.; Chen, L.; Xiao, W.; Liu, H.; Abruña, H. D.; Wang, D. Copper-Induced Formation of Structurally Ordered Pt−Fe−Cu Ternary Intermetallic Electrocatalysts with Tunable Phase Structure and Improved Stability. *Chem. Mater.* **2018**, *30*, 5987−5995.
(108) Zou, L.; Fan, J.; Zhou, Y.; Wang, C.; Li, J.; Zou, Z.; Yang, H. Conversion of PtNi Alloy from Disordered to Ordered for Enhanced Activity and Durability in Methanol-Tolerant Oxygen Reduction Reactions. *Nano Res.* **2015**, *8*, 2777−2788.
(109) Kim, D.; Xie, C.; Becknell, N.; Yu, Y.; Karamad, M.; Chan, K.; Crumlin, E. J.; Nørskov, J. K.; Yang, P. Electrochemical Activation of CO_2 through Atomic Ordering Transformations of AuCu Nanoparticles. *J. Am. Chem. Soc.* **2017**, *139*, 8329−8336.
(110) Cui, Z.; Li, L.; Manthiram, A.; Goodenough, J. B. Enhanced Cycling Stability of Hybrid Li−Air Batteries Enabled by Ordered Pd_3Fe Intermetallic Electrocatalyst. *J. Am. Chem. Soc.* **2015**, *137*, 7278−7281.
(111) Zhang, B.; Fu, G.; Li, Y.; Liang, L.; Grundish, N. S.; Tang, Y.; Goodenough, J. B.; Cui, Z. General Strategy for Synthesis of Ordered Pt_3M Intermetallics with Ultrasmall Particle Size. *Angew. Chem., Int. Ed.* **2020**, *59*, 7857−7863.
(112) Li, Q.; Wu, L.; Wu, G.; Su, D.; Lv, H.; Zhang, S.; Zhu, W.; Casimir, A.; Zhu, H.; Mendoza-Garcia, A.; Sun, S. New Approach to Fully Ordered *fct*-FePt Nanoparticles for Much Enhanced Electrocatalysis in Acid. *Nano Lett.* **2015**, *15*, 2468−2473.
(113) Lei, W.; Xu, J.; Yu, Y.; Yang, W.; Hou, Y.; Chen, D. Halide Ion-Mediated Synthesis of $L1_0$-FePt Nanoparticles with Tunable Magnetic Properties. *Nano Lett.* **2018**, *18*, 7839−7844.
(114) Li, J.; Sharma, S.; Liu, X.; Pan, Y.-T.; Spendelow, J. S.; Chi, M.; Jia, Y.; Zhang, P.; Cullen, D. A.; Xi, Z.; Lin, H.; Yin, Z.; Shen, B.; Muzzio, M.; Yu, C.; Kim, Y. S.; Peterson, A. A.; More, K. L.; Zhu, H.; Sun, S. Hard-Magnet $L1_0$-CoPt Nanoparticles Advance Fuel Cell Catalysis. *Joule* **2019**, *3*, 124−135.
(115) Cui, C.; Gan, L.; Heggen, M.; Rudi, S.; Strasser, P. Compositional Segregation in Shaped Pt Alloy Nanoparticles and Their Structural Behaviour During Electrocatalysis. *Nat. Mater.* **2013**, *12*, 765−771.
(116) Dionigi, F.; Weber, C. C.; Primbs, M.; Gocyla, M.; Bonastre, A. M.; Spöri, C.; Schmies, H.; Hornberger, E.; Kühl, S.; Drnec, J.; Heggen, M.; Sharman, J.; Dunin-Borkowski, R. E.; Strasser, P. Controlling Near-Surface Ni Composition in Octahedral PtNi(Mo) Nanoparticles by Mo Doping for a Highly Active Oxygen Reduction Reaction Catalyst. *Nano Lett.* **2019**, *19*, 6876−6885.
(117) Gan, L.; Cui, C.; Heggen, M.; Dionigi, F.; Rudi, S.; Strasser, P. Element-Specific Anisotropic Growth of Shaped Platinum Alloy Nanocrystals. *Science* **2014**, *346*, 1502−1506.
(118) Lin, R.; Zhao, T.; Shang, M.; Wang, J.; Tang, W.; Guterman, V. E.; Ma, J. Effect of Heat Treatment on the Activity and Stability of PtCo/C Catalyst and Application of *in-Situ* X-ray Absorption Near Edge Structure for Proton Exchange Membrane Fuel Cell. *J. Power Sources* **2015**, *293*, 274−282.
(119) Casado-Rivera, E.; Volpe, D. J.; Alden, L.; Lind, C.; Downie, C.; Vázquez-Alvarez, T.; Angelo, A. C. D.; DiSalvo, F. J.; Abruña, H. D. Electrocatalytic Activity of Ordered Intermetallic Phases for Fuel Cell Applications. *J. Am. Chem. Soc.* **2004**, *126*, 4043−4049.
(120) Bu, L.; Zhang, N.; Guo, S.; Zhang, X.; Li, J.; Yao, J.; Wu, T.; Lu, G.; Ma, J.-Y.; Su, D.; Huang, X. Biaxially Strained PtPb/Pt Core/Shell Nanoplate Boosts Oxygen Reduction Catalysis. *Science* **2016**, *354*, 1410−1414.
(121) Hoffman, Z. B.; Gray, T. S.; Moraveck, K. B.; Gunnoe, T. B.; Zangari, G. Electrochemical Reduction of Carbon Dioxide to Syngas and Formate at Dendritic Copper−Indium Electrocatalysts. *ACS Catal.* **2017**, *7*, 5381−5390.
(122) Qin, Y.; Luo, M.; Sun, Y.; Li, C.; Huang, B.; Yang, Y.; Li, Y.; Wang, L.; Guo, S. Intermetallic *hcp*-PtBi/*fcc*-Pt Core/Shell Nanoplates Enable Efficient Bifunctional Oxygen Reduction and Methanol Oxidation Electrocatalysis. *ACS Catal.* **2018**, *8*, 5581−5590.
(123) Tsai, A. P.; Kameoka, S.; Nozawa, K.; Shimoda, M.; Ishii, Y. Intermetallic: A Pseudoelement for Catalysis. *Acc. Chem. Res.* **2017**, *50*, 2879−2885.
(124) Chen, Y.-J.; Chen, Y.-R.; Chiang, C.-H.; Tung, K.-L.; Yeh, T.-K.; Tuan, H.-Y. Monodisperse Ordered Indium−Palladium Nanoparticles: Synthesis and Role of Indium for Boosting Superior Electrocatalytic Activity for Ethanol Oxidation Reaction. *Nanoscale* **2019**, *11*, 3336−3343.
(125) Luo, M.; Guo, S. Multimetallic Electrocatalyst Stabilized by Atomic Ordering. *Joule* **2019**, *3*, 9−10.
(126) Wang, D.; Peng, Q.; Li, Y. Nanocrystalline Intermetallics and Alloys. *Nano Res.* **2010**, *3*, 574−580.
(127) Wang, D.; Yu, Y.; Zhu, J.; Liu, S.; Muller, D. A.; Abruña, H. D. Morphology and Activity Tuning of Cu_3Pt/C Ordered Intermetallic

Nanoparticles by Selective Electrochemical Dealloying. *Nano Lett.* **2015**, *15*, 1343−1348.
(128) Chen, L.; Bock, C.; Mercier, P. H. J.; MacDougall, B. R. Ordered Alloy Formation for Pt_3Fe/C, PtFe/C and $Pt_{5.75}Fe_{5.75}Cuy$/CO_2-Reduction Electro-Catalysts. Electrochim. *Acta* **2012**, *77*, 212−224.
(129) Jiang, K.; Wang, P.; Guo, S.; Zhang, X.; Shen, X.; Lu, G.; Su, D.; Huang, X. Ordered PdCu-Based Nanoparticles as Bifunctional Oxygen-Reduction and Ethanol-Oxidation Electrocatalysts. *Angew. Chem., Int. Ed.* **2016**, *55*, 9030−9035.
(130) Xiong, Y.; Yang, Y.; Joress, H.; Padgett, E.; Gupta, U.; Yarlagadda, V.; Agyeman-Budu, D. N.; Huang, X.; Moylan, T. E.; Zeng, R.; Kongkanand, A.; Escobedo, F. A.; Brock, J. D.; DiSalvo, F. J.; Muller, D. A.; Abruña, H. D. Revealing the Atomic Ordering of Binary Intermetallics Using in Situ Heating Techniques at Multilength Scales. *Proc. Natl. Acad. Sci. U. S. A.* **2019**, *116*, 1974.
(131) Chi, M.; Wang, C.; Lei, Y.; Wang, G.; Li, D.; More, K. L.; Lupini, A.; Allard, L. F.; Markovic, N. M.; Stamenkovic, V. R. Surface Faceting and Elemental Diffusion Behaviour at Atomic Scale for Alloy Nanoparticles During *in Situ* Annealing. *Nat. Commun.* **2015**, *6*, 8925.
(132) Zhao, W.; Yang, L.; Yin, Y.; Jin, M. Thermodynamic Controlled Synthesis of Intermetallic Au_3Cu Alloy Nanocrystals from Cu Microparticles. *J. Mater. Chem. A* **2014**, *2*, 902−906.
(133) Yan, Q.; Kim, T.; Purkayastha, A.; Ganesan, P. G.; Shima, M.; Ramanath, G. Enhanced Chemical Ordering and Coercivity in FePt Alloy Nanoparticles by Sb-Doping. *Adv. Mater.* **2005**, *17*, 2233−2237.
(134) Kozlov, S. M.; Kovács, G.; Ferrando, R.; Neyman, K. M. How to Determine Accurate Chemical Ordering in Several Nanometer Large Bimetallic Crystallites from Electronic Structure Calculations. *Chem. Sci.* **2015**, *6*, 3868−3880.
(135) Ghosh, T.; Leonard, B. M.; Zhou, Q.; DiSalvo, F. J. Pt Alloy and Intermetallic Phases with V, Cr, Mn, Ni, and Cu: Synthesis As Nanomaterials and Possible Applications As Fuel Cell Catalysts. *Chem. Mater.* **2010**, *22*, 2190−2202.
(136) Liu, Q.; Du, L.; Fu, G.; Cui, Z.; Li, Y.; Dang, D.; Gao, X.; Zheng, Q.; Goodenough, J. B. Structurally Ordered Fe_3Pt Nanoparticles on Robust Nitride Support as a High Performance Catalyst for the Oxygen Reduction Reaction. *Adv. Energy Mater.* **2019**, *9*, 1803040.
(137) Ma, T.; Wang, S.; Chen, M.; Maligal-Ganesh, R. V.; Wang, L.-L.; Johnson, D. D.; Kramer, M. J.; Huang, W.; Zhou, L. Toward Phase and Catalysis Control: Tracking the Formation of Intermetallic Nanoparticles at Atomic Scale. *Chem.* **2019**, *5*, 1235−1247.
(138) Li, G.; Kobayashi, H.; Kusada, K.; Taylor, J. M.; Kubota, Y.; Kato, K.; Takata, M.; Yamamoto, T.; Matsumura, S.; Kitagawa, H. An Ordered *bcc* CuPd Nanoalloy Synthesised via the Thermal Decomposition of Pd Nanoparticles Covered with a Metal−Organic Framework under Hydrogen Gas. *Chem. Commun.* **2014**, *50*, 13750−13753.
(139) Wen, Y.-H.; Huang, R. Effect of Chemical Ordering on Thermal Stability of Pt−Co Nanoparticles. *J. Phys. Chem. C* **2019**, *123*, 12007−12014.
(140) Yu, Z.; Zhang, J.; Liu, Z.; Ziegelbauer, J. M.; Xin, H.; Dutta, I.; Muller, D. A.; Wagner, F. T. Comparison between Dealloyed $PtCo_3$ and $PtCu_3$ Cathode Catalysts for Proton Exchange Membrane Fuel Cells. *J. Phys. Chem. C* **2012**, *116*, 19877−19885.
(141) Kim, H. Y.; Kim, J. M.; Ha, Y.; Woo, J.; Byun, A.; Shin, T. J.; Park, K. H.; Jeong, H. Y.; Kim, H.; Kim, J. Y.; Joo, S. H. Activity Origin and Multifunctionality of Pt-Based Intermetallic Nanostructures for Efficient Electrocatalysis. *ACS Catal.* **2019**, *9*, 11242−11254.
(142) Ma, S.; Sadakiyo, M.; Heima, M.; Luo, R.; Haasch, R. T.; Gold, J. I.; Yamauchi, M.; Kenis, P. J. A. Electroreduction of Carbon Dioxide to Hydrocarbons Using Bimetallic Cu−Pd Catalysts with Different Mixing Patterns. *J. Am. Chem. Soc.* **2017**, *139*, 47−50.
(143) Antoniak, C.; Gruner, M. E.; Spasova, M.; Trunova, A. V.; Römer, F. M.; Warland, A.; Krumme, B.; Fauth, K.; Sun, S.; Entel, P.; Farle, M.; Wende, H. A Guideline for Atomistic Design and Understanding of Ultrahard Nanomagnets. *Nat. Commun.* **2011**, *2*, 528.
(144) Pavlišič, A.; Jovanovič, P.; Šelih, V. S.; Šala, M.; Bele, M.; Dražić, G.; Arčon, I.; Hočevar, S.; Kokalj, A.; Hodnik, N.; Gaberšček, M. Atomically Resolved Dealloying of Structurally Ordered Pt Nanoalloy as an Oxygen Reduction Reaction Electrocatalyst. *ACS Catal.* **2016**, *6*, 5530−5534.
(145) Greeley, J.; Stephens, I. E. L.; Bondarenko, A. S.; Johansson, T. P.; Hansen, H. A.; Jaramillo, T. F.; Rossmeisl, J.; Chorkendorff, I.; Nørskov, J. K. Alloys of Platinum and Early Transition Metals as Oxygen Reduction Electrocatalysts. *Nat. Chem.* **2009**, *1*, 552−556.
(146) He, J.; Johnson, N. J. J.; Huang, A.; Berlinguette, C. P. Electrocatalytic Alloys for CO_2 Reduction. *ChemSusChem* **2018**, *11*, 48−57.
(147) Praetorius, C.; Zinner, M.; Köhl, A.; Kießling, H.; Brück, S.; Muenzing, B.; Kamp, M.; Kachel, T.; Choueikani, F.; Ohresser, P.; Wilhelm, F.; Rogalev, A.; Fauth, K. Electronic Tuneability of a Structurally Rigid Surface Intermetallic and Kondo Lattice: $CePt_5$/Pt(111). *Phys. Rev. B: Condens. Matter Mater. Phys.* **2015**, *92*, 045116.
(148) Rößner, L.; Armbrüster, M. Electrochemical Energy Conversion on Intermetallic Compounds: A Review. *ACS Catal.* **2019**, *9*, 2018−2062.
(149) Mizutani, U. Hume-Rothery Rules for Structurally Complex Alloy Phases. *MRS Bull.* **2012**, *37*, 169.
(150) Oezaslan, M.; Hasché, F.; Strasser, P. In Situ Observation of Bimetallic Alloy Nanoparticle Formation and Growth Using High-Temperature XRD. *Chem. Mater.* **2011**, *23*, 2159−2165.
(151) Wu, L.; Fournier, A. P.; Willis, J. J.; Cargnello, M.; Tassone, C. J. In Situ X-ray Scattering Guides the Synthesis of Uniform PtSn Nanocrystals. *Nano Lett.* **2018**, *18*, 4053−4057.
(152) Furukawa, S.; Komatsu, T. Intermetallic Compounds: Promising Inorganic Materials for Well-Structured and Electronically Modified Reaction Environments for Efficient Catalysis. *ACS Catal.* **2017**, *7*, 735−765.
(153) Alloyeau, D.; Ricolleau, C.; Mottet, C.; Oikawa, T.; Langlois, C.; Le Bouar, Y.; Braidy, N.; Loiseau, A. Size and Shape Effects on the Order−Disorder Phase Transition in CoPt Nanoparticles. *Nat. Mater.* **2009**, *8*, 940−946.
(154) Ashberry, H. M.; Gamler, J. T. L.; Unocic, R. R.; Skrabalak, S. E. Disorder-to-Order Transition Mediated by Size Refocusing: A Route toward Monodisperse Intermetallic Nanoparticles. *Nano Lett.* **2019**, *19*, 6418−6423.
(155) Bauer, J. C.; Chen, X.; Liu, Q.; Phan, T.-H.; Schaak, R. E. Converting Nanocrystalline Metals Into Alloys and Intermetallic Compounds for Applications in Catalysis. *J. Mater. Chem.* **2008**, *18*, 275−282.
(156) Chen, L.; Zhu, J.; Xuan, C.; Xiao, W.; Xia, K.; Xia, W.; Lai, C.; Xin, H. L.; Wang, D. Effects of Crystal Phase and Composition on Structurally Ordered Pt−Co−Ni/C Ternary Intermetallic Electrocatalysts for the Formic Acid Oxidation Reaction. *J. Mater. Chem. A* **2018**, *6*, 5848−5855.
(157) Chung, D. Y.; Jun, S. W.; Yoon, G.; Kwon, S. G.; Shin, D. Y.; Seo, P.; Yoo, J. M.; Shin, H.; Chung, Y.-H.; Kim, H.; Mun, B. S.; Lee, K.-S.; Lee, N.-S.; Yoo, S. J.; Lim, D.-H.; Kang, K.; Sung, Y.-E.; Hyeon, T. Highly Durable and Active PtFe Nanocatalyst for Electrochemical Oxygen Reduction Reaction. *J. Am. Chem. Soc.* **2015**, *137*, 15478−15485.
(158) Dasgupta, A.; Rioux, R. M. Intermetallics in Catalysis: An Exciting Subset of Multimetallic Catalysts. Catal. *Catal. Today* **2019**, *330*, 2−15.
(159) Ji, X.; Lee, K. T.; Holden, R.; Zhang, L.; Zhang, J.; Botton, G. A.; Couillard, M.; Nazar, L. F. Nanocrystalline Intermetallics on Mesoporous Carbon for Direct Formic Acid Fuel Cell Anodes. *Nat. Chem.* **2010**, *2*, 286−293.
(160) Leonard, B. M.; Bhuvanesh, N. S. P.; Schaak, R. E. Low-Temperature Polyol Synthesis of $AuCuSn_2$ and $AuNiSn_2$: Using Solution Chemistry to Access Ternary Intermetallic Compounds as Nanocrystals. *J. Am. Chem. Soc.* **2005**, *127*, 7326−7327.
(161) Li, J.; Xi, Z.; Pan, Y.-T.; Spendelow, J. S.; Duchesne, P. N.; Su, D.; Li, Q.; Yu, C.; Yin, Z.; Shen, B.; Kim, Y. S.; Zhang, P.; Sun, S. Fe Stabilization by Intermetallic $L1_0$-FePt and Pt Catalysis Enhancement

https://dx.doi.org/10.1021/acs.chemrev.0c00436
Chem. Rev. 2021, 121, 736−795

in $L1_0$-FePt/Pt Nanoparticles for Efficient Oxygen Reduction Reaction in Fuel Cells. *J. Am. Chem. Soc.* **2018**, *140*, 2926−2932.
(162) Li, Z.; Qi, Z.; Wang, S.; Ma, T.; Zhou, L.; Wu, Z.; Luan, X.; Lin, F.-Y.; Chen, M.; Miller, J. T.; Xin, H.; Huang, W.; Wu, Y. In Situ Formed Pt_3Ti Nanoparticles on a Two-Dimensional Transition Metal Carbide (MXene) Used as Efficient Catalysts for Hydrogen Evolution Reactions. *Nano Lett.* **2019**, *19*, 5102−5108.
(163) Luo, S.; Chen, W.; Cheng, Y.; Song, X.; Wu, Q.; Li, L.; Wu, X.; Wu, T.; Li, M.; Yang, Q.; Deng, K.; Quan, Z. Trimetallic Synergy in Intermetallic PtSnBi Nanoplates Boosts Formic Acid Oxidation. *Adv. Mater.* **2019**, *31*, 1903683.
(164) Pirart, J.; Front, A.; Rapetti, D.; Andreazza-Vignolle, C.; Andreazza, P.; Mottet, C.; Ferrando, R. Reversed Size-Dependent Stabilization of Ordered Nanophases. *Nat. Commun.* **2019**, *10*, 1982.
(165) Abe, H.; Matsumoto, F.; Alden, L. R.; Warren, S. C.; Abruña, H. D.; DiSalvo, F. J. Electrocatalytic Performance of Fuel Oxidation by Pt_3Ti Nanoparticles. *J. Am. Chem. Soc.* **2008**, *130*, 5452−5458.
(166) Cui, Z.; Chen, H.; Zhao, M.; Marshall, D.; Yu, Y.; Abruña, H.; DiSalvo, F. J. Synthesis of Structurally Ordered Pt_3Ti and Pt_3V Nanoparticles as Methanol Oxidation Catalysts. *J. Am. Chem. Soc.* **2014**, *136*, 10206−10209.
(167) Kang, Y.; Murray, C. B. Synthesis and Electrocatalytic Properties of Cubic Mn−Pt Nanocrystals (Nanocubes). *J. Am. Chem. Soc.* **2010**, *132*, 7568−7569.
(168) Wang, D.; Xin, H. L.; Hovden, R.; Wang, H.; Yu, Y.; Muller, D. A.; DiSalvo, F. J.; Abruña, H. D. Structurally Ordered Intermetallic Platinum−Cobalt Core−Shell Nanoparticles with Enhanced Activity and Stability as Oxygen Reduction Electrocatalysts. *Nat. Mater.* **2013**, *12*, 81−87.
(169) Chen, H.; Wang, D.; Yu, Y.; Newton, K. A.; Muller, D. A.; Abruña, H.; DiSalvo, F. J. A Surfactant-Free Strategy for Synthesizing and Processing Intermetallic Platinum-Based Nanoparticle Catalysts. *J. Am. Chem. Soc.* **2012**, *134*, 18453−18459.
(170) Leonard, B. M.; Zhou, Q.; Wu, D.; DiSalvo, F. J. Facile Synthesis of PtNi Intermetallic Nanoparticles: Influence of Reducing Agent and Precursors on Electrocatalytic Activity. *Chem. Mater.* **2011**, *23*, 1136−1146.
(171) Wang, D.; Yu, Y.; Xin, H. L.; Hovden, R.; Ercius, P.; Mundy, J. A.; Chen, H.; Richard, J. H.; Muller, D. A.; DiSalvo, F. J.; Abruña, H. D. Tuning Oxygen Reduction Reaction Activity via Controllable Dealloying: A Model Study of Ordered Cu_3Pt/C Intermetallic Nanocatalysts. *Nano Lett.* **2012**, *12*, 5230−5238.
(172) Chen, Q.; Zhang, J.; Jia, Y.; Jiang, Z.; Xie, Z.; Zheng, L. Wet Chemical Synthesis of Intermetallic Pt_3Zn Nanocrystals via Weak Reduction Reaction together with UPD Process and Their Excellent Electrocatalytic Performances. *Nanoscale* **2014**, *6*, 7019−7024.
(173) Kang, Y.; Pyo, J. B.; Ye, X.; Gordon, T. R.; Murray, C. B. Synthesis, Shape Control, and Methanol Electro-Oxidation Properties of Pt−Zn Alloy and Pt_3Zn Intermetallic Nanocrystals. *ACS Nano* **2012**, *6*, 5642−5647.
(174) Miura, A.; Wang, H.; Leonard, B. M.; Abruña, H. D.; DiSalvo, F. J. Synthesis of Intermetallic PtZn Nanoparticles by Reaction of Pt Nanoparticles with Zn Vapor and Their Application as Fuel Cell Catalysts. *Chem. Mater.* **2009**, *21*, 2661−2667.
(175) Wang, X.; Altmann, L.; Stöver, J.; Zielasek, V.; Bäumer, M.; Al-Shamery, K.; Borchert, H.; Parisi, J.; Kolny-Olesiak, J. Pt/Sn Intermetallic, Core/Shell and Alloy Nanoparticles: Colloidal Synthesis and Structural Control. *Chem. Mater.* **2013**, *25*, 1400−1407.
(176) Xiong, Y.; Yang, Y.; DiSalvo, F. J.; Abruña, H. D. Pt-Decorated Composition-Tunable Pd−Fe@Pd/C Core−Shell Nanoparticles with Enhanced Electrocatalytic Activity toward the Oxygen Reduction Reaction. *J. Am. Chem. Soc.* **2018**, *140*, 7248−7255.
(177) Kuttiyiel, K. A.; Sasaki, K.; Su, D.; Wu, L.; Zhu, Y.; Adzic, R. R. Gold-Promoted Structurally Ordered Intermetallic Palladium Cobalt Nanoparticles for the Oxygen Reduction Reaction. *Nat. Commun.* **2014**, *5*, 5185.
(178) Cable, R. E.; Schaak, R. E. Solution Synthesis of Nanocrystalline M−Zn (M = Pd, Au, Cu) Intermetallic Compounds via Chemical Conversion of Metal Nanoparticle Precursors. *Chem. Mater.* **2007**, *19*, 4098−4104.
(179) Gunji, T.; Noh, S. H.; Tanabe, T.; Han, B.; Nien, C. Y.; Ohsaka, T.; Matsumoto, F. Enhanced Electrocatalytic Activity of Carbon-Supported Ordered Intermetallic Palladium−Lead (Pd_3Pb) Nanoparticles toward Electrooxidation of Formic Acid. *Chem. Mater.* **2017**, *29*, 2906−2913.
(180) Chen, W.; Yu, R.; Li, L.; Wang, A.; Peng, Q.; Li, Y. A Seed-Based Diffusion Route to Monodisperse Intermetallic CuAu Nanocrystals. *Angew. Chem., Int. Ed.* **2010**, *49*, 2917−2921.
(181) Wang, G.; Huang, B.; Xiao, L.; Ren, Z.; Chen, H.; Wang, D.; Abruña, H. D.; Lu, J.; Zhuang, L. Pt Skin on AuCu Intermetallic Substrate: A Strategy to Maximize Pt Utilization for Fuel Cells. *J. Am. Chem. Soc.* **2014**, *136*, 9643−9649.
(182) Sra, A. K.; Schaak, R. E. Synthesis of Atomically Ordered AuCu and $AuCu_3$ Nanocrystals from Bimetallic Nanoparticle Precursors. *J. Am. Chem. Soc.* **2004**, *126*, 6667−6672.
(183) Köhler, D.; Heise, M.; Baranov, A. I.; Luo, Y.; Geiger, D.; Ruck, M.; Armbrüster, M. Synthesis of BiRh Nanoplates with Superior Catalytic Performance in the Semihydrogenation of Acetylene. *Chem. Mater.* **2012**, *24*, 1639−1644.
(184) Vasquez, Y.; Luo, Z.; Schaak, R. E. Low-Temperature Solution Synthesis of the Non-Equilibrium Ordered Intermetallic Compounds Au_3Fe, Au_3Co, and Au_3Ni as Nanocrystals. *J. Am. Chem. Soc.* **2008**, *130*, 11866−11867.
(185) Wang, Y.; He, J.; Liu, C.; Chong, W. H.; Chen, H. Thermodynamics versus Kinetics in Nanosynthesis. *Angew. Chem., Int. Ed.* **2015**, *54*, 2022−2051.
(186) Peng, Z.; Yang, H. Designer Platinum Nanoparticles: Control of Shape, Composition in Alloy, Nanostructure and Electrocatalytic Property. *Nano Today* **2009**, *4*, 143−164.
(187) Ferrando, R.; Jellinek, J.; Johnston, R. L. Nanoalloys: From Theory to Applications of Alloy Clusters and Nanoparticles. *Chem. Rev.* **2008**, *108*, 845−910.
(188) Zhang, H.; Jin, M.; Xia, Y. Enhancing the Catalytic and Electrocatalytic Properties of Pt-Based Catalysts by Forming Bimetallic Nanocrystals with Pd. *Chem. Soc. Rev.* **2012**, *41*, 8035−8049.
(189) Zhang, L.; Doyle-Davis, K.; Sun, X. Pt-Based Electrocatalysts with High Atom Utilization Efficiency: from Nanostructures to Single Atoms. *Energy Environ. Sci.* **2019**, *12*, 492−517.
(190) Zhao, Z.; Chen, C.; Liu, Z.; Huang, J.; Wu, M.; Liu, H.; Li, Y.; Huang, Y. Pt-Based Nanocrystal for Electrocatalytic Oxygen Reduction. *Adv. Mater.* **2019**, *31*, 1808115.
(191) Liao, H.; Fisher, A.; Xu, Z. J. Surface Segregation in Bimetallic Nanoparticles: A Critical Issue in Electrocatalyst Engineering. *Small* **2015**, *11*, 3221−3246.
(192) Luo, M.; Sun, Y.; Zhang, X.; Qin, Y.; Li, M.; Li, Y.; Li, C.; Yang, Y.; Wang, L.; Gao, P.; Lu, G.; Guo, S. Stable High-Index Faceted Pt Skin on Zigzag-Like PtFe Nanowires Enhances Oxygen Reduction Catalysis. *Adv. Mater.* **2018**, *30*, 1705515.
(193) Ruban, A. V.; Skriver, H. L.; Nørskov, J. K. Surface Segregation Energies in Transition-Metal Alloys. *Phys. Rev. B: Condens. Matter Mater. Phys.* **1999**, *59*, 15990−16000.
(194) Wang, G.; Guan, J.; Xiao, L.; Huang, B.; Wu, N.; Lu, J.; Zhuang, L. Pd Skin on AuCu Intermetallic Nanoparticles: A Highly Active Electrocatalyst for Oxygen Reduction Reaction in Alkaline Media. *Nano Energy* **2016**, *29*, 268−274.
(195) Wang, H.; Shang, P.; Zhang, J.; Guo, M.; Mu, Y.; Li, Q.; Wang, H. One-Step Synthesis of High-Coercivity $L1_0$-FePtAg Nanoparticles: Effects of Ag on the Morphology and Chemical Ordering of FePt Nanoparticles. *Chem. Mater.* **2013**, *25*, 2450−2454.
(196) Avrami, M. Kinetics of Phase Change. I General Theory. *J. Chem. Phys.* **1939**, *7*, 1103−1112.
(197) Avrami, M. Kinetics of Phase Change. II Transformation-Time Relations for Random Distribution of Nuclei. *J. Chem. Phys.* **1940**, *8*, 212−224.
(198) Avrami, M. Granulation, Phase Change, and Microstructure Kinetics of Phase Change. III. *J. Chem. Phys.* **1941**, *9*, 177−184.

https://dx.doi.org/10.1021/acs.chemrev.0c00436
Chem. Rev. 2021, 121, 736−795

(199) Xia, Y.; Xia, X.; Peng, H.-C. Shape-Controlled Synthesis of Colloidal Metal Nanocrystals: Thermodynamic versus Kinetic Products. *J. Am. Chem. Soc.* **2015**, *137*, 7947−7966.
(200) Ngai, K. L.; Magill, J. H.; Plazek, D. J. Flow, Diffusion and Crystallization of Supercooled Liquids: Revisited. *J. Chem. Phys.* **2000**, *112*, 1887−1892.
(201) Guisbiers, G.; Mejia-Rosales, S.; Khanal, S.; Ruiz-Zepeda, F.; Whetten, R. L.; José-Yacaman, M. Gold−Copper Nano-Alloy, "Tumbaga", in the Era of Nano: Phase Diagram and Segregation. *Nano Lett.* **2014**, *14*, 6718−6726.
(202) Wang, G.; Xiao, L.; Huang, B.; Ren, Z.; Tang, X.; Zhuang, L.; Lu, J. AuCu Intermetallic Nanoparticles: Surfactant-Free Synthesis and Novel Electrochemistry. *J. Mater. Chem.* **2012**, *22*, 15769−15774.
(203) Zhang, N.; Chen, X.; Lu, Y.; An, L.; Li, X.; Xia, D.; Zhang, Z.; Li, J. Nano-Intermetallic $AuCu_3$ Catalyst for Oxygen Reduction Reaction: Performance and Mechanism. *Small* **2014**, *10*, 2662−2669.
(204) Zhang, N.; Yan, H.; Chen, X.; An, L.; Xia, Z.; Xia, D. Origins for the Synergetic Effects of $AuCu_3$ in Catalysis for Oxygen Reduction Reaction. *J. Phys. Chem. C* **2015**, *119*, 907−912.
(205) Zhang, S.; Guo, S.; Zhu, H.; Su, D.; Sun, S. Structure-Induced Enhancement in Electrooxidation of Trimetallic FePtAu Nanoparticles. *J. Am. Chem. Soc.* **2012**, *134*, 5060−5063.
(206) Zhang, S.; Qi, W.; Huang, B. Size Effect on Order-Disorder Transition Kinetics of FePt Nanoparticles. *J. Chem. Phys.* **2014**, *140*, 044328.
(207) Wang, H.; Li, Y.; Chen, X.; Shu, D.; Liu, X.; Wang, X.; Zhang, J.; Wang, H.; Wang, Y.; Ruterana, P. Effect of Cu Doping on the Structure and Phase Transition of Directly Synthesized FePt Nanoparticles. *J. Magn. Magn. Mater.* **2017**, *422*, 470−474.
(208) Wang, C.; Chen, D. P.; Sang, X.; Unocic, R. R.; Skrabalak, S. E. Size-Dependent Disorder−Order Transformation in the Synthesis of Monodisperse Intermetallic PdCu Nanocatalysts. *ACS Nano* **2016**, *10*, 6345−6353.
(209) Tzitzios, V.; Basina, G.; Gjoka, M.; Boukos, N.; Niarchos, D.; Devlin, E.; Petridis, D. The Effect of Mn Doping in FePt Nanoparticles on the Magnetic Properties of the $L1_0$ Phase. *Nanotechnology* **2006**, *17*, 4270−4273.
(210) Qi, W.; Li, Y.; Xiong, S.; Lee, S.-T. Modeling Size and Shape Effects on the Order−Disorder Phase-Transition Temperature of CoPt Nanoparticles. *Small* **2010**, *6*, 1996−1999.
(211) Oezaslan, M.; Heggen, M.; Strasser, P. Size-Dependent Morphology of Dealloyed Bimetallic Catalysts: Linking the Nano to the Macro Scale. *J. Am. Chem. Soc.* **2012**, *134*, 514−524.
(212) Miyazaki, T.; Kitakami, O.; Okamoto, S.; Shimada, Y.; Akase, Z.; Murakami, Y.; Shindo, D.; Takahashi, Y. K.; Hono, K. Size Effect on the Ordering of $L1_0$ FePt Nanoparticles. *Phys. Rev. B: Condens. Matter Mater. Phys.* **2005**, *72*, 144419.
(213) Magno, L. M.; Sigle, W.; van Aken, P. A.; Angelescu, D.; Stubenrauch, C. Size Control of PtPb Intermetallic Nanoparticles Prepared via Microemulsions. *Phys. Chem. Chem. Phys.* **2011**, *13*, 9134−9136.
(214) Kim, S.-I.; Eom, G.; Kang, M.; Kang, T.; Lee, H.; Hwang, A.; Yang, H.; Kim, B. Composition-Selective Fabrication of Ordered Intermetallic Au−Cu Nanowires and Their Application to Nano-Size Electrochemical Glucose Detection. *Nanotechnology* **2015**, *26*, 245702.
(215) Gatalo, M.; Jovanovič, P.; Polymeros, G.; Grote, J.-P.; Pavlišič, A.; Ruiz- Zepeda, F.; Šelih, V. S.; Šala, M.; Hočevar, S.; Bele, M.; Mayrhofer, K. J. J.; Hodnik, N.; Gaberšček, M. Positive Effect of Surface Doping with Au on the Stability of Pt-Based Electrocatalysts. *ACS Catal.* **2016**, *6*, 1630−1634.
(216) Dai, Z. R.; Sun, S.; Wang, Z. L. Phase Transformation, Coalescence, and Twinning of Monodisperse FePt Nanocrystals. *Nano Lett.* **2001**, *1*, 443−447.
(217) Alayoglu, S.; Eichhorn, B. Rh−Pt Bimetallic Catalysts: Synthesis, Characterization, and Catalysis of Core−Shell, Alloy, and Monometallic Nanoparticles. *J. Am. Chem. Soc.* **2008**, *130*, 17479−17486.
(218) Asset, T.; Chattot, R.; Fontana, M.; Mercier-Guyon, B.; Job, N.; Dubau, L.; Maillard, F. A Review on Recent Developments and Prospects for the Oxygen Reduction Reaction on Hollow Pt-Alloy Nanoparticles. *ChemPhysChem* **2018**, *19*, 1552−1567.
(219) Becknell, N.; Son, Y.; Kim, D.; Li, D.; Yu, Y.; Niu, Z.; Lei, T.; Sneed, B. T.; More, K. L.; Markovic, N. M.; Stamenkovic, V. R.; Yang, P. Control of Architecture in Rhombic Dodecahedral Pt−Ni Nanoframe Electrocatalysts. *J. Am. Chem. Soc.* **2017**, *139*, 11678−11681.
(220) Chen, C.; Kang, Y.; Huo, Z.; Zhu, Z.; Huang, W.; Xin, H. L.; Snyder, J. D.; Li, D.; Herron, J. A.; Mavrikakis, M.; Chi, M.; More, K. L.; Li, Y.; Markovic, N. M.; Somorjai, G. A.; Yang, P.; Stamenkovic, V. R. Highly Crystalline Multimetallic Nanoframes with Three-Dimensional Electrocatalytic Surfaces. *Science* **2014**, *343*, 1339−1343.
(221) Chen, Q.; Cao, Z.; Du, G.; Kuang, Q.; Huang, J.; Xie, Z.; Zheng, L. Excavated Octahedral Pt-Co Alloy Nanocrystals Built with Ultrathin Nanosheets as Superior Multifunctional Electrocatalysts for Energy Conversion Applications. *Nano Energy* **2017**, *39*, 582−589.
(222) Choi, S.-I.; Lee, S.-U.; Kim, W. Y.; Choi, R.; Hong, K.; Nam, K. M.; Han, S. W.; Park, J. T. Composition-Controlled PtCo Alloy Nanocubes with Tuned Electrocatalytic Activity for Oxygen Reduction. *ACS Appl. Mater. Interfaces* **2012**, *4*, 6228−6234.
(223) Dai, L.; Mo, S.; Qin, Q.; Zhao, X.; Zheng, N. Carbon Monoxide-Assisted Synthesis of Ultrathin $PtCu_3$ Alloy Wavy Nanowires and Their Enhanced Electrocatalysis. *Small* **2016**, *12*, 1572−1577.
(224) Deng, Y.-J.; Tian, N.; Zhou, Z.-Y.; Huang, R.; Liu, Z.-L.; Xiao, J.; Sun, S.-G. Alloy Tetrahexahedral Pd−Pt Catalysts: Enhancing Significantly the Catalytic Activity by Synergy Effect of High-Index Facets and Electronic Structure. *Chem. Sci.* **2012**, *3*, 1157−1161.
(225) Ding, L.-X.; Wang, A.-L.; Ou, Y.-N.; Li, Q.; Guo, R.; Zhao, W.-X.; Tong, Y.-X.; Li, G.-R. Hierarchical Pd-Sn Alloy Nanosheet Dendrites: An Economical and Highly Active Catalyst for Ethanol Electrooxidation. *Sci. Rep.* **2013**, *3*, 1181.
(226) Egeberg, A.; Dietrich, C.; Kind, C.; Popescu, R.; Gerthsen, D.; Behrens, S.; Feldmann, C. Bimetallic Nickel-Iridium and Nickel-Osmium Alloy Nanoparticles and Their Catalytic Performance in Hydrogenation Reactions. *ChemCatChem* **2017**, *9*, 3534−3543.
(227) Guo, S.; Li, D.; Zhu, H.; Zhang, S.; Markovic, N. M.; Stamenkovic, V. R.; Sun, S. FePt and CoPt Nanowires as Efficient Catalysts for the Oxygen Reduction Reaction. *Angew. Chem., Int. Ed.* **2013**, *52*, 3465−3468.
(228) Kim, C.; Dionigi, F.; Beermann, V.; Wang, X.; Möller, T.; Strasser, P. Alloy Nanocatalysts for the Electrochemical Oxygen Reduction (ORR) and the Direct Electrochemical Carbon Dioxide Reduction Reaction (CO_2RR). *Adv. Mater.* **2019**, *31*, 1805617.
(229) Lim, B.; Jiang, M.; Camargo, P. H. C.; Cho, E. C.; Tao, J.; Lu, X.; Zhu, Y.; Xia, Y. Pd-Pt Bimetallic Nanodendrites with High Activity for Oxygen Reduction. *Science* **2009**, *324*, 1302−1305.
(230) Liu, D.; Xie, M.; Wang, C.; Liao, L.; Qiu, L.; Ma, J.; Huang, H.; Long, R.; Jiang, J.; Xiong, Y. Pd-Ag Alloy Hollow Nanostructures with Interatomic Charge Polarization for Enhanced Electrocatalytic Formic Acid Oxidation. *Nano Res.* **2016**, *9*, 1590−1599.
(231) Liu, Q.; Yan, Z.; Henderson, N. L.; Bauer, J. C.; Goodman, D. W.; Batteas, J. D.; Schaak, R. E. Synthesis of CuPt Nanorod Catalysts with Tunable Lengths. *J. Am. Chem. Soc.* **2009**, *131*, 5720−5721.
(232) Liu, Y.; Chi, M.; Mazumder, V.; More, K. L.; Soled, S.; Henao, J. D.; Sun, S. Composition-Controlled Synthesis of Bimetallic PdPt Nanoparticles and Their Electro-oxidation of Methanol. *Chem. Mater.* **2011**, *23*, 4199−4203.
(233) Ortiz, N.; Weiner, R. G.; Skrabalak, S. E. Ligand-Controlled Co-reduction versus Electroless Co-deposition: Synthesis of Nanodendrites with Spatially Defined Bimetallic Distributions. *ACS Nano* **2014**, *8*, 12461−12467.
(234) Sun, X.; Qin, D. Co-Titration of $AgNO_3$ and $HAuCl_4$: A New Route to the Synthesis of Ag@Ag−Au Core−Frame Nanocubes with Enhanced Plasmonic and Catalytic Properties. *J. Mater. Chem. C* **2015**, *3*, 11833−11841.

https://dx.doi.org/10.1021/acs.chemrev.0c00436
Chem. Rev. 2021, 121, 736−795

(235) Cargnello, M.; Agarwal, R.; Klein, D. R.; Diroll, B. T.; Agarwal, R.; Murray, C. B. Uniform Bimetallic Nanocrystals by High-Temperature Seed-Mediated Colloidal Synthesis and Their Catalytic Properties for Semiconducting Nanowire Growth. *Chem. Mater.* **2015**, *27*, 5833−5838.
(236) Chatterjee, D.; Shetty, S.; Müller-Caspary, K.; Grieb, T.; Krause, F. F.; Schowalter, M.; Rosenauer, A.; Ravishankar, N. Ultrathin Au-Alloy Nanowires at the Liquid−Liquid Interface. *Nano Lett.* **2018**, *18*, 1903−1907.
(237) Kunz, M. R.; McClain, S. M.; Chen, D. P.; Koczkur, K. M.; Weiner, R. G.; Skrabalak, S. E. Seed-Mediated Co-Reduction in a Large Lattice Mismatch System: Synthesis of Pd−Cu Nanostructures. *Nanoscale* **2017**, *9*, 7570−7576.
(238) Zhu, X.; Yip, H. K.; Zhuo, X.; Jiang, R.; Chen, J.; Zhu, X.-M.; Yang, Z.; Wang, J. Realization of Red Plasmon Shifts up to ∼ 900 nm by AgPd-Tipping Elongated Au Nanocrystals. *J. Am. Chem. Soc.* **2017**, *139*, 13837−13846.
(239) Sun, S. Recent Advances in Chemical Synthesis, Self-Assembly, and Applications of FePt Nanoparticles. *Adv. Mater.* **2006**, *18*, 393−403.
(240) Chen, M.; Kim, J.; Liu, J. P.; Fan, H.; Sun, S. Synthesis of FePt Nanocubes and Their Oriented Self-Assembly. *J. Am. Chem. Soc.* **2006**, *128*, 7132−7133.
(241) Skrabalak, S. E.; Chen, J.; Sun, Y.; Lu, X.; Au, L.; Cobley, C. M.; Xia, Y. Gold Nanocages: Synthesis, Properties, and Applications. *Acc. Chem. Res.* **2008**, *41*, 1587−1595.
(242) Yang, Y.; Zhang, Q.; Fu, Z.-W.; Qin, D. Transformation of Ag Nanocubes into Ag−Au Hollow Nanostructures with Enriched Ag Contents to Improve SERS Activity and Chemical Stability. *ACS Appl. Mater. Interfaces* **2014**, *6*, 3750−3757.
(243) Huang, X.; Zhang, H.; Guo, C.; Zhou, Z.; Zheng, N. Simplifying the Creation of Hollow Metallic Nanostructures: One-Pot Synthesis of Hollow Palladium/Platinum Single-Crystalline Nanocubes. *Angew. Chem., Int. Ed.* **2009**, *48*, 4808−4812.
(244) Xu, L.; Luo, Z.; Fan, Z.; Yu, S.; Chen, J.; Liao, Y.; Xue, C. Controllable Galvanic Synthesis of Triangular Ag−Pd Alloy Nanoframes for Efficient Electrocatalytic Methanol Oxidation. *Chem. - Eur. J.* **2015**, *21*, 8691−8695.
(245) González, E.; Arbiol, J.; Puntes, V. F. Carving at the Nanoscale: Sequential Galvanic Exchange and Kirkendall Growth at Room Temperature. *Science* **2011**, *334*, 1377−1380.
(246) Wu, Y.; Wang, D.; Niu, Z.; Chen, P.; Zhou, G.; Li, Y. A Strategy for Designing a Concave Pt−Ni Alloy through Controllable Chemical Etching. *Angew. Chem., Int. Ed.* **2012**, *51*, 12524−12528.
(247) Lu, Y.; Chen, W. PdAg Alloy Nanowires: Facile One-Step Synthesis and High Electrocatalytic Activity for Formic Acid Oxidation. *ACS Catal.* **2012**, *2*, 84−90.
(248) Shi, L.; Wang, A.; Zhang, T.; Zhang, B.; Su, D.; Li, H.; Song, Y. One-Step Synthesis of Au−Pd Alloy Nanodendrites and Their Catalytic Activity. *J. Phys. Chem. C* **2013**, *117*, 12526−12536.
(249) Xia, B. Y.; Wu, H. B.; Li, N.; Yan, Y.; Lou, X. W.; Wang, X. One-Pot Synthesis of Pt−Co Alloy Nanowire Assemblies with Tunable Composition and Enhanced Electrocatalytic Properties. *Angew. Chem., Int. Ed.* **2015**, *54*, 3797−3801.
(250) Yang, P.; Jin, S.-Y.; Xu, Q.-Z.; Yu, S.-H. Decorating PtCo Bimetallic Alloy Nanoparticles on Graphene as Sensors for Glucose Detection by Catalyzing Luminol Chemiluminescence. *Small* **2013**, *9*, 199−204.
(251) You, H.; Fang, J. Particle-Mediated Nucleation and Growth of Solution-Synthesized Metal Nanocrystals: A New Story beyond the LaMer Curve. *Nano Today* **2016**, *11*, 145−167.
(252) LaMer, V. K.; Dinegar, R. H. Theory, Production and Mechanism of Formation of Monodispersed Hydrosols. *J. Am. Chem. Soc.* **1950**, *72*, 4847−4854.
(253) Zhu, C.; Guo, S.; Dong, S. PdM (M = Pt, Au) Bimetallic Alloy Nanowires with Enhanced Electrocatalytic Activity for Electro-Oxidation of Small Molecules. *Adv. Mater.* **2012**, *24*, 2326−2331.
(254) Zhou, M.; Wang, H.; Vara, M.; Hood, Z. D.; Luo, M.; Yang, T.-H.; Bao, S.; Chi, M.; Xiao, P.; Zhang, Y.; Xia, Y. Quantitative Analysis of the Reduction Kinetics Responsible for the One-Pot Synthesis of Pd−Pt Bimetallic Nanocrystals with Different Structures. *J. Am. Chem. Soc.* **2016**, *138*, 12263−12270.
(255) Wang, L.; Yamauchi, Y. Controlled Aqueous Solution Synthesis of Platinum−Palladium Alloy Nanodendrites with Various Compositions Using Amphiphilic Triblock Copolymers. *Chem. - Asian J.* **2010**, *5*, 2493−2498.
(256) Wang, C.; Markovic, N. M.; Stamenkovic, V. R. Advanced Platinum Alloy Electrocatalysts for the Oxygen Reduction Reaction. *ACS Catal.* **2012**, *2*, 891−898.
(257) Huang, X.; Li, Y.; Li, Y.; Zhou, H.; Duan, X.; Huang, Y. Synthesis of PtPd Bimetal Nanocrystals with Controllable Shape, Composition, and Their Tunable Catalytic Properties. *Nano Lett.* **2012**, *12*, 4265−4270.
(258) Wu, J.; Gross, A.; Yang, H. Shape and Composition-Controlled Platinum Alloy Nanocrystals Using Carbon Monoxide as Reducing Agent. *Nano Lett.* **2011**, *11*, 798−802.
(259) Wang, C.; Yin, H.; Chan, R.; Peng, S.; Dai, S.; Sun, S. One-Pot Synthesis of Oleylamine Coated AuAg Alloy NPs and Their Catalysis for CO Oxidation. *Chem. Mater.* **2009**, *21*, 433−435.
(260) Liu, Y.; Wei, M.; Raciti, D.; Wang, Y.; Hu, P.; Park, J. H.; Barclay, M.; Wang, C. Electro-Oxidation of Ethanol Using Pt_3Sn Alloy Nanoparticles. *ACS Catal.* **2018**, *8*, 10931−10937.
(261) Wu, J.; Zhang, J.; Peng, Z.; Yang, S.; Wagner, F. T.; Yang, H. Truncated Octahedral Pt_3Ni Oxygen Reduction Reaction Electrocatalysts. *J. Am. Chem. Soc.* **2010**, *132*, 4984−4985.
(262) Zhang, J.; Yang, H.; Fang, J.; Zou, S. Synthesis and Oxygen Reduction Activity of Shape-Controlled Pt_3Ni Nanopolyhedra. *Nano Lett.* **2010**, *10*, 638−644.
(263) Mallin, M. P.; Murphy, C. J. Solution-Phase Synthesis of Sub-10 nm Au−Ag Alloy Nanoparticles. *Nano Lett.* **2002**, *2*, 1235−1237.
(264) Lv, F.; Zhang, W.; Yang, W.; Feng, J.; Wang, K.; Zhou, J.; Zhou, P.; Guo, S. Ir-Based Alloy Nanoflowers with Optimized Hydrogen Binding Energy as Bifunctional Electrocatalysts for Overall Water Splitting. *Small Methods* **2020**, *4*, 1900129.
(265) Mazumder, V.; Chi, M.; Mankin, M. N.; Liu, Y.; Metin, Ö.; Sun, D.; More, K. L.; Sun, S. A Facile Synthesis of MPd (M = Co, Cu) Nanoparticles and Their Catalysis for Formic Acid Oxidation. *Nano Lett.* **2012**, *12*, 1102−1106.
(266) Menghuan, C.; Zhou, L.; Di, L.; Yue, L.; Honghui, N.; Yaxi, P.; Hongkun, X.; Weiwei, P.; Shuren, Z. RuCo Bimetallic Alloy Nanoparticles Immobilized on Multi-Porous MIL-53(Al) as a Highly Efficient Catalyst for the Hydrolytic Reaction of Ammonia Borane. *Int. J. Hydrogen Energy* **2018**, *43*, 1439−1450.
(267) Motl, N. E.; Smith, A. F.; DeSantis, C. J.; Skrabalak, S. E. Engineering Plasmonic Metal Colloids through Composition and Structural Design. *Chem. Soc. Rev.* **2014**, *43*, 3823−3834.
(268) Nugroho, F. A. A.; Iandolo, B.; Wagner, J. B.; Langhammer, C. Bottom-Up Nanofabrication of Supported Noble Metal Alloy Nanoparticle Arrays for Plasmonics. *ACS Nano* **2016**, *10*, 2871−2879.
(269) Park, J. Y.; Zhang, Y.; Grass, M.; Zhang, T.; Somorjai, G. A. Tuning of Catalytic CO Oxidation by Changing Composition of Rh−Pt Bimetallic Nanoparticles. *Nano Lett.* **2008**, *8*, 673−677.
(270) Shevchenko, E. V.; Talapin, D. V.; Rogach, A. L.; Kornowski, A.; Haase, M.; Weller, H. Colloidal Synthesis and Self-Assembly of $CoPt_3$ Nanocrystals. *J. Am. Chem. Soc.* **2002**, *124*, 11480−11485.
(271) Wang, F.; Kusada, K.; Wu, D.; Yamamoto, T.; Toriyama, T.; Matsumura, S.; Nanba, Y.; Koyama, M.; Kitagawa, H. Solid-Solution Alloy Nanoparticles of the Immiscible Iridium−Copper System with a Wide Composition Range for Enhanced Electrocatalytic Applications. *Angew. Chem., Int. Ed.* **2018**, *57*, 4505−4509.
(272) Wu, J.; Qi, L.; You, H.; Gross, A.; Li, J.; Yang, H. Icosahedral Platinum Alloy Nanocrystals with Enhanced Electrocatalytic Activities. *J. Am. Chem. Soc.* **2012**, *134*, 11880−11883.
(273) Xu, J.; White, T.; Li, P.; He, C.; Yu, J.; Yuan, W.; Han, Y.-F. Biphasic Pd−Au Alloy Catalyst for Low-Temperature CO Oxidation. *J. Am. Chem. Soc.* **2010**, *132*, 10398−10406.
(274) Xue, S.; Deng, W.; Yang, F.; Yang, J.; Amiinu, I. S.; He, D.; Tang, H.; Mu, S. Hexapod PtRuCu Nanocrystalline Alloy for Highly

https://dx.doi.org/10.1021/acs.chemrev.0c00436
Chem. Rev. 2021, 121, 736−795

Efficient and Stable Methanol Oxidation. *ACS Catal.* **2018**, *8*, 7578−7584.
(275) Hsu, S.-C.; Chuang, Y.-C.; Sneed, B. T.; Cullen, D. A.; Chiu, T.-W.; Kuo, C.-H. Turning the Halide Switch in the Synthesis of Au−Pd Alloy and Core−Shell Nanoicosahedra with Terraced Shells: Performance in Electrochemical and Plasmon-Enhanced Catalysis. *Nano Lett.* **2016**, *16*, 5514−5520.
(276) Xu, D.; Bliznakov, S.; Liu, Z.; Fang, J.; Dimitrov, N. Composition-Dependent Electrocatalytic Activity of Pt-Cu Nanocube Catalysts for Formic Acid Oxidation. *Angew. Chem., Int. Ed.* **2010**, *49*, 1282−1285.
(277) Yin, A.-X.; Min, X.-Q.; Zhang, Y.-W.; Yan, C.-H. Shape-Selective Synthesis and Facet-Dependent Enhanced Electrocatalytic Activity and Durability of Monodisperse Sub-10 nm Pt−Pd Tetrahedrons and Cubes. *J. Am. Chem. Soc.* **2011**, *133*, 3816−3819.
(278) Han, Y.; Wu, S.; Dai, E.; Ye, Y.; Liu, J.; Tian, Z.; Cai, Y.; Zhu, X.; Liang, C. Laser-Irradiation-Induced Melting and Reduction Reaction for the Formation of Pt-Based Bimetallic Alloy Particles in Liquids. *ChemPhysChem* **2017**, *18*, 1133−1139.
(279) García, S.; Zhang, L.; Piburn, G. W.; Henkelman, G.; Humphrey, S. M. Microwave Synthesis of Classically Immiscible Rhodium−Silver and Rhodium−Gold Alloy Nanoparticles: Highly Active Hydrogenation Catalysts. *ACS Nano* **2014**, *8*, 11512−11521.
(280) Ksar, F.; Ramos, L.; Keita, B.; Nadjo, L.; Beaunier, P.; Remita, H. Bimetallic Palladium−Gold Nanostructures: Application in Ethanol Oxidation. *Chem. Mater.* **2009**, *21*, 3677−3683.
(281) Xu, H.; Zeiger, B. W.; Suslick, K. S. Sonochemical Synthesis of Nanomaterials. *Chem. Soc. Rev.* **2013**, *42*, 2555−2567.
(282) Bang, J. H.; Suslick, K. S. Applications of Ultrasound to the Synthesis of Nanostructured Materials. *Adv. Mater.* **2010**, *22*, 1039−1059.
(283) Vinodgopal, K.; He, Y.; Ashokkumar, M.; Grieser, F. Sonochemically Prepared Platinum−Ruthenium Bimetallic Nanoparticles. *J. Phys. Chem. B* **2006**, *110*, 3849−3852.
(284) Abdelsayed, V.; Aljarash, A.; El-Shall, M. S.; Al Othman, Z. A.; Alghamdi, A. H. Microwave Synthesis of Bimetallic Nanoalloys and CO Oxidation on Ceria-Supported Nanoalloys. *Chem. Mater.* **2009**, *21*, 2825−2834.
(285) Zhang, Z.; Nenoff, T. M.; Huang, J. Y.; Berry, D. T.; Provencio, P. P. Room Temperature Synthesis of Thermally Immiscible Ag−Ni Nanoalloys. *J. Phys. Chem. C* **2009**, *113*, 1155−1159.
(286) Sakamoto, M.; Fujistuka, M.; Majima, T. Light as a Construction Tool of Metal Nanoparticles: Synthesis and Mechanism. *J. Photochem. Photobiol., C* **2009**, *10*, 33−56.
(287) Ghosh Chaudhuri, R.; Paria, S. Core/Shell Nanoparticles: Classes, Properties, Synthesis Mechanisms, Characterization, and Applications. *Chem. Rev.* **2012**, *112*, 2373−2433.
(288) Habas, S. E.; Lee, H.; Radmilovic, V.; Somorjai, G. A.; Yang, P. Shaping Binary Metal Nanocrystals through Epitaxial Seeded Growth. *Nat. Mater.* **2007**, *6*, 692−697.
(289) Xie, S.; Choi, S.-I.; Lu, N.; Roling, L. T.; Herron, J. A.; Zhang, L.; Park, J.; Wang, J.; Kim, M. J.; Xie, Z.; Mavrikakis, M.; Xia, Y. Atomic Layer-by-Layer Deposition of Pt on Pd Nanocubes for Catalysts with Enhanced Activity and Durability toward Oxygen Reduction. *Nano Lett.* **2014**, *14*, 3570−3576.
(290) Zeng, J.; Zhu, C.; Tao, J.; Jin, M.; Zhang, H.; Li, Z.-Y.; Zhu, Y.; Xia, Y. Controlling the Nucleation and Growth of Silver on Palladium Nanocubes by Manipulating the Reaction Kinetics. *Angew. Chem., Int. Ed.* **2012**, *51*, 2354−2358.
(291) Lv, T.; Yang, X.; Zheng, Y.; Huang, H.; Zhang, L.; Tao, J.; Pan, L.; Xia, Y. Controlling the Growth of Au on Icosahedral Seeds of Pd by Manipulating the Reduction Kinetics. *J. Phys. Chem. C* **2016**, *120*, 20768−20774.
(292) Lim, B.; Xia, Y. Metal Nanocrystals with Highly Branched Morphologies. *Angew. Chem., Int. Ed.* **2011**, *50*, 76−85.
(293) Liu, X.; Liu, X. Bimetallic Nanoparticles: Kinetic Control Matters. *Angew. Chem., Int. Ed.* **2012**, *51*, 3311−3313.
(294) Lohse, S. E.; Burrows, N. D.; Scarabelli, L.; Liz-Marzán, L. M.; Murphy, C. J. Anisotropic Noble Metal Nanocrystal Growth: The Role of Halides. *Chem. Mater.* **2014**, *26*, 34−43.
(295) Rioux, D.; Meunier, M. Seeded Growth Synthesis of Composition and Size-Controlled Gold−Silver Alloy Nanoparticles. *J. Phys. Chem. C* **2015**, *119*, 13160−13168.
(296) DeSantis, C. J.; Sue, A. C.; Bower, M. M.; Skrabalak, S. E. Seed-Mediated Co-reduction: A Versatile Route to Architecturally Controlled Bimetallic Nanostructures. *ACS Nano* **2012**, *6*, 2617−2628.
(297) Hong, J. W.; Kim, M.; Kim, Y.; Han, S. W. Trisoctahedral Au−Pd Alloy Nanocrystals with High-Index Facets and Their Excellent Catalytic Performance. *Chem. - Eur. J.* **2012**, *18*, 16626−16630.
(298) Liu, H.-l.; Nosheen, F.; Wang, X. Noble Metal Alloy Complex Nanostructures: Controllable Synthesis and Their Electrochemical Property. *Chem. Soc. Rev.* **2015**, *44*, 3056−3078.
(299) Xia, Y.; Gilroy, K. D.; Peng, H.-C.; Xia, X. Seed-Mediated Growth of Colloidal Metal Nanocrystals. *Angew. Chem., Int. Ed.* **2017**, *56*, 60−95.
(300) Han, L.; Cui, P.; He, H.; Liu, H.; Peng, Z.; Yang, J. A Seed-Mediated Approach to the Morphology-Controlled Synthesis of Bimetallic Copper−Platinum Alloy Nanoparticles with Enhanced Electrocatalytic Performance for the Methanol Oxidation Reaction. *J. Power Sources* **2015**, *286*, 488−494.
(301) Huang, J.; Zhu, Y.; Lin, M.; Wang, Q.; Zhao, L.; Yang, Y.; Yao, K. X.; Han, Y. Site-Specific Growth of Au−Pd Alloy Horns on Au Nanorods: A Platform for Highly Sensitive Monitoring of Catalytic Reactions by Surface Enhancement Raman Spectroscopy. *J. Am. Chem. Soc.* **2013**, *135*, 8552−8561.
(302) Zhang, L.; Choi, S.-I.; Tao, J.; Peng, H.-C.; Xie, S.; Zhu, Y.; Xie, Z.; Xia, Y. Pd−Cu Bimetallic Tripods: A Mechanistic Understanding of the Synthesis and Their Enhanced Electrocatalytic Activity for Formic Acid Oxidation. *Adv. Funct. Mater.* **2014**, *24*, 7520−7529.
(303) Yuan, Q.; Zhou, Z.; Zhuang, J.; Wang, X. Seed Displacement, Epitaxial Synthesis of Rh/Pt Bimetallic Ultrathin Nanowires for Highly Selective Oxidizing Ethanol to CO_2. *Chem. Mater.* **2010**, *22*, 2395−2402.
(304) Shore, M. S.; Wang, J.; Johnston-Peck, A. C.; Oldenburg, A. L.; Tracy, J. B. Synthesis of Au(Core)/Ag(Shell) Nanoparticles and Their Conversion to AuAg Alloy Nanoparticles. *Small* **2011**, *7*, 230−234.
(305) Gao, C.; Hu, Y.; Wang, M.; Chi, M.; Yin, Y. Fully Alloyed Ag/Au Nanospheres: Combining the Plasmonic Property of Ag with the Stability of Au. *J. Am. Chem. Soc.* **2014**, *136*, 7474−7479.
(306) Zhou, S.; Varughese, B.; Eichhorn, B.; Jackson, G.; McIlwrath, K. Pt−Cu Core−Shell and Alloy Nanoparticles for Heterogeneous NO_x Reduction: Anomalous Stability and Reactivity of a Core−Shell Nanostructure. *Angew. Chem., Int. Ed.* **2005**, *44*, 4539−4543.
(307) Alayoglu, S.; Nilekar, A. U.; Mavrikakis, M.; Eichhorn, B. Ru−Pt Core−Shell Nanoparticles for Preferential Oxidation of Carbon Monoxide in Hydrogen. *Nat. Mater.* **2008**, *7*, 333−338.
(308) Alayoglu, S.; Zavalij, P.; Eichhorn, B.; Wang, Q.; Frenkel, A. I.; Chupas, P. Structural and Architectural Evaluation of Bimetallic Nanoparticles: A Case Study of Pt−Ru Core−Shell and Alloy Nanoparticles. *ACS Nano* **2009**, *3*, 3127−3137.
(309) Weiner, R. G.; Kunz, M. R.; Skrabalak, S. E. Seeding a New Kind of Garden: Synthesis of Architecturally Defined Multimetallic Nanostructures by Seed-Mediated Co-Reduction. *Acc. Chem. Res.* **2015**, *48*, 2688−2695.
(310) Chen, S.; Jenkins, S. V.; Tao, J.; Zhu, Y.; Chen, J. Anisotropic Seeded Growth of Cu−M (M = Au, Pt, or Pd) Bimetallic Nanorods with Tunable Optical and Catalytic Properties. *J. Phys. Chem. C* **2013**, *117*, 8924−8932.
(311) Habas, S. E.; Yang, P.; Mokari, T. Selective Growth of Metal and Binary Metal Tips on CdS Nanorods. *J. Am. Chem. Soc.* **2008**, *130*, 3294−3295.

https://dx.doi.org/10.1021/acs.chemrev.0c00436
Chem. Rev. 2021, 121, 736−795

(312) Cozzoli, P. D.; Pellegrino, T.; Manna, L. Synthesis, Properties and Perspectives of Hybrid Nanocrystal Structures. *Chem. Soc. Rev.* **2006**, *35*, 1195−1208.
(313) Cozzoli, P. D.; Manna, L. Tips on Growing Nanocrystals. *Nat. Mater.* **2005**, *4*, 801−802.
(314) Puntes, V. F.; Krishnan, K. M.; Alivisatos, A. P. Colloidal Nanocrystal Shape and Size Control: The Case of Cobalt. *Science* **2001**, *291*, 2115−2117.
(315) Wang, C.; Chi, M.; Li, D.; van der Vliet, D.; Wang, G.; Lin, Q.; Mitchell, J. F.; More, K. L.; Markovic, N. M.; Stamenkovic, V. R. Synthesis of Homogeneous Pt-Bimetallic Nanoparticles as Highly Efficient Electrocatalysts. *ACS Catal.* **2011**, *1*, 1355−1359.
(316) Wu, B.; Huang, H.; Yang, J.; Zheng, N.; Fu, G. Selective Hydrogenation of α,β-Unsaturated Aldehydes Catalyzed by Amine-Capped Platinum-Cobalt Nanocrystals. *Angew. Chem., Int. Ed.* **2012**, *51*, 3440−3443.
(317) Yang, H.; Zhang, J.; Sun, K.; Zou, S.; Fang, J. Enhancing by Weakening: Electrooxidation of Methanol on Pt_3Co and Pt Nanocubes. *Angew. Chem., Int. Ed.* **2010**, *49*, 6848−6851.
(318) Zhu, H.; Zhang, S.; Guo, S.; Su, D.; Sun, S. Synthetic Control of FePtM Nanorods (M = Cu, Ni) To Enhance the Oxygen Reduction Reaction. *J. Am. Chem. Soc.* **2013**, *135*, 7130−7133.
(319) Guo, S.; Zhang, S.; Sun, X.; Sun, S. Synthesis of Ultrathin FePtPd Nanowires and Their Use as Catalysts for Methanol Oxidation Reaction. *J. Am. Chem. Soc.* **2011**, *133*, 15354−15357.
(320) Shao, Q.; Wang, P.; Zhu, T.; Huang, X. Low Dimensional Platinum-Based Bimetallic Nanostructures for Advanced Catalysis. *Acc. Chem. Res.* **2019**, *52*, 3384−3396.
(321) Shevchenko, E. V.; Talapin, D. V.; Schnablegger, H.; Kornowski, A.; Festin, Ö.; Svedlindh, P.; Haase, M.; Weller, H. Study of Nucleation and Growth in the Organometallic Synthesis of Magnetic Alloy Nanocrystals: The Role of Nucleation Rate in Size Control of $CoPt_3$ Nanocrystals. *J. Am. Chem. Soc.* **2003**, *125*, 9090−9101.
(322) Son, S. U.; Jang, Y.; Park, J.; Na, H. B.; Park, H. M.; Yun, H. J.; Lee, J.; Hyeon, T. Designed Synthesis of Atom-Economical Pd/Ni Bimetallic Nanoparticle-Based Catalysts for Sonogashira Coupling Reactions. *J. Am. Chem. Soc.* **2004**, *126*, 5026−5027.
(323) Sun, S.; Murray, C. B.; Weller, D.; Folks, L.; Moser, A. Monodisperse FePt Nanoparticles and Ferromagnetic FePt Nanocrystal Superlattices. *Science* **2000**, *287*, 1989−1992.
(324) Chen, M.; Liu, J. P.; Sun, S. One-Step Synthesis of FePt Nanoparticles with Tunable Size. *J. Am. Chem. Soc.* **2004**, *126*, 8394−8395.
(325) Yu, Y.; Yang, W.; Sun, X.; Zhu, W.; Li, X. Z.; Sellmyer, D. J.; Sun, S. Monodisperse MPt (M = Fe, Co, Ni, Cu, Zn) Nanoparticles Prepared from a Facile Oleylamine Reduction of Metal Salts. *Nano Lett.* **2014**, *14*, 2778−2782.
(326) Rutledge, R. D.; Morris, W. H.; Wellons, M. S.; Gai, Z.; Shen, J.; Bentley, J.; Wittig, J. E.; Lukehart, C. M. Formation of FePt Nanoparticles Having High Coercivity. *J. Am. Chem. Soc.* **2006**, *128*, 14210−14211.
(327) Robinson, I.; Zacchini, S.; Tung, L. D.; Maenosono, S.; Thanh, N. T. K. Synthesis and Characterization of Magnetic Nanoalloys from Bimetallic Carbonyl Clusters. *Chem. Mater.* **2009**, *21*, 3021−3026.
(328) Mohl, M.; Dobo, D.; Kukovecz, A.; Konya, Z.; Kordas, K.; Wei, J.; Vajtai, R.; Ajayan, P. M. Formation of CuPd and CuPt Bimetallic Nanotubes by Galvanic Replacement Reaction. *J. Phys. Chem. C* **2011**, *115*, 9403−9409.
(329) Wang, D.-Y.; Chou, H.-L.; Lin, Y.-C.; Lai, F.-J.; Chen, C.-H.; Lee, J.-F.; Hwang, B.-J.; Chen, C.-C. Simple Replacement Reaction for the Preparation of Ternary $Fe_{1-x}PtRu_x$ Nanocrystals with Superior Catalytic Activity in Methanol Oxidation Reaction. *J. Am. Chem. Soc.* **2012**, *134*, 10011−10020.
(330) Zhang, H.; Jin, M.; Liu, H.; Wang, J.; Kim, M. J.; Yang, D.; Xie, Z.; Liu, J.; Xia, Y. Facile Synthesis of Pd−Pt Alloy Nanocages and Their Enhanced Performance for Preferential Oxidation of CO in Excess Hydrogen. *ACS Nano* **2011**, *5*, 8212−8222.
(331) Zhang, H.; Jin, M.; Wang, J.; Li, W.; Camargo, P. H. C.; Kim, M. J.; Yang, D.; Xie, Z.; Xia, Y. Synthesis of Pd−Pt Bimetallic Nanocrystals with a Concave Structure through a Bromide-Induced Galvanic Replacement Reaction. *J. Am. Chem. Soc.* **2011**, *133*, 6078−6089.
(332) Zhang, Q.; Xie, J.; Lee, J. Y.; Zhang, J.; Boothroyd, C. Synthesis of Ag@AgAu Metal Core/Alloy Shell Bimetallic Nanoparticles with Tunable Shell Compositions by a Galvanic Replacement Reaction. *Small* **2008**, *4*, 1067−1071.
(333) Zhou, K.; Li, Y. Catalysis Based on Nanocrystals with Well-Defined Facets. *Angew. Chem., Int. Ed.* **2012**, *51*, 602−613.
(334) Zhang, H.; Jin, M.; Xia, Y. Noble-Metal Nanocrystals with Concave Surfaces: Synthesis and Applications. *Angew. Chem., Int. Ed.* **2012**, *51*, 7656−7673.
(335) Xie, C.; Niu, Z.; Kim, D.; Li, M.; Yang, P. Surface and Interface Control in Nanoparticle Catalysis. *Chem. Rev.* **2020**, *120*, 1184−1249.
(336) Luo, S.; Shen, P. K. Concave Platinum−Copper Octopod Nanoframes Bounded with Multiple High-Index Facets for Efficient Electrooxidation Catalysis. *ACS Nano* **2017**, *11*, 11946−11953.
(337) Liu, W.; Haubold, D.; Rutkowski, B.; Oschatz, M.; Hübner, R.; Werheid, M.; Ziegler, C.; Sonntag, L.; Liu, S.; Zheng, Z.; Herrmann, A.-K.; Geiger, D.; Terlan, B.; Gemming, T.; Borchardt, L.; Kaskel, S.; Czyrska-Filemonowicz, A.; Eychmüller, A. Self-Supporting Hierarchical Porous PtAg Alloy Nanotubular Aerogels as Highly Active and Durable Electrocatalysts. *Chem. Mater.* **2016**, *28*, 6477−6483.
(338) Liu, M.; Lu, Y.; Chen, W. PdAg Nanorings Supported on Graphene Nanosheets: Highly Methanol-Tolerant Cathode Electrocatalyst for Alkaline Fuel Cells. *Adv. Funct. Mater.* **2013**, *23*, 1289−1296.
(339) Liu, H.; Liu, K.; Zhong, P.; Qi, J.; Bian, J.; Fan, Q.; Ren, K.; Zheng, H.; Han, L.; Yin, Y.; Gao, C. Ultrathin Pt−Ag Alloy Nanotubes with Regular Nanopores for Enhanced Electrocatalytic Activity. *Chem. Mater.* **2018**, *30*, 7744−7751.
(340) Lin, R.; Cai, X.; Zeng, H.; Yu, Z. Stability of High-Performance Pt-Based Catalysts for Oxygen Reduction Reactions. *Adv. Mater.* **2018**, *30*, 1705332.
(341) Hong, X.; Wang, D.; Cai, S.; Rong, H.; Li, Y. Single-Crystalline Octahedral Au−Ag Nanoframes. *J. Am. Chem. Soc.* **2012**, *134*, 18165−18168.
(342) Hong, J. W.; Kang, S. W.; Choi, B.-S.; Kim, D.; Lee, S. B.; Han, S. W. Controlled Synthesis of Pd−Pt Alloy Hollow Nanostructures with Enhanced Catalytic Activities for Oxygen Reduction. *ACS Nano* **2012**, *6*, 2410−2419.
(343) Guo, S.; Dong, S.; Wang, E. A General Method for the Rapid Synthesis of Hollow Metallic or Bimetallic Nanoelectrocatalysts with Urchinlike Morphology. *Chem. - Eur. J.* **2008**, *14*, 4689−4695.
(344) Chen, J.; Wiley, B.; McLellan, J.; Xiong, Y.; Li, Z.-Y.; Xia, Y. Optical Properties of Pd−Ag and Pt−Ag Nanoboxes Synthesized via Galvanic Replacement Reactions. *Nano Lett.* **2005**, *5*, 2058−2062.
(345) Ding, J.; Zhu, X.; Bu, L.; Yao, J.; Guo, J.; Guo, S.; Huang, X. Highly Open Rhombic Dodecahedral PtCu Nanoframes. *Chem. Commun.* **2015**, *51*, 9722−9725.
(346) Moreau, L. M.; Schurman, C. A.; Kewalramani, S.; Shahjamali, M. M.; Mirkin, C. A.; Bedzyk, M. J. How Ag Nanospheres Are Transformed into AgAu Nanocages. *J. Am. Chem. Soc.* **2017**, *139*, 12291−12298.
(347) Nosheen, F.; Anwar, T.; Siddique, A.; Hussain, N. Noble Metal Based Alloy Nanoframes: Syntheses and Applications in Fuel Cells. *Front. Chem.* **2019**, *7*, 455−456.
(348) Yang, X.; Roling, L. T.; Vara, M.; Elnabawy, A. O.; Zhao, M.; Hood, Z. D.; Bao, S.; Mavrikakis, M.; Xia, Y. Synthesis and Characterization of Pt−Ag Alloy Nanocages with Enhanced Activity and Durability toward Oxygen Reduction. *Nano Lett.* **2016**, *16*, 6644−6649.
(349) Yin, Y.; Rioux, R. M.; Erdonmez, C. K.; Hughes, S.; Somorjai, G. A.; Alivisatos, A. P. Formation of Hollow Nanocrystals Through the Nanoscale Kirkendall Effect. *Science* **2004**, *304*, 711−714.

https://dx.doi.org/10.1021/acs.chemrev.0c00436
Chem. Rev. 2021, 121, 736−795

(350) Fan, H. J.; Knez, M.; Scholz, R.; Hesse, D.; Nielsch, K.; Zacharias, M.; Gösele, U. Influence of Surface Diffusion on the Formation of Hollow Nanostructures Induced by the Kirkendall Effect: The Basic Concept. *Nano Lett.* **2007**, *7*, 993−997.
(351) Wang, W.; Dahl, M.; Yin, Y. Hollow Nanocrystals through the Nanoscale Kirkendall Effect. *Chem. Mater.* **2013**, *25*, 1179−1189.
(352) Wang, J. X.; Ma, C.; Choi, Y.; Su, D.; Zhu, Y.; Liu, P.; Si, R.; Vukmirovic, M. B.; Zhang, Y.; Adzic, R. R. Kirkendall Effect and Lattice Contraction in Nanocatalysts: A New Strategy to Enhance Sustainable Activity. *J. Am. Chem. Soc.* **2011**, *133*, 13551−13557.
(353) Tianou, H.; Wang, W.; Yang, X.; Cao, Z.; Kuang, Q.; Wang, Z.; Shan, Z.; Jin, M.; Yin, Y. Inflating Hollow Nanocrystals through a Repeated Kirkendall Cavitation Process. *Nat. Commun.* **2017**, *8*, 1261.
(354) Guria, A. K.; Prusty, G.; Patra, B. K.; Pradhan, N. Dopant-Controlled Selenization in Pd Nanocrystals: The Triggered Kirkendall Effect. *J. Am. Chem. Soc.* **2015**, *137*, 5123−5129.
(355) Chee, S. W.; Tan, S. F.; Baraissov, Z.; Bosman, M.; Mirsaidov, U. Direct Observation of the Nanoscale Kirkendall Effect during Galvanic Replacement Reactions. *Nat. Commun.* **2017**, *8*, 1224.
(356) Wang, L.; Yamauchi, Y. Metallic Nanocages: Synthesis of Bimetallic Pt−Pd Hollow Nanoparticles with Dendritic Shells by Selective Chemical Etching. *J. Am. Chem. Soc.* **2013**, *135*, 16762−16765.
(357) Wu, Y.; Sun, X.; Yang, Y.; Li, J.; Zhang, Y.; Qin, D. Enriching Silver Nanocrystals with a Second Noble Metal. *Acc. Chem. Res.* **2017**, *50*, 1774−1784.
(358) Ahn, J.; Wang, D.; Ding, Y.; Zhang, J.; Qin, D. Site-Selective Carving and Co-Deposition: Transformation of Ag Nanocubes into Concave Nanocrystals Encased by Au−Ag Alloy Frames. *ACS Nano* **2018**, *12*, 298−307.
(359) Oh, A.; Baik, H.; Choi, D. S.; Cheon, J. Y.; Kim, B.; Kim, H.; Kwon, S. J.; Joo, S. H.; Jung, Y.; Lee, K. Skeletal Octahedral Nanoframe with Cartesian Coordinates via Geometrically Precise Nanoscale Phase Segregation in a Pt@Ni Core−Shell Nanocrystal. *ACS Nano* **2015**, *9*, 2856−2867.
(360) Long, R.; Zhou, S.; Wiley, B. J.; Xiong, Y. Oxidative Etching for Controlled Synthesis of Metal Nanocrystals: Atomic Addition and Subtraction. *Chem. Soc. Rev.* **2014**, *43*, 6288−6310.
(361) Zheng, Y.; Zeng, J.; Ruditskiy, A.; Liu, M.; Xia, Y. Oxidative Etching and Its Role in Manipulating the Nucleation and Growth of Noble-Metal Nanocrystals. *Chem. Mater.* **2014**, *26*, 22−33.
(362) Gong, M.; Fu, G.; Chen, Y.; Tang, Y.; Lu, T. Autocatalysis and Selective Oxidative Etching Induced Synthesis of Platinum−Copper Bimetallic Alloy Nanodendrites Electrocatalysts. *ACS Appl. Mater. Interfaces* **2014**, *6*, 7301−7308.
(363) Kang, E.; Jung, H.; Park, J.-G.; Kwon, S.; Shim, J.; Sai, H.; Wiesner, U.; Kim, J. K.; Lee, J. Block Copolymer Directed One-Pot Simple Synthesis of $L1_0$-Phase FePt Nanoparticles inside Ordered Mesoporous Aluminosilicate/Carbon Composites. *ACS Nano* **2011**, *5*, 1018−1025.
(364) Bernal, S.; Calvino, J. J.; Gatica, J. M.; Larese, C.; López-Cartes, C.; Pérez-Omil, J. A. Nanostructural Evolution of a Pt/CeO_2 Catalyst Reduced at Increasing Temperatures (473−1223 K): A HREM Study. *J. Catal.* **1997**, *169*, 510−515.
(365) Kim, J.; Rong, C.; Liu, J. P.; Sun, S. Dispersible Ferromagnetic FePt Nanoparticles. *Adv. Mater.* **2009**, *21*, 906−909.
(366) Maligal-Ganesh, R. V.; Xiao, C.; Goh, T. W.; Wang, L.-L.; Gustafson, J.; Pei, Y.; Qi, Z.; Johnson, D. D.; Zhang, S.; Tao, F.; Huang, W. A Ship-in-a-Bottle Strategy To Synthesize Encapsulated Intermetallic Nanoparticle Catalysts: Exemplified for Furfural Hydrogenation. *ACS Catal.* **2016**, *6*, 1754−1763.
(367) Qi, Z.; Xiao, C.; Liu, C.; Goh, T. W.; Zhou, L.; Maligal-Ganesh, R.; Pei, Y.; Li, X.; Curtiss, L. A.; Huang, W. Sub-4 nm PtZn Intermetallic Nanoparticles for Enhanced Mass and Specific Activities in Catalytic Electrooxidation Reaction. *J. Am. Chem. Soc.* **2017**, *139*, 4762−4768.
(368) Maksimuk, S.; Yang, S.; Peng, Z.; Yang, H. Synthesis and Characterization of Ordered Intermetallic PtPb Nanorods. *J. Am. Chem. Soc.* **2007**, *129*, 8684−8685.
(369) Gao, Q.; Ju, Y.-M.; An, D.; Gao, M.-R.; Cui, C.-H.; Liu, J.-W.; Cong, H.-P.; Yu, S.-H. Shape-Controlled Synthesis of Monodisperse PdCu Nanocubes and Their Electrocatalytic Properties. *ChemSusChem* **2013**, *6*, 1878−1882.
(370) Kinge, S.; Gang, T.; Naber, W. J. M.; Boschker, H.; Rijnders, G.; Reinhoudt, D. N.; van der Wiel, W. G. Low-Temperature Solution Synthesis of Chemically Functional Ferromagnetic FePtAu Nanoparticles. *Nano Lett.* **2009**, *9*, 3220−3224.
(371) Chou, N. H.; Schaak, R. E. Shape-Controlled Conversion of β-Sn Nanocrystals into Intermetallic M-Sn (M = Fe, Co, Ni, Pd). *J. Am. Chem. Soc.* **2007**, *129*, 7339−7345.
(372) Chou, N. H.; Schaak, R. E. A Library of Single-Crystal Metal−Tin Nanorods: Using Diffusion as a Tool for Controlling the Morphology of Intermetallic Nanocrystals. *Chem. Mater.* **2008**, *20*, 2081−2085.
(373) Xia, B. Y.; Wu, H. B.; Wang, X.; Lou, X. W. One-Pot Synthesis of Cubic $PtCu_3$ Nanocages with Enhanced Electrocatalytic Activity for the Methanol Oxidation Reaction. *J. Am. Chem. Soc.* **2012**, *134*, 13934−13937.
(374) Rong, H.; Mao, J.; Xin, P.; He, D.; Chen, Y.; Wang, D.; Niu, Z.; Wu, Y.; Li, Y. Kinetically Controlling Surface Structure to Construct Defect-Rich Intermetallic Nanocrystals: Effective and Stable Catalysts. *Adv. Mater.* **2016**, *28*, 2540−2546.
(375) Cao, Z.; Chen, Q.; Zhang, J.; Li, H.; Jiang, Y.; Shen, S.; Fu, G.; Lu, B.-a.; Xie, Z.; Zheng, L. Platinum-Nickel Alloy Excavated Nano-Multipods with Hexagonal Close-Packed Structure and Superior Activity towards Hydrogen Evolution Reaction. *Nat. Commun.* **2017**, *8*, 15131.
(376) Reiss, B. D.; Mao, C.; Solis, D. J.; Ryan, K. S.; Thomson, T.; Belcher, A. M. Biological Routes to Metal Alloy Ferromagnetic Nanostructures. *Nano Lett.* **2004**, *4*, 1127−1132.
(377) Kumar, V. B.; Sanetuntikul, J.; Ganesan, P.; Porat, Z.; Shanmugam, S.; Gedanken, A. e.; Shanmugam, S.; Gedanken, A. Sonochemical Formation of Ga-Pt Intermetallic Nanoparticles Embedded in Graphene and its Potential Use as an Electrocatalyst. Electrochim. *Electrochim. Acta* **2016**, *190*, 659−667.
(378) Arumugam, B.; Tamaki, T.; Yamaguchi, T. Beneficial Role of Copper in the Enhancement of Durability of Ordered Intermetallic PtFeCu Catalyst for Electrocatalytic Oxygen Reduction. *ACS Appl. Mater. Interfaces* **2015**, *7*, 16311−16321.
(379) Armbrüster, M.; Wowsnick, G.; Friedrich, M.; Heggen, M.; Cardoso-Gil, R. Synthesis and Catalytic Properties of Nanoparticulate Intermetallic Ga−Pd Compounds. *J. Am. Chem. Soc.* **2011**, *133*, 9112−9118.
(380) Alloyeau, D.; Langlois, C.; Ricolleau, C.; Le Bouar, Y.; Loiseau, A. A TEM in Situ Experiment as a Guideline for the Synthesis of As-Grown Ordered CoPt Nanoparticles. *Nanotechnology* **2007**, *18*, 375301.
(381) Bai, X.; Chen, W.; Zhao, C.; Li, S.; Song, Y.; Ge, R.; Wei, W.; Sun, Y. Exclusive Formation of Formic Acid from CO_2 Electroreduction by a Tunable Pd-Sn Alloy. *Angew. Chem., Int. Ed.* **2017**, *56*, 12219−12223.
(382) Cui, Z.; Chen, H.; Zhao, M.; DiSalvo, F. J. High-Performance Pd_3Pb Intermetallic Catalyst for Electrochemical Oxygen Reduction. *Nano Lett.* **2016**, *16*, 2560−2566.
(383) Cui, Z.; Chen, H.; Zhou, W.; Zhao, M.; DiSalvo, F. J. Structurally Ordered Pt_3Cr as Oxygen Reduction Electrocatalyst: Ordering Control and Origin of Enhanced Stability. *Chem. Mater.* **2015**, *27*, 7538−7545.
(384) Reiss, P.; Carrière, M.; Lincheneau, C.; Vaure, L.; Tamang, S. Synthesis of Semiconductor Nanocrystals, Focusing on Nontoxic and Earth-Abundant Materials. *Chem. Rev.* **2016**, *116*, 10731−10819.
(385) Wang, D.; Xin, H. L.; Hovden, R.; Wang, H.; Yu, Y.; Muller, D. A.; DiSalvo, F. J.; Abruña, H. D. Structurally Ordered Intermetallic Platinum−Cobalt Core−Shell Nanoparticles with Enhanced Activity and Stability as Oxygen Reduction Electrocatalysts. *Nat. Mater.* **2013**, *12*, 81.
(386) Wang, Z.; Yao, X.; Kang, Y.; Miao, L.; Xia, D.; Gan, L. Structurally Ordered Low-Pt Intermetallic Electrocatalysts toward

https://dx.doi.org/10.1021/acs.chemrev.0c00436
Chem. Rev. 2021, 121, 736−795

Durably High Oxygen Reduction Reaction Activity. *Adv. Funct. Mater.* **2019**, *29*, 1902987.
(387) Xiong, Y.; Xiao, L.; Yang, Y.; DiSalvo, F. J.; Abruña, H. D. High-Loading Intermetallic Pt_3Co/C Core−Shell Nanoparticles as Enhanced Activity Electrocatalysts toward the Oxygen Reduction Reaction (ORR). *Chem. Mater.* **2018**, *30*, 1532−1539.
(388) Xiao, W.; Lei, W.; Wang, J.; Gao, G.; Zhao, T.; Cordeiro, M. A. L.; Lin, R.; Gong, M.; Guo, X.; Stavitski, E.; Xin, H. L.; Zhu, Y.; Wang, D. Tuning the Electrocatalytic Activity of Pt by Structurally Ordered PdFe/C for the Hydrogen Oxidation Reaction in Alkaline Media. *J. Mater. Chem. A* **2018**, *6*, 11346−11352.
(389) Zhu, H.; Cai, Y.; Wang, F.; Gao, P.; Cao, J. Scalable Preparation of the Chemically Ordered Pt−Fe−Au Nanocatalysts with High Catalytic Reactivity and Stability for Oxygen Reduction Reactions. *ACS Appl. Mater. Interfaces* **2018**, *10*, 22156−22166.
(390) LiBretto, N. J.; Yang, C.; Ren, Y.; Zhang, G.; Miller, J. T. Identification of Surface Structures in Pt_3Cr Intermetallic Nanocatalysts. *Chem. Mater.* **2019**, *31*, 1597−1609.
(391) Matsumoto, F.; Saravanan, G.; Kobayashi, G. Application of Ordered Intermetallic Phases to Electrocatalysis. *ECS Trans.* **2013**, *50*, 3−8.
(392) Roy, C.; Knudsen, B. P.; Pedersen, C. M.; Velázquez-Palenzuela, A.; Christensen, L. H.; Damsgaard, C. D.; Stephens, I. E. L.; Chorkendorff, I. Scalable Synthesis of Carbon-Supported Platinum−Lanthanide and − Rare-Earth Alloys for Oxygen Reduction. *ACS Catal.* **2018**, *8*, 2071−2080.
(393) Schulenburg, H.; Müller, E.; Khelashvili, G.; Roser, T.; Bönnemann, H.; Wokaun, A.; Scherer, G. G. Heat-Treated $PtCo_3$ Nanoparticles as Oxygen Reduction Catalysts. *J. Phys. Chem. C* **2009**, *113*, 4069−4077.
(394) Wang, T.; Liang, J.; Zhao, Z.; Li, S.; Lu, G.; Xia, Z.; Wang, C.; Luo, J.; Han, J.; Ma, C.; Huang, Y.; Li, Q. Sub-6 nm Fully Ordered $L1_0$-Pt−Ni−Co Nanoparticles Enhance Oxygen Reduction via Co Doping Induced Ferromagnetism Enhancement and Optimized Surface Strain. *Adv. Energy Mater.* **2019**, *9*, 1803771.
(395) Yamamoto, S.; Morimoto, Y.; Ono, T.; Takano, M. Magnetically Superior and Easy to Handle $L1_0$-FePt Nanocrystals. *Appl. Phys. Lett.* **2005**, *87*, 032503.
(396) Yano, H.; Arima, I.; Watanabe, M.; Iiyama, A.; Uchida, H. Oxygen Reduction Activity and Durability of Ordered and Disordered Pt_3Co Alloy Nanoparticle Catalysts at Practical Temperatures of Polymer Electrolyte Fuel Cells. *J. Electrochem. Soc.* **2017**, *164*, F966−F972.
(397) Zhang, D.; Wu, F.; Peng, M.; Wang, X.; Xia, D.; Guo, G. One-Step, Facile and Ultrafast Synthesis of Phase- and Size-Controlled Pt−Bi Intermetallic Nanocatalysts through Continuous-Flow Microfluidics. *J. Am. Chem. Soc.* **2015**, *137*, 6263−6269.
(398) Zhang, L.; Xia, D. Electrocatalytic Activity of Ordered Intermetallic PtSb for Methanol Electro-Oxidation. *Appl. Surf. Sci.* **2006**, *252*, 2191−2195.
(399) Zhu, J.; Zheng, X.; Wang, J.; Wu, Z.; Han, L.; Lin, R.; Xin, H. L.; Wang, D. Structurally Ordered Pt−Zn/C Series Nanoparticles as Efficient Anode Catalysts for Formic Acid Electrooxidation. *J. Mater. Chem. A* **2015**, *3*, 22129−22135.
(400) Wang, X. X.; Hwang, S.; Pan, Y.-T.; Chen, K.; He, Y.; Karakalos, S.; Zhang, H.; Spendelow, J. S.; Su, D.; Wu, G. Ordered Pt_3Co Intermetallic Nanoparticles Derived from Metal−Organic Frameworks for Oxygen Reduction. *Nano Lett.* **2018**, *18*, 4163−4171.
(401) Zou, L.; Li, J.; Yuan, T.; Zhou, Y.; Li, X.; Yang, H. Structural Transformation of Carbon-Supported Pt_3Cr Nanoparticles from a Disordered to an Ordered Phase as a Durable Oxygen Reduction Electrocatalyst. *Nanoscale* **2014**, *6*, 10686−10692.
(402) Bele, M.; Jovanovič, P.; Pavlišič, A.; Jozinović, B.; Zorko, M.; Rečnik, A.; Chernyshova, E.; Hočevar, S.; Hodnik, N.; Gaberšček, M. A Highly Active $PtCu_3$ Intermetallic Core−Shell, Multilayered Pt-Skin, Carbon Embedded Electrocatalyst Produced by a Scale-Up Sol−Gel Synthesis. *Chem. Commun.* **2014**, *50*, 13124−13126.
(403) Bu, L.; Guo, S.; Zhang, X.; Shen, X.; Su, D.; Lu, G.; Zhu, X.; Yao, J.; Guo, J.; Huang, X. Surface Engineering of Hierarchical Platinum-Cobalt Nanowires for Efficient Electrocatalysis. *Nat. Commun.* **2016**, *7*, 11850.
(404) Chen, S.; Ferreira, P. J.; Sheng, W.; Yabuuchi, N.; Allard, L. F.; Shao-Horn, Y. Enhanced Activity for Oxygen Reduction Reaction on "Pt_3Co" Nanoparticles: Direct Evidence of Percolated and Sandwich-Segregation Structures. *J. Am. Chem. Soc.* **2008**, *130*, 13818−13819.
(405) Cui, Z.; Fu, G.; Li, Y.; Goodenough, J. B. Ni_3FeN-Supported Fe_3Pt Intermetallic Nanoalloy as a High-Performance Bifunctional Catalyst for Metal−Air Batteries. *Angew. Chem., Int. Ed.* **2017**, *56*, 9901−9905.
(406) Demortière, A.; Petit, C. CoPt Magnetic Nanocrystals in the $A_1/L1_0$ Transformation. *J. Appl. Phys.* **2011**, *109*, 084344.
(407) DeSario, D. Y.; DiSalvo, F. J. Ordered Intermetallic Pt−Sn Nanoparticles: Exploring Ordering Behavior across the Bulk Phase Diagram. *Chem. Mater.* **2014**, *26*, 2750−2757.
(408) Du, X. X.; He, Y.; Wang, X. X.; Wang, J. N. Fine-Grained and Fully Ordered Intermetallic PtFe Catalysts with Largely Enhanced Catalytic Activity and Durability. *Energy Environ. Sci.* **2016**, *9*, 2623−2632.
(409) Ghosh, T.; Vukmirovic, M. B.; DiSalvo, F. J.; Adzic, R. R. Intermetallics as Novel Supports for Pt Monolayer O_2 Reduction Electrocatalysts: Potential for Significantly Improving Properties. *J. Am. Chem. Soc.* **2010**, *132*, 906−907.
(410) Gregoire, J. M.; Tague, M. E.; Cahen, S.; Khan, S.; Abruña, H. D.; DiSalvo, F. J.; van Dover, R. B. Improved Fuel Cell Oxidation Catalysis in $Pt_{1-x}Ta_x$. *Chem. Mater.* **2010**, *22*, 1080−1087.
(411) Guo, H.; Liu, X.; Bai, C.; Chen, Y.; Wang, L.; Zheng, M.; Dong, Q.; Peng, D.-L. Effect of Component Distribution and Nanoporosity in CuPt Nanotubes on Electrocatalysis of the Oxygen Reduction Reaction. *ChemSusChem* **2015**, *8*, 486−494.
(412) Guo, S.; Sun, S. FePt Nanoparticles Assembled on Graphene as Enhanced Catalyst for Oxygen Reduction Reaction. *J. Am. Chem. Soc.* **2012**, *134*, 2492−2495.
(413) Hodnik, N.; Jeyabharathi, C.; Meier, J. C.; Kostka, A.; Phani, K. L.; Rečnik, A.; Bele, M.; Hočevar, S.; Gaberšček, M.; Mayrhofer, K. J. J. Effect of Ordering of $PtCu_3$ Nanoparticle Structure on the Activity and Stability for the Oxygen Reduction Reaction. *Phys. Chem. Chem. Phys.* **2014**, *16*, 13610−13615.
(414) Hong, Y.; Kim, H. J.; Yang, D.; Lee, G.; Nam, K. M.; Jung, M.-H.; Kim, Y.-M.; Choi, S.-I.; Seo, W. S. Facile Synthesis of Fully Ordered $L1_0$-FePt Nanoparticles with Controlled Pt-Shell Thicknesses for Electrocatalysis. *Nano Res.* **2017**, *10*, 2866−2880.
(415) Hu, G.; Nitze, F.; Gracia-Espino, E.; Ma, J.; Barzegar, H. R.; Sharifi, T.; Jia, X.; Shchukarev, A.; Lu, L.; Ma, C.; Yang, G.; Wågberg, T. Small Palladium Islands Embedded in Palladium−Tungsten Bimetallic Nanoparticles form Catalytic Hotspots for Oxygen Reduction. *Nat. Commun.* **2014**, *5*, 5253.
(416) Kodiyath, R.; Ramesh, G. V.; Koudelkova, E.; Tanabe, T.; Ito, M.; Manikandan, M.; Ueda, S.; Fujita, T.; Umezawa, N.; Noguchi, H.; Ariga, K.; Abe, H. Promoted C−C Bond Cleavage over Intermetallic $TaPt_3$ Catalyst toward Low-Temperature Energy Extraction from Ethanol. *Energy Environ. Sci.* **2015**, *8*, 1685−1689.
(417) Shao, L.; Zhang, W.; Armbrüster, M.; Teschner, D.; Girgsdies, F.; Zhang, B.; Timpe, O.; Friedrich, M.; Schlögl, R.; Su, D. S. Nanosizing Intermetallic Compounds Onto Carbon Nanotubes: Active and Selective Hydrogenation Catalysts. *Angew. Chem., Int. Ed.* **2011**, *50*, 10231−10235.
(418) Shim, J.; Lee, J.; Ye, Y.; Hwang, J.; Kim, S.-K.; Lim, T.-H.; Wiesner, U.; Lee, J. One-Pot Synthesis of Intermetallic Electrocatalysts in Ordered, Large-Pore Mesoporous Carbon/Silica toward Formic Acid Oxidation. *ACS Nano* **2012**, *6*, 6870−6881.
(419) Chen, H.-S.; Benedetti, T. M.; Gonçales, V. R.; Bedford, N. M.; Scott, R. W. J.; Webster, R. F.; Cheong, S.; Gooding, J. J.; Tilley, R. D. Preserving the Exposed Facets of Pt_3Sn Intermetallic Nanocubes During an Order to Disorder Transition Allows the Elucidation of the Effect of the Degree of Alloy Ordering on Electrocatalysis. *J. Am. Chem. Soc.* **2020**, *142*, 3231−3239.
(420) Yu, Y.; Sun, K.; Tian, Y.; Li, X. Z.; Kramer, M. J.; Sellmyer, D. J.; Shield, J. E.; Sun, S. One-Pot Synthesis of Urchin-like FePd−Fe_3O_4

https://dx.doi.org/10.1021/acs.chemrev.0c00436
Chem. Rev. 2021, 121, 736−795

and Their Conversion into Exchange-Coupled $L1_0$−FePd−Fe Nanocomposite Magnets. *Nano Lett.* **2013**, *13*, 4975−4979.
(421) Zhou, H.; Yang, X.; Li, L.; Liu, X.; Huang, Y.; Pan, X.; Wang, A.; Li, J.; Zhang, T. PdZn Intermetallic Nanostructure with Pd−Zn−Pd Ensembles for Highly Active and Chemoselective Semi-Hydrogenation of Acetylene. *ACS Catal.* **2016**, *6*, 1054−1061.
(422) Li, C.; Chen, Y.; Zhang, S.; Xu, S.; Zhou, J.; Wang, F.; Wei, M.; Evans, D. G.; Duan, X. Ni−In Intermetallic Nanocrystals as Efficient Catalysts toward Unsaturated Aldehydes Hydrogenation. *Chem. Mater.* **2013**, *25*, 3888−3896.
(423) Kim, J.; Yang, S.; Lee, H. Platinum−Titanium Intermetallic Nanoparticle Catalysts for Oxygen Reduction Reaction with Enhanced Activity and Durability. *Electrochem. Commun.* **2016**, *66*, 66−70.
(424) Lang, X.-Y.; Han, G.-F.; Xiao, B.-B.; Gu, L.; Yang, Z.-Z.; Wen, Z.; Zhu, Y.-F.; Zhao, M.; Li, J.-C.; Jiang, Q. Mesostructured Intermetallic Compounds of Platinum and Non-Transition Metals for Enhanced Electrocatalysis of Oxygen Reduction Reaction. *Adv. Funct. Mater.* **2015**, *25*, 230−237.
(425) Penner, S.; Armbrüster, M. Formation of Intermetallic Compounds by Reactive Metal−Support Interaction: A Frequently Encountered Phenomenon in Catalysis. *ChemCatChem* **2015**, *7*, 374−392.
(426) Niu, Y.; Liu, X.; Wang, Y.; Zhou, S.; Lv, Z.; Zhang, L.; Shi, W.; Li, Y.; Zhang, W.; Su, D. S.; Zhang, B. Visualizing Formation of Intermetallic PdZn in a Palladium/Zinc Oxide Catalyst: Interfacial Fertilization by PdH_x. *Angew. Chem.* **2019**, *131*, 4276−4281.
(427) Najafishirtari, S.; Brescia, R.; Guardia, P.; Marras, S.; Manna, L.; Colombo, M. Nanoscale Transformations of Alumina-Supported AuCu Ordered Phase Nanocrystals and Their Activity in CO Oxidation. *ACS Catal.* **2015**, *5*, 2154−2163.
(428) Lee, D. C.; Mikulec, F. V.; Pelaez, J. M.; Koo, B.; Korgel, B. A. Synthesis and Magnetic Properties of Silica-Coated FePt Nanocrystals. *J. Phys. Chem. B* **2006**, *110*, 11160−11166.
(429) Liu, Z.; Jackson, G. S.; Eichhorn, B. W. Tuning the CO-Tolerance of Pt-Fe Bimetallic Nanoparticle Electrocatalysts through Architectural Control. *Energy Environ. Sci.* **2011**, *4*, 1900−1903.
(430) Teng, X.; Yang, H. Synthesis of Face-Centered Tetragonal FePt Nanoparticles and Granular Films from $Pt@Fe_2O_3$ Core−Shell Nanoparticles. *J. Am. Chem. Soc.* **2003**, *125*, 14559−14563.
(431) Zhao, Y.; Wang, C.; Liu, J.; Wang, F. PDA-Assisted Formation of Ordered Intermetallic $CoPt_3$ Catalysts with Enhanced Oxygen Reduction Activity and Stability. *Nanoscale* **2018**, *10*, 9038−9043.
(432) Zhao, E. W.; Maligal-Ganesh, R.; Xiao, C.; Goh, T.-W.; Qi, Z.; Pei, Y.; Hagelin-Weaver, H. E.; Huang, W.; Bowers, C. R. Silica-Encapsulated Pt-Sn Intermetallic Nanoparticles: A Robust Catalytic Platform for Parahydrogen-Induced Polarization of Gases and Liquids. *Angew. Chem.* **2017**, *129*, 3983−3987.
(433) Tamada, Y.; Yamamoto, S.; Takano, M.; Nasu, S.; Ono, T. Well-Ordered $L1_0$-FePt Nanoparticles Synthesized by Improved SiO_2-Nanoreactor Method. *Appl. Phys. Lett.* **2007**, *90*, 162509.
(434) Jiang, G.; Zhu, H.; Zhang, X.; Shen, B.; Wu, L.; Zhang, S.; Lu, G.; Wu, Z.; Sun, S. Core/Shell Face-Centered Tetragonal FePd/Pd Nanoparticles as an Efficient Non-Pt Catalyst for the Oxygen Reduction Reaction. *ACS Nano* **2015**, *9*, 11014−11022.
(435) Zhang, S.; Zhang, X.; Jiang, G.; Zhu, H.; Guo, S.; Su, D.; Lu, G.; Sun, S. Tuning Nanoparticle Structure and Surface Strain for Catalysis Optimization. *J. Am. Chem. Soc.* **2014**, *136*, 7734−7739.
(436) Yamamoto, S.; Morimoto, Y.; Tamada, Y.; Takahashi, Y. K.; Hono, K.; Ono, T.; Takano, M. Preparation of Monodisperse and Highly Coercive $L1_0$-FePt Nanoparticles Dispersible in Nonpolar Organic Solvents. *Chem. Mater.* **2006**, *18*, 5385−5388.
(437) Lorenz, H.; Rameshan, C.; Bielz, T.; Memmel, N.; Stadlmayr, W.; Mayr, L.; Zhao, Q.; Soisuwan, S.; Klötzer, B.; Penner, S. From Oxide-Supported Palladium to Intermetallic Palladium Phases: Consequences for Methanol Steam Reforming. *ChemCatChem* **2013**, *5*, 1273−1285.
(438) Kim, J.; Lee, Y.; Sun, S. Structurally Ordered FePt Nanoparticles and Their Enhanced Catalysis for Oxygen Reduction Reaction. *J. Am. Chem. Soc.* **2010**, *132*, 4996−4997.
(439) Kim, H. Y.; Cho, S.; Sa, Y. J.; Hwang, S.-M.; Park, G.-G.; Shin, T. J.; Jeong, H. Y.; Yim, S.-D.; Joo, S. H. Self-Supported Mesostructured Pt-Based Bimetallic Nanospheres Containing an Intermetallic Phase as Ultrastable Oxygen Reduction Electrocatalysts. *Small* **2016**, *12*, 5347−5353.
(440) Kuroki, H.; Tamaki, T.; Matsumoto, M.; Arao, M.; Kubobuchi, K.; Imai, H.; Yamaguchi, T. Platinum−Iron−Nickel Trimetallic Catalyst with Superlattice Structure for Enhanced Oxygen Reduction Activity and Durability. *Ind. Eng. Chem. Res.* **2016**, *55*, 11458−11466.
(441) Li, D.; Poudyal, N.; Nandwana, V.; Jin, Z.; Elkins, K.; Liu, J. P. Hard Magnetic FePt Nanoparticles by Salt-Matrix Annealing. *J. Appl. Phys.* **2006**, *99*, 08E911.
(442) Chen, H.; Yu, Y.; Xin, H. L.; Newton, K. A.; Holtz, M. E.; Wang, D.; Muller, D. A.; Abruña, H. D.; DiSalvo, F. J. Coalescence in the Thermal Annealing of Nanoparticles: An in Situ STEM Study of the Growth Mechanisms of Ordered Pt−Fe Nanoparticles in a KCl Matrix. *Chem. Mater.* **2013**, *25*, 1436−1442.
(443) Elkins, K.; Li, D.; Poudyal, N.; Nandwana, V.; Jin, Z.; Chen, K.; Liu, J. P. Monodisperse Face-Centred Tetragonal FePt Nanoparticles with Giant Coercivity. *J. Phys. D: Appl. Phys.* **2005**, *38*, 2306−2309.
(444) Mizuno, M.; Sasaki, Y.; Yu, A. C. C.; Inoue, M. Prevention of Nanoparticle Coalescence under High-Temperature Annealing. *Langmuir* **2004**, *20*, 11305−11307.
(445) Cable, R. E.; Schaak, R. E. Low-Temperature Solution Synthesis of Nanocrystalline Binary Intermetallic Compounds Using the Polyol Process. *Chem. Mater.* **2005**, *17*, 6835−6841.
(446) Bu, L.; Shao, Q.; E, B.; Guo, J.; Yao, J.; Huang, X. PtPb/PtNi Intermetallic Core/Atomic Layer Shell Octahedra for Efficient Oxygen Reduction Electrocatalysis. *J. Am. Chem. Soc.* **2017**, *139*, 9576−9582.
(447) Bondi, J. F.; Misra, R.; Ke, X.; Sines, I. T.; Schiffer, P.; Schaak, R. E. Optimized Synthesis and Magnetic Properties of Intermetallic Au_3Fe_{1-x}, Au_3Co_{1-x}, and Au_3Ni_{1-x} Nanoparticles. *Chem. Mater.* **2010**, *22*, 3988−3994.
(448) Cable, R. E.; Schaak, R. E. Reacting the Unreactive: A Toolbox of Low-Temperature Solution-Mediated Reactions for the Facile Interconversion of Nanocrystalline Intermetallic Compounds. *J. Am. Chem. Soc.* **2006**, *128*, 9588−9589.
(449) Gao, L.; Li, X.; Yao, Z.; Bai, H.; Lu, Y.; Ma, C.; Lu, S.; Peng, Z.; Yang, J.; Pan, A.; Huang, H. Unconventional p−d Hybridization Interaction in PtGa Ultrathin Nanowires Boosts Oxygen Reduction Electrocatalysis. *J. Am. Chem. Soc.* **2019**, *141*, 18083−18090.
(450) Kariuki, N. N.; Wang, X.; Mawdsley, J. R.; Ferrandon, M. S.; Niyogi, S. G.; Vaughey, J. T.; Myers, D. J. Colloidal Synthesis and Characterization of Carbon-Supported Pd−Cu Nanoparticle Oxygen Reduction Electrocatalysts. *Chem. Mater.* **2010**, *22*, 4144−4152.
(451) Leonard, B. M.; Schaak, R. E. Multistep Solution-Mediated Formation of $AuCuSn_2$: Mechanistic Insights for the Guided Design of Intermetallic Solid-State Materials and Complex Multimetal Nanocrystals. *J. Am. Chem. Soc.* **2006**, *128*, 11475−11482.
(452) Liao, H.; Zhu, J.; Hou, Y. Synthesis and Electrocatalytic Properties of PtBi Nanoplatelets and PdBi Nanowires. *Nanoscale* **2014**, *6*, 1049−1055.
(453) Liu, Z.; Jackson, G. S.; Eichhorn, B. W. PtSn Intermetallic, Core−Shell, and Alloy Nanoparticles as CO-Tolerant Electrocatalysts for H_2 Oxidation. *Angew. Chem., Int. Ed.* **2010**, *49*, 3173−3176.
(454) Pan, Y.-T.; Yan, Y.; Shao, Y.-T.; Zuo, J.-M.; Yang, H. Ag−Pt Compositional Intermetallics Made from Alloy Nanoparticles. *Nano Lett.* **2016**, *16*, 6599−6603.
(455) Sra, A. K.; Ewers, T. D.; Schaak, R. E. Direct Solution Synthesis of Intermetallic AuCu and $AuCu_3$ Nanocrystals and Nanowire Networks. *Chem. Mater.* **2005**, *17*, 758−766.
(456) Wang, K.; Qin, Y.; Lv, F.; Li, M.; Liu, Q.; Lin, F.; Feng, J.; Yang, C.; Gao, P.; Guo, S. Intermetallic Pd_3Pb Nanoplates Enhance

https://dx.doi.org/10.1021/acs.chemrev.0c00436
Chem. Rev. 2021, 121, 736−795

Oxygen Reduction Catalysis with Excellent Methanol Tolerance. *Small Methods* **2018**, *2*, 1700331.
(457) Xia, D.; Chen, G.; Wang, Z.; Zhang, J.; Hui, S.; Ghosh, D.; Wang, H. Synthesis of Ordered Intermetallic $PtBi_2$ Nanoparticles for Methanol-Tolerant Catalyst in Oxygen Electroreduction. *Chem. Mater.* **2006**, *18*, 5746−5749.
(458) Yu, Y.; Mukherjee, P.; Tian, Y.; Li, X. Z.; Shield, J. E.; Sellmyer, D. J. Direct Chemical Synthesis of $L1_0$-FePtAu Nanoparticles with High Coercivity. *Nanoscale* **2014**, *6*, 12050−12055.
(459) Zhang, N.; Bu, L.; Guo, S.; Guo, J.; Huang, X. Screw Thread-Like Platinum−Copper Nanowires Bounded with High-Index Facets for Efficient Electrocatalysis. *Nano Lett.* **2016**, *16*, 5037−5043.
(460) Zhang, J.; Shao, Q.; Zhang, Y.; Bai, S.; Feng, Y.; Huang, X. Promoting the Direct H_2O_2 Generation Catalysis by Using Hollow Pd−Sn Intermetallic Nanoparticles. *Small* **2018**, *14*, 1703990.
(461) Alden, L. R.; Han, D. K.; Matsumoto, F.; Abruña, H. D.; DiSalvo, F. J. Intermetallic PtPb Nanoparticles Prepared by Sodium Naphthalide Reduction of Metal-Organic Precursors: Electrocatalytic Oxidation of Formic Acid. *Chem. Mater.* **2006**, *18*, 5591−5596.
(462) Choi, R.; Jung, J.; Kim, G.; Song, K.; Kim, Y.-I.; Jung, S. C.; Han, Y.-K.; Song, H.; Kang, Y.-M. Ultra-Low Overpotential and High Rate Capability in Li−O_2 Batteries through Surface Atom Arrangement of PdCu Nanocatalysts. *Energy Environ. Sci.* **2014**, *7*, 1362−1368.
(463) Feng, Q.; Zhao, S.; He, D.; Tian, S.; Gu, L.; Wen, X.; Chen, C.; Peng, Q.; Wang, D.; Li, Y. Strain Engineering to Enhance the Electrooxidation Performance of Atomic-Layer Pt on Intermetallic Pt_3Ga. *J. Am. Chem. Soc.* **2018**, *140*, 2773−2776.
(464) Gamler, J. T. L.; Leonardi, A.; Ashberry, H. M.; Daanen, N. N.; Losovyj, Y.; Unocic, R. R.; Engel, M.; Skrabalak, S. E. Achieving Highly Durable Random Alloy Nanocatalysts through Intermetallic Cores. *ACS Nano* **2019**, *13*, 4008−4017.
(465) Kanady, J. S.; Leidinger, P.; Haas, A.; Titlbach, S.; Schunk, S.; Schierle-Arndt, K.; Crumlin, E. J.; Wu, C. H.; Alivisatos, A. P. Synthesis of Pt_3Y and Other Early−Late Intermetallic Nanoparticles by Way of a Molten Reducing Agent. *J. Am. Chem. Soc.* **2017**, *139*, 5672−5675.
(466) Liu, Y.; Liu, X.; Feng, Q.; He, D.; Zhang, L.; Lian, C.; Shen, R.; Zhao, G.; Ji, Y.; Wang, D.; Zhou, G.; Li, Y. Intermetallic Ni_xM_y (M = Ga and Sn) Nanocrystals: A Non-Precious Metal Catalyst for Semi-Hydrogenation of Alkynes. *Adv. Mater.* **2016**, *28*, 4747−4754.
(467) Liu, Z.; Guo, B.; Tay, S. W.; Hong, L.; Zhang, X. Physical and Electrochemical Characterizations of PtPb/C Catalyst Prepared by Pyrolysis of Platinum(II) and Lead(II) Acetylacetonate. *J. Power Sources* **2008**, *184*, 16−22.
(468) Magno, L. M.; Sigle, W.; van Aken, P. A.; Angelescu, D. G.; Stubenrauch, C. Microemulsions as Reaction Media for the Synthesis of Bimetallic Nanoparticles: Size and Composition of Particles. *Chem. Mater.* **2010**, *22*, 6263−6271.
(469) Roychowdhury, C.; Matsumoto, F.; Zeldovich, V. B.; Warren, S. C.; Mutolo, P. F.; Ballesteros, M.; Wiesner, U.; Abruña, H. D.; DiSalvo, F. J. Synthesis, Characterization, and Electrocatalytic Activity of PtBi and PtPb Nanoparticles Prepared by Borohydride Reduction in Methanol. *Chem. Mater.* **2006**, *18*, 3365−3372.
(470) Marakatti, V. S.; Sarma, S. C.; Sarkar, S.; Krajčí, M.; Gaigneaux, E. M.; Peter, S. C. Synthetically Tuned Pd-Based Intermetallic Compounds and Their Structural Influence on the O_2 Dissociation in Benzylamine Oxidation. *ACS Appl. Mater. Interfaces* **2019**, *11*, 37602−37616.
(471) Luo, Z.; Lu, J.; Flox, C.; Nafria, R.; Genç, A.; Arbiol, J.; Llorca, J.; Ibáñez, M.; Morante, J. R.; Cabot, A. Pd_2Sn [010] Nanorods as a Highly Active and Stable Ethanol Oxidation Catalyst. *J. Mater. Chem. A* **2016**, *4*, 16706−16713.
(472) Yang, S.; Peng, Z.; Yang, H. Platinum Lead Nanostructures: Formation, Phase Behavior, and Electrocatalytic Properties. *Adv. Funct. Mater.* **2008**, *18*, 2745−2753.
(473) Chen, X.; Wang, H.; Wan, H.; Wu, T.; Shu, D.; Shen, L.; Wang, Y.; Ruterana, P.; Lund, P. D.; Wang, H. Core/Shell Cu/FePtCu Nanoparticles with Face-Centered Tetragonal Texture: An Active and Stable Low-Pt Catalyst for Enhanced Oxygen Reduction. *Nano Energy* **2018**, *54*, 280−287.
(474) Zhao, Y.; Liu, J.; Zhao, Y.; Wang, F.; Song, Y. Pt−Co Secondary Solid Solution Nanocrystals Supported on Carbon as Next-Generation Catalysts for the Oxygen Reduction Reaction. *J. Mater. Chem. A* **2015**, *3*, 20086−20091.
(475) Wang, C.; Sang, X.; Gamler, J. T. L.; Chen, D. P.; Unocic, R. R.; Skrabalak, S. E. Facet-Dependent Deposition of Highly Strained Alloyed Shells on Intermetallic Nanoparticles for Enhanced Electrocatalysis. *Nano Lett.* **2017**, *17*, 5526−5532.
(476) Wang, X.-L.; Feygenson, M.; Chen, H.; Lin, C.-H.; Ku, W.; Bai, J.; Aronson, M. C.; Tyson, T. A.; Han, W.-Q. Nanospheres of a New Intermetallic $FeSn_5$ Phase: Synthesis, Magnetic Properties and Anode Performance in Li-ion Batteries. *J. Am. Chem. Soc.* **2011**, *133*, 11213−11219.
(477) Yang, J.; Chen, X.; Yang, X.; Ying, J. Y. Stabilization and Compressive Strain Effect of AuCu Core on Pt Shell for Oxygen Reduction Reaction. *Energy Environ. Sci.* **2012**, *5*, 8976−8981.
(478) Yang, J.; Chng, L. L.; Yang, X.; Chen, X.; Ying, J. Y. Multiply-Twinned Intermetallic AuCu Pentagonal Nanorods. *Chem. Commun.* **2014**, *50*, 1141−1143.
(479) Du, C.; Chen, M.; Wang, W.; Tan, Q.; Xiong, K.; Yin, G. Platinum-Based Intermetallic Nanotubes with a Core−Shell Structure as Highly Active and Durable Catalysts for Fuel Cell Applications. *J. Power Sources* **2013**, *240*, 630−635.
(480) Götsch, T.; Stöger-Pollach, M.; Thalinger, R.; Penner, S. The Nanoscale Kirkendall Effect in Pd-Based Intermetallic Phases. *J. Phys. Chem. C* **2014**, *118*, 17810−17818.
(481) Gamler, J. T. L.; Ashberry, H. M.; Sang, X.; Unocic, R. R.; Skrabalak, S. E. Building Random Alloy Surfaces from Intermetallic Seeds: A General Route to Strain-Engineered Electrocatalysts with High Durability. *ACS Applied Nano Materials* **2019**, *2*, 4538−4546.
(482) Jana, R.; Peter, S. C. One-Pot Solvothermal Synthesis of Ordered Intermetallic Pt_2In_3 as Stable and Efficient Electrocatalyst towards Direct Alcohol Fuel Cell Application. *J. Solid State Chem.* **2016**, *242*, 133−139.
(483) Jana, R.; Subbarao, U.; Peter, S. C. Ultrafast Synthesis of Flower-Like Ordered Pd_3Pb Nanocrystals with Superior Electrocatalytic Activities towards Oxidation of Formic Acid and Ethanol. *J. Power Sources* **2016**, *301*, 160−169.
(484) Wang, J.; Asmussen, R. M.; Adams, B.; Thomas, D. F.; Chen, A. Facile Synthesis and Electrochemical Properties of Intermetallic PtPb Nanodendrites. *Chem. Mater.* **2009**, *21*, 1716−1724.
(485) Sarkar, S.; Jana, R.; Suchitra; Waghmare, U. V.; Kuppan, B.; Sampath, S.; Peter, S. C. Ordered Pd_2Ge Intermetallic Nanoparticles as Highly Efficient and Robust Catalyst for Ethanol Oxidation. *Chem. Mater.* **2015**, *27*, 7459−7467.
(486) Cui, C.-H.; Li, H.-H.; Liu, X.-J.; Gao, M.-R.; Yu, S.-H. Surface Composition and Lattice Ordering-Controlled Activity and Durability of CuPt Electrocatalysts for Oxygen Reduction Reaction. *ACS Catal.* **2012**, *2*, 916−924.
(487) Gunji, T.; Noh, S. H.; Ando, F.; Tanabe, T.; Han, B.; Ohsaka, T.; Matsumoto, F. Electrocatalytic Activity of Electrochemically Dealloyed $PdCu_3$ Intermetallic Compound towards Oxygen Reduction Reaction in Acidic Media. *J. Mater. Chem. A* **2018**, *6*, 14828−14837.
(488) Sun, D.; Wang, Y.; Livi, K. J. T.; Wang, C.; Luo, R.; Zhang, Z.; Alghamdi, H.; Li, C.; An, F.; Gaskey, B.; Mueller, T.; Hall, A. S. Ordered Intermetallic Pd_3Bi Prepared by an Electrochemically Induced Phase Transformation for Oxygen Reduction Electrocatalysis. *ACS Nano* **2019**, *13*, 10818−10825.
(489) Sun, D.; Si, L.; Fu, G.; Liu, C.; Sun, D.; Chen, Y.; Tang, Y.; Lu, T. Nanobranched Porous Palladium−Tin Intermetallics: One-Step Synthesis and Their Superior Electrocatalysis towards Formic Acid Oxidation. *J. Power Sources* **2015**, *280*, 141−146.
(490) Han, G.-F.; Gu, L.; Lang, X.-Y.; Xiao, B.-B.; Yang, Z.-Z.; Wen, Z.; Jiang, Q. Scalable Nanoporous $(Pt_{1-x}Ni_x)_3Al$ Intermetallic Compounds as Highly Active and Stable Catalysts for Oxygen Electroreduction. *ACS Appl. Mater. Interfaces* **2016**, *8*, 32910−32917.

https://dx.doi.org/10.1021/acs.chemrev.0c00436
Chem. Rev. 2021, 121, 736−795

(491) Jia, Q.; Caldwell, K.; Strickland, K.; Ziegelbauer, J. M.; Liu, Z.; Yu, Z.; Ramaker, D. E.; Mukerjee, S. Improved Oxygen Reduction Activity and Durability of Dealloyed $PtCo_x$ Catalysts for Proton Exchange Membrane Fuel Cells: Strain, Ligand, and Particle Size Effects. *ACS Catal.* **2015**, *5*, 176−186.
(492) Xu, C.; Liu, Y.; Wang, J.; Geng, H.; Qiu, H. Nanoporous PdCu Alloy for Formic Acid Electro-Oxidation. *J. Power Sources* **2012**, *199*, 124−131.
(493) Sarkar, S.; Subbarao, U.; Peter, S. C. Evolution of Dealloyed $PdBi_2$ Nanoparticles as Electrocatalysts with Enhanced Activity and Remarkable Durability in Hydrogen Evolution Reactions. *J. Mater. Chem. A* **2017**, *5*, 15950−15960.
(494) Sode, A.; Musgrove, A.; Bizzotto, D. Stability of PtZn Nanoparticles Supported on Carbon in Acidic Electrochemical Environments. *J. Phys. Chem. C* **2010**, *114*, 546−553.
(495) Tokushige, M.; Nishikiori, T.; Lafouresse, M. C.; Michioka, C.; Yoshimura, K.; Fukunaka, Y.; Ito, Y. Formation of FePt Intermetallic Compound Nanoparticles by Plasma-Induced Cathodic Discharge Electrolysis. Electrochim. *Electrochim. Acta* **2010**, *55*, 8154−8159.
(496) Sanetuntikul, J.; Ketpang, K.; Shanmugam, S. Hierarchical Nanostructured Pt_8Ti-TiO_2/C as an Efficient and Durable Anode Catalyst for Direct Methanol Fuel Cells. *ACS Catal.* **2015**, *5*, 7321−7327.
(497) Lee, J.; Yoo, J. M.; Ye, Y.; Mun, Y.; Lee, S.; Kim, O.-H.; Rhee, H.-W.; Lee, H. I.; Sung, Y.-E.; Lee, J. Development of Highly Stable and Mass Transfer-Enhanced Cathode Catalysts: Support-Free Electrospun Intermetallic FePt Nanotubes for Polymer Electrolyte Membrane Fuel Cells. *Adv. Energy Mater.* **2015**, *5*, 1402093.
(498) Wang, Y.; Sun, D.; Chowdhury, T.; Wagner, J. S.; Kempa, T. J.; Hall, A. S. Rapid Room-Temperature Synthesis of a Metastable Ordered Intermetallic Electrocatalyst. *J. Am. Chem. Soc.* **2019**, *141*, 2342−2347.
(499) Nguyen, H. L.; Howard, L. E. M.; Giblin, S. R.; Tanner, B. K.; Terry, I.; Hughes, A. K.; Ross, I. M.; Serres, A.; Bürckstümmer, H.; Evans, J. S. O. Synthesis of Monodispersed *fcc* and *fct* FePt/FePd Nanoparticles by Microwave Irradiation. *J. Mater. Chem.* **2005**, *15*, 5136−5143.
(500) Lekse, J. W.; Stagger, T. J.; Aitken, J. A. Microwave Metallurgy: Synthesis of Intermetallic Compounds via Microwave Irradiation. *Chem. Mater.* **2007**, *19*, 3601−3603.
(501) Gunji, T.; Jeevagan, A. J.; Hashimoto, M.; Nozawa, T.; Tanabe, T.; Kaneko, S.; Miyauchi, M.; Matsumoto, F. Photocatalytic Decomposition of Various Organic Compounds over WO_3-Supported Ordered Intermetallic PtPb Co-Catalysts. *Appl. Catal., B* **2016**, *181*, 475−480.
(502) Huang, Y.; Zheng, S.; Lin, X.; Su, L.; Guo, Y. Microwave Synthesis and Electrochemical Performance of a PtPb Alloy Catalyst for Methanol and Formic Acid Oxidation. Electrochim. *Electrochim. Acta* **2012**, *63*, 346−353.
(503) Jeevagan, A. J.; Gunji, T.; Sawano, N.; Saravanan, G.; Kojima, T.; Kaneko, S.; Kobayashi, G.; Matsumoto, F. Two-Step Microwave Synthesis of Highly Dispersed Ordered Intermetallic PtPb Nanoparticles on Carbon Black. *ECS Trans.* **2014**, *58*, 25−31.
(504) Heise, M.; Chang, J.-H.; Schönemann, R.; Herrmannsdörfer, T.; Wosnitza, J.; Ruck, M. Full Access to Nanoscale Bismuth−Palladium Intermetallics by Low-Temperature Syntheses. *Chem. Mater.* **2014**, *26*, 5640−5646.
(505) Martin, A. J.; Larrazábal, G. O.; Pérez-Ramírez, J. Towards Sustainable Fuels and Chemicals through the Electrochemical Reduction of CO_2: Lessons from Water Electrolysis. *Green Chem.* **2015**, *17*, 5114−5130.
(506) Zhu, S.; Jiang, B.; Cai, W.-B.; Shao, M. Direct Observation on Reaction Intermediates and the Role of Bicarbonate Anions in CO_2 Electrochemical Reduction Reaction on Cu Surfaces. *J. Am. Chem. Soc.* **2017**, *139*, 15664−15667.
(507) White, J. L.; Baruch, M. F.; Pander, J. E.; Hu, Y.; Fortmeyer, I. C.; Park, J. E.; Zhang, T.; Liao, K.; Gu, J.; Yan, Y.; Shaw, T. W.; Abelev, E.; Bocarsly, A. B. Light-Driven Heterogeneous Reduction of Carbon Dioxide: Photocatalysts and Photoelectrodes. *Chem. Rev.* **2015**, *115*, 12888−12935.
(508) Wei, Y.; Wu, X.; Zhao, Y.; Wang, L.; Zhao, Z.; Huang, X.; Liu, J.; Li, J. Efficient Photocatalysts of TiO_2 Nanocrystals-Supported PtRu Alloy Nanoparticles for CO_2 Reduction with H_2O: Synergistic Effect of Pt-Ru. *Appl. Catal., B* **2018**, *236*, 445−457.
(509) Balandin, A. A. In *Advances in Catalysis*; Eley, D. D., Pines, H., Weisz, P. B., Eds.; Academic Press, 1969; Vol. *19*.
(510) Medford, A. J.; Vojvodic, A.; Hummelshøj, J. S.; Voss, J.; Abild-Pedersen, F.; Studt, F.; Bligaard, T.; Nilsson, A.; Nørskov, J. K. From the Sabatier Principle to a Predictive Theory of Transition-Metal Heterogeneous Catalysis. *J. Catal.* **2015**, *328*, 36−42.
(511) Weller, S. W. In *Chemical Reaction Engineering Reviews*; Advances in Chemistry; American Chemical Society: Washington, D.C., **1975**; Vol. *148*, p 26, .
(512) Cheng, H.; Yang, N.; Lu, Q.; Zhang, Z.; Zhang, H. Syntheses and Properties of Metal Nanomaterials with Novel Crystal Phases. *Adv. Mater.* **2018**, *30*, 1707189.
(513) Zhang, H.; Jin, M.; Xiong, Y.; Lim, B.; Xia, Y. Shape-Controlled Synthesis of Pd Nanocrystals and Their Catalytic Applications. *Acc. Chem. Res.* **2013**, *46*, 1783−1794.
(514) Sabatier, P. Hydrogénations et Déshydrogénations par Catalyse. *Ber. Dtsch. Chem. Ges.* **1911**, *44*, 1984−2001.
(515) Nørskov, J. K.; Bligaard, T.; Hvolbæk, B.; Abild-Pedersen, F.; Chorkendorff, I.; Christensen, C. H. The Nature of the Active Site in Heterogeneous Metal Catalysis. *Chem. Soc. Rev.* **2008**, *37*, 2163−2171.
(516) Laursen, A. B.; Varela, A. S.; Dionigi, F.; Fanchiu, H.; Miller, C.; Trinhammer, O. L.; Rossmeisl, J.; Dahl, S. Electrochemical Hydrogen Evolution: Sabatier's Principle and the Volcano Plot. *J. Chem. Educ.* **2012**, *89*, 1595−1599.
(517) Busch, M.; Wodrich, M. D.; Corminboeuf, C. Linear Scaling Relationships and Volcano Plots in Homogeneous Catalysis - Revisiting the Suzuki Reaction. *Chem. Sci.* **2015**, *6*, 6754−6761.
(518) Calle-Vallejo, F.; Tymoczko, J.; Colic, V.; Vu, Q. H.; Pohl, M. D.; Morgenstern, K.; Loffreda, D.; Sautet, P.; Schuhmann, W.; Bandarenka, A. S. Finding Optimal Surface Sites on Heterogeneous Catalysts by Counting Nearest Neighbors. *Science* **2015**, *350*, 185−189.
(519) Xin, H.; Vojvodic, A.; Voss, J.; Nørskov, J. K.; Abild-Pedersen, F. Effects of *d*-Band Shape on the Surface Reactivity of Transition-Metal Alloys. *Phys. Rev. B: Condens. Matter Mater. Phys.* **2014**, *89*, 115114.
(520) Gorzkowski, M. T.; Lewera, A. Probing the Limits of *d*-Band Center Theory: Electronic and Electrocatalytic Properties of Pd-Shell−Pt-Core Nanoparticles. *J. Phys. Chem. C* **2015**, *119*, 18389−18395.
(521) Acerbi, N.; Tsang, S. C. E.; Jones, G.; Golunski, S.; Collier, P. Rationalization of Interactions in Precious Metal/Ceria Catalysts Using the d-Band Center Model. *Angew. Chem., Int. Ed.* **2013**, *52*, 7737−7741.
(522) Nørskov, J. K.; Abild-Pedersen, F.; Studt, F.; Bligaard, T. Density Functional Theory in Surface Chemistry and Catalysis. *Proc. Natl. Acad. Sci. U. S. A.* **2011**, *108*, 937−943.
(523) Wang, W.; Wang, S.; Ma, X.; Gong, J. Recent Advances in Catalytic Hydrogenation of Carbon Dioxide. *Chem. Soc. Rev.* **2011**, *40*, 3703−3727.
(524) Karunadasa, H. I.; Montalvo, E.; Sun, Y.; Majda, M.; Long, J. R.; Chang, C. J. A Molecular MoS_2 Edge Site Mimic for Catalytic Hydrogen Generation. *Science* **2012**, *335*, 698−702.
(525) Luo, M.; Guo, S. Strain-Controlled Electrocatalysis on Multimetallic Nanomaterials. *Nat. Rev. Mater.* **2017**, *2*, 17059.
(526) Strasser, P.; Koh, S.; Anniyev, T.; Greeley, J.; More, K.; Yu, C.; Liu, Z.; Kaya, S.; Nordlund, D.; Ogasawara, H.; Toney, M. F.; Nilsson, A. Lattice-Strain Control of the Activity in Dealloyed Core-Shell Fuel Cell Catalysts. *Nat. Chem.* **2010**, *2*, 454−460.
(527) Maroun, F.; Ozanam, F.; Magnussen, O. M.; Behm, R. J. The Role of Atomic Ensembles in the Reactivity of Bimetallic Electrocatalysts. *Science* **2001**, *293*, 1811−1814.

https://dx.doi.org/10.1021/acs.chemrev.0c00436
Chem. Rev. 2021, 121, 736−795

(528) Chen, M.; Kumar, D.; Yi, C.-W.; Goodman, D. W. The Promotional Effect of Gold in Catalysis by Palladium-Gold. *Science* **2005**, *310*, 291−293.
(529) Moseley, P.; Curtin, W. A. Computational Design of Strain in Core-Shell Nanoparticles for Optimizing Catalytic Activity. *Nano Lett.* **2015**, *15*, 4089−4095.
(530) Shao, M.; Odell, J. H.; Peles, A.; Su, D. The Role of Transition Metals in the Catalytic Activity of Pt Alloys: Quantification of Strain and Ligand Effects. *Chem. Commun.* **2014**, *50*, 2173−2176.
(531) Wroblowa, H. S.; Yen-Chi-Pan; Razumney, G. Electro-reduction of Oxygen: A New Mechanistic Criterion. *J. Electroanal. Chem. Interfacial Electrochem.* **1976**, *69*, 195−201.
(532) Marković, N. M.; Schmidt, T. J.; Stamenković, V.; Ross, P. N. Oxygen Reduction Reaction on Pt and Pt Bimetallic Surfaces: A Selective Review. *Fuel Cells* **2001**, *1*, 105−116.
(533) Oezaslan, M.; Hasché, F.; Strasser, P. Pt-Based Core−Shell Catalyst Architectures for Oxygen Fuel Cell Electrodes. *J. Phys. Chem. Lett.* **2013**, *4*, 3273−3291.
(534) Zhang, Y.; Bu, L.; Jiang, K.; Guo, S.; Huang, X. Concave Pd-Pt Core−Shell Nanocrystals with Ultrathin Pt Shell Feature and Enhanced Catalytic Performance. *Small* **2016**, *12*, 706−712.
(535) Lai, J.; Guo, S. Design of Ultrathin Pt-Based Multimetallic Nanostructures for Efficient Oxygen Reduction Electrocatalysis. *Small* **2017**, *13*, 1702156.
(536) Zhang, S.; Hao, Y.; Su, D.; Doan-Nguyen, V. V. T.; Wu, Y.; Li, J.; Sun, S.; Murray, C. B. Monodisperse Core/Shell Ni/FePt Nanoparticles and Their Conversion to Ni/Pt to Catalyze Oxygen Reduction. *J. Am. Chem. Soc.* **2014**, *136*, 15921−15924.
(537) Lv, H.; Li, D.; Strmcnik, D.; Paulikas, A. P.; Markovic, N. M.; Stamenkovic, V. R. Recent Advances in the Design of Tailored Nanomaterials for Efficient Oxygen Reduction Reaction. *Nano Energy* **2016**, *29*, 149−165.
(538) Wang, X.; Choi, S.-I.; Roling, L. T.; Luo, M.; Ma, C.; Zhang, L.; Chi, M.; Liu, J.; Xie, Z.; Herron, J. A.; Mavrikakis, M.; Xia, Y. Palladium−Platinum Core-Shell Icosahedra with Substantially Enhanced Activity and Durability towards Oxygen Reduction. *Nat. Commun.* **2015**, *6*, 7594.
(539) Sun, Z.; Masa, J.; Xia, W.; König, D.; Ludwig, A.; Li, Z.-A.; Farle, M.; Schuhmann, W.; Muhler, M. Rapid and Surfactant-Free Synthesis of Bimetallic Pt−Cu Nanoparticles Simply via Ultrasound-Assisted Redox Replacement. *ACS Catal.* **2012**, *2*, 1647−1653.
(540) Xu, X.; Zhang, X.; Sun, H.; Yang, Y.; Dai, X.; Gao, J.; Li, X.; Zhang, P.; Wang, H.-H.; Yu, N.-F.; Sun, S.-G. Synthesis of Pt−Ni Alloy Nanocrystals with High-Index Facets and Enhanced Electrocatalytic Properties. *Angew. Chem.* **2014**, *126*, 12730−12735.
(541) Han, L.; Liu, H.; Cui, P.; Peng, Z.; Zhang, S.; Yang, J. Alloy Cu_3Pt Nanoframes through the Structure Evolution in Cu-Pt Nanoparticles with a Core-Shell Construction. *Sci. Rep.* **2015**, *4*, 6414.
(542) Ding, J.; Bu, L.; Guo, S.; Zhao, Z.; Zhu, E.; Huang, Y.; Huang, X. Morphology and Phase Controlled Construction of Pt−Ni Nanostructures for Efficient Electrocatalysis. *Nano Lett.* **2016**, *16*, 2762−2767.
(543) Chen, S.; Niu, Z.; Xie, C.; Gao, M.; Lai, M.; Li, M.; Yang, P. Effects of Catalyst Processing on the Activity and Stability of Pt−Ni Nanoframe Electrocatalysts. *ACS Nano* **2018**, *12*, 8697−8705.
(544) Tu, W.; Chen, K.; Zhu, L.; Zai, H.; E, B.; Ke, X.; Chen, C.; Sui, M.; Chen, Q.; Li, Y. Tungsten-Doping-Induced Surface Reconstruction of Porous Ternary Pt-Based Alloy Electrocatalyst for Oxygen Reduction. *Adv. Funct. Mater.* **2019**, *29*, 1807070.
(545) Koh, S.; Leisch, J.; Toney, M. F.; Strasser, P. Structure-Activity-Stability Relationships of Pt-Co Alloy Electrocatalysts in Gas-Diffusion Electrode Layers. *J. Phys. Chem. C* **2007**, *111*, 3744−3752.
(546) Stamenkovic, V.; Mun, B. S.; Mayrhofer, K. J. J.; Ross, P. N.; Markovic, N. M.; Rossmeisl, J.; Greeley, J.; Nørskov, J. K. Changing the Activity of Electrocatalysts for Oxygen Reduction by Tuning the Surface Electronic Structure. *Angew. Chem., Int. Ed.* **2006**, *45*, 2897−2901.
(547) Stamenkovic, V. R.; Fowler, B.; Mun, B. S.; Wang, G.; Ross, P. N.; Lucas, C. A.; Marković, N. M. Improved Oxygen Reduction Activity on $Pt_3Ni(111)$ via Increased Surface Site Availability. *Science* **2007**, *315*, 493−497.
(548) Mukerjee, S.; Srinivasan, S.; Soriaga, M. P.; McBreen, J. Effect of Preparation Conditions of Pt Alloys on Their Electronic, Structural, and Electrocatalytic Activities for Oxygen Reduction - XRD, XAS, and Electrochemical Studies. *J. Phys. Chem.* **1995**, *99*, 4577−4589.
(549) Stamenkovic, V. R.; Mun, B. S.; Arenz, M.; Mayrhofer, K. J. J.; Lucas, C. A.; Wang, G.; Ross, P. N.; Markovic, N. M. Trends in Electrocatalysis on Extended and Nanoscale Pt-Bimetallic Alloy Surfaces. *Nat. Mater.* **2007**, *6*, 241−247.
(550) Ruban, A.; Hammer, B.; Stoltze, P.; Skriver, H. L.; Nørskov, J. K. Surface Electronic Structure and Reactivity of Transition and Noble Metals. *J. Mol. Catal. A: Chem.* **1997**, *115*, 421−429.
(551) Zhang, S.; Metin, Ö.; Su, D.; Sun, S. Monodisperse AgPd Alloy Nanoparticles and Their Superior Catalysis for the Dehydrogenation of Formic Acid. *Angew. Chem., Int. Ed.* **2013**, *52*, 3681−3684.
(552) Xu, D.; Liu, Z.; Yang, H.; Liu, Q.; Zhang, J.; Fang, J.; Zou, S.; Sun, K. Solution-Based Evolution and Enhanced Methanol Oxidation Activity of Monodisperse Platinum−Copper Nanocubes. *Angew. Chem., Int. Ed.* **2009**, *48*, 4217−4221.
(553) Zhang, J.; Yang, H.; Yang, K.; Fang, J.; Zou, S.; Luo, Z.; Wang, H.; Bae, I.-T.; Jung, D. Y. Monodisperse Pt_3Fe Nanocubes: Synthesis, Characterization, Self-Assembly, and Electrocatalytic Activity. *Adv. Funct. Mater.* **2010**, *20*, 3727−3733.
(554) Luo, M.; Zhao, Z.; Zhang, Y.; Sun, Y.; Xing, Y.; Lv, F.; Yang, Y.; Zhang, X.; Hwang, S.; Qin, Y.; Ma, J.-Y.; Lin, F.; Su, D.; Lu, G.; Guo, S. PdMo Bimetallene for Oxygen Reduction Catalysis. *Nature* **2019**, *574*, 81−85.
(555) Li, X.; An, L.; Wang, X.; Li, F.; Zou, R.; Xia, D. Supported sub-5nm Pt−Fe Intermetallic Compounds for Electrocatalytic Application. *J. Mater. Chem.* **2012**, *22*, 6047−6052.
(556) Cheng, N.; Zhang, L.; Mi, S.; Jiang, H.; Hu, Y.; Jiang, H.; Li, C. $L1_2$ Atomic Ordered Substrate Enhanced Pt-Skin Cu_3Pt Catalyst for Efficient Oxygen Reduction Reaction. *ACS Appl. Mater. Interfaces* **2018**, *10*, 38015−38023.
(557) Rahul, R.; Singh, R. K.; Neergat, M. Effect of Oxidative Heat-Treatment on Electrochemical Properties and Oxygen Reduction Reaction (ORR) Activity of Pd−Co Alloy Catalysts. *J. Electroanal. Chem.* **2014**, *712*, 223−229.
(558) Liu, J.; Sun, C. Q.; Zhu, W. Origin of Efficient Oxygen Reduction Reaction on Pd Monolayer Supported on Pd-M (M = Ni, Fe) Intermetallic Alloy. Electrochim. *Electrochim. Acta* **2018**, *282*, 680−686.
(559) Spendelow, J. S.; Wieckowski, A. Electrocatalysis of Oxygen Reduction and Small Alcohol Oxidation in Alkaline Media. *Phys. Chem. Chem. Phys.* **2007**, *9*, 2654−2675.
(560) Ramaswamy, N.; Mukerjee, S. Fundamental Mechanistic Understanding of Electrocatalysis of Oxygen Reduction on Pt and Non-Pt Surfaces: Acid versus Alkaline Media. *Adv. Phys. Chem.* **2012**, *2012*, 1.
(561) Ge, X.; Sumboja, A.; Wuu, D.; An, T.; Li, B.; Goh, F. W. T.; Hor, T. S. A.; Zong, Y.; Liu, Z. Oxygen Reduction in Alkaline Media: From Mechanisms to Recent Advances of Catalysts. *ACS Catal.* **2015**, *5*, 4643−4667.
(562) Nilsson, A.; Pettersson, L. G. M.; Hammer, B.; Bligaard, T.; Christensen, C. H.; Nørskov, J. K. The Electronic Structure Effect in Heterogeneous Catalysis. *Catal. Lett.* **2005**, *100*, 111−114.
(563) Mavrikakis, M.; Hammer, B.; Nørskov, J. K. Effect of Strain on the Reactivity of Metal Surfaces. *Phys. Rev. Lett.* **1998**, *81*, 2819−2822.
(564) Erikson, H.; Sarapuu, A.; Alexeyeva, N.; Tammeveski, K.; Solla-Gullón, J.; Feliu, J. M. Electrochemical Reduction of Oxygen on Palladium Nanocubes in Acid and Alkaline Solutions. Electrochim. *Electrochim. Acta* **2012**, *59*, 329−335.
(565) Oliveira, M. C.; Rego, R.; Fernandes, L. S.; Tavares, P. B. Evaluation of the Catalytic Activity of Pd−Ag Alloys on Ethanol Oxidation and Oxygen Reduction Reactions in Alkaline Medium. *J. Power Sources* **2011**, *196*, 6092−6098.
(566) Nguyen, A. T. N.; Shim, J. H. Facile One-Step Synthesis of Ir-Pd Bimetallic Alloy Networks as Efficient Bifunctional Catalysts for

https://dx.doi.org/10.1021/acs.chemrev.0c00436
Chem. Rev. 2021, 121, 736−795

Oxygen Reduction and Oxygen Evolution Reactions. *J. Electroanal. Chem.* **2018**, *827*, 120−127.
(567) Gobal, F.; Arab, R. A preliminary Study of the Electro-Catalytic Reduction of Oxygen on Cu−Pd Alloys in Alkaline Solution. *J. Electroanal. Chem.* **2010**, *647*, 66−73.
(568) Shi, Q.; Zhu, C.; Bi, C.; Xia, H.; Engelhard, M. H.; Du, D.; Lin, Y. Intermetallic Pd_3Pb Nanowire Networks Boost Ethanol Oxidation and Oxygen Reduction Reactions with Significantly Improved Methanol Toleranc. *J. Mater. Chem. A* **2017**, *5*, 23952−23959.
(569) Ji, X.; Gao, P.; Zhang, L.; Wang, X.; Wang, F.; Zhu, H.; Yu, J. High-Performance Ordered PdCuFe/C Intermetallic Catalyst for Electrochemical Oxygen Reduction in Proton Exchange Membrane Fuel Cells. *ChemElectroChem* **2019**, *6*, 3065−3070.
(570) Yang, Y.; Xiao, W.; Feng, X.; Xiong, Y.; Gong, M.; Shen, T.; Lu, Y.; Abruña, H. D.; Wang, D. Golden Palladium Zinc Ordered Intermetallics as Oxygen Reduction Electrocatalysts. *ACS Nano* **2019**, *13*, 5968−5974.
(571) Luo, S.; Ou, Y.; Li, L.; Li, J.; Wu, X.; Jiang, Y.; Gao, M.; Yang, X.; Zhang, H.; Yang, D. Intermetallic Pd_3Pb Ultrathin Nanoplate-Constructed Flowers with Low-Coordinated Edge Sites Boost Oxygen Reduction Performance. *Nanoscale* **2019**, *11*, 17301−17307.
(572) Yin, A.-X.; Min, X.-Q.; Zhu, W.; Liu, W.-C.; Zhang, Y.-W.; Yan, C.-H. Pt−Cu and Pt−Pd−Cu Concave Nanocubes with High-Index Facets and Superior Electrocatalytic Activity. *Chem. - Eur. J.* **2012**, *18*, 777−782.
(573) Xia, Z.; Zhang, P.; Feng, G.; Xia, D.; Zhang, J. Crossed PtCoCu Alloy Nanocrystals with High-Index Facets as Highly Active Catalyst for Methanol Oxidation Reaction. *Adv. Mater. Interfaces* **2018**, *5*, 1800297.
(574) Wang, Y.; Zhuo, H.; Sun, H.; Zhang, X.; Dai, X.; Luan, C.; Qin, C.; Zhao, H.; Li, J.; Wang, M.; Ye, J.-Y.; Sun, S.-G. Implanting Mo Atoms into Surface Lattice of Pt_3Mn Alloys Enclosed by High-Indexed Facets: Promoting Highly Active Sites for Ethylene Glycol Oxidation. *ACS Catal.* **2019**, *9*, 442−455.
(575) Xu, Y.; Cui, X.; Wei, S.; Zhang, Q.; Gu, L.; Meng, F.; Fan, J.; Zheng, W. Highly Active Zigzag-Like Pt-Zn Alloy Nanowires with High-Index Facets for Alcohol Electrooxidation. *Nano Res.* **2019**, *12*, 1173−1179.
(576) Tian, N.; Zhou, Z.-Y.; Sun, S.-G.; Ding, Y.; Wang, Z. L. Synthesis of Tetrahexahedral Platinum Nanocrystals with High-Index Facets and High Electro-Oxidation Activity. *Science* **2007**, *316*, 732−735.
(577) Tian, N.; Zhou, Z.-Y.; Sun, S.-G. Platinum Metal Catalysts of High-Index Surfaces: From Single-Crystal Planes to Electrochemically Shape-Controlled Nanoparticles. *J. Phys. Chem. C* **2008**, *112*, 19801−19817.
(578) Wang, C.; Lin, C.; Zhao, B.; Zhang, L.; Kumbhar, A.; Fan, G.; Sun, K.; Zhang, J.; Chen, S.; Fang, J. High-Indexed Pt_3Fe Nanocatalysts and Their Enhanced Catalytic Performance in Dual Organic Reactions. *ChemNanoMat* **2015**, *1*, 331−337.
(579) Zhang, B.-W.; He, C.-L.; Jiang, Y.-X.; Chen, M.-H.; Li, Y.-Y.; Rao, L.; Sun, S.-G. High Activity of PtBi Intermetallics Supported on Mesoporous Carbon towards HCOOH Electro-Oxidation. *Electrochem. Commun.* **2012**, *25*, 105−108.
(580) Kwon, T.; Lim, S.; Jun, M.; Kang, M.; Joo, J.; Oh, A.; Baik, H.; Hong, C. S.; Lee, K. $Pt2^+$-Exchanged ZIF-8 Nanocube as a Solid-State Precursor for $L1_0$-PtZn Intermetallic Nanoparticles Embedded in a Hollow Carbon Nanocage. *Nanoscale* **2020**, *12*, 1118−1127.
(581) Wang, H.; Abruña, H. D. Rh and Rh Alloy Nanoparticles as Highly Active H_2 Oxidation Catalysts for Alkaline Fuel Cells. *ACS Catal.* **2019**, *9*, 5057−5062.
(582) Saleem, F.; Zhang, Z.; Cui, X.; Gong, Y.; Chen, B.; Lai, Z.; Yun, Q.; Gu, L.; Zhang, H. Elemental Segregation in Multimetallic Core−Shell Nanoplates. *J. Am. Chem. Soc.* **2019**, *141*, 14496−14500.
(583) Yun, Q.; Lu, Q.; Li, C.; Chen, B.; Zhang, Q.; He, Q.; Hu, Z.; Zhang, Z.; Ge, Y.; Yang, N.; Ge, J.; He, Y.-B.; Gu, L.; Zhang, H. Synthesis of PdM (M = Zn, Cd, ZnCd) Nanosheets with an Unconventional Face-Centered Tetragonal Phase as Highly Efficient Electrocatalysts for Ethanol Oxidation. *ACS Nano* **2019**, *13*, 14329−14336.
(584) Voiry, D.; Shin, H. S.; Loh, K. P.; Chhowalla, M. Low-Dimensional Catalysts for Hydrogen Evolution and CO_2 Reduction. *Nat. Rev. Chem.* **2018**, *2*, 0105.
(585) van Troostwijk, A. P.; Deiman, J. Sur Une Manière de Décomposer l'Eau en Air Inflammable et en Air Vital. Obs. *Phys.* **1789**, *35*, 369.
(586) Jing, S.; Zhang, L.; Luo, L.; Lu, J.; Yin, S.; Shen, P. K.; Tsiakaras, P. N-Doped Porous Molybdenum Carbide Nanobelts as Efficient Catalysts for Hydrogen Evolution Reaction. *Appl. Catal., B* **2018**, *224*, 533−540.
(587) Han, N.; Yang, K. R.; Lu, Z.; Li, Y.; Xu, W.; Gao, T.; Cai, Z.; Zhang, Y.; Batista, V. S.; Liu, W.; Sun, X. Nitrogen-Doped Tungsten Carbide Nanoarray as An Efficient Bifunctional Electrocatalyst for Water Splitting in Acid. *Nat. Commun.* **2018**, *9*, 924.
(588) Chen, J. G. Carbide and Nitride Overlayers on Early Transition Metal Surfaces: Preparation, Characterization, and Reactivities. *Chem. Rev.* **1996**, *96*, 1477−1498.
(589) Hwu, H. H.; Chen, J. G. Surface Chemistry of Transition Metal Carbides. *Chem. Rev.* **2005**, *105*, 185−212.
(590) Chen, W.-F.; Muckerman, J. T.; Fujita, E. Recent Developments in Transition Metal Carbides and Nitrides as Hydrogen Evolution Electrocatalysts. *Chem. Commun.* **2013**, *49*, 8896−8909.
(591) Cabán-Acevedo, M.; Stone, M. L.; Schmidt, J. R.; Thomas, J. G.; Ding, Q.; Chang, H.-C.; Tsai, M.-L.; He, J.-H.; Jin, S. Efficient Hydrogen Evolution Catalysis Using Ternary Pyrite-Type Cobalt Phosphosulphide. *Nat. Mater.* **2015**, *14*, 1245−1251.
(592) Jaramillo, T. F.; Jørgensen, K. P.; Bonde, J.; Nielsen, J. H.; Horch, S.; Chorkendorff, I. Identification of Active Edge Sites for Electrochemical H_2 Evolution from MoS_2 Nanocatalysts. *Science* **2007**, *317*, 100−102.
(593) Kibsgaard, J.; Jaramillo, T. F.; Besenbacher, F. Building an Appropriate Active-Site Motif into a Hydrogen-Evolution Catalyst with Thiomolybdate $[Mo_3S_{13}]^{2-}$ Clusters. *Nat. Chem.* **2014**, *6*, 248−253.
(594) Subbaraman, R.; Tripkovic, D.; Chang, K.-C.; Strmcnik, D.; Paulikas, A. P.; Hirunsit, P.; Chan, M.; Greeley, J.; Stamenkovic, V.; Markovic, N. M. Trends in Activity for the Water Electrolyser Reactions on 3d M(Ni,Co,Fe,Mn) Hydr(oxy)oxide Catalysts. *Nat. Mater.* **2012**, *11*, 550−557.
(595) Menezes, P. W.; Panda, C.; Garai, S.; Walter, C.; Guiet, A.; Driess, M. Structurally Ordered Intermetallic Cobalt Stannide Nanocrystals for High-Performance Electrocatalytic Overall Water-Splitting. *Angew. Chem.* **2018**, *130*, 15457−15462.
(596) Wang, C.; Yang, H.; Zhang, Y.; Wang, Q. NiFe Alloy Nanoparticles with *hcp* Crystal Structure Stimulate Superior Oxygen Evolution Reaction Electrocatalytic Activity. *Angew. Chem., Int. Ed.* **2019**, *58*, 6099−6103.
(597) Stamenkovic, V. R.; Strmcnik, D.; Lopes, P. P.; Markovic, N. M. Energy and Fuels from Electrochemical Interfaces. *Nat. Mater.* **2017**, *16*, 57−69.
(598) Mahmood, N.; Yao, Y.; Zhang, J.-W.; Pan, L.; Zhang, X.; Zou, J.-J. Electrocatalysts for Hydrogen Evolution in Alkaline Electrolytes: Mechanisms, Challenges, and Prospective Solutions. *Adv. Sci.* **2018**, *5*, 1700464.
(599) Sheng, W.; Gasteiger, H. A.; Shao-Horn, Y. Hydrogen Oxidation and Evolution Reaction Kinetics on Platinum: Acid vs Alkaline Electrolytes. *J. Electrochem. Soc.* **2010**, *157*, B1529−B1536.
(600) Subbaraman, R.; Tripkovic, D.; Strmcnik, D.; Chang, K.-C.; Uchimura, M.; Paulikas, A. P.; Stamenkovic, V.; Markovic, N. M. Enhancing Hydrogen Evolution Activity in Water Splitting by Tailoring Li^+-Ni$(OH)_2$-Pt Interfaces. *Science* **2011**, *334*, 1256−1260.
(601) Staszak-Jirkovsky, J.; Malliakas, C. D.; Lopes, P. P.; Danilovic, N.; Kota, S. S.; Chang, K.-C.; Genorio, B.; Strmcnik, D.; Stamenkovic, V. R.; Kanatzidis, M. G.; Markovic, N. M. Design of Active and Stable Co−Mo−S_x Chalcogels as pH-Universal Catalysts for the Hydrogen Evolution Reaction. *Nat. Mater.* **2016**, *15*, 197−203.

https://dx.doi.org/10.1021/acs.chemrev.0c00436
Chem. Rev. 2021, 121, 736−795

(602) Liu, Z.; Qi, J.; Liu, M.; Zhang, S.; Fan, Q.; Liu, H.; Liu, K.; Zheng, H.; Yin, Y.; Gao, C. Aqueous Synthesis of Ultrathin Platinum/Non-Noble Metal Alloy Nanowires for Enhanced Hydrogen Evolution Activity. *Angew. Chem.* **2018**, *130*, 11852−11856.
(603) Shan, J.; Ling, T.; Davey, K.; Zheng, Y.; Qiao, S.-Z. Transition-Metal-Doped RuIr Bifunctional Nanocrystals for Overall Water Splitting in Acidic Environments. *Adv. Mater.* **2019**, *31*, 1900510.
(604) Strmcnik, D.; Uchimura, M.; Wang, C.; Subbaraman, R.; Danilovic, N.; van der Vliet, D.; Paulikas, A. P.; Stamenkovic, V. R.; Markovic, N. M. Improving the Hydrogen Oxidation Reaction Rate by Promotion of Hydroxyl Adsorption. *Nat. Chem.* **2013**, *5*, 300−306.
(605) Fabbri, E.; Habereder, A.; Waltar, K.; Kötz, R.; Schmidt, T. J. Developments and Perspectives of Oxide-Based Catalysts for the Oxygen Evolution Reaction. *Catal. Sci. Technol.* **2014**, *4*, 3800−3821.
(606) Danilovic, N.; Subbaraman, R.; Chang, K. C.; Chang, S. H.; Kang, Y.; Snyder, J.; Paulikas, A. P.; Strmcnik, D.; Kim, Y. T.; Myers, D.; Stamenkovic, V. R.; Markovic, N. M. Using Surface Segregation To Design Stable Ru-Ir Oxides for the Oxygen Evolution Reaction in Acidic Environments. *Angew. Chem., Int. Ed.* **2014**, *53*, 14016−14021.
(607) Chauhan, M.; Reddy, K. P.; Gopinath, C. S.; Deka, S. Copper Cobalt Sulfide Nanosheets Realizing a Promising Electrocatalytic Oxygen Evolution Reaction. *ACS Catal.* **2017**, *7*, 5871−5879.
(608) Artz, J.; Müller, T. E.; Thenert, K.; Kleinekorte, J.; Meys, R.; Sternberg, A.; Bardow, A.; Leitner, W. Sustainable Conversion of Carbon Dioxide: An Integrated Review of Catalysis and Life Cycle Assessment. *Chem. Rev.* **2018**, *118*, 434−504.
(609) Kato, S.; Matam, S. K.; Kerger, P.; Bernard, L.; Battaglia, C.; Vogel, D.; Rohwerder, M.; Züttel, A. The Origin of the Catalytic Activity of a Metal Hydride in CO_2 Reduction. *Angew. Chem.* **2016**, *128*, 6132−6136.
(610) Kubacka, A.; Fernández-García, M.; Colón, G. Advanced Nanoarchitectures for Solar Photocatalytic Applications. *Chem. Rev.* **2012**, *112*, 1555−1614.
(611) Roy, S. C.; Varghese, O. K.; Paulose, M.; Grimes, C. A. Toward Solar Fuels: Photocatalytic Conversion of Carbon Dioxide to Hydrocarbons. *ACS Nano* **2010**, *4*, 1259−1278.
(612) Benson, E. E.; Kubiak, C. P.; Sathrum, A. J.; Smieja, J. M. Electrocatalytic and Homogeneous Approaches to Conversion of CO_2 to Liquid Fuels. *Chem. Soc. Rev.* **2009**, *38*, 89−99.
(613) Costentin, C.; Robert, M.; Saveant, J.-M. Catalysis of the Electrochemical Reduction of Carbon Dioxide. *Chem. Soc. Rev.* **2013**, *42*, 2423−2436.
(614) Li, C. W.; Ciston, J.; Kanan, M. W. Electroreduction of Carbon Monoxide to Liquid Fuel on Oxide-Derived Nanocrystalline Copper. *Nature* **2014**, *508*, 504−507.
(615) Spinner, N. S.; Vega, J. A.; Mustain, W. E. Recent Progress in the Electrochemical Conversion and Utilization of CO_2. *Catal. Sci. Technol.* **2012**, *2*, 19−28.
(616) Qiao, J.; Liu, Y.; Hong, F.; Zhang, J. A Review of Catalysts for the Electroreduction of Carbon Dioxide to Produce Low-Carbon Fuels. *Chem. Soc. Rev.* **2014**, *43*, 631−675.
(617) Hanc-Scherer, F. A.; Montiel, M. A.; Montiel, V.; Herrero, E.; Sánchez-Sánchez, C. M. Surface Structured Platinum Electrodes for the Electrochemical Reduction of Carbon Dioxide in Imidazolium Based Ionic Liquids. *Phys. Chem. Chem. Phys.* **2015**, *17*, 23909−23916.
(618) Umeda, M.; Niitsuma, Y.; Horikawa, T.; Matsuda, S.; Osawa, M. Electrochemical Reduction of CO_2 to Methane on Platinum Catalysts without Overpotentials: Strategies for Improving Conversion Efficiency. *ACS Appl. Energy Mater.* **2020**, *3*, 1119−1127.
(619) Gao, D.; Zhou, H.; Wang, J.; Miao, S.; Yang, F.; Wang, G.; Wang, J.; Bao, X. Size-Dependent Electrocatalytic Reduction of CO_2 over Pd Nanoparticles. *J. Am. Chem. Soc.* **2015**, *137*, 4288−4291.
(620) Zhu, W.; Michalsky, R.; Metin, Ö.; Lv, H.; Guo, S.; Wright, C. J.; Sun, X.; Peterson, A. A.; Sun, S. Monodisperse Au Nanoparticles for Selective Electrocatalytic Reduction of CO_2 to CO. *J. Am. Chem. Soc.* **2013**, *135*, 16833−16836.
(621) Takahashi, I.; Koga, O.; Hoshi, N.; Hori, Y. Electrochemical Reduction of CO_2 at Copper Single Crystal Cu(S)-[n(111)×(111)] and Cu(S)-[n(110)×(100)] Electrodes. *J. Electroanal. Chem.* **2002**, *533*, 135−143.
(622) Vasileff, A.; Xu, C.; Jiao, Y.; Zheng, Y.; Qiao, S.-Z. Surface and Interface Engineering in Copper-Based Bimetallic Materials for Selective CO_2 Electroreduction. *Chem.* **2018**, *4*, 1809−1831.
(623) Jiang, K.; Sandberg, R. B.; Akey, A. J.; Liu, X.; Bell, D. C.; Nørskov, J. K.; Chan, K.; Wang, H. Metal Ion Cycling of Cu Foil for Selective C−C Coupling in Electrochemical CO_2 Reduction. *Nat. Catal.* **2018**, *1*, 111−119.
(624) Gao, S.; Lin, Y.; Jiao, X.; Sun, Y.; Luo, Q.; Zhang, W.; Li, D.; Yang, J.; Xie, Y. Partially Oxidized Atomic Cobalt Layers for Carbon Dioxide Electroreduction to Liquid Fuel. *Nature* **2016**, *529*, 68−71.
(625) Bohlen, B.; Wastl, D.; Radomski, J.; Sieber, V.; Vieira, L. Electrochemical CO_2 Reduction to Formate on Indium Catalysts Prepared by Electrodeposition in Deep Eutectic Solvents. *Electrochem. Commun.* **2020**, *110*, 106597.
(626) Lu, Q.; Rosen, J.; Zhou, Y.; Hutchings, G. S.; Kimmel, Y. C.; Chen, J. G.; Jiao, F. A Selective and Efficient Electrocatalyst for Carbon Dioxide Reduction. *Nat. Commun.* **2014**, *5*, 3242.
(627) Kuhl, K. P.; Hatsukade, T.; Cave, E. R.; Abram, D. N.; Kibsgaard, J.; Jaramillo, T. F. Electrocatalytic Conversion of Carbon Dioxide to Methane and Methanol on Transition Metal Surfaces. *J. Am. Chem. Soc.* **2014**, *136*, 14107−14113.
(628) Hegner, R.; Rosa, L. F. M.; Harnisch, F. Electrochemical CO_2 Reduction to Formate at Indium Electrodes with High Efficiency and Selectivity in pH Neutral Electrolytes. *Appl. Catal., B* **2018**, *238*, 546−556.
(629) Yin, Z.; Gao, D.; Yao, S.; Zhao, B.; Cai, F.; Lin, L.; Tang, P.; Zhai, P.; Wang, G.; Ma, D.; Bao, X. Highly Selective Palladium-Copper Bimetallic Electrocatalysts for the Electrochemical Reduction of CO_2 to CO. *Nano Energy* **2016**, *27*, 35−43.
(630) Nie, X.; Jiang, X.; Wang, H.; Luo, W.; Janik, M. J.; Chen, Y.; Guo, X.; Song, C. Mechanistic Understanding of Alloy Effect and Water Promotion for Pd-Cu Bimetallic Catalysts in CO_2 Hydrogenation to Methanol. *ACS Catal.* **2018**, *8*, 4873−4892.
(631) Watanabe, M.; Shibata, M.; Kato, A.; Azuma, M.; Sakata, T. Design of Alloy Electrocatalysts for CO_2 Reduction. *J. Electrochem. Soc.* **1991**, *138*, 3382−3389.
(632) Larrazábal, G. n. O.; Martin, A. J.; Mitchell, S.; Hauert, R.; Pérez-Ramírez, J. Enhanced Reduction of CO_2 to CO over Cu−In Electrocatalysts: Catalyst Evolution Is the Key. *ACS Catal.* **2016**, *6*, 6265−6274.
(633) Rasul, S.; Anjum, D. H.; Jedidi, A.; Minenkov, Y.; Cavallo, L.; Takanabe, K. A Highly Selective Copper−Indium Bimetallic Electrocatalyst for the Electrochemical Reduction of Aqueous CO_2 to CO. *Angew. Chem., Int. Ed.* **2015**, *54*, 2146−2150.
(634) Kuhl, K. P.; Cave, E. R.; Abram, D. N.; Jaramillo, T. F. New Insights into the Electrochemical Reduction of Carbon Dioxide on Metallic Copper Surfaces. *Energy Environ. Sci.* **2012**, *5*, 7050−7059.
(635) Manthiram, K.; Beberwyck, B. J.; Alivisatos, A. P. Enhanced Electrochemical Methanation of Carbon Dioxide with a Dispersible Nanoscale Copper Catalyst. *J. Am. Chem. Soc.* **2014**, *136*, 13319−13325.
(636) Baturina, O. A.; Lu, Q.; Padilla, M. A.; Xin, L.; Li, W.; Serov, A.; Artyushkova, K.; Atanassov, P.; Xu, F.; Epshteyn, A.; Brintlinger, T.; Schuette, M.; Collins, G. E. CO_2 Electroreduction to Hydrocarbons on Carbon-Supported Cu Nanoparticles. *ACS Catal.* **2014**, *4*, 3682−3695.
(637) Reske, R.; Mistry, H.; Behafarid, F.; Roldan Cuenya, B.; Strasser, P. Particle Size Effects in the Catalytic Electroreduction of CO_2 on Cu Nanoparticles. *J. Am. Chem. Soc.* **2014**, *136*, 6978−6986.
(638) Kortlever, R.; Shen, J.; Schouten, K. J. P.; Calle-Vallejo, F.; Koper, M. T. M. Catalysts and Reaction Pathways for the Electrochemical Reduction of Carbon Dioxide. *J. Phys. Chem. Lett.* **2015**, *6*, 4073−4082.
(639) Graves, C.; Ebbesen, S. D.; Mogensen, M.; Lackner, K. S. Sustainable Hydrocarbon Fuels by Recycling CO_2 and H_2O with

https://dx.doi.org/10.1021/acs.chemrev.0c00436
Chem. Rev. 2021, 121, 736−795

Renewable or Nuclear Energy. *Renewable Sustainable Energy Rev.* **2011**, *15*, 1−23.
(640) Schouten, K. J. P.; Kwon, Y.; van der Ham, C. J. M.; Qin, Z.; Koper, M. T. M. A New Mechanism for the Selectivity to C_1 and C_2 Species in the Electrochemical Reduction of Carbon Dioxide on Copper Electrodes. *Chem. Sci.* **2011**, *2*, 1902−1909.
(641) Gattrell, M.; Gupta, N.; Co, A. A Review of the Aqueous Electrochemical Reduction of CO_2 to Hydrocarbons at Copper. *J. Electroanal. Chem.* **2006**, *594*, 1−19.
(642) Schouten, K. J. P.; Pérez Gallent, E.; Koper, M. T. M. Structure Sensitivity of the Electrochemical Reduction of Carbon Monoxide on Copper Single Crystals. *ACS Catal.* **2013**, *3*, 1292−1295.
(643) Schouten, K. J. P.; Qin, Z.; Perez Gallent, E.; Koper, M. T. M. Two Pathways for the Formation of Ethylene in CO Reduction on Single-Crystal Copper Electrodes. *J. Am. Chem. Soc.* **2012**, *134*, 9864−9867.
(644) Gawande, M. B.; Goswami, A.; Felpin, F.-X.; Asefa, T.; Huang, X.; Silva, R.; Zou, X.; Zboril, R.; Varma, R. S. Cu and Cu-Based Nanoparticles: Synthesis and Applications in Catalysis. *Chem. Rev.* **2016**, *116*, 3722−3811.
(645) Mistry, H.; Varela, A. S.; Kühl, S.; Strasser, P.; Cuenya, B. R. Nanostructured Electrocatalysts with Tunable Activity and Selectivity. *Nat. Rev. Mater.* **2016**, *1*, 16009.
(646) Wang, Z.; Yang, G.; Zhang, Z.; Jin, M.; Yin, Y. Selectivity on Etching: Creation of High-Energy Facets on Copper Nanocrystals for CO_2 Electrochemical Reduction. *ACS Nano* **2016**, *10*, 4559−4564.
(647) De Luna, P.; Quintero-Bermudez, R.; Dinh, C.-T.; Ross, M. B.; Bushuyev, O. S.; Todorović, P.; Regier, T.; Kelley, S. O.; Yang, P.; Sargent, E. H. Catalyst Electro-Redeposition Controls Morphology and Oxidation State for Selective Carbon Dioxide Reduction. *Nat. Catal.* **2018**, *1*, 103−110.
(648) Roberts, F. S.; Kuhl, K. P.; Nilsson, A. High Selectivity for Ethylene from Carbon Dioxide Reduction over Copper Nanocube Electrocatalysts. *Angew. Chem.* **2015**, *127*, 5268−5271.
(649) Loiudice, A.; Lobaccaro, P.; Kamali, E. A.; Thao, T.; Huang, B. H.; Ager, J. W.; Buonsanti, R. Tailoring Copper Nanocrystals towards C_2 Products in Electrochemical CO_2 Reduction. *Angew. Chem., Int. Ed.* **2016**, *55*, 5789−5792.
(650) Yang, Y.; White, M. G.; Liu, P. Theoretical Study of Methanol Synthesis from CO_2 Hydrogenation on Metal-Doped Cu(111) Surfaces. *J. Phys. Chem. C* **2012**, *116*, 248−256.
(651) Ross, M. B.; De Luna, P.; Li, Y.; Dinh, C.-T.; Kim, D.; Yang, P.; Sargent, E. H. Designing Materials for Electrochemical Carbon Dioxide Recycling. *Nat. Catal.* **2019**, *2*, 648−658.
(652) Ross, M. B.; Dinh, C. T.; Li, Y.; Kim, D.; De Luna, P.; Sargent, E. H.; Yang, P. Tunable Cu Enrichment Enables Designer Syngas Electrosynthesis from CO_2. *J. Am. Chem. Soc.* **2017**, *139*, 9359−9363.
(653) Foit, S. R.; Vinke, I. C.; de Haart, L. G. J.; Eichel, R.-A. Power-to-Syngas: An Enabling Technology for the Transition of the Energy System? *Angew. Chem., Int. Ed.* **2017**, *56*, 5402−5411.
(654) Burch, R. Platinum-Tin Reforming Catalysts: I. The Oxidation State of Tin and the Interaction between Platinum and Tin. *J. Catal.* **1981**, *71*, 348−359.
(655) Jin, X.; Zhao, M.; Shen, J.; Yan, W.; He, L.; Thapa, P. S.; Ren, S.; Subramaniam, B.; Chaudhari, R. V. Exceptional Performance of Bimetallic Pt_1Cu_3/TiO_2 Nanocatalysts for Oxidation of Gluconic Acid and Glucose with O_2 to Glucaric Acid. *J. Catal.* **2015**, *330*, 323−329.
(656) Shiraishi, Y.; Sakamoto, H.; Sugano, Y.; Ichikawa, S.; Hirai, T. Pt−Cu Bimetallic Alloy Nanoparticles Supported on Anatase TiO_2: Highly Active Catalysts for Aerobic Oxidation Driven by Visible Light. *ACS Nano* **2013**, *7*, 9287−9297.
(657) Jin, X.; Yan, H.; Zeng, C.; Thapa, P. S.; Subramaniam, B.; Chaudhari, R. V. Phase Transformed PtFe Nanocomposites Show Enhanced Catalytic Performances in Oxidation of Glycerol to Tartronic Acid. *Ind. Eng. Chem. Res.* **2017**, *56*, 13157−13164.
(658) Jin, X.; Zhao, M.; Vora, M.; Shen, J.; Zeng, C.; Yan, W.; Thapa, P. S.; Subramaniam, B.; Chaudhari, R. V. Synergistic Effects of Bimetallic $PtPd/TiO_2$ Nanocatalysts in Oxidation of Glucose to Glucaric Acid: Structure Dependent Activity and Selectivity. *Ind. Eng. Chem. Res.* **2016**, *55*, 2932−2945.
(659) Wu, Y.; Cai, S.; Wang, D.; He, W.; Li, Y. Syntheses of Water-Soluble Octahedral, Truncated Octahedral, and Cubic Pt−Ni Nanocrystals and Their Structure−Activity Study in Model Hydrogenation Reactions. *J. Am. Chem. Soc.* **2012**, *134*, 8975−8981.
(660) Ab Rahim, M. H.; Forde, M. M.; Jenkins, R. L.; Hammond, C.; He, Q.; Dimitratos, N.; Lopez-Sanchez, J. A.; Carley, A. F.; Taylor, S. H.; Willock, D. J.; Murphy, D. M.; Kiely, C. J.; Hutchings, G. J. Oxidation of Methane to Methanol with Hydrogen Peroxide Using Supported Gold−Palladium Alloy Nanoparticles. *Angew. Chem., Int. Ed.* **2013**, *52*, 1280−1284.
(661) Wang, L.; Zhao, S.; Liu, C.; Li, C.; Li, X.; Li, H.; Wang, Y.; Ma, C.; Li, Z.; Zeng, J. Aerobic Oxidation of Cyclohexane on Catalysts Based on Twinned and Single-Crystal $Au_{75}Pd_{25}$ Bimetallic Nanocrystals. *Nano Lett.* **2015**, *15*, 2875−2880.
(662) Giannakakis, G.; Trimpalis, A.; Shan, J.; Qi, Z.; Cao, S.; Liu, J.; Ye, J.; Biener, J.; Flytzani-Stephanopoulos, M. NiAu Single Atom Alloys for the Non-Oxidative Dehydrogenation of Ethanol to Acetaldehyde and Hydrogen. *Top. Catal.* **2018**, *61*, 475−486.
(663) Sachtler, J. W. A.; Somorjai, G. A. Cyclohexane Dehydrogenation Catalyzed by Bimetallic Au-Pt(111) Single-Crystal Surfaces. *J. Catal.* **1984**, *89*, 35−43.
(664) Kumar, M.; Deka, S. Multiply Twinned AgNi Alloy Nanoparticles as Highly Active Catalyst for Multiple Reduction and Degradation Reactions. *ACS Appl. Mater. Interfaces* **2014**, *6*, 16071−16081.
(665) Armbrüster, M.; Schlögl, R.; Grin, Y. Intermetallic Compounds in Heterogeneous Catalysis—A Quickly Developing Field. *Sci. Technol. Adv. Mater.* **2014**, *15*, 034803.
(666) Cao, S.; Tao, F.; Tang, Y.; Li, Y.; Yu, J. Size- and Shape-Dependent Catalytic Performances of Oxidation and Reduction Reactions on Nanocatalysts. *Chem. Soc. Rev.* **2016**, *45*, 4747−4765.
(667) Armbrüster, M.; Kovnir, K.; Behrens, M.; Teschner, D.; Grin, Y.; Schlögl, R. Pd-Ga Intermetallic Compounds as Highly Selective Semihydrogenation Catalysts. *J. Am. Chem. Soc.* **2010**, *132*, 14745−14747.
(668) Friedrich, M.; Villaseca, S. A.; Szentmiklósi, L.; Teschner, D.; Armbrüster, M. Order-Induced Selectivity Increase of $Cu_{60}Pd_{40}$ in the Semi-Hydrogenation of Acetylene. Mater. *Materials* **2013**, *6*, 2958−2977.
(669) Fiordaliso, E. M.; Sharafutdinov, I.; Carvalho, H. W. P.; Grunwaldt, J.-D.; Hansen, T. W.; Chorkendorff, I.; Wagner, J. B.; Damsgaard, C. D. Intermetallic $GaPd_2$ Nanoparticles on SiO_2 for Low-Pressure CO_2 Hydrogenation to Methanol: Catalytic Performance and In Situ Characterization. *ACS Catal.* **2015**, *5*, 5827−5836.
(670) Garcia-Trenco, A.; Regoutz, A.; White, E. R.; Payne, D. J.; Shaffer, M. S.P.; Williams, C. K. PdIn Intermetallic Nanoparticles for the Hydrogenation of CO_2 to Methanol. *Appl. Catal., B* **2018**, *220*, 9−18.
(671) Gentzen, M.; Doronkin, D. E.; Sheppard, T. L.; Zimina, A.; Li, H.; Jelic, J.; Studt, F.; Grunwaldt, J. D.; Sauer, J.; Behrens, S. Supported Intermetallic PdZn Nanoparticles as Bifunctional Catalysts for the Direct Synthesis of Dimethyl Ether from CO-Rich Synthesis Gas. *Angew. Chem., Int. Ed.* **2019**, *58*, 15655−15659.
(672) Liz-Marzán, L. M.; Murphy, C. J.; Wang, J. *Chem. Soc. Rev.* **2014**, *43*, 3820−3822.
(673) Rycenga, M.; Cobley, C. M.; Zeng, J.; Li, W.; Moran, C. H.; Zhang, Q.; Qin, D.; Xia, Y. Controlling the Synthesis and Assembly of Silver Nanostructures for Plasmonic Applications. *Chem. Rev.* **2011**, *111*, 3669−3712.
(674) Willets, K. A.; Van Duyne, R. P. Localized Surface Plasmon Resonance Spectroscopy and Sensing. *Annu. Rev. Phys. Chem.* **2007**, *58*, 267−297.
(675) Sanz, J. M.; Ortiz, D.; Alcaraz de la Osa, R.; Saiz, J. M.; González, F.; Brown, A. S.; Losurdo, M.; Everitt, H. O.; Moreno, F. UV Plasmonic Behavior of Various Metal Nanoparticles in the Near- and Far-Field Regimes: Geometry and Substrate Effects. *J. Phys. Chem. C* **2013**, *117*, 19606−19615.

https://dx.doi.org/10.1021/acs.chemrev.0c00436
Chem. Rev. 2021, 121, 736−795

(676) Link, S.; Wang, Z. L.; El-Sayed, M. A. Alloy Formation of Gold−Silver Nanoparticles and the Dependence of the Plasmon Absorption on Their Composition. *J. Phys. Chem. B* **1999**, *103*, 3529−3533.
(677) Moskovits, M.; Srnová-Šloufová, I.; Vlčková, B. Bimetallic Ag−Au Nanoparticles: Extracting Meaningful Optical Constants from the Surface-Plasmon Extinction Spectrum. *J. Chem. Phys.* **2002**, *116*, 10435−10446.
(678) Kim, M.-J.; Na, H.-J.; Lee, K. C.; Yoo, E. A.; Lee, M. Preparation and Characterization of Au−Ag and Au−Cu Alloy Nanoparticles in Chloroform. *J. Mater. Chem.* **2003**, *13*, 1789−1792.
(679) Smetana, A. B.; Klabunde, K. J.; Sorensen, C. M.; Ponce, A. A.; Mwale, B. Low-Temperature Metallic Alloying of Copper and Silver Nanoparticles with Gold Nanoparticles through Digestive Ripening. *J. Phys. Chem. B* **2006**, *110*, 2155−2158.
(680) Liu, K.; Bai, Y.; Zhang, L.; Yang, Z.; Fan, Q.; Zheng, H.; Yin, Y.; Gao, C. Porous Au-Ag Nanospheres with High-Density and Highly Accessible Hotspots for SERS Analysis. *Nano Lett.* **2016**, *16*, 3675−3681.
(681) Wei, J.; Guo, Y.; Li, J.; Yuan, M.; Long, T.; Liu, Z. Optically Active Ultrafine Au-Ag Alloy Nanoparticles Used for Colorimetric Chiral Recognition and Circular Dichroism Sensing of Enantiomers. *Anal. Chem.* **2017**, *89*, 9781−9787.
(682) Cattaruzza, E.; Battaglin, G.; Gonella, F.; Polloni, R.; Scremin, B. F.; Mattei, G.; Mazzoldi, P.; Sada, C. Au-Cu Nanoparticles in Silica Glass as Composite Material for Photonic Applications. *Appl. Surf. Sci.* **2007**, *254*, 1017−1021.
(683) Andolina, C. M.; Dewar, A. C.; Smith, A. M.; Marbella, L. E.; Hartmann, M. J.; Millstone, J. E. Photoluminescent Gold-Copper Nanoparticle Alloys with Composition-Tunable Near-Infrared Emission. *J. Am. Chem. Soc.* **2013**, *135*, 5266−5269.
(684) Hajfathalian, M.; Gilroy, K. D.; Yaghoubzade, A.; Sundar, A.; Tan, T.; Hughes, R. A.; Neretina, S. Photocatalytic Enhancements to the Reduction of 4-Nitrophenol by Resonantly Excited Triangular Gold-Copper Nanostructures. *J. Phys. Chem. C* **2015**, *119*, 17308−17315.
(685) Cortie, M. B.; McDonagh, A. M. Synthesis and Optical Properties of Hybrid and Alloy Plasmonic Nanoparticles. *Chem. Rev.* **2011**, *111*, 3713−3735.
(686) Zhang, J.; Winget, S. A.; Wu, Y.; Su, D.; Sun, X.; Xie, Z.-X.; Qin, D. Ag@Au Concave Cuboctahedra: A Unique Probe for Monitoring Au-Catalyzed Reduction and Oxidation Reactions by Surface-Enhanced Raman Spectroscopy. *ACS Nano* **2016**, *10*, 2607−2616.
(687) Wu, D.-Y.; Liu, X.-M.; Duan, S.; Xu, X.; Ren, B.; Lin, S.-H.; Tian, Z.-Q. Chemical Enhancement Effects in SERS Spectra: A Quantum Chemical Study of Pyridine Interacting with Copper, Silver, Gold and Platinum Metals. *J. Phys. Chem. C* **2008**, *112*, 4195−4204.
(688) Yang, M.; Chen, T.; Lau, W. S.; Wang, Y.; Tang, Q.; Yang, Y.; Chen, H. Development of Polymer-Encapsulated Metal Nanoparticles as Surface-Enhanced Raman Scattering Probes. *Small* **2009**, *5*, 198−202.
(689) Linic, S.; Aslam, U.; Boerigter, C.; Morabito, M. Photochemical Transformations on Plasmonic Metal Nanoparticles. *Nat. Mater.* **2015**, *14*, 567−576.
(690) Liu, Z.; Hou, W.; Pavaskar, P.; Aykol, M.; Cronin, S. B. Plasmon Resonant Enhancement of Photocatalytic Water Splitting Under Visible Illumination. *Nano Lett.* **2011**, *11*, 1111−1116.
(691) Christopher, P.; Xin, H.; Linic, S. Visible-Light-Enhanced Catalytic Oxidation Reactions on Plasmonic Silver Nanostructures. *Nat. Chem.* **2011**, *3*, 467−472.
(692) Honda, M.; Kumamoto, Y.; Taguchi, A.; Saito, Y.; Kawata, S. Plasmon-Enhanced UV Photocatalysis. *Appl. Phys. Lett.* **2014**, *104*, 061108.
(693) Sun, M.; Xu, H. A Novel Application of Plasmonics: Plasmon-Driven Surface-Catalyzed Reactions. *Small* **2012**, *8*, 2777−2786.
(694) Reineck, P.; Lee, G. P.; Brick, D.; Karg, M.; Mulvaney, P.; Bach, U. A Solid-State Plasmonic Solar Cell via Metal Nanoparticle Self-Assembly. *Adv. Mater.* **2012**, *24*, 4750−4755.
(695) Mubeen, S.; Lee, J.; Singh, N.; Krämer, S.; Stucky, G. D.; Moskovits, M. An Autonomous Photosynthetic Device in Which All Charge Carriers Derive from Surface Plasmons. *Nat. Nanotechnol.* **2013**, *8*, 247−251.
(696) Dreaden, E. C.; Alkilany, A. M.; Huang, X.; Murphy, C. J.; El-Sayed, M. A. The Golden Age: Gold Nanoparticles for Biomedicine. *Chem. Soc. Rev.* **2012**, *41*, 2740−2779.
(697) Gobin, A. M.; Lee, M. H.; Halas, N. J.; James, W. D.; Drezek, R. A.; West, J. L. Near-Infrared Resonant Nanoshells for Combined Optical Imaging and Photothermal Cancer Therapy. *Nano Lett.* **2007**, *7*, 1929−1934.
(698) Sreethawong, T.; Yoshikawa, S. Impact of Photochemically Deposited Monometallic Pt and Bimetallic Pt−Au Nanoparticles on Photocatalytic Dye-Sensitized H_2 Production Activity of Mesoporous-Assembled TiO_2−SiO_2 Mixed Oxide Nanocrystal. *Chem. Eng. J.* **2012**, *197*, 272−282.
(699) Chiu, C.-Y.; Yang, M.-Y.; Lin, F.-C.; Huang, J.-S.; Huang, M. H. Facile Synthesis of Au-Pd Core-Shell Nanocrystals with Systematic Shape Evolution and Tunable Size for Plasmonic Property Examination. *Nanoscale* **2014**, *6*, 7656−7665.
(700) Tsukamoto, D.; Shiro, A.; Shiraishi, Y.; Sugano, Y.; Ichikawa, S.; Tanaka, S.; Hirai, T. Photocatalytic H_2O_2 Production from Ethanol/O_2 System Using TiO_2 Loaded with Au−Ag Bimetallic Alloy Nanoparticles. *ACS Catal.* **2012**, *2*, 599−603.
(701) Guo, L.; Jackman, J. A.; Yang, H.-H.; Chen, P.; Cho, N.-J.; Kim, D.-H. Strategies for Enhancing the Sensitivity of Plasmonic Nanosensors. *Nano Today* **2015**, *10*, 213−239.
(702) Aslam, U.; Chavez, S.; Linic, S. Controlling Energy Flow in Multimetallic Nanostructures for Plasmonic Catalysis. *Nat. Nanotechnol.* **2017**, *12*, 1000−1005.
(703) Ng, C.; Cadusch, J. J.; Dligatch, S.; Roberts, A.; Davis, T. J.; Mulvaney, P.; Gómez, D. E. Hot Carrier Extraction with Plasmonic Broadband Absorbers. *ACS Nano* **2016**, *10*, 4704−4711.
(704) Zhang, Y.; He, S.; Guo, W.; Hu, Y.; Huang, J.; Mulcahy, J. R.; Wei, W. D. Surface-Plasmon-Driven Hot Electron Photochemistry. *Chem. Rev.* **2018**, *118*, 2927−2954.
(705) Wang, S.; Gao, Y.; Miao, S.; Liu, T.; Mu, L.; Li, R.; Fan, F.; Li, C. Positioning the Water Oxidation Reaction Sites in Plasmonic Photocatalysts. *J. Am. Chem. Soc.* **2017**, *139*, 11771−11778.
(706) Sakamoto, H.; Imai, J.; Shiraishi, Y.; Tanaka, S.; Ichikawa, S.; Hirai, T. Photocatalytic Dehalogenation of Aromatic Halides on Ta_2O_5-Supported Pt-Pd Bimetallic Alloy Nanoparticles Activated by Visible Light. *ACS Catal.* **2017**, *7*, 5194−5201.
(707) Yu, S.; Wilson, A. J.; Heo, J.; Jain, P. K. Plasmonic Control of Multi-Electron Transfer and C−C Coupling in Visible-Light-Driven CO_2 Reduction on Au Nanoparticles. *Nano Lett.* **2018**, *18*, 2189−2194.
(708) Zhang, J.; Lu, Y.; Ge, L.; Han, C.; Li, Y.; Gao, Y.; Li, S.; Xu, H. Novel AuPd Bimetallic Alloy Decorated 2D $BiVO_4$ Nanosheets with Enhanced Photocatalytic Performance under Visible Light Irradiation. *Appl. Catal., B* **2017**, *204*, 385−393.
(709) Bhunia, K.; Chandra, M.; Khilari, S.; Pradhan, D. Bimetallic PtAu Alloy Nanoparticles-Integrated g-C_3N_4 Hybrid as an Efficient Photocatalyst for Water-to-Hydrogen Conversion. *ACS Appl. Mater. Interfaces* **2019**, *11*, 478−488.
(710) Skrabalak, S. E.; Chen, J.; Au, L.; Lu, X.; Li, X.; Xia, Y. Gold Nanocages for Biomedical Applications. *Adv. Mater.* **2007**, *19*, 3177−3184.
(711) Xia, Y.; Li, W.; Cobley, C. M.; Chen, J.; Xia, X.; Zhang, Q.; Yang, M.; Cho, E. C.; Brown, P. K. Gold Nanocages: From Synthesis to Theranostic Applications. *Acc. Chem. Res.* **2011**, *44*, 914−924.
(712) Tong, L.; Cobley, C. M.; Chen, J.; Xia, Y.; Cheng, J.-X. Bright Three-Photon Luminescence from Gold/Silver Alloyed Nanostructures for Bioimaging with Negligible Photothermal Toxicity. *Angew. Chem., Int. Ed.* **2010**, *49*, 3485−3488.
(713) Chen, H.; Wang, H.; Slipchenko, M. N.; Jung, Y.; Shi, Y.; Zhu, J.; Buhman, K. K.; Cheng, J.-X. A Multimodal Platform for Nonlinear Optical Microscopy and Microspectroscopy. Opt. *Opt. Express* **2009**, *17*, 1282−1290.

https://dx.doi.org/10.1021/acs.chemrev.0c00436
Chem. Rev. 2021, 121, 736−795

(714) Gu, H.; Ho, P.-L.; Wt Tsang, K.; Yu, C.-W.; Xu, B. Using Biofunctional Magnetic Nanoparticles to Capture Gram-Negative Bacteria at an Ultra-Low Concentration. *Chem. Commun.* **2003**, 1966−1967.
(715) Gu, H.; Ho, P.-L.; Tsang, K. W. T.; Wang, L.; Xu, B. Using Biofunctional Magnetic Nanoparticles to Capture Vancomycin-Resistant Enterococci and Other Gram-Positive Bacteria at Ultralow Concentration. *J. Am. Chem. Soc.* **2003**, *125*, 15702−15703.
(716) Pan, L.; Bogy, D. B. Heat-Assisted Magnetic Recording. Nat. *Nat. Photonics* **2009**, *3*, 189−190.
(717) Weller, D.; Mosendz, O.; Parker, G.; Pisana, S.; Santos, T. S. $L1_0$ FePtX−Y Media for Heat-Assisted Magnetic Recording. Phys. *Phys. Status Solidi A* **2013**, *210*, 1245−1260.
(718) Seo, W. S.; Lee, J. H.; Sun, X.; Suzuki, Y.; Mann, D.; Liu, Z.; Terashima, M.; Yang, P. C.; McConnell, M. V.; Nishimura, D. G.; Dai, H. FeCo/Graphitic-Shell Nanocrystals as Advanced Magnetic-Resonance-Imaging and Near-Infrared Agents. *Nat. Mater.* **2006**, *5*, 971−976.
(719) Ullah, A. K. M. A.; Kabir, M. F.; Akter, M.; Tamanna, A. N.; Hossain, A.; Tareq, A. R. M.; Khan, M. N. I.; Kibria, A. K. M. F.; Kurasaki, M.; Rahman, M. M. Green Synthesis of Bio-Molecule Encapsulated Magnetic Silver Nanoparticles and Their Antibacterial Activity. *RSC Adv.* **2018**, *8*, 37176−37183.
(720) Peng, B.; Zhang, X.; Aarts, D. G. A. L.; Dullens, R. P. A. Superparamagnetic Nickel Colloidal Nanocrystal Clusters with Antibacterial Activity and Bacteria Binding Ability. *Nat. Nanotechnol.* **2018**, *13*, 478−482.
(721) Kittel, C. Theory of the Structure of Ferromagnetic Domains in Films and Small Particles. *Phys. Rev.* **1946**, *70*, 965−971.
(722) Brown, W. F. Thermal Fluctuations of a Single-Domain Particle. *Phys. Rev.* **1963**, *130*, 1677−1686.
(723) Kneller, E. F.; Luborsky, F. E. Particle Size Dependence of Coercivity and Remanence of Single-Domain Particles. *J. Appl. Phys.* **1963**, *34*, 656−658.
(724) Kim, D.; Lee, N.; Park, M.; Kim, B. H.; An, K.; Hyeon, T. Synthesis of Uniform Ferrimagnetic Magnetite Nanocubes. *J. Am. Chem. Soc.* **2009**, *131*, 454−455.
(725) Song, Q.; Zhang, Z. J. Shape Control and Associated Magnetic Properties of Spinel Cobalt Ferrite Nanocrystals. *J. Am. Chem. Soc.* **2004**, *126*, 6164−6168.
(726) Jun, Y.-w.; Huh, Y.-M.; Choi, J.-s.; Lee, J.-H.; Song, H.-T.; Kim, S.; Yoon, S.; Kim, K.-S.; Shin, J.-S.; Suh, J.-S.; Cheon, J. Nanoscale Size Effect of Magnetic Nanocrystals and Their Utilization for Cancer Diagnosis via Magnetic Resonance Imaging. *J. Am. Chem. Soc.* **2005**, *127*, 5732−5733.
(727) Kota, Y.; Sakuma, A. Magnetocrystalline Anisotropy in FePt with $L1_0$ Ordering and Tetragonal Distortion. *J. Appl. Phys.* **2012**, *111*, 07A310.
(728) Alikhanzadeh-Arani, S.; Salavati-Niasari, M.; Almasi-Kashi, M. Morphologies and Magnetic Properties of FeCo Nanoparticles Modulated by Changing the Types of Ligands of Co. *J. Magn. Magn. Mater.* **2012**, *324*, 3652−3657.
(729) Liu, C.; Wu, X.; Klemmer, T.; Shukla, N.; Weller, D.; Roy, A. G.; Tanase, M.; Laughlin, D. Reduction of Sintering during Annealing of FePt Nanoparticles Coated with Iron Oxide. *Chem. Mater.* **2005**, *17*, 620−625.
(730) Park, J.-I.; Kim, M. G.; Jun, Y.-w.; Lee, J. S.; Lee, W.-r.; Cheon, J. Characterization of Superparamagnetic "Core−Shell" Nanoparticles and Monitoring Their Anisotropic Phase Transition to Ferromagnetic "Solid Solution" Nanoalloys. *J. Am. Chem. Soc.* **2004**, *126*, 9072−9078.
(731) Lee, D. C.; Smith, D. K.; Heitsch, A. T.; Korgel, B. A. Colloidal Magnetic Nanocrystals: Synthesis, Properties and Applications. *Annu. Rep. Prog. Chem., Sect. C: Phys. Chem.* **2007**, *103*, 351−402.
(732) Huh, Y.-M.; Jun, Y.-w.; Song, H.-T.; Kim, S.; Choi, J.-s.; Lee, J.-H.; Yoon, S.; Kim, K.-S.; Shin, J.-S.; Suh, J.-S.; Cheon, J. In Vivo Magnetic Resonance Detection of Cancer by Using Multifunctional Magnetic Nanocrystals. *J. Am. Chem. Soc.* **2005**, *127*, 12387−12391.
(733) Song, Q.; Ding, Y.; Wang, Z. L.; Zhang, Z. J. Formation of Orientation-Ordered Superlattices of Magnetite Magnetic Nanocrystals from Shape-Segregated Self-Assemblies. *J. Phys. Chem. B* **2006**, *110*, 25547−25550.
(734) Li, D.; Poudyal, N.; Nandwana, V.; Jin, Z.; Elkins, K.; Liu, J. P. Hard Magnetic FePt Nanoparticles by Salt-Matrix Annealing. *J. Appl. Phys.* **2006**, *99*, 08E911.
(735) Szczytko, J.; Osewski, P.; Bystrzejewski, M.; Borysiuk, J.; Grabias, A.; Huczko, A.; Lange, H.; Majhofer, A.; Twardowski, A. Carbon-Encapsulated Magnetic Nanoparticles Based on Fe, Mn, and Cr for Spintronics Applications. *Acta Phys. Pol., A* **2007**, *112*, 305−310.
(736) Jana, N. R.; Chen, Y.; Peng, X. Size- and Shape-Controlled Magnetic (Cr, Mn, Fe, Co, Ni) Oxide Nanocrystals via a Simple and General Approach. *Chem. Mater.* **2004**, *16*, 3931−3935.
(737) Moser, A.; Takano, K.; Margulies, D. T.; Albrecht, M.; Sonobe, Y.; Ikeda, Y.; Sun, S.; Fullerton, E. E. Magnetic Recording: Advancing into the Future. *J. Phys. D: Appl. Phys.* **2002**, *35*, R157−R167.
(738) Dai, Z. R.; Sun, S.; Wang, Z. L. Shapes, Multiple Twins and Surface Structures of Monodisperse FePt Magnetic Nanocrystals. *Surf. Sci.* **2002**, *505*, 325−335.
(739) Millstone, J. E.; Wei, W.; Jones, M. R.; Yoo, H.; Mirkin, C. A. Iodide Ions Control Seed-Mediated Growth of Anisotropic Gold Nanoparticles. *Nano Lett.* **2008**, *8*, 2526−2529.

https://dx.doi.org/10.1021/acs.chemrev.0c00436
Chem. Rev. 2021, 121, 736−795